Bio-Inspired Optical Components

by

Joseph John Walish

B.S. Materials Science and Engineering
University of Arizona, 2001

SUBMITTED TO THE DEPARTMENT OF MATERIALS SCIENCE AND ENGINEERING IN PARTIAL FULFILLMENT OF THE REQUIREMENTS FOR THE DEGREE OF

DOCTOR OF PHILOSOPHY IN MATERIALS SCIENCE AND ENGINEERING
AT THE
MASSACHUSETTS INSTITUTE OF TECHNOLOGY

JUNE 2008

Signature of Author: _____
Department of Materials Science and Engineering
May 15th, 2008

Certified by: _____
Edwin L. Thomas
Morris Cohen Professor of Materials Science and Engineering
Thesis Supervisor

Accepted by: _____
Samuel M. Allen
POSCO Professor of Physical Metallurgy
Chair, Departmental Committee on Graduate Students

Bio-Inspired Optical Components

by

Joseph John Walish

B.S. Materials Science and Engineering
University of Arizona, 2001

Submitted to the Department of Materials Science and Engineering on May 15th, 2008, in Partial Fulfillment of the Requirements for the Degree of Doctor of Philosophy in Materials Science and Engineering.

Abstract

Guiding electro-magnetic radiation is fundamental to optics. Lenses, mirrors, and photonic crystals all accomplish this task by different routes. Understanding the interaction of light with materials is fundamental to improving and extending optical science and engineering as well as producing novel optical elements. Improvement in this understanding should not only include work to understand the interaction with traditional engineering materials but also should target the understanding of the interaction of electromagnetic radiation with biological structures as millions of years of evolution have sorted out numerous ways to modulate light (e.g. the fish eye or the skin of the octopus). The goal of this thesis work is to fabricate novel optical elements by taking cues from nature and extending the state of the art in light guiding behavior. Here, optical elements are defined as structured materials that guide or direct electromagnetic radiation in a predetermined manner. The work presented in this thesis encompasses biologically inspired tunable multilayer reflectors made from block copolymers and improvements to liquid filled lenses which mimic the human eye.

In this thesis a poly(styrene)-poly(2-vinylpyridine) block copolymer was used to create a bio-mimetic, one-dimensional, multilayer reflector. The wavelengths of light reflected from this multilayer reflector or Bragg stack were tuned by the application of stimuli which included temperature, change in the solvent environment, pH, salt concentration in the solvent, and electrochemistry. A linear-shear rheometer was also built to investigate the mechanochromic color change brought about through the shearing of a one-dimensional, high molecular-weight, block-copolymer, photonic gel. Biologically inspired lenses were also studied through the construction of a finite element model which simulated the behavior of a liquid-filled lens. Several tunable parameters, such as the modulus, internal residual stress, and thickness of the membrane were studied for their influence on the shape of the lens membrane. Based on these findings, suggestions for the reduction of spherical aberration in a liquid filled lens were made. A gradient in the elastic modulus of the membrane was also investigated for use in the reduction of spherical aberration.

Thesis Supervisor: Edwin L. Thomas
Title: Department Head and Morris Cohen Professor of Materials Science and Engineering

Acknowledgements

From a young age I think I've always had a passion for engineering and I'd like to take this brief opportunity to thank those who have helped me learn this wonderful discipline. In graduate school, the relationship between advisor and advisee is an important one and I have had the great fortune of being able to work for Professor Edwin Thomas. I have benefited immensely from his tutelage and have been blessed with steady funding, interesting projects, and enormous latitude to explore a wide variety of topics. Under his guidance I have not only been able to conduct research, but have improved my abilities to communicate results through both oral and written communication.

As always, labmates are key to the success of any graduate student and I would like to especially thank Raf Mickewicz and (now Dr.) Nick Tsui. Dr. Taras Gorishnyy and Henry Koh also deserve special mention as does Dr. Thomas Breiner.

Professor Youngjong Kang of Hanyang University in Korea deserves special recognition as I am following in his footsteps with the work on the poly(styrene)-b-poly(2-vinylpyridine) photonic gels. Without his initial contributions, chapters three, four, and five would not exist and for this I am indebted to him.

Dr. Roger Hanlon and Professors Cima, Sadoway, and Swager helped me understand various biological, physical, and chemical phenomena and I appreciate the time they have taken to help me through my course of study. Also Dr. Ranji Vaidyanathan, who was my mentor while working as an undergraduate, deserves special recognition and without his help and encouragement I would never have made it into MIT in the first place.

I would like to thank the members of my thesis committee, Professor Samuel Allen and Professor Michael Rubner, for their helpful comments, patience, and understanding as I made my way through the process of putting together my thesis. I want to especially acknowledge Professor Rubner for his guidance and support not only while I was working on the Bio-Inspired Optical Synthetic Systems (BOSS) project but afterwards as well.

I would like to thank my UROPs (Josh Lake, Leslie Nachbar, Josh Dittrich, Tyco Skinner, and Xavier Gonzalez) who put in countless hours and helped produces the experimental results detailed in the rest of this work.

I will always have fond memories of my time with Craig Forest, Alex Yip, and Andy Copeland, former residents of the suite 504 in Ashdown House. Craig for putting up with my collection of treasures found in various places and for the experience known appropriately as "the biz" and Alex, for his enthusiasm for bike riding and projects of all sorts. Also, thanks to my most recent roommate, Philippe Block, for being as messy as I am and for introducing me to some quality Belgian music. The group of students in my incoming graduate class deserves mention especially Adam Nolte, Brad Peterson, Caroline Lau, Amanda Giermann, and the rest of the first year crew who helped me survive the first year in grad school. I am probably forever indebted (possibly indentured) to Judy Lin, my one and only "beautiful lab assistant," who even became slave labor at one point in time.

Most of all, I would like to thank my Mom and Dad for their constant love and support for without their good example I would not be here.

Contents

List of Figures

List of Tables

Thesis Overview

Chapter one provides the reader an overview of the interaction of light with materials and specifically concentrates on the topic of interference-reflection which forms a basis for the majority of the work in this thesis. The topics of natural and synthetic interference reflectors (photonic crystals), block copolymers, polymeric gels and solubility will also be covered.

Chapter two focuses on the experimental techniques and procedures used while conducting the thesis research with special attention is paid to sample preparation techniques used to ensure alignment and ordering of the block copolymer reflectors. Sample preparation procedures for the poly(styrene)-poly(2-vinylpyridine) (PS-P2VP) and poly(styrene)-poly(methyl methacrylate) (PS-PMMA) block copolymer reflectors are detailed and various annealing practices discussed.

In chapter three the behavior of PS-P2VP block copolymer photonic gels in various solvents is investigated. This copolymer photonic system requires the use of a solvent to swell the P2VP domains in order to reflect visible wavelengths of light. The optical properties of this multilayer structured reflector are explored through the use of various solvent swelling agents as well as different molecular weights of PS-P2VP. The effects of chemical reactions (specifically protonation and quaternization of the P2VP) on the swelling behavior and thus the optical properties are investigated.

Chapter four covers the thermochromic or temperature-related color change in PS-P2VP photonic gels. Natural and synthetic thermochromic materials are explored as a way of providing a background for the study of the PS-P2VP system. Color changes (or

lack thereof) in methanol, acetic acid/water solutions, and de-ionized water (quaternized P2VP) are explained.

The electrochemical color change in PS-P2VP is explored in chapter five including the behavior of quaternized PS-P2VP samples in ethanol, protonated PS-P2VP samples in trifluoroacetic acid-ethanol solutions, and 2,2,2-trifluoroethanol swollen PS-P2VP under the influence of an applied electrical potential. A brief overview of electrochemical processes is also provided.

Chapter six highlights the design and construction of a linear shear rheometer for the measurement of the rheological and optical properties of high molecular-weight block copolymers. Design ambitions and the specific parameters chosen for the construction of the device are explained after a discussion of the previous research into materials that change color with mechanical deformation (mechanochromics). Preliminary experiments are performed on a 25% solution of a high molecular weight block copolymer (poly(styrene)-poly(methyl methacrylate) 360k-280k) in toluene. Slow, linear shear produced no color change and fast, uni-directional shear produced a change from colored to transparent samples. Fast, cyclic shear produced a color change from the initial green color to a bright red upon shearing one direction while cycling back produced a blue-green color (slightly blue-shifted from the original green color).

Chapter seven details the finite-element modeling and optimization studies which were done on a liquid filled lens which changes its focal length by increasing the pressure of a liquid contained between one or two transparent, elastomeric membranes. An overview of previous work is presented followed by a discussion of the two-dimensional, axi-symmetric model constructed for the optimization experiments. The optimum

surface profile for the elimination of spherical aberration is identified and three parameters are tested for their ability to make the shape of the inflated lens match more closely the perfect lens profile.

Finally, the conclusions and future work chapter highlights the research presented in this thesis as well as suggests several new directions for the continuation of the work. Three appendices are included detailing other aspects of the thesis work, including nanoparticle gradient-index lenses, the finite-element simulation of the phononic properties of polymer multilayers, and research related artwork.

Chapter 1:
Introduction and Background

Nature provides striking examples of dynamic coloration in many animal families and most especially in the cephalopods. The ability of the octopus (a member of the cephalopod family) to change the color and texture of its skin to match that of the surrounding environment is simply amazing[1] (see Figure 1.1) and this manipulability is unmatched by man-made materials. Other animals, as will be seen later in this chapter and throughout this thesis, have similar abilities to change the color of *structural* reflectors contained within their bodies. These reflectors do not contain absorbing pigments or molecules but instead use the principle of diffraction to reflect certain wavelengths of light.

Taking cues from the natural world and extracting design principles from naturally occurring optical elements is the overarching theme of this thesis. By giving dynamic aspects to traditionally static elements such as multilayer reflectors, new and

interesting devices can be made. The work described in subsequent chapters dealing with tunable multilayer reflectors builds off of knowledge of biological reflectors contained in many terrestrial and aquatic animals.

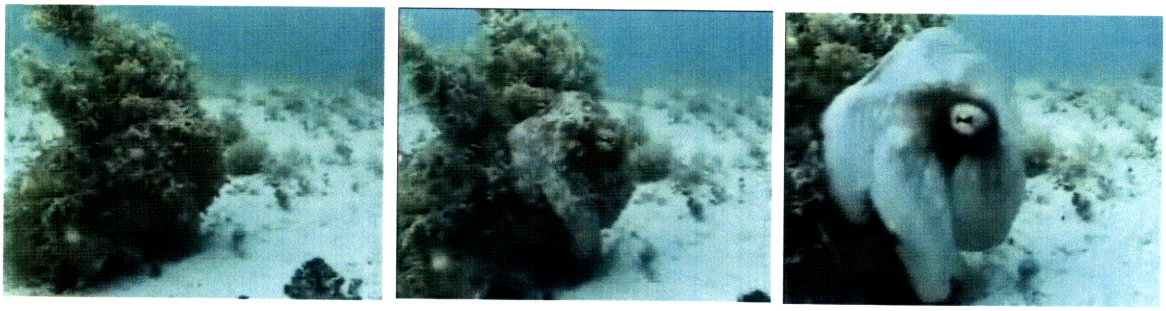

Concealed | Deciding to flee | Aggressive display before fleeing

Figure 1.1: The amazing abilities of an octopus to conceal itself - (Top) Cephalopods are able to change the color and texture of their skin through manipulation of absorbent pigment saccules controlled by muscles within the skin. In this series of images taken by Roger Hanlon of Woods Hole Oceanographic Institute, the octopus blends seamlessly into its surroundings and is only visible after deciding to flee. Some members of the cephalopod family (which the octopus belongs to) also have the ability to rapidly change the color of their skin through manipulating multilayer reflectors.

By observing the way that the human eye accommodates or changes its focal length, principles for constructing tunable focal-length lenses can be obtained which give optical engineers additional parameters to use when designing a lens system. By adjusting the curvature and/or the index of refraction of the lens, one can create a *dynamic* focal length lens as is employed in many biological optical systems. Advances in computation and materials research have extended the suite of materials and analysis techniques available to the optical engineer. The material presented in chapter seven takes advantage of this fact through the use of the finite-element method to improve the deformation behavior of a liquid filled lens such that it deforms with a shape that more closely matches the optimal curvature that will eliminate spherical aberration in the lens.

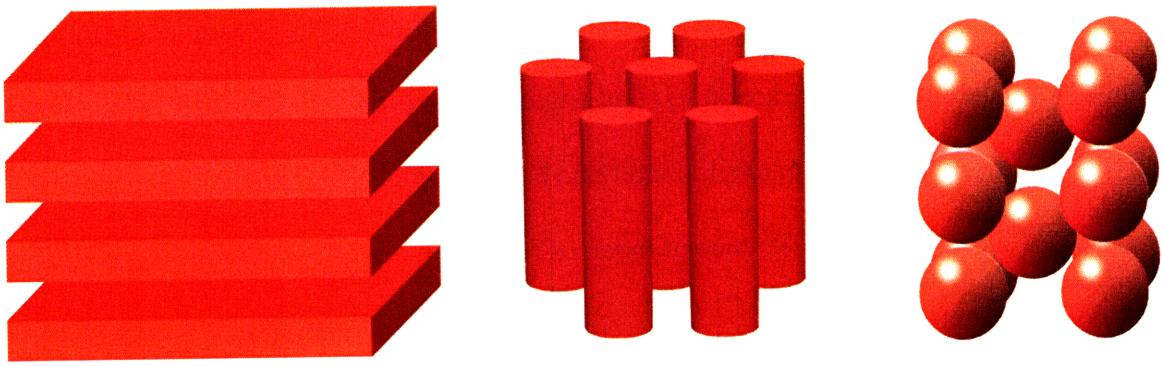

Figure 1.2: One, two, and three-dimensional photonic crystals – Periodic arrangements of high and low refractive index materials have the ability to reflect certain wavelengths of light if the angle which with light interacts with the structure and the spatial modulation of a material's index of refraction satisfy the diffraction condition.

Multilayer reflectors or Bragg stacks are layered structures which reflect different wavelengths of light depending on the angle of incidence of the light and the thickness and index of refraction of the layers. These traditionally static elements can be made dynamic by a change in any of the aforementioned variables. These layered structures are a subclass of heterogeneous materials known as photonic crystals which through interference phenomena forbid or limit the propagation of certain modes of light in certain directions through the periodic modulation of a material's index of refraction. A material is said to have a 'band gap' if all directions and polarizations are prohibited from propagating in a material for a given set of wavelengths. A 'stop band' is a partial band gap where certain wavelengths of light are prohibited over some but not all angles and polarizations.

1.1 Color through diffraction

One effect of the mysterious wave/particle duality is the wave nature of light and its ability to interfere with itself. The phenomenon of interference gives rise to constructive amplification and destructive cancellation. Consider the case where a wave

(visible light) travels through a medium with index of refraction n_1 toward an object with thickness d and index of refraction n_2 at an angle θ with respect to the surface normal (see figure 1.3). The light encounters the interface between the media and is partially reflected (because of the difference in index of refraction between materials 1 and 2) and partially transmitted.

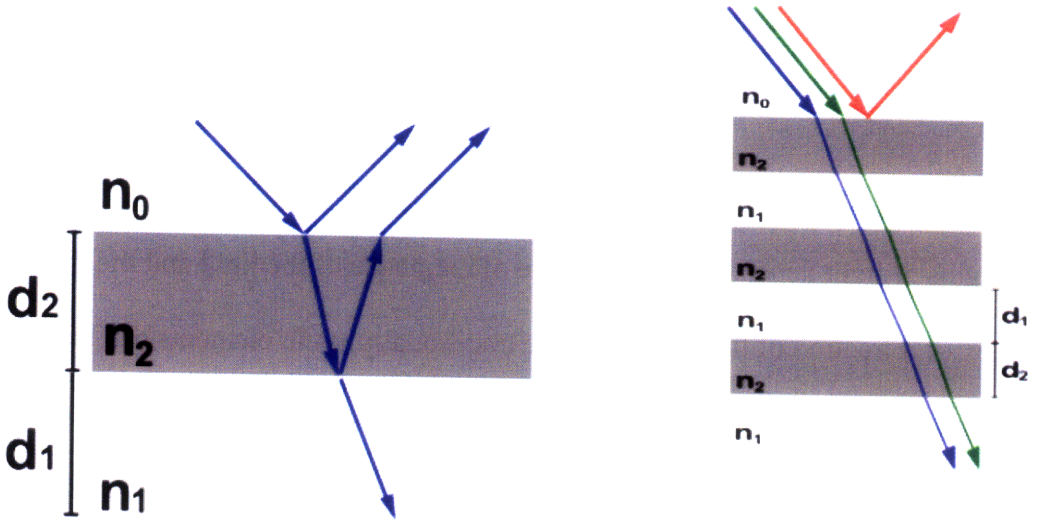

Figure 1.3: Reflection, refraction, and diffraction of incoming waves – Light impinges on the substrate (grey slab on the left) and is reflected and refracted at the interface. The refracted light hits the second interface and is again reflected and refracted. Light reflected from the second interface encounters the first interface again. If the optical path length (the product of n_2 and d) is equal to half of the wavelength of light, diffraction will occur and that wavelength will be selectively reflected from the structure while other wavelengths will be transmitted. The intensity of the reflection will increase if multiple layers are used. The figure on the right illustrates a multilayer reflector selectively reflecting red light.

The transmitted light is refracted and travels through the material until it hits the backside of the slab where again a portion is reflected and a portion transmitted. The reflected portion of light travels back through the slab until it reaches the first interface where again refraction and reflection take place. If the optical path length (index of refraction multiplied by the thickness of the layer) is equal to half the wavelength of light, the light coming out of the slab will be 180° out of phase with the incoming light. This leads to the diffraction of that wave, since it cannot propagate inside the medium it is reflected at an angle commensurate with the angle of incidence. Color from interference

effects is produced by selective reflection of particular wavelengths of light while others are transmitted (see figure 1.3). This can be seen in daily life from the iridescent colors produced by thin films of gasoline on water to the subtle coloration of soap bubbles produced by thin films of surfactant soap molecules. These effects are produced through the reflection of light through single layers of material. The intensity of the reflection can be increased by employing an increasing number of layers.

For the designer of multilayer reflectors, relationships have been developed which predict the wavelength of peak reflective intensity. For a stack consisting of two materials of thicknesses d_1 and d_2 with indices of refraction of n_1 and n_2 the wavelength of maximum intensity at normal incidence is described by the following equation[2]:

$$\lambda_{max} = 2\ (n_1 d_1 + n_2 d_2)$$

This general case is labeled "ideal" when $n_1 d_1 = n_2 d_2$ as it produces the most efficient reflective properties[3] (i.e. for a given number of repeat units the percent of incoming light reflected is highest.) When the optical path lengths for each layer are the same (the "ideal" case) the above relationship reduces to:

$$\lambda_{max} = 4\ (n_x d_x)$$

This "ideal" multilayer reflector is dubbed a quarter-wave stack and the choice of subscript on the index and thickness variables is arbitrary (represented with an x) since the optical path lengths of both layers are equal.

As will be shown in the next section, multilayer reflectors such as these and other more complicated photonic structures are plentiful in nature. Through the careful examination of these structures and their design principles, advances in synthetic photonic materials can be made.

1.2 Natural Photonic Crystals

Although coloration through the absorbance of selected wavelengths of light through natural dyes and pigments produces the majority of color in nature,[4] several early (and notable) researchers such as Robert Hooke and Isaac Newton identified structural color in the animal kingdom with Hooke describing an insect[5] in 1665 and Newton explaining the color of peacock feathers[6] in 1730. However, it was not until the advent of the electron microscope in the 20th century that the study of natural structural color (photonic structures) in flora and fauna was undertaken with earnest[7]. A number of excellent review articles[2,4,8,9,10,11] surveying the field of structural color in animals exist some noteworthy examples of natural reflectors are discussed below.

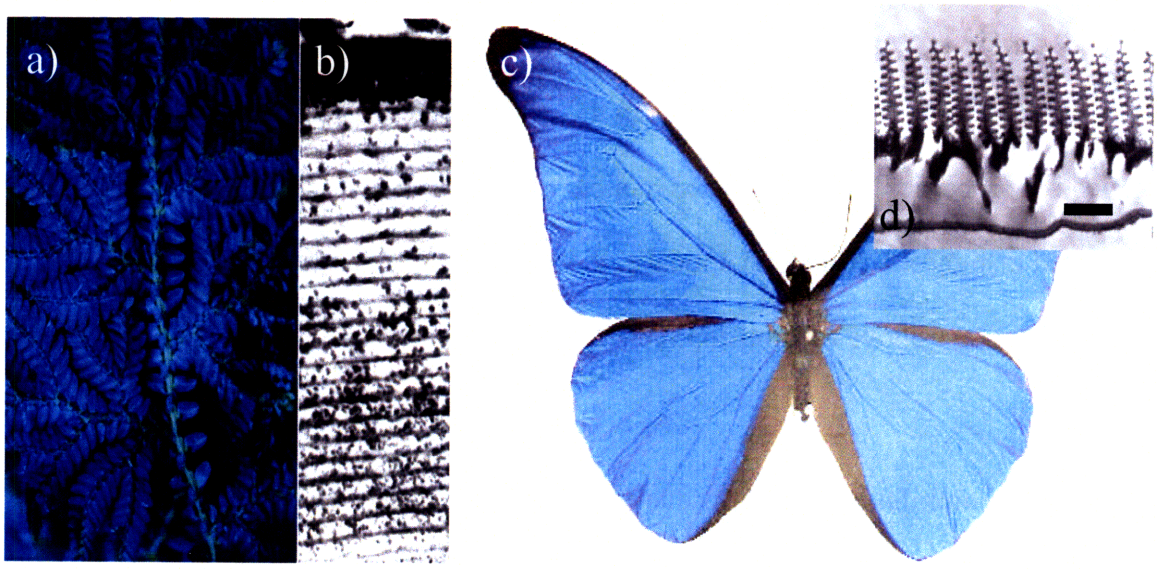

Figure 1.4: Natural photonic crystals – The blue, iridescent color of tropical fern-like plants of the genus *Selaginella* (a) is brought about through multilayer reflectors such as the one pictured in (b) and the blue color of the morpho butterfly wing (c) is produced through diffraction in the complex, three dimensional structures seen in (d) (scale bar 1.8 microns). (adapted from references 9 and 10)

An extremely wide variety of species have developed structural coloration for a variety of purposes including, but not limited to: camouflage to escape predation,[12,13,14] light gathering to enhance the efficiency of the eye, [15,16] and pattern display for inter- and

intraspecies communication.[17,18,19] Commonly one-dimensional multilayer stacks are used to produce natural structural color but other structures such as the chiral structures in the cuticle of a scarab beetle,[20] the chitin structures with tree-like cross-sections in the wing of the morpho butterfly (see figure 1.4), and the three-dimensional cuticle structure in the butterfly *Parides sesostris* which displays almost diamond lattice-like symmetry[21,22] are used to create brilliant colors.

Commonly encountered features such as the silver color of fish scales are usually produced through deposits of a crystalline substance known as guanine ($n_{guanine}$~1.83) in a matrix of cytoplasm ($n_{cytoplasm}$~1.33)[4] although a material similar to guanine, hypoxanthine is also found in some species.[23] These silver or golden colored fish scales exhibit broad-band reflectivity due in part to the high refractive index difference between the guanine and cytoplasm and a non-uniform spacing of the platelets. It has been noted though that the high index guanine platelets do exhibit notable birefringence (n=1.81 perpendicular to the platelet and 1.46 in the plane of the platelet)[24] leading to a possibility that other more complicated effects could be at play similar to those found in the broad-band, birefringent, reflecting plastics recently commercially produced by the 3M company.[25] Other strategies have been used by nature to create broad-band reflectivity including (see figure 1.5) layering of multiple discrete multilayer stacks, the systematic variation of layer thickness from thick to thin (a chirped stack), or an arbitrary arrangement of low- and high-index layer spacings as in the fish reflectors mentioned above.

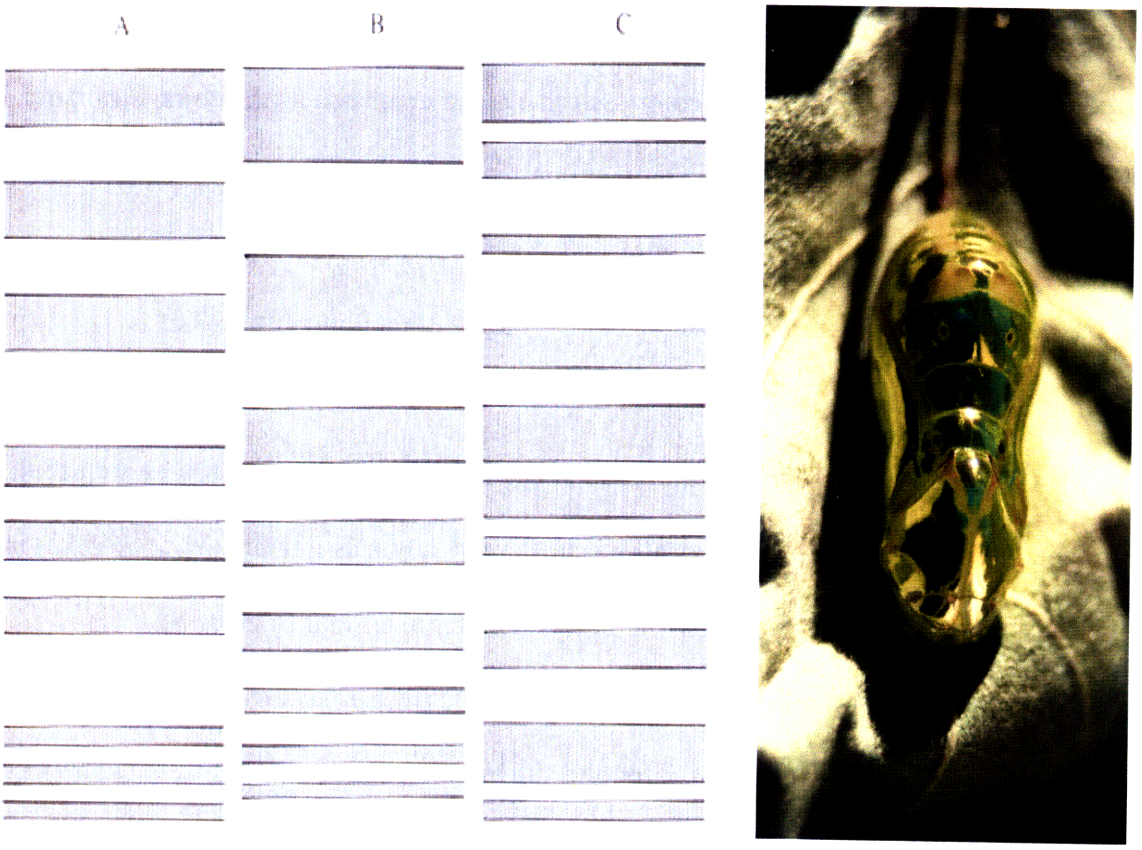

Figure 1.5: Natural strategies for the production of broad-band reflectivity – A) The additive effect of using multiple stacks with different periods produces the effect of a silver surface (i.e. a broad band reflector). B) A set of stacks continuously changing periodicity. This is known as 'chirping' the stack and produces a broad reflectivity peak. C) An irregular spaced array can also produce similar results. The gold chrysalis of the Euoplea core butterfly is an example of the chirping of a multilayer stack. (adapted from reference 8)

Although most structural coloration is comprised of static components and therefore cannot change, there are several species of both terrestrial and aquatic animals that have the ability to *change* the spacing of the photonic crystals contained in their bodies and thus the color of reflected light.[26,27,28,29] All of these animals possess cells known as iridophores which contain one-dimensionally periodic reflectors composed of alternating high- and low-index layers. The high-index material commonly takes the form of crystalline platelets composed of guanine or hypoxanthine as mentioned earlier, but some species of squid use a self assembling protein.[30,31] The low-index layer is usually water-filled cytoplasm or extra-cellular space that when the called upon can

collapse by expelling water through triggering by secretions from the endocrine or central nervous system.[32] The paradise whiptail (seen in figure 1.6) can change the wavelength reflected by its stripes by almost 200nm from 460nm to 650nm in approximately a quarter of a second. These quick changes in natural tunable photonic crystals are akin to the spectral changes in gel-based synthetic colloidal crystals discussed in the next section.

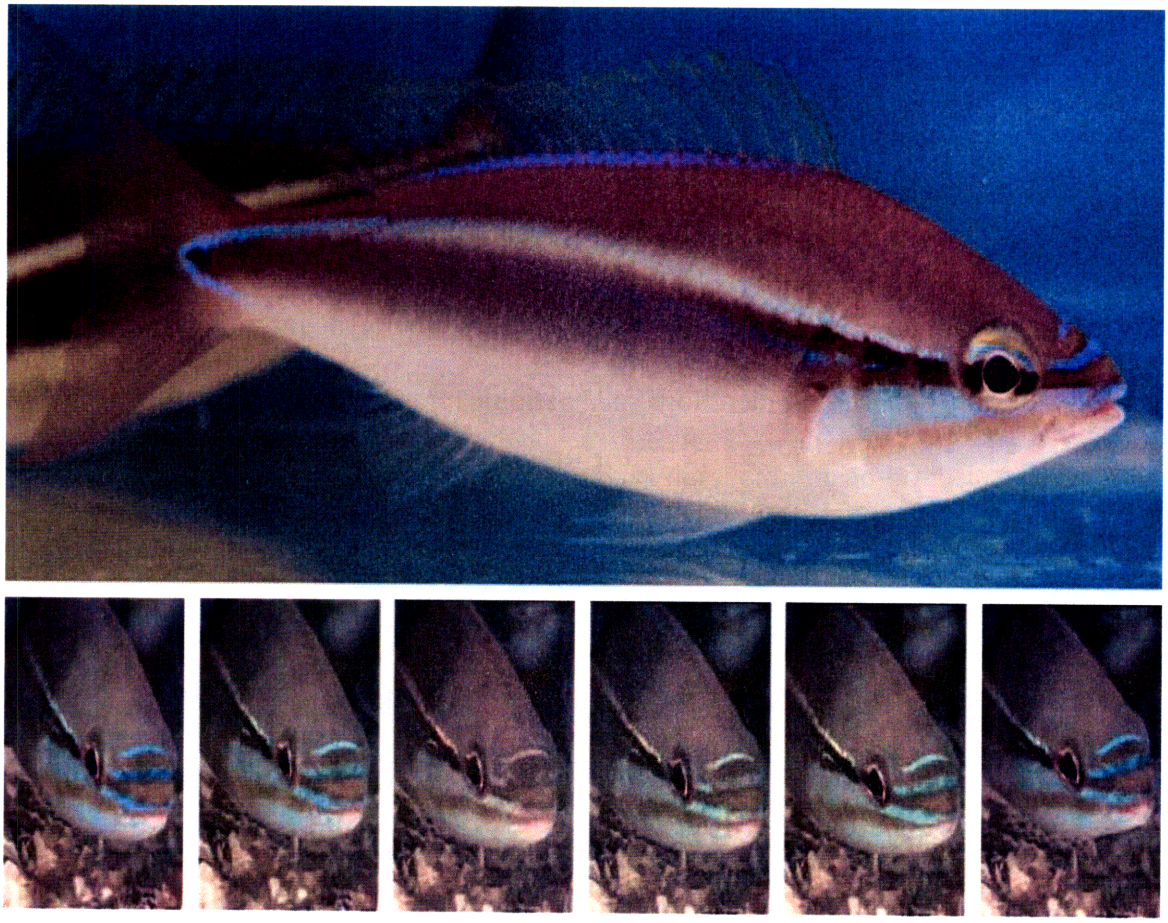

Figure 1.6: Motile iridophores in the paradise whiptail – Motile or tunable photonic structures in this fish change from blue to red within 0.25 seconds. A change in spacing between the high index platelets in the multilayer reflector is responsible for this effect. This change is under the control of the sympathetic nervous system and is thought to be a signaling device. (adapted from reference 29)

1.3 Synthetic Photonic Crystals

Although a variety of 'photonic' multilayer films made from either sequentially evaporated semiconductors and/or oxides[33] or the co-extrusion of plastics and/or elastomers[34] have been produced for over 60 years to make extremely high-reflectivity

mirrors at specific wavelengths, it was not until 1987 with the paper by Yablonovich[35] that the wider scientific community realized that the 3D spatial modulation of a materials index of refraction could lead to the control of spontaneous emission (and thus more generally light propagation) in a material. A wide variety of man-made photonic crystals have been constructed since this seminal insight, many targeting a complete photonic band-gap in three dimensions with the goal of providing a platform for integrated microphotonic circuitry.[36] For this purpose photonic crystals with diamond or diamond-like symmetry have been sought after because of their large and robust photonic band gap.[37] A common example of an experimentally produced photonic crystal which approximates diamond symmetry is the woodpile structure made by stacking lithographically patterned silicon 'logs' in a periodic array.[38] Other techniques such as direct write electron-beam lithography and interference lithography have been able to produce three-dimensionally periodic photonic crystals with extremely large and robust band-gaps, but thus far the tunability of those gaps has been rather limited. A one-dimensional stack of silicon and air can be used as a tunable photonic crystals. The work by Sailor, et al. has demonstrated electrochemically etched periodic structures which were filled with organic polymers. After the removal of the silica the stimulus responsive replica can be used for sensing vapors or the monitoring of drug delivery.[39,40] The rest of this brief overview will focus on *tunable* photonic crystals and their stimuli.

Colloidal crystalline arrays (CCAs),[41,42,43] produced from monodisperse spheres usually made out of silica or polystyrene, were the first photonic crystals to be constructed with extensive stimulus responsive optical properties. In 1996 Asher and co-workers described a method to produce temperature responsive colloidal crystals by

making the constituent particles not out of silica or polystyrene, but out of a hydrogel called poly(N-isopropyl acrylimide) (NIPAM). The reflectivity of this gel-based photonic crystal spanned the entire visible wavelength regime by varying the temperature from 11.7°C (red) to 34.9°C (blue). This breakthrough has been reproduced and expanded upon by several different researchers and is also further developed in chapter four of this thesis.

The use of a gel in combination with the photonic crystal to provide stimulus responsive reflectivity was a key insight that opened the door to tunability with a number of different stimuli. Along with temperature, 3D periodic photonic colloidal crystals were fabricated and manipulated via changes in ionic strength,[44,45] pH,[46,47,48] magnetic field,[49,50,51,52] the type of solvent or specific ions in the solution,[53,54,55] solvent vapor,[56,57,58] electric field,[59,60,61] and photochemical stimulation.[62,63]

Other methods of producing stimulus-responsive photonic crystals include spin coating of polymers[64,65] which were subsequently swelled with solvents or solvent vapors. Ceramic precursors have also been sequentially spun onto substrates and subsequently fired to produce mesoporous layers that could be infiltrated with different liquids to change the effective index of refraction of the layers.[66]

Similarly, photonic crystals have also been produced by layer-by-layer dip coating of polyelectrolyte/nanoparticle films which were calcined to form structurally stable multilayer reflectors.[67] Layer-by-layer processing, although slow, gives extreme flexibility in terms of the layer spacings and indices as shown in the construction of a rugate filter (apodized, sinusoidal index profile).[68] All of the previously mentioned gel-based photonic crystals need to be swollen with a fluid to obtain their optical reflection

peaks but polyelectrolyte multilayers, through a reversible phase-separation process at low pH, can form nanoporous structures that, when dry, will reflect visible light.[69] Photochemically active crosslinkers have also been incorporated into these systems giving the ability to selective tailor the crosslink density and thus the color of the films.[70] Because of their one-dimensionally periodic, lamellar, polyelectrolyte nature these layer-by-layer photonic crystals are perhaps the closest technology to the gel-forming block copolymers under study in this thesis.

1.4 Polymers and Gels

As discussed previously in the context of colloidal crystal photonics, polymeric gels are sensitive to a number of stimuli including temperature, pH, solvent environment, types of ions in solution, electric field, and light. The polymer chains which make up these gels are constructed of repeated monomer units, the chemical nature of which determines the properties of the gel. A portrayal of several monomer types used in this thesis work can be seen in figure 1.7.

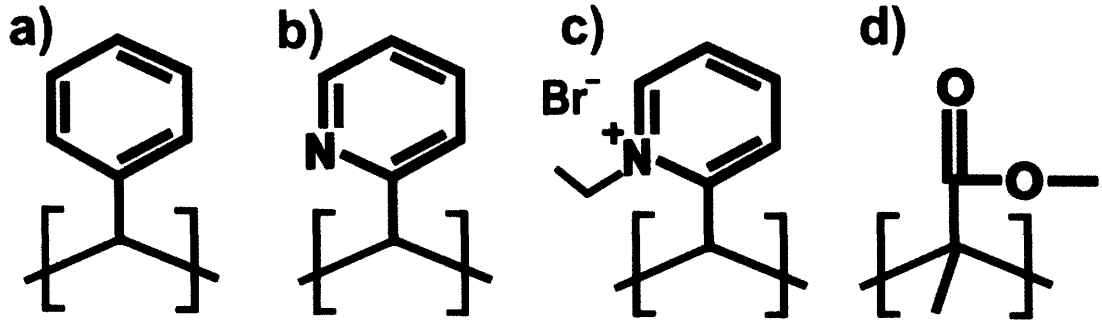

Figure 1.7: Monomer units of polymers used in this thesis – Illustrated above are the monomeric units that comprise: (a) poly(styrene), (b) poly(2-vinyl pyridine), (c) poly (2-ethylpyridinium bromide), and (d) poly(methyl methacrylate). A carbon atom resides at the terminus of every line (which indicates a bond). Hydrogen atoms have been omitted for clarity.

Gels can be created from polymers by swelling with a suitable solvent if physical or chemical crosslinks are present. Physical entanglement, covalent linking with tertiary reactive groups, and hydrogen bonding can all lead to crosslink points that keep the polymer network from dissolving in solution. Depending on the local environment, the chains in these networks are highly responsive: (1) becoming closely associated with each other, including actual collapse of the gel, when polymer-polymer interactions are preferred over solvent-polymer interactions, or (2) becoming expanded (and swelling the gel), when solvent-polymer interactions are preferred over polymer-polymer interactions. The preference for shrinking or swelling depends on a number of readily adjusted parameters including temperature, pH, solvent quality, electric field, pressure, and interactions with light. Changes in these stimuli can also induce phase transitions where the change in size of the gel does not increase or decrease monotonically but changes drastically from one state to the other (e.g. ΔV=1000%). This phase transformation behavior was first observed in poly(acrylic acid) and poly(methacrylic acid) gels in 1950[71] and subsequent work by Tanaka and colleagues have advanced the state of the art considerably since that time.[72] Highly swollen polymer gels and their stimuli responsiveness play a key role in the extensive tunability of the block copolymer photonic gels studied in this thesis.

1.5 Block Copolymers

A block polymer is a polymer in which two (or more) distinct polymers are covalently bonded to one another typically in a linear manner (but not necessarily). If the individual polymers that make up the block polymer are not miscible in each other, the

block polymer will separate into separate domains each containing only one of the constituent polymers. The polymers in a block polymer, being covalently attached to one another, cannot macroscopically phase separate into large-scale regions of each of the component polymers in the system as is the case of a simple homopolymer-homopolymer mixture.

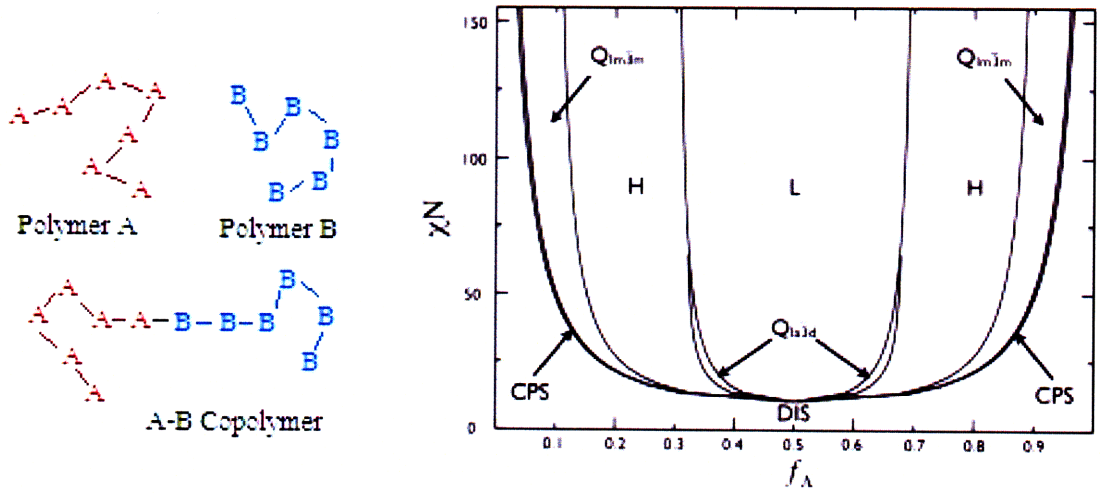

Figure 1.8: Individual polymers and an A/B diblock copolymer (left) and a generic phase diagram for diblock copolymers – Block copolymers are composed of two distinct types of polymers which are covalently bonded at a central junction. In most all cases the two polymers are not miscible in one another and micro-phase separate on a length scale of tens to hundreds of nanometers depending on the molecular weight of the copolymer and the strength of the immiscibility. The structure or morphology that the particular BCP takes on when it microphase separates depends on the polymer-polymer interaction strength (χ), the number of monomer units (N) and the volume fraction of polymer A relative to polymer B. CPS = close packed spheres, QIm3m = body centered spheres, H = hexagonally packed cylinders, QIa3d = double gyroid, L = lamellae, Dis = disordered (homogeneously mixed). (The block copolymer phase diagram is from reference 73.)

The covalent bonding between blocks forces micro-phase separation and small-scale periodic order can develop. The amount of attraction or repulsion of one polymer for another is characterized by the Flory-Huggins χ (chi) parameter which plays a central role in determining the phase behavior of the block polymer. This parameter, along with the number of monomer units comprising the polymer and the volume fraction of each block, dictates the thermodynamically stable structure of the micro-phase separated block

polymer. For non-polar polymers, the generic diblock copolymer (two polymers covalently joined at a single junction) phase diagram is shown in figure 1.8.[73] The Flory-Huggins interaction parameter for nonpolar polymer pairs can be estimated by the following relationship:[74]

$$\chi = V(\delta_a - \delta_b)^2/RT$$

where V is the reference volume of a monomer unit, δ_a and δ_b are the solubility parameters of the two interacting species, R is the gas constant, and T is temperature. For solvent-polymer solutions, an additional factor of 0.34 is added to the equation to account for free-volume effects.[74] If two components have an interaction parameter of less than 0.5 then they are most likely miscible.

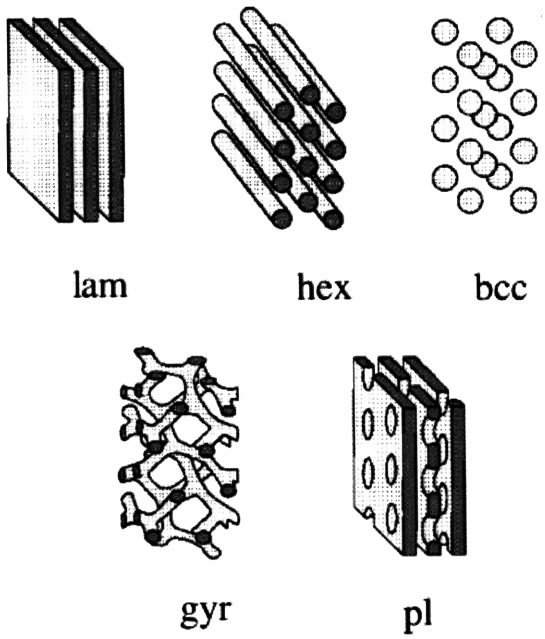

Figure 1.9: A selection of possible block copolymer morphologies – Depending on the molecular weights of the two chains in the copolymer and the value of χN, several different morphologies have been observed in block copolymers. The similarity between these morphologies and the 1-, 2-, and 3-D photonic crystals pictured in figure 1.2 is clearly evident. Additional morphologies can also be obtained by adding additional components. (figure taken from reference 75)

1.6 Solubility parameters

Rather than rely on experimental observations to determine solvent-polymer (or polymer-polymer miscibility and solubility, efforts were made by Hildebrand and Scott[76] and later Hansen[77] to quantify the interaction between the solvent and polymer so a priori estimates of solubility could be made. The later insight by Hansen focused on categorizing contributions to the total solubility parameter from the three separate sources of interaction in organic molecules: atomic or dispersion forces arising from the interaction of temporary dipoles caused by random charge oscillations on every atom, permanent dipole - permanent dipole or polar forces which roughly correlate with the dipole moments of particular chemical groups, and hydrogen bonding forces coming from electron exchange between molecules[78]. These forces characterize the types of interations between solvents and polymers. Dispersion forces are present in all substances due to their atomistic nature, polar forces are interactions inherent in molecules and will at least be somewhat present in all molecules, and hydrogen bonding forces are weaker than covalent bonds but are much stronger than dipole-dipole interactions and thus can add significantly to the magnitude of the total solubility parameter[79]. These attractive forces combine to form the total cohesive energy of a system:

$$E_{tot}=E_d+E_p+E_h$$

This energy is related to the solubility parameter defined by Hildebrand as:

$$\delta=(E_{tot}/V_{solv})^{1/2}$$

where E_{tot} is the total cohesive energy[i] and V_{solv} is the molar volume of the pure solvent. The ability of a polymer and solvent to mix can be represented by the Gibbs free energy

[i] Found by measuring the latent heat of evaporation. $E=\Delta H_v-RT$ where ΔH_v is the heat of vaporization, R is the gas constant and T is the temperature in Kelvin.

of mixing:

$$\Delta G_{mix} = \Delta H_{mix} - T\Delta S_{mix}$$

Where ΔH_{mix} represents the energy gained or lost by mixing, T is the temperature, and ΔS_{mix} is the change in entropy upon mixing. The solubility parameter can be related to these thermodynamic quantities by the following relation proposed by Patterson, et al.[80]:

$$\Delta G_{mix,non\text{-}S} = \varphi_1 \varphi_2 V_m (\delta_1 - \delta_2)^2$$

$\Delta G_{mix,non\text{-}S}$ is the energy contribution to the energy of mixing from all terms except for the entropic energy of mixing, φ_1 and φ_1 are the volume fractions of the components, V_m is the molar volume of the mixture, and δ_1 and δ_2 are the solubility parameters for the components[ii]. For mixing to occur, ΔG_{mix} must be negative, therefore $\Delta G_{mix,non\text{-}S}$ must be less than the energy of mixing ($T\Delta S_{mix}$) and thus the difference between δ_1 and δ_2 must be minimized. Although choosing two constituents with similar solubility parameters can work well to predict solubility, care must be taken in systems in which hydrogen bonding or other interactions are prevailent (for example ethanol (δ =26.1 $MPa^{1/2}$) and water mix but nitromethane (δ =25.1 $MPa^{1/2}$) and water (δ =47.1 $MPa^{1/2}$) do not.)[79] As Hansen realized, because the solubility parameter includes contributions from three separate cohesive forces, a more appropriate predictor of solubility is to take into account differences between individual components of the solubility parameter rather than comparing the difference between overall solubility parameters.

1.7 Block copolymer photonics

As seen in this introduction, a material comprised of periodic regions having different refractive indices will reflect light of a frequency commensurate with the

[ii] The term $\varphi_1 \varphi_2 V_m (\delta_1 - \delta_2)^2$ was originally proposed by Hildebrand to be the ΔH_{mix} term in the Gibbs free energy of mixing equation, but as ΔH_{mix} can take on both positive and negative values it was correctly assigned to a $\Delta G_{mix,non\text{-}S}$ term by Patterson.

spacing and the respective indices of refraction of the regions. The large 'L' or lamellar region in the block copolymer phase diagram in figure 1.8 corresponds to a layered structure such that if the polymers in the block copolymer are chosen so that they have different indices of refraction, and if the molecular weight of the copolymer and thus the domain spacing is large enough, the structure will behave as a multilayer reflector.[81,82,83,84] Block copolymer photonic crystals require extremely large molecular weights as the lamellar period scales as:

$$d \sim N^{2/3}$$

in the strong segregation limit ($\chi N > 100$). Depending on the monomer sizes of the two polymers in the BCP, the minimum number of monomer units making up the photonic block copolymer needs to be >5000 (i.e. the total molecular weight of the polymer needs to be greater than approximately half a million grams per mole.) Producing polymers of this length with a low polydispersity is necessary for producing a well ordered sample and special high-purity synthetic conditions needed to be employed.[85] Also, since the chains are quite long, processing these high molecular weight copolymers to produce uniform, well ordered samples can be a challenge.

In order to reduce the need for these rather large molecular weight BCPs, additives have been introduced to occupy volume and hence increase the domain spacing. Homopolymers of poly(styrene) and poly(isoprene) have been blended into the poly(styrene)-b-poly(isoprene) (PS-PI) system increasing the d spacing by as much as 60% leading to a substantial reduction in the BCP molecular weight needed to form a photonic crystal (>274 kg/mol as opposed to >500 kg/mol.)[86,87] Liquid-crystal mesogens have also been selectively incorporated into the poly(4-vinylpyridine) domains in 1D

photonic block copolymers comprised of 239kg/mol poly(styrene) and 50kg/mol (before mesogens were added) poly(4-vinylpyridine).[88,89] Through hydrogen bonding interactions, the mesogens were linked to the P4VP chains increasing the size of the domain. This composite photonic crystal was tunable by varying the temperature which disrupted the hydrogen bonding interactions between the poly(4-vinylpyridine) and the mesogens. Similarly, liquid-crystal side chains were covalently grafted onto the poly(methacrylic acid) block of a poly(styrene)-b-poly(methacrylic acid) (500kg/mol – 96kg/mol) BCP producing a photonic block copolymer whose peak position could be permanently shifted with an increase in temperature above 80°C.[90] The temperature related peak shift of a PS-PI block copolymer in a non-selective solvent has also been explored.[85]

The next three chapters are devoted to measuring and explaining the response of a photonic gel copolymer formed by selectively swelling one domain with a solvent, is exposed to changes in the temperature, solvent environment, and electrochemical stimuli. The concept of tunable block-copolymer photonics will be extended to shear-induced color change in chapter six and finally chapter seven will detail the finite-element optimization of a liquid-filled lens.

1.8 References

1 Hanlon, R. and Messenger, J., Cephalopod Behaviour, Cambridge University Press, (1996)

2 Land, M.F., The physics and biology of animal reflectors, Prog. Biophys. and Molec. Bio., 24, 75-106 (1972)

3 Hecht, E., Optics, 3rd edition, Addison-Wesley, Reading, Massachusetts, (2001)

4 Vukusic, P. in *Optical Interference Coatings* (eds Kaiser, N. & Pulker, H. K.), 1-34, Springer, New York, (2003)

5 Hooke, R., Micrographia, Dover Publications, New York, (1961)

6 Newton, I., Optiks, Dover Publications, New York, (1952)

7 Anderson, T.F. and Richards, A.G., An electron microscope study of some structural colours of insects, J. Appl. Phys., 13, 748-58 (1942)

8 Parker, A.R., 515 million years of structural colour, J. Opt. A: Pure Appl. Opt. 2 R15-R28 (2000)

9 Vukusic, P. and Sambles, J.R., Photonic structures in biology, Nature, 424, 852-5 (2003)

10 Parker, A.R., and Townley, H.E., Biomimetics of photonic nanostructures, Nature Nanotechnology, 2, 347-53 (2007)

11 Herring, P.J., Reflective systems in aquatic animals, Comparitive biochemistry and physiology, A: physiology, 109, 512-46 (1994)

12 Denton, E.J., On the organization of reflecting surfaces in some marine animals, Phil. Trans. Roy. Soc. B, 258, 285-313, (1970)

13 Kawaguti, S. and Kamishima, Y., Electron microscopy on iridophores and guanophores of fish, 6th International Congress for Electron Microscopy, 419, (1966)

14 Mathger, L.M. and Hanlon, R.T., Anatomical basis for camouflaged polarized light communication in squid, Biology Letters, 2, 494-6, (2006)

15 Walls, G.L., The vertebrate eye, Scientific bulletin of cranbrook institute, No. 9 Michigan, (1942)

16 Denton, E.J. and Nicol, J.A.C., The chorioidal tapeta of some cartilaginous fishes (Chondrichthyes), J. Mar. Biol. Ass. UK, 45, 711-38 (1964)

17 Denton, E.J. and Rowe, D.M., Reflective communication between fish, with special reference to the greater sand eel, hyperoplus lanceolatus, Philosophical Transactions: Biological Sciences, 334(1309), 221-37, (1994)

18 Denton, E.J. and Rowe, D.M., Reflective communication between fish, with special reference to the horse mackerel, trachurus trachurus, Philosophical Transactions: Biological Sciences, 352(1353), 531-49 (1997)

19 Greenwalt, C.H., Brandt, W., and Friel, D.D., Iridescent colors of humming-bird feathers, J. opt. Soc. Am., 50, 1005-13, (1960)

20 DeSilva, L. et al. Natural and nanoengineered chiral reflectors: structural colour of manuka beetles and titania coatings. Electromagnetics, 25, 391–408 (2005)

21 Argyros, A., Manos, S., Large, M. C. J., McKenzie, D. R., Cox G. C. & Dwarte, D. M. Electron tomography and computer visualisation of a three-dimensional 'photonic' crystal in a butterfly wingscale. Micron, 33, 483–487 (2002)

22 Vukusic, P., Shedding light on butterfly wings, Proc. SPIE, 4438, 85–95 (2001)

23 Denton, E.J., Reflectors in fishes, Scientific American, 224(1), 64-72 (1971)

24 Greenstein, L.M., Nacreous pigments and their properties, Proc. Scient. Sect. Toilet Goods Ass., 45, 20-26 (1966)

25 Weber, et al., Giant birefringent optics in multilayer polymer mirrors, Science, 287, 2451-2456 (2000)

26 Lythgoe, J.N. and Shand, J., The structural basis for iridescent colour changes in dermal and corneal iridophores in fish, J. exp. biol., 141, 313-325, (1989)

27 Lythgoe, J. N. and Shand, J. Changes in spectral reflexions from the iridophores of the neon tetra. J. Physiol., 325, 23-34 (1982)

28 Nagaishi, H. and Oshima, N. Neural control of motile activity of light-sensitive iridophores in the neon tetra. Pigment Cell. Res., 2, 485-492 (1989)

29 Mathger, L.M., Land, M.F., Siebeck, U.E., and Marshall, N.J., Rapid colour changes in multilayer reflecting stripes in the paradise whiptail, Pentapodus paradiseus, J. Exp. Biol., 206, 3607-13 (2003)

30 Crookes, W., Ding, L.L., Huang, Q.H, Kimbell, J.R., Horwitz, J., McFall-Ngai, M.J., Reflectins: the unusual proteins of squid tissues, Science, 303, 235-238 (2004)

31 Kramer, R.M., Crookes-Goodson, W.J., Naik, R.R., The self-organizing properties of squid reflectin protein, Nature Materials, 6, 533-538, (2007)

32 Fujii, R., The regulation of motile activity in fish chromatophores, Pigment cell research, 13, 300-319 (2000)

33 Greenland, K.M. High-reflexion films Journal of Scientific Instruments, 23, 48-50 (1946)

34 Alfrey, et al, Polym. Eng. Sci., 9, 400 (1969)

35 Yablonovitch, E., Inhibited Spontaneous Emission in Solid-State Physics and Electronics, Phys. Rev. Lett., 58, 2059 (1987)

36 Chutinan, A., John, S., and Toader, O., Diffractionless Flow of Light in All-Optical Microchips, Phys. Rev. Lett., 90, 123901, (2003)

37 Ho, K.M., Chan, C.T., and Soukoulis, C.M., Existence of a photonic gap in periodic dielectric structures, Phys. Rev. Lett., 65, 3152, (1990)

38 Lin, S.Y., Fleming, J.G., Hetherington, D.L., Smith, B.K., Biswas, R., Ho, K.M., Sigalas, M.M., Zubrzycki, W., Kurtz, S.R., and Bur, J., A three-dimensional photonic crystal operating at infrared wavelengths, Nature, 394, 251, (1998)

39 Li, Y.Y., Cunin, F., Link, J.R., Gao, T., Betts, R.E., Reiver, S.H., Chin, V., Bhatia, S.N., and Sailor, M.J., Polymer replicas of photonic porous silicon for sensing and drug delivery applications, Science, 299, 2045-7 (2003)

40 Segal, E., Perelman, L.A., Cunin, F., Di Renzo, F., Devoisselle, J-M., Li, Y.Y. and Sailor, M.J., Confinement of thermoresponsive hydrogels in nanostructured porous silicon dioxide templates, Advance Funct. Mat., 17, 1153-62, (2007)

41 Norris, D.J., Arlinghaus, E.G., Meng, L., Heiny, R., and Scriven, L.E., Opaline photonic crystals: how does self-assembly work?, Advanced Materials, 16(16), 1393-99 (2004)

42 Texter, J., Polymer colloids in photonic materials, C. R. Chimie, 6, 1425-33, (2003)

43 Arsenault, A., Fournier-Bidoz, S., Hatton, B., Miguez, H., Tetreault, N., Vekris, E., wong, S., Yang, S.M., Kitaev, V., and Ozin, G.A., Towards the synthetic all-optical computer: science fiction or reality, J. Mat. Chem., 14, 781-94, (2004)

44 Lee K. and Asher S. A., Photonic Crystal Chemical Sensors: pH and Ionic Strength, J. Am. Chem. Soc., **122**, 9534-9537 (2000)

45 Saito, H., Takeoka, Y., and Watanabe, M., Simple and precision design of porous gel as a visible indicator for ionic species and concentration, Chem. Commun,, 2126-7 (2003)

46 Debord, J.D. and Lyon, L.A., Thermoresponsive photonic crystals, J. Phys. Chem. B, 104(27), 6327-31 (2000)

47 Tunable inverse opal hydrogel pH sensors, Advanced Materials, 15(7-8), 563-6, (2003)

48 X. Xu, A.V. Goponenko and S.A. Asher, Polymerized PolyHEMA Photonic Crystals: pH and Ethanol Sensor Materials, *J. Am. Chem. Soc.*, DOI: 10.1021/ja077979+ (2008)

49 X. Xu, G. Friedman, K. Humfeld, S. Majetich and S. A. Asher, Superparamagnetic Photonic Crystals, *Advanced Materials,* 13, 1681-1684 (2001)

50 X. Xu, G. Friedman, K. Humfeld, S. Majetich and S. A. Asher, Synthesis and Utilization of Monodisperse Superparamagnetic Colloidal Particles for Magnetically Controllable Photonic Crystals, *Chemistry of Materials*, 14, 1249-1256 (2002)

51 X. Xu, S. Majetick, and S. Asher, Mesoscopic Monodisperse Ferromagnetic Colloids Enable Magnetically Controlled Photonic Crystals, *J. Am. Chem. Soc.*, 124, 13864-13868 (2002)

52 Ge, J., Hu, Y., and Yin Y., Highly Tunable Superparamagnetic Colloidal Photonic Crystals, Angew. Chem. Int. Ed., 46, 7428 –743 (2007)

53 J. H. Holtz, J. S. W. Holtz, C. H. Munro, and S. A. Asher, Intelligent Polymerized Crystalline Colloidal Arrays: Novel Chemical Sensor Materials*Anal. Chem.* 70, 780-791 (1998)

54 C.Reese, M. Baltusavich, J. Keim and S. A. Asher, Development of an Intelligent Polymerized Crystalline Colloidal Array Colorimetric Reagent, Analytical Chemistry, 73, 5038-5042 (2001)

55 Jiang, P., Smith, D.W., Ballato, J.M., and Foulger, S.H., Multicolor pattern generation in photonic bandgap composites, Advanced materials, 17(2), 179-84 (2005)

56 J. H. Holtz and S. A. Asher, Polymerized Colloidal Crystal Hydrogel Films as Intelligent Chemical Sensing Materials, Nature, 389, 829-832 (1997)

57 Arsenault, A.C., Kitaev, V., Manners, I., Ozin, G.A., Mihi, A., and Miguez, H., Vapor swellable colloidal photonic crystals with pressure tunability, J. Mater. Chem., 15, 133-138 (2005)

58 Arsenault, A.C., Miguez, H., Kitaev, V., Ozin, G.A., and Manners, I., A polychromic, fast response metallopolymer gel photonic crystal with solvent and redox tunability: a step towards phtonic ink (P-Ink), Advanced Materials, 15(6), 503-7 (2003)

59 Arsenault, A., Puzzo, D., Manners, I., Ozin, G., Photonic-crystal full-colour displays, Nature Photonics, 1, 468-472 (2007)

60 Foulger, S., Jiang, P., Lattam, A., Smith, D., Ballato, J., Dausch, D., Grego, S., and Stoner, B., Photonic crystal composites with reversible high-frequency stop band shifts, Adv. Mater., 15(9), 685-9 (2003)

61 Ueno, K., Matsubara, K., Watanabe, M., and Takeoka, Y., An electro- and thermochromic hydrogel as a full-color indicator, Adv. Mat., 19, 2807-12 (2007)

62 M. Kamenjicki, I. Lednev and S.A. Asher, Photoswitchable Spirobenzopyran-based Photochemically Controlled Photonic Crystals, *Adv. Funct. Matl.*, 15, 1401 (2005)

63 M. Kamenjicki, I.K. Lednev, A. Mikhonin, R. Kesavamoorthy and S.A. Asher, Photochemically Controlled Photonic Crystals, Advanced Functional Materials, 13, 774 (2003)

64 Monch, W., Dehnert, J., Jaufmann, E., and Zappe, H., Flory-Huggins swelling of polymer Bragg mirrors, Applied Physics Letters, 89, 164104 (2006)

65 Monch, W., Dehnert, J., Prucker, O., Ruhe, J., and Zappe, H., Tunable Bragg filters based on polymer swelling, Applied Optics, 45(18), 4284-90 (2006)

66 Choi, S.Y., Mamak, M., von Freymann, G., Chopra, N., and Ozin, G.A., Mesoporous bragg stack color tunable sensors, Nano letters, 6(11), 2456-2461, (2006)

67 Wu, Z., Lee, D., Rubner, M.F., and Cohen, R.E., Structural color in porous, superhydrophilic, and self cleaning SiO_2/TiO_2 Bragg stacks, Small, 3(8), 1445-51, (2007)

68 Nolte, A.J., Rubner, M.F., and Cohen, R.E. Creating effective refractive index

gradients within polyelectrolyte multilayer films: molecularly assembled rugate filters, Langmuir, 20, 3304-10 (2004)

69 Zhai, L., Nolte, A.J., Cohen, R.E., and Rubner, M.F., pH-gated porosity transitions of polyelectrolyte multilayers in confined geometries and their application as tunable bragg reflectors, Macromolecules, 37, 6113-6123 (2004)

70 Olugebefola, S.C., Ryu, S.W., Nolte, A.J., Rubner, M.F., and Mayes, A.M., Photo-cross-linkable polyelectrolyte multilayers for 2-D and 3-D patterning, Langmuir, 22, 5958-62 (2006)

71 Kuhn, W., Hargitay, B., Katchalsky, A., Hisenberg, H., Reversible Dilation and Contraction by Changing the State of Ionization of High-Polymer Acid Networks, Nature, 165, 514-6, (1950)

72 Li, Y. and Tanaka, T., Phase transitions of gels, Annual Rev. Mater. Sci., 22, 243-277 (1992)

73. Matsen MW, Bates FS, Unifying weak- and strong-segregation block copolymer theories, Macromolecules 29 (4), 1091-1098 (1996)

74 Painter, P.C. and Coleman, M.M., Fundamentals of polymer science: an introductory text, 2nd edition, Technomic Publishing Company, Lancaster, PA, (1997)

75 Ryan, A.J., Mai, S.M., Patrick, J., Fairclough, A., Hamley, I.W., and Booth, C., Ordered melts of block copolymers of ethylene oxide and 1,2-butylene oxide, Phys. Chem. Chem. Phys., 3, 2961-2971, (2001)

76 Hildebrand, J. and Scott, R.L., Regular solutions, Prentice-Hall Inc., Englewood Cliffs, NJ, (1962)

77 Hansen, C.M., The three dimensional solubility parameter – key to paint component affinities I, J. Paint Technol., 39(505), 104-117, (1967)

78 Bicerano, J., Prediction of polymer properties, Marcel Dekker, New York, NY (1996)

79 Hansen, C.M., Hansen solubility parameters: a users handbook, CRC press, Boca Raton, FL, (2000)

80 Patterson, D. and Delmas, G., New aspects of polymer solution thermodynamics, Off. Dig. Fed. Soc. Paint Technol., 34(450), 677-692, (1962)

81 Fink, Y., Polymer photonic crystals, Ph.D. Thesis, Massachusetts Institute of

Technology, (2000)

82 Fink, Y., Urbas, A.M., Bawendi, M.G. Joannopoulos, J.D. Thomas, E.L. Block copolymers as photonic bandgap materials Journal of Lightwave Technology, 17(11), 1963-1969 (1999)

83 Edrington, A.C., Urbas, A.M., DeRege, P., Chen. C.X., Swager, T.M., Hadjichristidis, N., Xenidou, M., Fetters, L.J., Joannopoulos, J.D., Fink, Y., and Thomas, E.L., Polymer-based photonic crystals, Adv. Mat., 13(6), 421-425 (2001)

84 Cromie, MJ, Multifunctional Systems With Polymer Actuators: Mechanochromism And Peristaltic Pumping, Master's thesis, Thomas group, (2005)

85 Yoon, J.S., Block copolymer photonic crystals: towards self-assembled active optical elements, Ph.D. Thesis, Massachusetts Institute of Technology, (2006)

86 Urbas, A. M., Block copolymer photonic crystals, Ph.D. Thesis, Massachusetts Institute of Technology, (2003)

87 Urbas, A., *et al.,* Tunable block copolymer/homopolymer photonic crystals. *Adv. Mater.* 12, 812–814 (2000)

88 Valkama, S., Kosonen, H., Ruokolainen, J., Haatainen, T., Torkkeli, M., Serimaa, R., Ten Brinke, G., and Ikkala, O., Self-assembled polymeric solid films with temperature-induced large and reversible photonic-bandgap switching, Nature Materials, (3), 872-6, (2004)

89 Kosonen, H., Valkama, S., Ruokolainen, J., Torkkeli, M., Serimaa, R., ten Brinke, G., and Ikkala, O., One-dimensional optical reflectors based on self-organization of polymeric comb-shaped supramolecules, Eur. Phys. J. E, 10, 69–75 (2003)

90 Osuji, C., Chao, C.Y., Bita, I., Ober, C.K., and Thomas, E.L., Temperature-dependent photonic bandgap in a self-assembled hydrogen-bonded liquid-crystalline diblock copolymer, Advenced Functional Materials, 12(11-12), 753-8, (2002)

Chapter 2:
Experimental Techniques and Procedures

Before embarking on the bulk of the thesis, it is necessary to provide some experimental details so that the interested reader may replicate or expand upon the experiments described in later chapters. The details of the sample preparation are important for block copolymer photonics as the attainment of uniform, well ordered microstructure is key for the production of structural color. It is especially important for the PS-P2VP photonic gels which rely not only on a well ordered structure to produce color but also on defects in that structure that allow solvents to rapidly penetrate and swell all layers. Observations and remarks on sample preparation for each set of experiments are followed by notes on the experimental equipment used to obtain the results. With the exception of 3-iodopropyl trimethoxysilane (IPS) which was purchased

from Aldrich (Milwaukee, WI), all other chemicals were purchased from Alfa Aesar (Ward Hill, Massachusetts).

2.1 Sample preparation for PS-P2VP solvatochromic and thermochromic structured photonic gels

The PS-P2VP block copolymer was purchased from Polymer Source (Duval, Canada) and dissolved in propylene glycol monomethyl ether acetate (PGMEA) to make a 5% solution by weight. After dissolution, a 0.2μm syringe filter was used to remove any particulate contaminants and the solution was degassed in a vacuum oven prior to spin coating. Glass substrates (usually 1" by 3" borosilicate laboratory slide glass) were first treated with (3-Iodopropyl) trimethoxysilane (IPS) to ensure that the films did not delaminate from the substrate after immersion into the swelling liquid. The IPS coating also provides a surface for the preferential adsorption of the P2VP over the PS chains thus creating a favored orientation for the lamellae. Further, the iodo groups in the IPS can bond to the pyridine ring in the P2VP and provide a covalent link to the substrate.

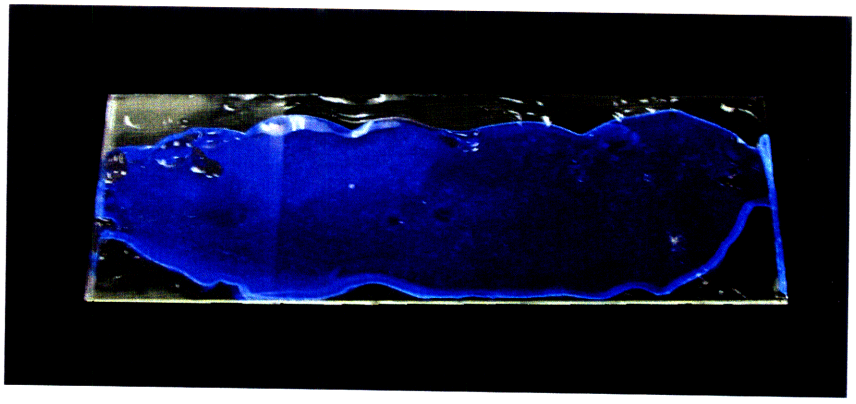

Figure 2.1: A methanol swollen 57k-57k PS-P2VP photonic gel – The P2VP layers of the lamellar block copolymer are selectively swollen by the methanol. The increase in layer thickness and change in index of refraction of the P2VP/methanol layers causes the film to reflect blue light.

To apply the coating, an open vial of IPS was placed in a vacuum desiccator along with

the substrates. (See figure 2.2 for pictures of all BCP film production equipment) Vacuum was applied for 10 minutes, the vacuum connection was closed and the samples were allowed to sit for 5 more minutes. The slides were then used for spin coating within the next 15 minutes.

Figure 2.2: Equipment used in the production of block copolymer thin films – (Top) The films were produced by using a spin coater. A 5% solution of PS-P2VP and PGMEA was spun at 500rpm for one minute to produce a ~1 micron thick PS-P2VP film. (Bottom left) After spin coating, the samples were placed in an annealing chamber which contained a high concentration of chloroform vapor. The hotplate was kept at 40°C. The bottom of the dish was filled with chloroform, the samples were placed on top of a scaffold to keep them out of the liquid chloroform and the top was loosely sealed with aluminum foil. (Bottom right) The glass substrates were coated with IPS before spin coating to increase the adhesion of the BCP film to the substrate.

The 5% PS-P2VP solution was uniformly distributed across the surface of the treated slide and then spun at 500 rpm for 90 seconds. After spin coating, samples were suspended above chloroform in a jar (with a loose fitting lid) which was then maintained at 40°C on a hotplate for at least 8 hours. Care must be taken such that the samples do not touch the liquid chloroform as it is an excellent solvent for the block copolymer and will dissolve the film. Likewise, the chloroform vapor must not completely saturate the air in the sample chamber otherwise temperature fluctuations could cause the chloroform to condense on the sample causing dissolution. Upon completion of the chloroform vapor annealing treatment, samples were checked for alignment by application of methanol which produced a uniform blue reflective film (see figure 2.1).

2.2 Sample preparation for electrochemically tuned PS-P2VP structured photonic gels

PS-P2VP block copolymers with a number average molecular weights of 57k PS – 57k P2VP (protonated and quaternized experiments) and 102k PS – 97k P2VP (trifluoroethanol experiments) grams/mol were used as received from Polymer Source, Inc. The copolymer was spun onto indium-tin oxide coated glass slides according to the procedure outlined above. Indium-tin oxide coated glass slides with a resistivity of 30-60 Ω/□ were purchased from Delta Technologies (Stillwater, MN). This resistivity was chosen for its optimum balance of transmissivity and conductivity. As the ITO layer becomes thicker, the inherent absorbtion from the ITO causes the slides to appear yellow while a coating that is too thin leads to large electrode resistivity and an accompanying voltage drop over the length of the electrode. The 198 μm ACLAR® fluoropolymer film

spacer material was purchased from Structure Probe Incorporated (West Chester, PA). A Velleman PS613U 0-30 volt power supply was used to apply voltage to the device and a CARY 6000i UV-vis spectrophotometer was used to collect the transmitted spectra. TEM images were obtained from a JEOL 2010 at 200 keV using focused ion beam cross-sectioned samples subsequently stained in iodine vapor. The iodine reacts with the pyridine group and gives the P2VP a darker appearance when observed in the TEM due to the increased electron density contrast.

The electrochemical cell was constructed as follows: The substrate, previously coated with PS-P2VP as described above, was separated from the superstrate, an unmodified ITO coated slide, by a 200μm fluoropolymer spacer and clamped together. An electrolyte was then introduced into the gap between the two slides and electrodes attached to the respective slides.

2.3 Sample preparation for high molecular weight mechanochromic block copolymers

PS-PMMA (290kg/mol – 360 kg/mol) purchased from Polymer Source, Inc. was used as received and added to spectrophotometric grade toluene (Alfa Aesar, Ward Hill, Massachusetts) inside a 20mL glass vial. The percentage of PS-PMMA in the copolymer/solvent solution was 25 percent by weight. The vial was tightly sealed and the sample was allowed to dissolve in the toluene and equilibrate for three days. After the equilibration period, the sample displayed a blue-green color and was then removed and placed onto the shear apparatus via a laboratory spatula for testing. 50 milligrams of the copolymer were sufficient for four shear test samples. More information can be found in chapter six of this thesis.

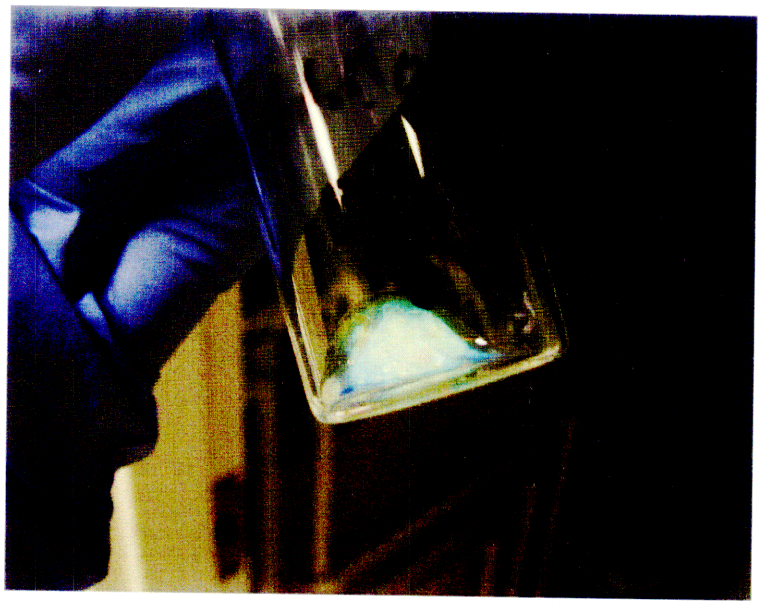

Figure 2.3: A toluene swollen 290k-360k PS-PMMA photonic block copolymer – Both the PS and PMMA layers of the lamellar block copolymer are swollen by the toluene turning the copolymer into a viscous gel. The solution contains 25% copolymer by weight.

2.4 Chemicals used to swell the PS-P2VP block copolymer

Through the course of experimentation, the affinity of numerous solvents for the copolymer was checked. Table 2.1 lists solvents, non-solvents, and solvents selective for the P2VP block. Solvents are chemicals that will completely dissolve (at least at concentrations less than 5% polymer) the block copolymer. Samples soaked in non-solvents did not dissolve or show any change in reflectivity when soaked for at least one day. The term "non-solvent" is used rather loosely here as some of these chemicals may actually be slightly soluble in the PS or P2VP blocks but do not swell them enough to cause the sample to reflect even the shortest visible wavelengths which require swelling ratios of around 8-9x. The selective solvents listed were those chemicals that swelled the P2VP layers enough to allow interference of visible light and coloration of the film.

Table 2.1: Solvents, non-solvents, and selective solvents for PS-P2VP

PS-P2VP solvents and non-solvents		
Solvents	**Non-solvents**	**Selective solvents (for the P2VP)**
Benzene	Hexane	Methanol
Acetone	Water	Ethanol
Chloroform	Acetaldehyde	Isopropyl alcohol
Bromoethane	2-vinylpyridine	Ethylene glycol
Methylacetate	Diethyl ether	Glycerol (very slow)
Ethylacetate	1-n-butyl-3-methylimidazolium hexafluorophosphate (ionic liquid)	2,2,2-Trifluoroethanol
Dimethylformamide		1-butanol
2-butanone		1,4 butanediol
Divinylbenzene		Aqueous acidic solutions (below pH ~4)
Propylene glycol monomethyl ether acetate (PGMEA)		

2.5 Methods for making liquid filled lens membranes

Although the liquid lens work described in chapter seven is largely a theoretical study, it will benefit the reader to understand the process for making the lenses. The transparent elastomer used for the construction of these liquid-lens membranes was Sylgard 184 (Dow Corning, Midland, MI.) The lenses used to test the validity of the finite-element model were produced by Rockwell Scientific, Inc. (Thousand Oaks, CA). A 120 micron layer of Sylgard 184 was spun onto a silicon wafer with a poly(vinyl alcohol) release layer and cured at 90°C in an oven. After curing for one hour, the wafer was removed from the oven and allowed to cool to room temperature. Because of the high thermal expansion of silicone (960 x 10^{-6}/C) relative to silicon (3 x 10^{-6}/C), the Sylgard 184, on cooling, is put in tension because it is attached to the silicon wafer.

The aluminum support rings used to hold the lens membrane are fashioned from aluminum washers having a thickness of 2mm, a 10mm inside diameter and a 19mm

outside diameter. Silica is deposited onto the front surface, which previously had been polished to a mirror finish, using a radio-frequency plasma.

The wafer with the silicone on it is then plasma treated for one minute in an oxygen plasma. This allows the silicone to bond to the silica on the aluminum washer when they are brought in contact. The silicone membrane, now attached to the aluminum ring, is removed from the wafer by dissolving the poly(vinyl alcohol) release layer. Since the membrane was bonded to the aluminum washer while the film was under tension, this residual stress (or "pre-strain") remains in the film.

Additionally, membranes prepared in the above manner were also subjected to irradiation at the High Voltage Research Laboratory at MIT. This process creates a higher crosslink density in the polymer membranes and increases their modulus. A decrease in the residual stress in the membranes was observed post-irradiation.

2.6 Experimental techniques

The collection of spectral information from samples was of the utmost importance to this thesis and all spectra were collected on a CARY 6000i UV-vis spectrophotometer at the Institute for Soldier Nanotechnologies. This instrument was used in transmission mode and the spectra were later converted to reflectance through the assumption that the absorbance of both the sample and the solution were negligible.

A laser-scanning confocal microscope (LSCM), Leica model TCS SPII, was used in the lab of Professor T. Swager to observe the defects in the swollen PS-P2VP system. A 488nm blue laser was used to illuminate the sample through a glass-refractive-index-matched oil immersion lens (Leica HCX PL APO 63Xl1.40-0.60) and since no

fluorescent materials were added to the films only the reflected/scattered light from the sample interfaces was used for imaging.

Chapter 3:
Solvent regulated photonic behavior of PS-P2VP

In the previous chapter, gel-based tunable photonic crystals and their remarkable ability to dramatically change volume and thus the reflected wavelengths of light were introduced and compared with analogous systems in several natural species. The present chapter is dedicated to exploring a new form of gel-based photonic crystals composed of hydrophilic-chain /hydrophobic-chain block copolymers swollen with an exceedingly selective solvent. Previously, block copolymers (BCPs) had been used for creating photonic crystals[1,2,3] and photonic crystals had been rendered highly tunable through the incorporation of a gel into synthetic opals[4,5,6] and from layer-by-layer polyelectrolyte deposition to create tunable multilayer reflectors[7,8,9], but the self-assembling

characteristics of a block copolymer had not been combined with the tunable characteristics of gels (and polyelectrolyte gels in particular.)

3.1 Introduction

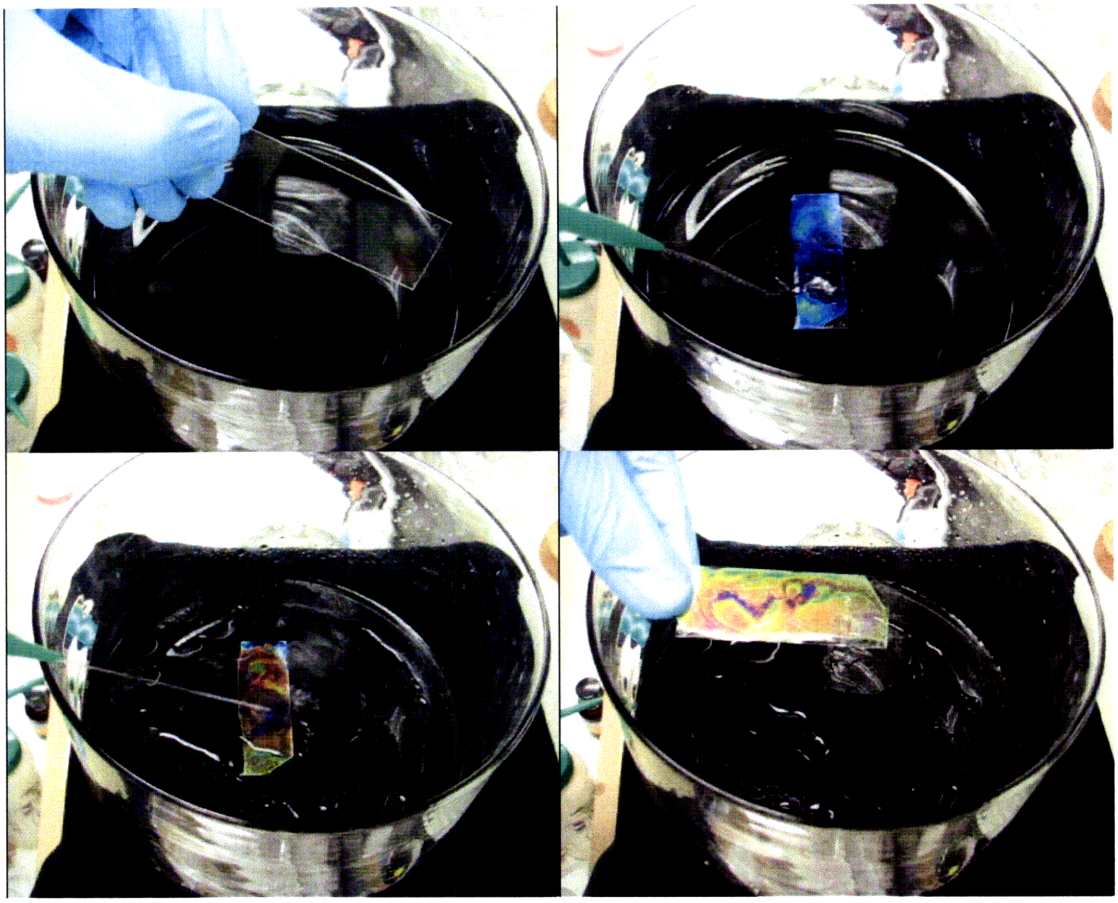

Figure 3.1: Reflectivity changes in a 97k-102k PS-P2VP block copolymer swollen with different solvents – (a) A glass slide with the copolymer film spun onto its surface is originally transparent due to the small domain periodicity and low refractive index contrast between poly(styrene) and poly(2-vinylpyridine). (b) Methanol is sprayed onto the film which selectively swells the P2VP domains and increases the refractive index contrast between the PS and P2VP/solvent layers and the film reflects blue light. (c) One molar acetic acid is sprayed onto the film causing the P2VP to become protonated which increases the solubility of the chains causing them to swell further and reflect red light. (d) Different regions of the film have been exposed to varying amounts of methanol and acetic acid and thus have different spacings and thus reflect different colors.

This key observation made by Dr. Youngjong Kang in the lab of Professor Edwin Thomas, lead to the discovery of an extensively tunable block copolymer photonic crystal (see figure 3.1).[10] This copolymer was composed of hard poly(styrene) (PS) hydrophobic segments which were chemically linked to extensively-tunable, gel-forming, hydrophilic

poly(2-vinylpyridine) (P2VP) segments. A symmetric copolymer (roughly 50% by volume of each constituent) was chosen to form a lamellar morphology which, if the indices of refraction and layer spacings satisfy the Bragg diffraction condition, would reflect light. The beauty of this approach lies in the use of relatively small molecular weight polymers to achieve this condition by swelling one layer with an extremely selective solvent. In this case, the P2VP domain is swollen to over 10 times its original thickness while the PS domains remain glassy, holding the structure together and forcing the P2VP gel to expand in only one dimension – parallel to the layer normal thus increasing the layer thickness change when compared to the three dimensional isotropic change in volume of a homogeneous gel.[a,11,12] This chapter will explore the optical response of this polymer to different solvent swelling environments including: the response of a quaternized PS-P2VP copolymer to a change in salt concentration, the response of different molecular weight PS-P2VP copolymers to methanol, the response of PS-P2VP to different molecular weight alcohols, and the response of a PS-P2VP copolymer to a change in solution pH.

As seen in the introduction, previous block copolymer photonic crystals needed to be synthesized with very high molecular weights in order to achieve large enough domain spacings to diffract light. The PS-P2VP materials under study employ a gel forming block which can be highly swollen with a variety of common solvents.

[a] Imagine a gel in the form of a 1mm x 1mm x 1mm cube. If the gel can swell 1000 times its original volume and expands in all three dimensions, the cube will become 10mm x 10mm x 10mm. If swelling is restricted to only one dimension (only along the vertical axis) the cube will become 1mm x 1mm x 1000mm. In the first case the height only changed by a factor of 10 whereas in the second it changed by a factor of a thousand. This is an important consideration as the position of the reflectivity peak depends only on vertical thickness of the layers rather than their lateral extent.

When maximally swollen, the P2VP/solvent layers can contain more than 90% solvent. Using the solvent to swell the gel layers not only reduces the cost of producing the copolymer by reducing the molecular weight requirements but also reduces the overall cost of producing the multilayer reflector because the structure is mostly composed of an inexpensive solvent. The solvent also plays a dual role in the formation of the photonic properties of the gel. It swells the P2VP layers creating a large change in spacing, but also can be selected such that it substantially enhances the refractive index contrast between PS domain and the P2VP/solvent domain.

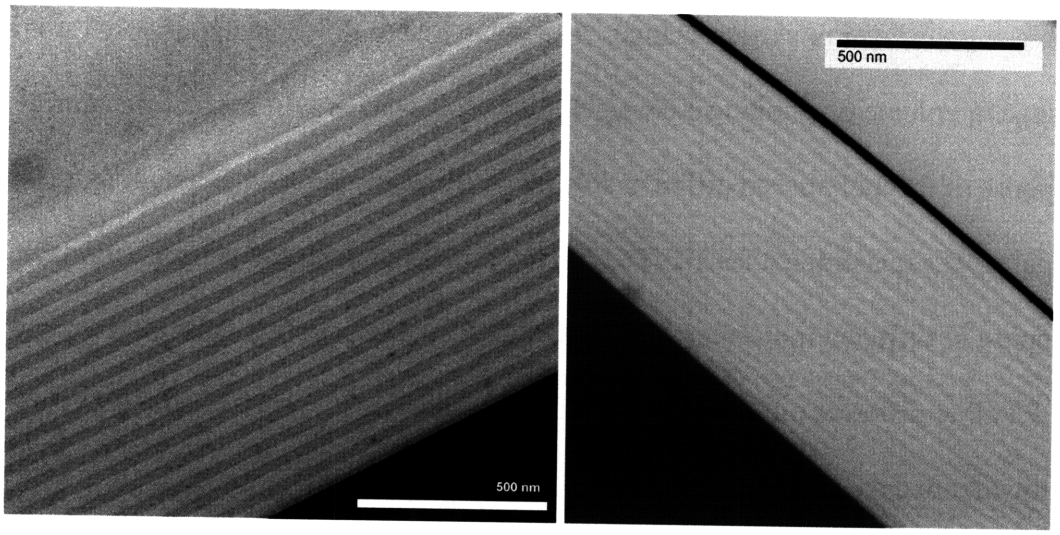

Figure 3.2: TEM micrographs of layer forming PS-P2VP (380kg/mol and 114kg/mol) block copolymers – A focused ion beam (FIB) was used to cut cross sectional samples of a 190k-190k PS-P2VP (left) and a 57k-57k PS-P2VP (right) block copolymer. The samples were stained in iodine vapor which reacts with the P2VP to enhance the electron-density contrast. The dark region in the micrographs is the glass substrate. The sample is also encased from above by epoxy (the 57k-57k sample also has gold sputtered on top (thin black region)). Both samples also have a ½ layer of P2VP next to the glass due to the treatment of the glass with 3-iodopropyl trimethoxy silane which is selective for P2VP. (TEM micrographs courtesy of R. Mickiewicz)

The unswollen PS-P2VP copolymer has a very small refractive index contrast (n_{PS} ~ 1.59 versus n_{P2VP}~1.61)[13] and relatively thin layer spacings (periodicity of ~34nm for 57kg/mol - 57kg/mol and 63nm for 190kg/mol -190kg/mol PS-P2VP – see figure 3.2) which make it unsuitable for diffraction of visible light. By the addition of solvent which

swells the P2VP layers, the thickness of the P2VP solvent-swollen domains increases and if a suitable solvent is chosen so does the refractive index contrast. In the case of P2VP swollen with 90% methanol (n~1.33), the refractive index contrast (n_2-n_1) between the swollen domain and the PS domain increases from 0.02 to 0.232. The incorporation of a gel-forming domain also increases the tunability of the photonic crystal as gels are known for their extensive set of responses to different stimuli (see Chapter 1).

One particularly sensitive tunable aspect of the photonic gel copolymer is the response of the polymer to the concentration of salt in solution. In the original work by Dr. Kang, the P2VP domains were quaternized which means that P2VP was converted to a permanent polyelectrolyte (charged) polymer when the nitrogen in the pyridine ring was chemically reacted with bromoethane at elevated temperatures (40°C in hexane – see figure 3.3). This quaternization process which converts poly(2-vinylpyridine) to poly(2-ethylpyridinium bromide) (QP2VP) allows the previously water-insoluble P2VP domains to become water soluble.

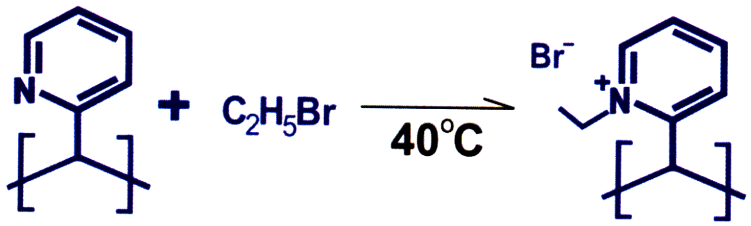

Figure 3.3: The conversion of P2VP to QP2VP via a quaternization reaction – The cast and annealed PS-P2VP sample is placed in a bath of ten percent by weight of bromoethane in hexane and is heated for at least 24 hours to attain maximum conversion of P2VP to QP2VP.

After spin coating and solvent annealing a 190 kg/mol – 190 kg/mol PS-P2VP polymer (from Polymer Source - Duval, Canada) was fully quaternized and then swollen with several solutions containing various concentrations of ammonium chloride. In pure water the structure was maximally swollen and produced a first-order reflectivity peak at

1627 nm followed by 2nd through 5th order peaks in the near infrared (NIR), visible, and ultraviolet (UV) regions of the spectrum (labeled 1- 5 on the spectra in figure 3.4a). When ammonium chloride is added to the water it dissociated into NH_4^+ and Cl^- ions which screen the interaction of the pyridinium ions with the solvent, reducing the affinity of the gel to the solvent and thus de-swelling the layers. As more salt is added, the layers shrink further and the first order reflectivity peak recedes from 1627nm with no salt to 364nm with an ammonium chloride concentration of 2.5 moles/liter (see figure 3.4).

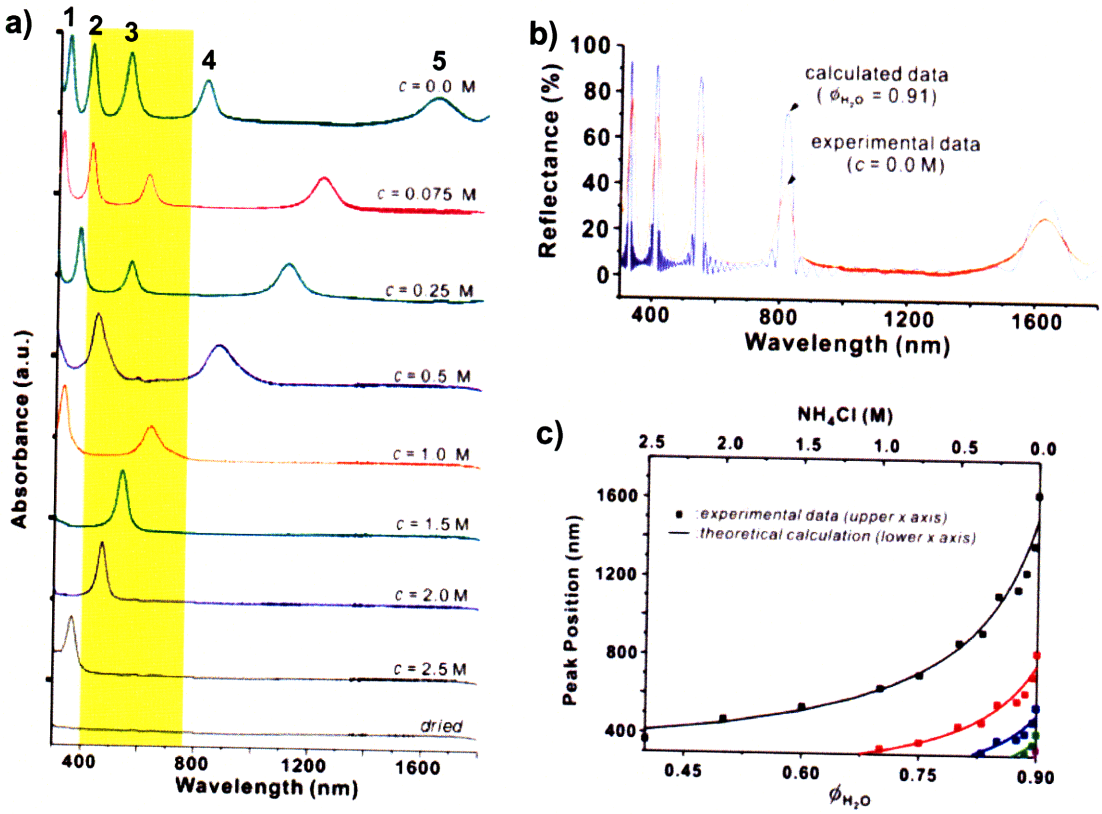

Figure 3.4: The optical response of a quaternized PS-P2VP copolymer to the concentration of a salt in solution – (a) Ultraviolet–visible–near-infrared absorbance spectra of PS-b-QP2VP photonic gels swollen by contact with different concentrations of NH_4Cl aqueous solution. The yellow region represents the visible wavelength region. (b) The comparison of the experimentally measured reflectance with a calculation by the transfer matrix method at Φ_{H2O} =0.91. (c) The change of stop-band position by approximately 575% from 364 to 1,627 nm as a function of the NH_4Cl concentration (symbols), or versus Φ_{H2O} (solid line) for each band. (figure by Dr. Y. Kang and published in reference 10)

3.2 Structural defects as fast diffusion pathways for rapid swelling

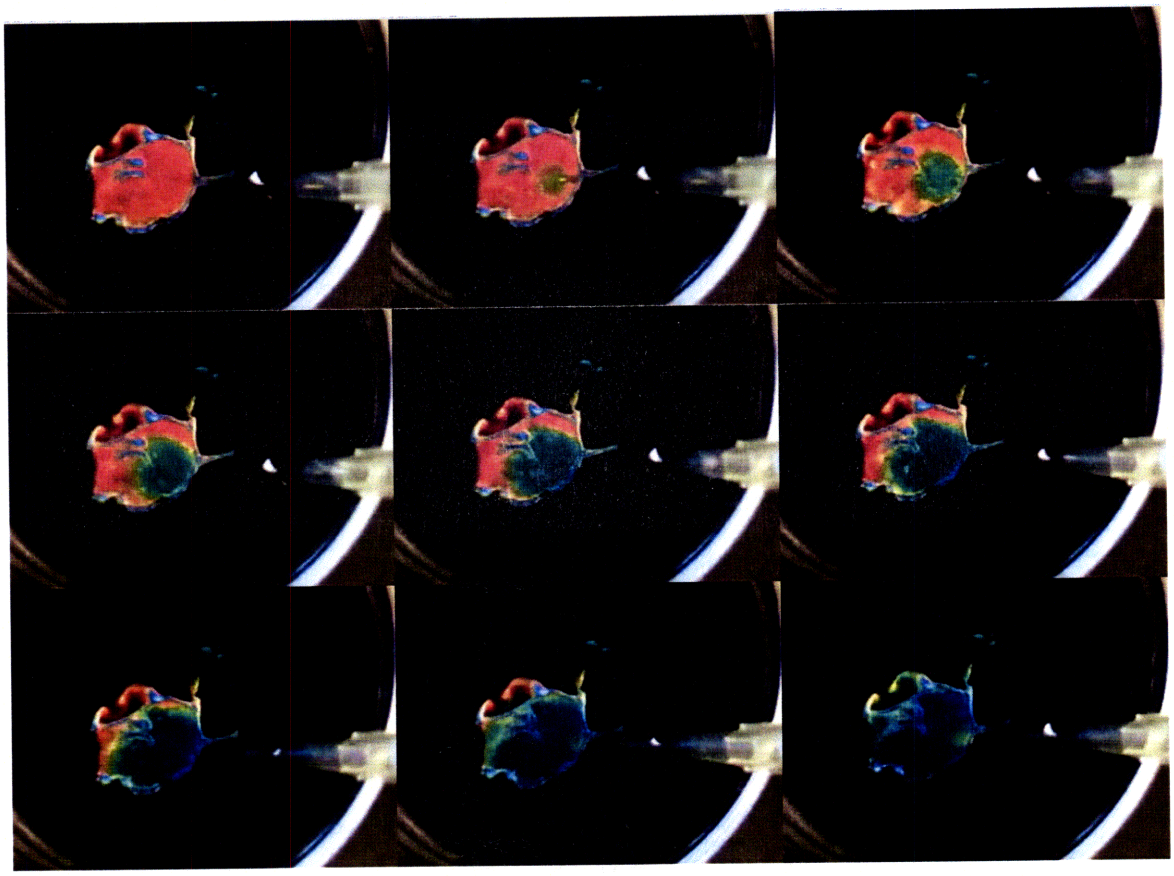

Figure 3.5: De-swelling of a quaternized 190k-190k PS-P2VP photonic gel by an ammonium chloride salt solution – Originally red, the addition of an ammonium chloride changes the color reflected by the BCP film to yellow in less than 0.1 seconds. As more salt is added to the solution the quaternized P2VP gel layers continue to shrink and reflect shorter wavelengths. The time elapsed from the first to the final frame is 1.7 seconds. (adapted from a video by Dr. Y. Kang)

Another advantage of these structured gels is the speed at which they swell in the presence of low-viscosity solvents and it is somewhat surprising that they do so considering the relatively defect-free lamellar morphologies presented in figure 3.2. If the poly(styrene) layers were truly unbroken, parallel sheets, the solvent swelling the P2VP layers would have to enter from the edges of the lamellae at the film periphery resulting in a slow swelling process governed by solvent transport in the plane of the film.

Fortunately, defects do exist in these structures both on the microscopic and macroscopic levels to facilitate diffusion fast diffusion kinetics.

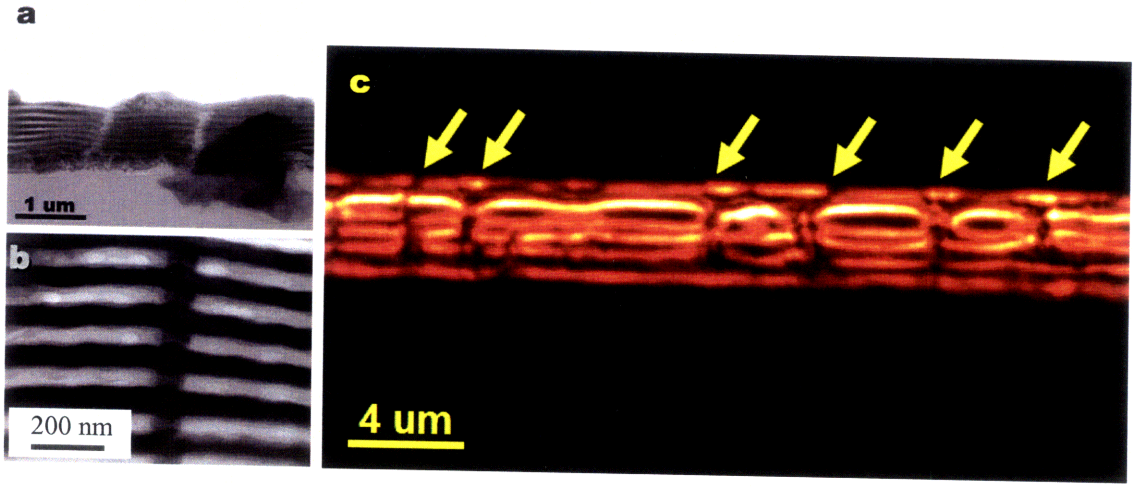

Figure 3.6: Microscopic fast diffusion pathways in PS-P2VP – (a) TEM cross-section showing cracks in the PS-P2VP film (b) Possible helicoidal screw dislocations which contribute to the fast transport for aqueous solvents and ions when the film is immersed in aqueous solution. (c) Vertical pores evident in the swollen film as viewed with laser scanning confocal microscopy. (TEM micrographs a and b from Dr. Y. Kang)

Figure 3.6 shows micro- and nanoscopic vertical defects in the layered structure of the BCP allowing solvent to gain access to successive P2VP layers through the PS layers. Other larger features such as pinholes in the film from spin coating, small holes from the dissolution of the BCP by chloroform condensation during annealing, or defects created by inclusions or impurities in the casting solution also serve to improve the transport of solvent throughout the structure.

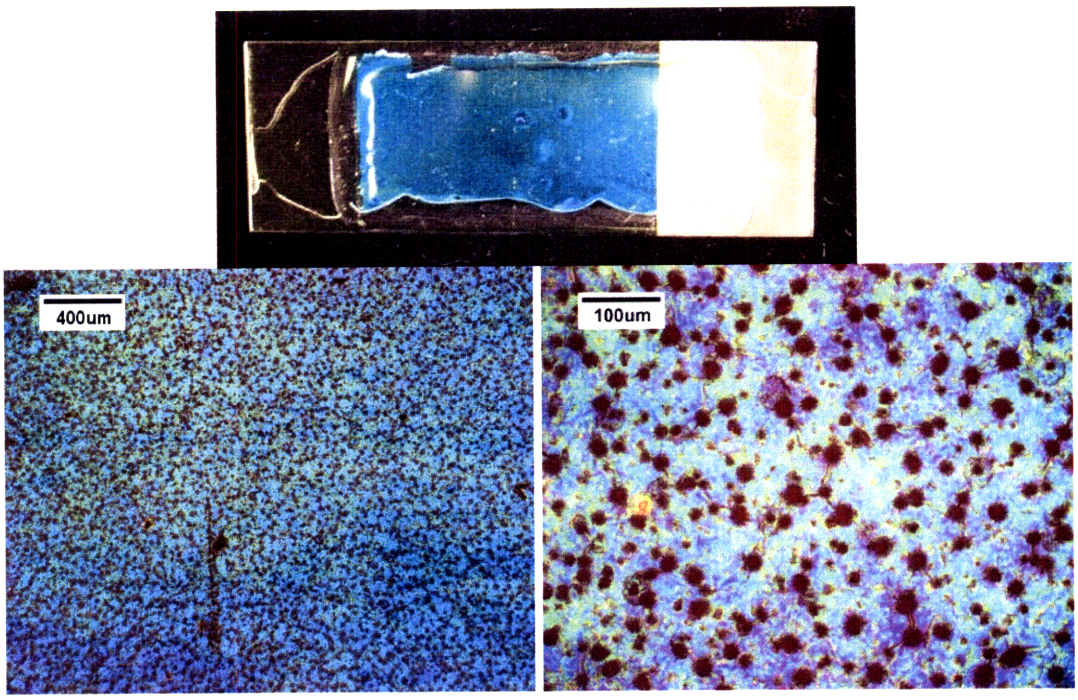

Figure 3.7: Microscopic fast diffusion pathways in PS-P2VP – (a) A 1"x3" microscope slide coated with 57k-57k PS-P2VP and swollen with 0.005M acetic acid. To the naked eye, the film appears quite uniform. A coverslip was placed on top of the solution and was sealed to the bottom slide through the use of a UV curable adhesive. (b) An image of the film showing the film actually contains numerous defects. (c) An enlarged image of the pores/pinholes in the film. Also notice the multiple colors reflected by the film that contribute to the broadening of the reflectivity peak.

3.3 Reflectivity tuning of PS-P2VP with different molecular weights in methanol

The 190k-190k PS-QP2VP system has the advantage of being able to change the position of its reflectivity peak by over 575% from the NIR to UV spectral region but if such a large change is not needed, a lower molecular weight polymer may be used. Figure 3.8 presents reflectivity data from three lower molecular weight PS-P2VP polymers (57k-57k, 102k-97k, and 130k-135k) immersed in methanol. As the molecular weight of the PS-P2VP is increased, the domain thicknesses are increased and hence the resulting reflectivity peak is shifted towards longer wavelengths. Methanol is not as good a solvent for P2VP as water is for QP2VP, so the fraction of methanol in the P2VP

domains is slightly less at 87% (calculated through transfer matrix method (TMM) modeling).

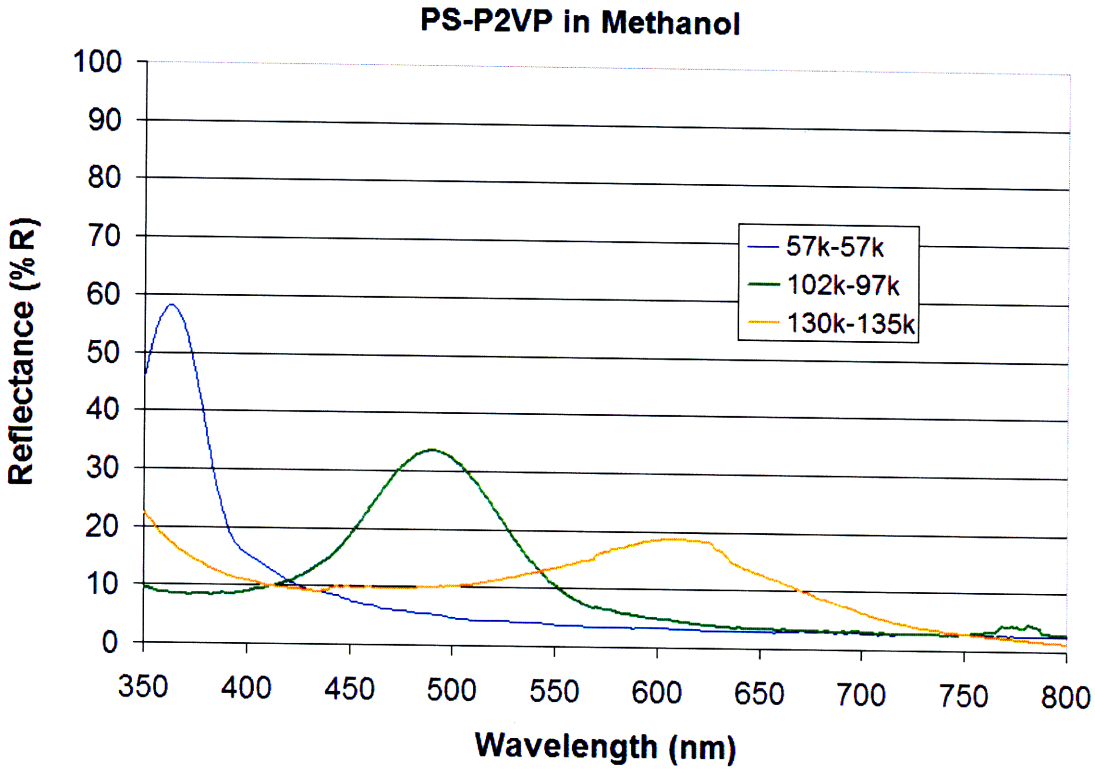

Figure 3.8: Reflectivity measurements of three PS-P2VP polymers (57k-57k, 102k-97k, and 130k-135k) swollen with methanol – Increasing the molecular weight of the copolymer increases the domain spacing of the PS layers as well as the maximum thickness of the P2VP layers when swollen. The color of the lines in the plot represents the approximate color seen by the human eye when viewing each individual sample. The broadening of the 102k-97k and 130k-135k samples is attributed to insufficient annealing as well as increasing polydispersity compared to the 57k-57k sample. The reduction of the intensity of the reflectivity peak is due to the reduction in refractive-index contrast between the methanol and the poly(styrene).

As the molecular weight is increased, the peaks broaden and decrease in intensity. This is attributed to the reduction of long-range order within the samples. All samples were exposed to chloroform vapor by annealing for one day after spin-coating. As molecular reorientation is increasingly difficult as molecular weight increases, it is assumed that these copolymers are not fully annealed. Because of this, layer orientations

will not always be parallel to the substrate and since the reflectivity peak position depends on the angle at which light interacts with the structure. The peaks will broaden as they will be the summation of the reflections from all spacings and orientations in the illuminated area. Another possibility in addition to orientation effects brought on by insufficient annealing is that the polydispersity (PDI) of these samples (which increased with increasing molecular weight) caused irregularities in layer spacing. 57k-57k had the lowest PDI (1.08) and highest reflectivity of the three while the 102k-97k sample was slightly higher at 1.12. The PDI of the 130k-135k sample was 1.3 and it shows the broadest reflectivity peak. Although PDI is a factor, inadequate annealing is thought to be the dominant cause of the diminished reflectivities.

3.4 Reflectivity tuning of a 57k-57k PS-P2VP copolymer in alcohol solutions

Changing the molecular weight of the sample swollen with the same solvent (methanol) created a change in the reflectivity of the sample through the difference in layer spacing in the polymers. Reflectivity peak tuning can also be accomplished through the use of a single diblock and simply varying the solvent. In this case, four different alcohols were used to swell a 57k-57k photonic gel (see figure 3.9). Four samples were cut from a single glass slide onto which the PS-P2VP polymer had been spun. The polymer was annealed in chloroform vapor for 24 hours. One sample was immersed each of the following alcohols: methanol, ethanol, 1-propanol, and 1-butanol (all 99% pure or greater) after which transmission measurements were taken with a UV-vis spectrophotometer.

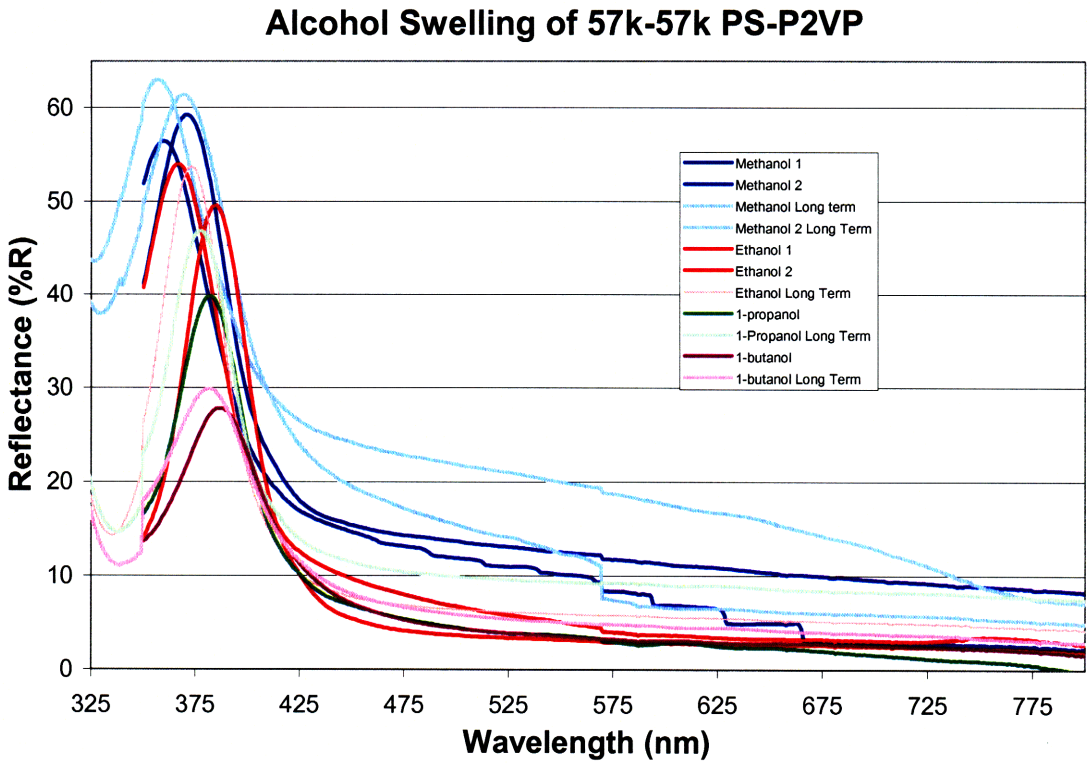

Figure 3.9: Reflectivity measurements of 57k-57k in methanol, ethanol, 1-propanol, and 1-butanol – Because of differences in refractive index of the different alcohols, a red-shift in the reflected wavelength can be seen as the number of carbon atoms in the alcohol increase. The sample was spun onto a 1" x 3" glass slide which was annealed and then broken into four different pieces. These pieces were tested immediately after immersion into the alcohols as well as one week later to check if there were any kinetic effects. Because of inhomogeneities in the samples it is impossible to definitive conclusions about differences in solubility but by using transfer matrix method calculations it was found that all runs produced approximately the same P2VP layer spacing (~115nm).

All of these solvents swelled the structure which reflected blue light after immersion. Immediately after immersion into the solvents, reflectivity measurements were made. These were then compared with later measurements made after the samples were allowed to soak in the solvents for 24 hours. Originally it was thought that a difference in solvent solubility parameters (seen in table 3.1) would cause a difference in solvent affinity for the P2VP and thus differences in layer thickness. Upon quick inspection of the data, the reflectivity peak of the 1-butanol (which has the smallest difference between its solubility parameter and that of P2VP) swollen sample is

positioned at a longer wavelength compared to the other alcohols which would suggest increased solubility. Transfer matrix method calculations were carried out in order to extract the layer spacings of the P2VP domains which would be a measure of solvent affinity.

Table 3.1: Properties of the alcoholic solvents used in the experimentation (values for 20°C)

Solvent Properties[14]			
Name	Refractive index (at 400nm)	Solubility parameter $(MPa)^{1/2}$	Hydrogen Bonding Solubility Parameter[15] $(MPa)^{1/2}$
Methanol	1.338	29.66	22.3
Ethanol	1.373	26.43	19.4
1-Propanol	1.390	24.91	17.4
1-Butanol	1.416	23.73	15.8
P2VP	1.63	19.86[16]	--
PS	1.63	--	--

TMM calculations were carried out in order to model the reflectivity and find the layer spacing of the P2VP/solvent layer. Literature values for refractive index data at 400nm was used for all constituent materials (except P2VP values which were assumed to be close to PS). The layer thickness for the PS domains was extracted from TEM micrographs (averaging over several periods) and was found to be 17 nm. Transfer matrix method calculations showed an almost constant spacing value for all samples with the biggest differences explained by the difference in refractive index between the different liquids (see table 3.1). Because of the variability in the reflected wavelength in different regions of the same sample (see methanol and ethanol samples 1 and 2 in figure 3.9) and slight differences after soaking for a week, no definitive conclusions can be drawn but the preliminary data points to similar solubility in P2VP for all four alcohols tested. Although the solubility parameters for all the solvents are quite different, this

difference is mainly due to the hydrogen bonding portion of the solubility parameter. Since the solubility of the polymer seems not change much in any of these alcohols, this points to limited or no hydrogen bonding interactions between the P2VP and the alcohols which has been suggested by other researchers.[17]

3.5 Reflectivity tuning of a 57k-57k PS-P2VP copolymer in acetic and hydrochloric acid – water solutions

The extreme degree of swelling seen in the quaternized PS-P2VP system in figure 3.4 can be attributed to the high affinity of water for the polyelectrolyte QP2VP domains. The quaternization reaction produces a chemical change in the P2VP that converts it permanently to a charged polymer that is highly soluble in water. The same effect can also be brought about through a protonation reaction where the percent ionization is a function of the pH of the solution and the pKa of the compound undergoing the reaction. In the PS-P2VP system, water is a non-solvent for both PS and P2VP. As the pH is lowered by adding acetic acid to the water, P2VP is partially converted to protonated P2VP ($P2VP^+$). Water has a strong affinity for $P2VP^+$ and at a certain pH when a high enough percentage of P2VP has been converted to P2VP, the solution swells the domain. As the pH is further lowered, more P2VP is converted to $P2VP^+$ and the polymer swells shifting the reflectivity peak to even longer wavelengths.

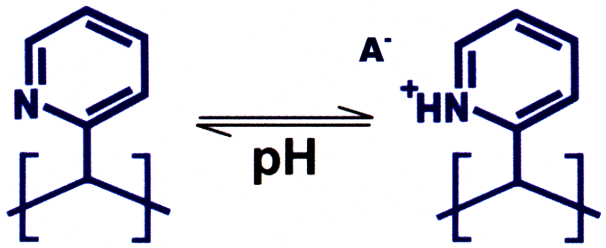

Figure 3.10: The conversion of P2VP to P2VP$^+$ via a protonation reaction – Lowering the pH of the solution causes the pyridine ring to convert to a charged pyridinium ring which has an affinity for water. When enough P2VP is converted to P2VP$^+$, the P2VP/ P2VP$^+$ layer swells. Adding more acid to the solution increases the percentage of P2VP+ in the polymer and thus increases the solubility of the solution in the domain. When enough acid has been added to fully protonate the P2VP, maximum swelling occurs. After this point adding more acid only adds ions that will screen the interactions between P2VP+ and the solvent which will de-swell the layers because of the reduced the solubility of the solvent in the layers.

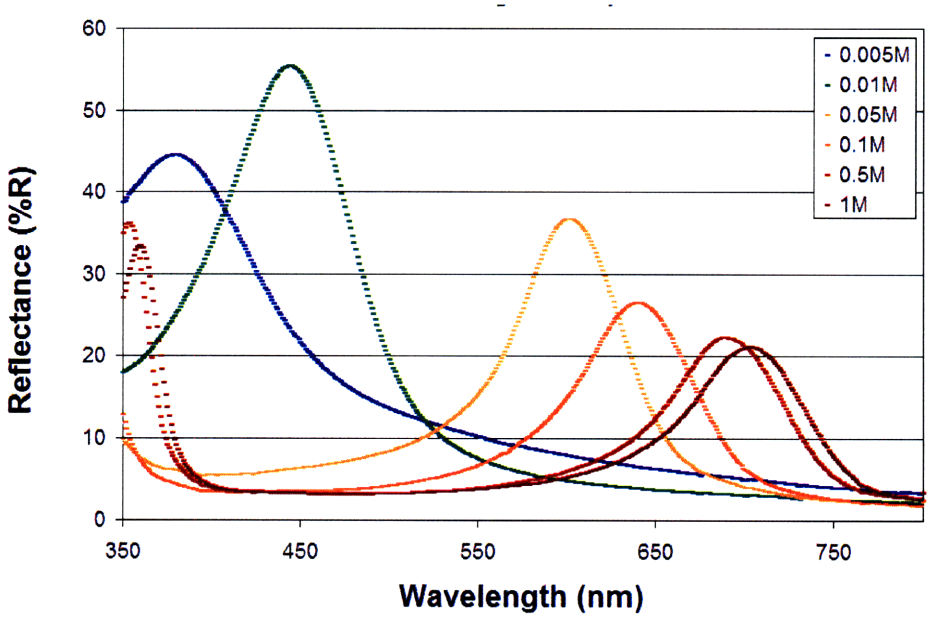

Figure 3.11: The change in reflectivity with increasing acetic acid concentration – As the pH is decreased (concentration of acid increased) the polymer becomes more and more protonated increasing the solubility of the solution in the hydrophilic layers. The color of the line for each sample is the approximate color seen by the human eye. The decreasing reflectivity towards longer wavelengths is due to the reduction in refractive-index contrast between the solvent and the poly(styrene).

As the pH is decreased even further, all available P2VP has been converted to P2VP$^+$ and the reflectivity peak position reaches a maximum. As seen in figure 3.12, this is approximately 1M acetic acid. If the pH is lowered even further, the excess ions in solution start to screen the polyelectrolyte from interacting with the solution and de-swelling occurs moving the reflectivity peak to smaller wavelengths. This can be seen

for the hydrochloric acid data in figure 3.13. Initially, when the pH is decreased, an increase in layer spacing is seen but after fully protonating the P2VP excess ions cause the reflectivity to blue-shift. The positional difference between the hydrochloric and acetic acid curves can be attributed to inconsistencies in sample preparation process, specifically the solvent vapor annealing step or possibly the change in solubility when different counter-ions are present.

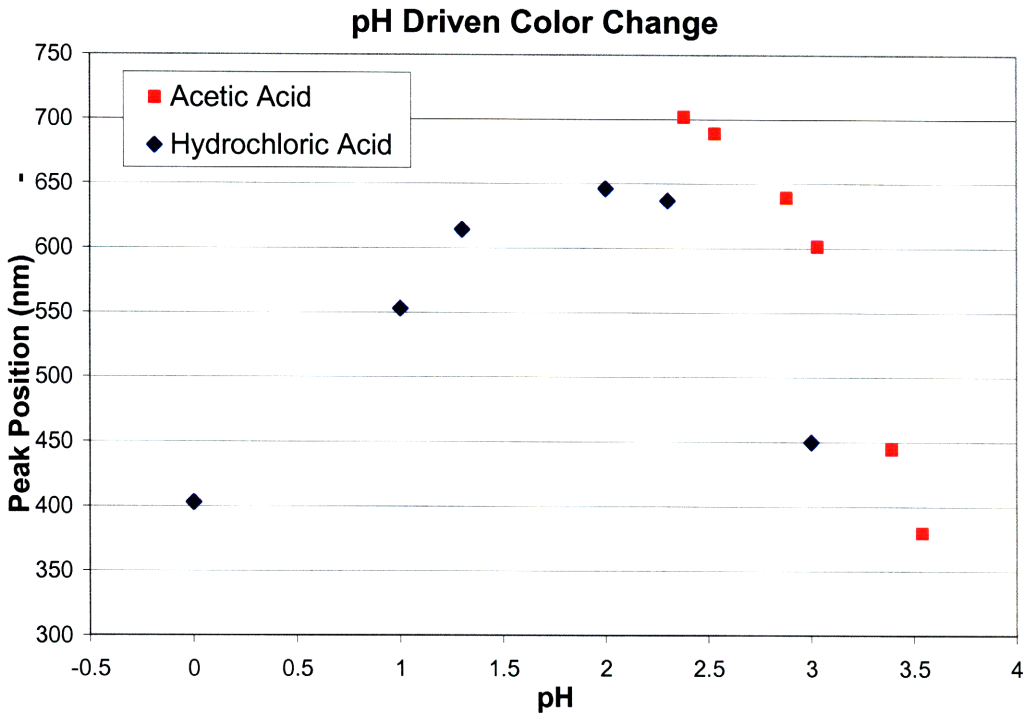

Figure 3.12: Reflectivity peak position as a function of solution pH for acetic and hydrochloric acid – water solutions – As the polymer is protonated the reflectivity peak shifts towards longer wavelengths as the P2VP layer becomes more hydrophilic. The blue-shifting effect of adding additional acid past the point of full protonation can be seen in the hydrochloric acid data.

A pKa value for P2VP in acetic acid-water solutions at 23°C can be found if it is assumed that the increase in ionization of the P2VP is proportional to the change in reflectivity peak position. Using the Henderson-Hasselbalch equation, the ratio of P2VP to $P2VP^+$ can be computed if the pH and pKa are known:

$$pH = pKa + \log([P2VP]/[P2VP^+])$$

Rearranging to find the ratio of the P2VP and $P2VP^+$ concentrations:

$$[P2VP]/[P2VP^+] = 10^{\,pH-pKa}$$

Finally, the percent of P2VP that is ionized to P2VP+ is:

$$\% \text{ Ionization} = 100/(1+ 10^{\,pH-pKa})$$

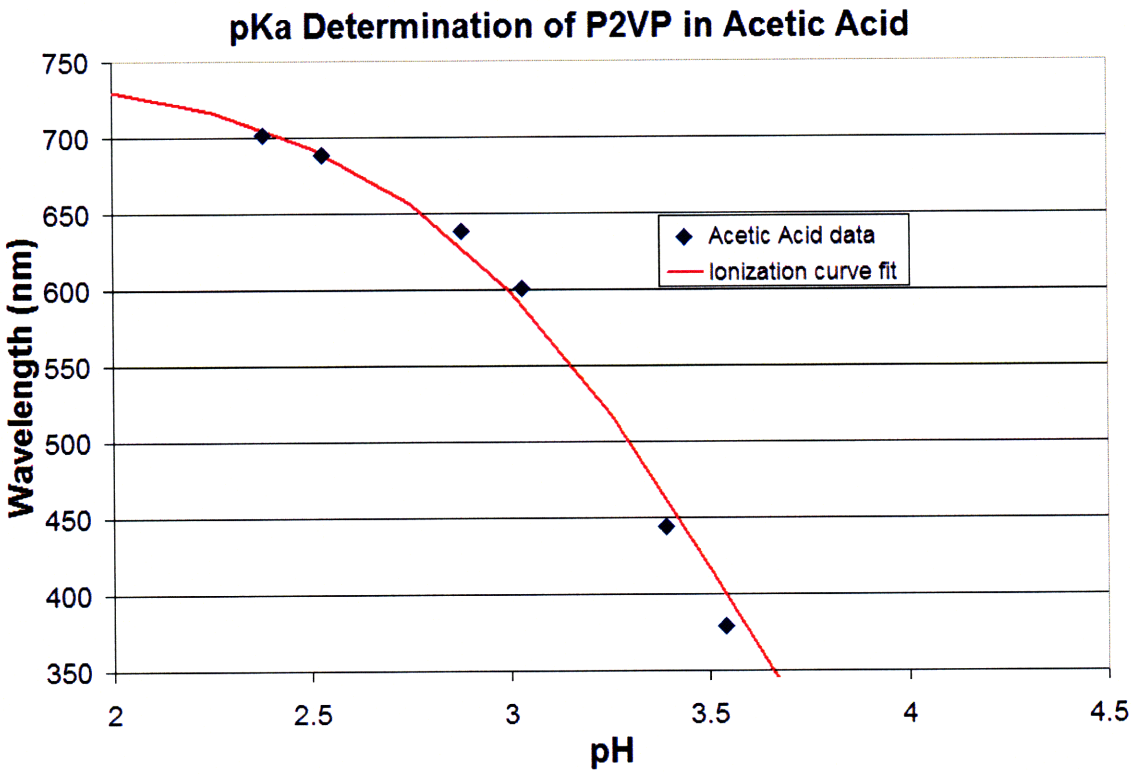

Figure 3.13: Calculation of the pKa of P2VP through fitting of an ionization curve to the acetic acid pH-reflectivity peak position data– The pKa of P2VP was calculated by fitting an ionization curve to the reflectivity peak positions for PS-P2VP in acetic acid. The two-parameter (constant of proportionality between ionization percentage and peak position and pKa) best-fit curve gave a pKa value of 3.6.

This percent ionization term was multiplied by a constant in order to convert to reflectivity peak position through the following equation:

$$\lambda_{peak} = \alpha\,[100/(1+ 10^{\,pH-pKa})]$$

where α is the constant of proportionality and λ_{peak} is the reflectivity peak position. α and pKa were used as fitting parameters and the curve was fit to the experimental data using the least-squares method which yielded the following parameters: $\alpha = 7.48$ and a pKa value at 23°C of 3.6. This value is quite close to the value found by Ferruti and Barbucci of 3.45 in a 45% ethanol/55% water solution[18] at 25°C and somewhat lower than the value of 4.5 reported by Tantavichet et al. for electropolymerized P2VP at 25°C in a 0.5M potassium chloride/hydrochloric acid solution in water.[19]

3.6 Conclusions

This chapter has shown the remarkably broad range of tuning possible in the PS-P2VP system including: salt induced de-swelling of a quaternized 190k-190k PS-QP2VP block copolymer, swelling changes through changing the pH and thus the protonation level of a 57k-57k PS-P2VP BCP, the change in solubility for several alcohols in 57k-57k PS-P2VP, and the photonic behavior of three different molecular weight samples in methanol. Through these studies a number of 'handles' which can be turned to control the reflected color of these lamellar BCPs have been demonstrated. The next two chapters will be dedicated to further exploration of this system, specifically the temperature-dependent reflectivity (chapter 4) and the change in reflectivity peak position with electrochemical stimulation (chapter 5.)

3.7 References

1 Fink, Y., Urbas, A.M., Bawendi, M.G. Joannopoulos, J.D. Thomas, E.L. Block copolymers as photonic bandgap materials Journal of Lightwave Technology, 17(11), 1963-1969 (1999)

2 Edrington, A.C., Urbas, A.M., DeRege, P., Chen. C.X., Swager, T.M., Hadjichristidis, N., Xenidou, M., Fetters, L.J., Joannopoulos, J.D., Fink, Y., and Thomas, E.L., Polymer-based photonic crystals, Adv. Mat., 13(6), 421-425 (2001)

3 Yoon, J.S., Block copolymer photonic crystals: towards self-assembled active optical elements, Ph.D. Thesis, Massachusetts Institute of Technology, (2006)

4 Weissman, J.M., Sunkara, H.B., Tse, A.S., and Asher, S.A., Thermally switchable periodicities and diffraction from mesoscopically ordered materials, Science, 274 p. 959-960 (1996)

5 Matsubara, K., Watanabe, M., and Takeoka, Y., A thermally adjustable multicolor photochromic hydrogel, Angew. Chem. Int. Ed., 46, 1688-92 (2007)

6 Kumoda, M., Watanabe, M., and Takeoka, Y., Preparations and optical properties of ordered arrays of submicron gel particles: interconnected state and trapped state, Langmuir, 22, p.4403-7, (2006)

7 Zhai, L., Nolte, A.J., Cohen, R.E., and Rubner, M.F., pH-Gated Porosity Transitions of Polyelectrolyte Multilayers in Confined Geometries and Their Application as Tunable Bragg Reflectors, Macromolecules, 37, 6113-6123 (2004)

8 Nolte, A. J.; Rubner, M. F.; Cohen, R. E., Creating effective refractive index gradients within polyelectrolyte multilayer films: molecularly assembled rugate filters, Langmuir, 20, 3304 (2004)

9 Olugebefola, S.C., Ryu, S.W., Nolte, A.J., Rubner, M.F., and Mayes, A.M., Photo-cross-linkable Polyelectrolyte Multilayers for 2-D and 3-D patterning, Langmuir 22, 5958-5962 (2006)

10 Kang, Y.J., Walish, J.J., Gorishnyy, T., and Thomas, E.L., Broad-wavelength-range chemically tunable block-copolymer photonic gels, Nature Materials, 6, 957 - 960 (2007)

11 Yamaue, T. and Doi, M., Theory of one-dimensional swelling dynamics of polymer gels under mechanical constraint, Physical Review E 69, 041402 (2004)

12 Suzuki, A. and Hara, T., Kinetics of one-dimensional swelling and shrinking of polymer gels under mechanical constraint, Journal Of Chemical Physics, 114(11), 5012-15 (2001)

13 Brandrup, J.; Immergut, Edmund H.; Grulke, Eric A.; Abe, Akihiro; Bloch, Daniel R. Polymer Handbook (4th Edition). John Wiley & Sons.

14 Wypych, George, Knovel Solvents - A Properties Database, ChemTec Publishing, (2000)

15 Hansen, C.M., Hansen solubility parameters: a users handbook, CRC press, Boca Raton, FL, (2000)

16 Shaw, M.T., Studies of polymer-polymer solubility using a two-dimensional solubility parameter approach, J. Appl. Polym. Sci., 18, 449, (1974)

17 Arichi, S., Matsuura, H., Tanimoto, Y., and Murata, H., Studies of poly-2-vinylpyridine. II. Solubilities in various solvents, Bulletin of the chemical society of Japan, 39(3), 434-9 (1966)

18 Ferruti, P. and Barbucci, R., Linear amino polymers: synthesis, protonation and complex formation, Advances in polymer science, 58, 55-92, (1984)

19 Tantavichet, N., Pritzker, M.D., and Burns, C.M., Proton uptake by poly(2-vinylpyridine) coatings, Journal of Applied Polymer Science, 81, 1493-7, (2001)

Chapter 4:

Thermochromic Behavior of PS-P2VP in Different Solvents

Previously in chapter 3, changes in the reflectivity spectrum of the photonic gels were brought about by changing the global chemical environment of the gel through increasing the pH of the solution or by using solvents having different refractive indices and affinities to P2VP. The response of the gel (expansion or contraction) to a change in pH or to the quality of the solvent was studied at a constant temperature. A more complete understanding of the photonic gel system requires knowledge of the temperature-related behavior of the system not only to satisfy scientific curiosity but to possibly use this knowledge to construct more robust sensors for commercial applications (e.g. accurately sensing salt concentration changes while temperature is fluctuating). Depending on the application, both a temperature-dependent change in the reflectivity

peak position (for measuring temperature) and temperature-independent behavior (for sensing other phenomena with the photonic gel) would be desirable. Through the work shown and discussed in this chapter, a new mechanism for thermally tuning the size of the P2VP domains and thus the reflectivity of the photonic gel has been elucidated. This discovery leads to the ability to control the thermochromic behavior of the photonic gel from no change with temperature to a change of -1.5nm/°C opening up applications for this block copolymer thermochromic gel in applications in either temperature-responsive or temperature-independent applications.

Currently, major commercial applications for thermochromic materials are color changing security labels, thermometers, paper coatings for thermal printing, and coatings for novelty items such as shirts and toys[9]. Apart from commercial uses of artificial materials with temperature dependent color, a change in temperature is also known to affect the natural color of animals signaling a change in activity or regulation of body temperature.

4.1 Natural Thermochromic Materials

Masters of camouflage on land, certain species of chameleons (*Chamaeleo jacksonii* and *Chamaeleo dilepis*) have temperature dependent skin coloration linked to the modulation of the rate of heat gain from the environment[1]. The change in skin color is linked to the ability of the animal to control the distribution of certain pigment cells in its skin. The chameleon, a cold blooded reptile, is thought to use the change in absorbance and reflectance in its skin to reduce the amount of time it spends at suboptimal performance temperatures while basking in the sun. The dark coloration in

these chameleons which was observed in the morning basking period turned lighter (and presumably more reflective) later in the day when the temperature was warmer[2]. This change in absorption has important consequences for the cold blooded chameleon as its locomotory speed is extremely temperature dependent and can be reduced by as much as 40% by a drop in temperature from ~35-~20°C (unpublished data from Bennett, Walton, and Losos cited in reference 1.)

Much like the aforementioned chameleons, other lizard species are known to regulate their body temperature through the use of optical elements[3]. *Phrynosoma modestum* is a lizard that lives in the Chihuahauan desert in north-central Mexico and southern New Mexico which has skin that uses both absorbers and reflectors to control the rate of heat influx[4]. The reflectors, called iridophores, are cells that contain small platelets usually made out of a crystalline substance such as guanine[5]. In *P. modestum*, the platelets in the iridophores are not well ordered and thus diffusely scatter incoming light giving the skin a white color. Below these iridophore cells are absorbers called melanophores. These cells have melanin containing pigment sacs (melanosomes) that absorb light (see figure 4.1). When the animal wants to increase its body temperature rapidly, melanosomes are shuttled above the iridophores causing a darkening of the skin. When the melanosomes are retracted, the iridophores again scatter light and the skin is white, reflecting most of the incoming thermal energy rather than absorbing it.

Figure 4.1: Melanosomes in the skin of a thermochromic lizard – In this cross section, the dark pigment cells (labeled M) extend towards the skin (E) of the lizard. When the lizard needs to absorb solar energy quickly, these absorbers are pushed up towards the skin and deployed sideways where they occupy a larger area than when they are in the retracted state. This causes the skin to appear dark and absorb more energy. When the pigment cells are retracted, the skin appears white due to scattering by randomly oriented high index of refraction platelets (labeled I). (Image from reference 4).

In *P. modestum* the iridophores lack regular arrangement and thus do not produce specific colors through interference reflection. Other species of lizard such as *Anolis carolinensis* possess much more regularly arrayed platelets in the iridophore cells and thus are capable of producing colors through interference phenomena[6] (see figure 4.2). In this lizard, color is thought to be produced through both Tyndall and interference mechanisms which explain the strong blue color (Tyndall scattering is proportional to $1/\lambda^4$ and is produced by incoherent scattering from inhomogeneously spaced particles with sizes greater than the wavelength of light) coupled with the specular reflection and angle-dependent coloration associated with interference effects. By changing the spacing

between the platelets inside of the iridophores, other lizard species use thermally tunable color as a signaling device.

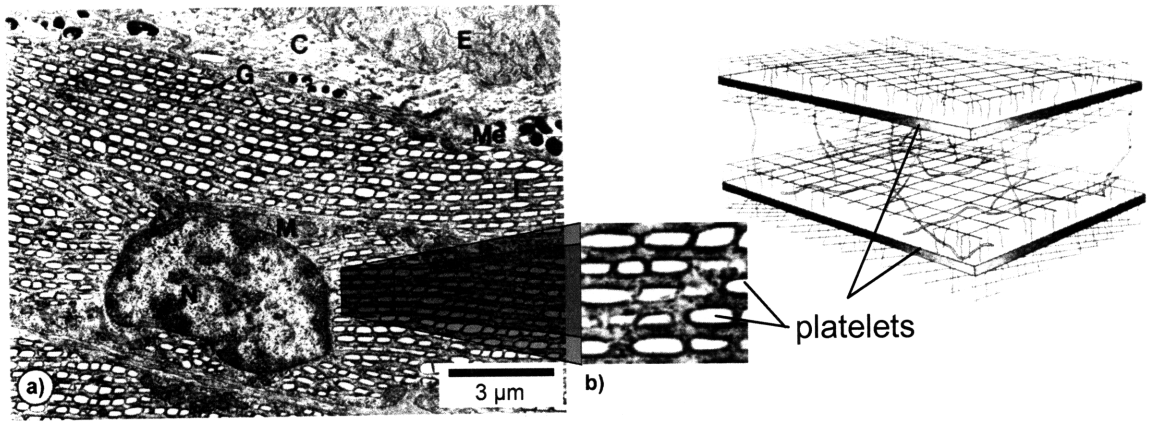

Figure 4.2: Structural similarities between lizard iridophores and photonic gel block polymers –Cells containing arrays of high index particles (left) which can produce interference colors reside close to outermost layer of skin (marked E) are common in some species of lizards. The high index platelets (which are the dark sheets on the right and the white platelets labeled G on left) are held together by a filament network. These polymer-like chains are functionally similar to the P2VP in the photonic gel block copolymer. (Images adapted from reference 6).

Body temperature in cold-blooded reptiles significantly affects their activity and to communicate this state of activity, one species of lizard use a color change controlled by its body temperature. The skin covering the belly of the common tree lizard (Urosaurus ornatus – see figure 4.3) changes its color in response to temperature with the peak color intensity corresponding to optimum temperatures of activity[7]. At temperatures outside of the optimum, these colored patches revert to colors that more closely resemble colors in the environment and thus help to conceal the animal. Unlike the chameleon which changes the distribution of pigments that absorb light in its skin to change color, the tree lizard modulates the spacing between plates in a simple one-dimensional (1D) photonic crystal to change its color[8]. These natural photonic crystals are comprised of alternating layers of high refractive index crystalline platelets (n~1.8) and lower

refractive index cytoplasm (n~1.33) and exhibit angular reflectivity dependence and specular reflection as opposed to the angle-independent color of absorbers.

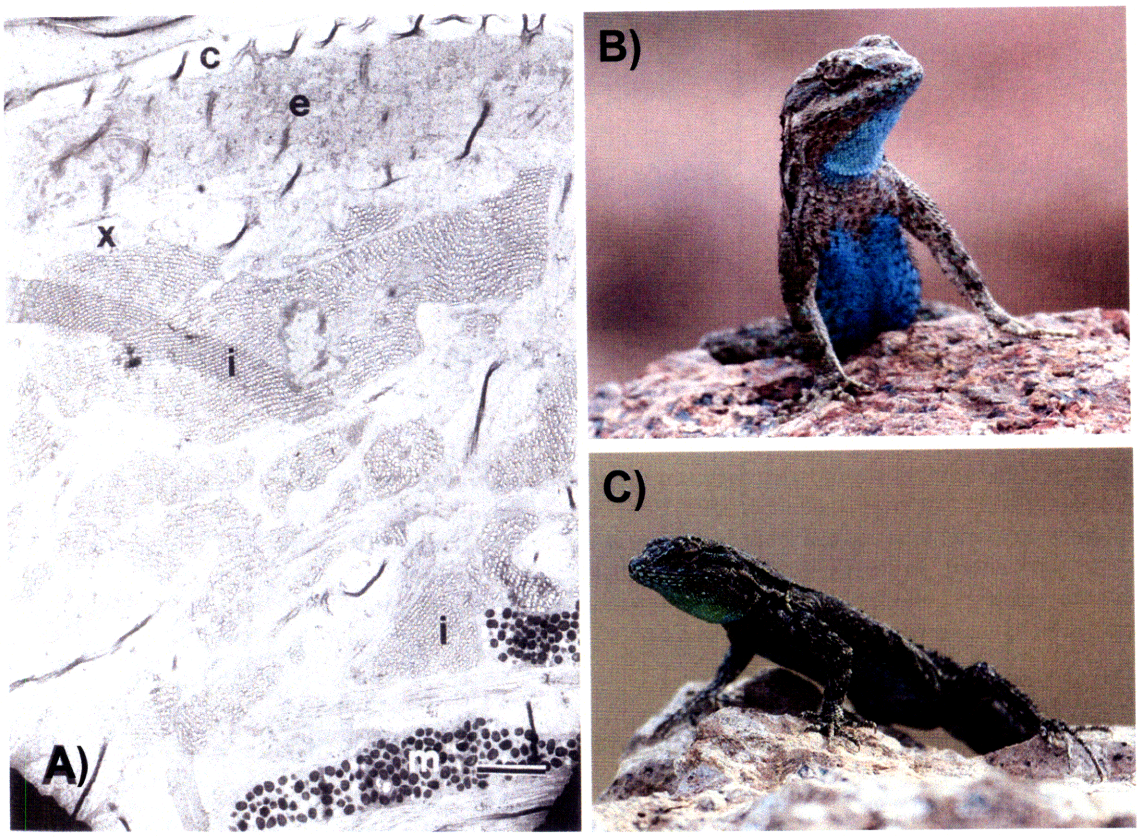

Figure 4.3: Thermochromic photonic crystals in *Urosaurus ornatus* – A) In response to temperature changes, the spacing between high index of refraction platelets in the iridophores (regions labeled i) of this lizard change causing a shift in the wavelength of reflected color (scale bar is 3μm). When the lizard's body temperature is optimal (higher temperatures) a conspicuous blue color (B) is displayed while at sub-optimal (lower) temperatures a green (C) or light red color is displayed which is better matched to the lizard's surroundings. (Pictures by Brad Weinert and TEM micrograph from reference 7)

The reflectivity of these natural photonic crystals is changed by changing the spacing of the platelets. Several hypotheses have been given for this spacing change including the temperature dependent behavior of proteins in the cellular membranes or thermoreceptors that are coupled to an opening or closing of an ion channel that would change the osmotic pressure of the cells thus changing the spacing between the platelets. The exact mechanism has not been clarified, but a link between osmolarity and temperature

response has been observed.[7] The current chapter is dedicated to studying the effects of temperature on block copolymer photonic crystals similar to those in the common tree lizard that have a hard, high-index segment and an expandable, lower-index segment that is used to control the reflectivity of the structure. Research into new, synthetic thermochromic materials has recently focused on the temperature-dependent coloration of photonic crystals similar to those in certain lizard species, especially gel-based systems which have shown exceptional color tunability.

4.2 Synthetic Thermochromic Materials

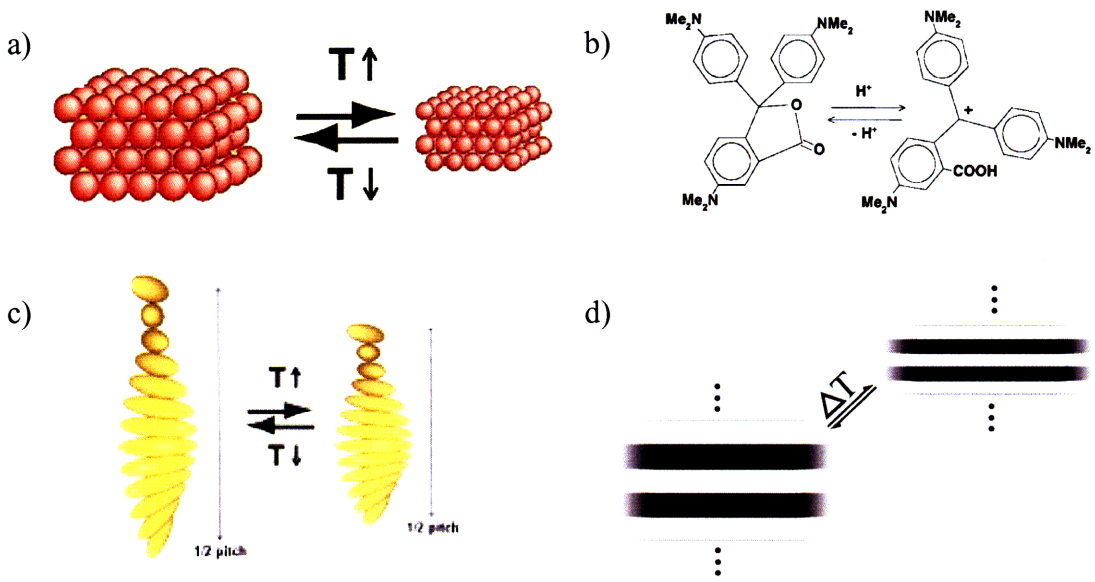

Figure 4.4: Major classes of thermochromic materials - a) A synthetic opal is constructed by packing sub-micron size spheres usually made of silica or polystyrene into regular arrays and the spaces between the spheres can then be infiltrated with other materials (e.g. gels). In this example the opal is made out of spherical hydrogel particles that themselves expand and contract with a change in temperature (adapted from reference 17). b) Thermochromic dyes which change absorbance with temperature due to a change in bonding are commonly used in commercial products that change color with temperature. (figure from reference 9) c) Cholesteric liquid crystals form helices which expand when heated changing the periodicity of the structure and thus changing the reflected wavelengths of light. The size of the liquid-crystal molecules do not change, just the rate of rotation between the molecules. (adapted from http://www.doitpoms.ac.uk/tlplib/liquid_crystals/images/cholesteric.png) d) Block copolymers also self assemble to form periodic structures which can reflect light. Here, the lamellar morphology is shown with a periodicity that is changed by the effects of temperature on parameters such as the Flory-Huggins interaction parameter or the change in solubility of a swelling agent with temperature.

The majority of commercial thermochromic materials are based on molecular transitions in dye molecules (see figure 4.4b). In the case of leuco dyes, this molecular transformation changes the molecule from a non-absorbing to an absorbing state at a particular temperature with the help of an acid commonly known as a developer. The dye and developer are mixed with a solvent which is usually an alcohol, ketone, ester, or ether whose melting point controls the fixed-temperature color transition of the mixture by controlling the dissociation of ions in the developer.[9] The color change is reversible upon the solidification of the solvent below its melting temperature (-100°C to 200°C according to patent literature cited in reference 9.) The three-component mixture is encapsulated for protection from the outside environment when used in commercial products. In terms of commercial applications, thermochromic dyes are only rivaled by liquid crystals which, unlike dyes, produce a continuous color change upon heating or cooling.

Cholesteric liquid crystals (CLCs) are comprised of rod-like molecules and have an anisotropic dielectric tensor meaning their index of refraction varies with direction. At certain temperatures these rod-like molecules pack themselves together into helical structures (see figure 4.4c) that produce a 1D periodic change in the index of refraction. Reflection of light occurs because of the interaction of light with the structure of the liquid crystal making it a type of 1D photonic crystal which derives its color through reflection of incident light. When the period of the helical structure (the pitch - p) is on the order of the wavelength of light, destructive interference occurs and light of certain wavelengths cannot propagate and is reflected depending on the anisotropy of the refractive index of the liquid crystal (n) and the pitch of the helix formed by the

molecules. The peak wavelength reflected from the structure is determined by the following equation:[13]

$$\lambda_{peak} = p^{*}\bar{n} \qquad (4.1)$$

where p is the helical pitch and $\bar{n}$ is the average of the ordinary (n_o) and extraordinary (n_e) refractive indices of the mesogen ($(n_o + n_e)/2$).

Because the CLC forms a helical structure, only light of a certain polarization is reflected and thus the maximum reflectivity of a CLC is 50% for incident light from non-polarized sources (e.g. the sun and normal household lighting) although recently this reflectivity limit has been surpassed by doping the CLC with a chemical that locally inverts the helix allowing the structure (now composed of both right and left-handed regions) to potentially reflect 100% of the incoming light.[10,11] When heated, the pitch of the CLC extends due the anisotropy of inter-molecular interactions and the wavelengths of light that are reflected change in proportion to the change in pitch.

Other research has focused on making CLCs with stop bands that do not move when the material is heated and only diminish in intensity. This is accomplished by fixing the pitch through light crosslinking of the liquid-crystal mesogens so that changing the temperature changes only the refractive index.[12,13] Commercially, CLC technology is employed to make inexpensive thermometers whose color correlates to a certain temperature. Table 4.1 contains a comparative listing of the temperature related peak shifts in various types of photonic crystals.

Table 4.1: Comparison of different thermochromic photonic crystals

Thermally Tunable Photonic Crystals				
Technology	Reference number	Temperature range (°C)	Wavelength range (nm)	$d\lambda_{peak}/dT$ (nm/°C)
Cholesteric Liquid Crystals*	10	50-68	2900-4200	+72.2
	12	30-55	475-600	+5
	14	75.9-74.5	450-650	-143
Opals	15	120-150	630-600	-1
	16	12-35	700-450	-10.9
	17	11-25	790-400	-27.9
	18	16-31	650-350	-20
	21	15-30	510-423	-5.8
Block copolymers	22	30-140	510-450	-0.55
	23	30-90	520-575	+1.1**
	24	80-134	530-370	-3.0

*Non-linear change with temperature.
**Irreversible change with temperature.

Another approach that utilizes a periodic modulation of the refractive index of a material to reflect light is that of artificial opals. These structures (see figure 4.4a) which are produced by arranging small spheres in a lattice through sedimentation or electrostatic repulsion are directly analogous to the natural opal gemstone which is colored due to light diffracting from a face-centered cubic (fcc) lattice of precipitated silica inclusions. The small spherical particles used for the artificial opals are commonly made out of silica or polystyrene (PS) and need to have a narrow size distribution in order for long range order to occur. Once made, these structures can be infiltrated with other materials to create thermally tunable reflectors. High temperature thermochromic opals have been produced experimentally by infiltrating barium titanate, a ferroelectric material with a

tunable index of refraction, around silica spheres with a sol-gel process[15] but the majority of thermally tunable opals have been constructed with polymeric gels as the active material.

In 1996, Asher and co-workers prepared a lattice of polystyrene spheres which was infiltrated with a monomer which was subsequently crosslinked and swollen with water to form a poly(n-isopropylacrylamide) (NIPAM) gel.[16] The NIPAM gel undergoes a reversible volume phase transition around 32°C where it is collapsed above the transition temperature and swollen below that temperature (~2700% change in volume). Subsequent researchers have explored variations on the same theme by changing the infiltrating gel to a more responsive copolymer,[17,18] by directly using NIPAM based spherical particles to form the colloidal crystal,[19,20] and by filling an inverse opal (silica opal infiltrated with PS where the silica is subsequently etched out leaving a hollow PS photonic crystal) with a temperature-responsive gel. The PS inverse opal structure was then dissolved away leaving a network of interconnected gel particles that displayed a temperature-dependent reflectivity peak.[21]

Block copolymers are self assembling materials which form microstructured morphologies and if properly engineered can form photonic crystals that display thermochromic properties. Other investigators have probed the temperature-dependent reflectivity of one-dimensional block copolymer reflectors composed of solvent swollen block copolymers (BCPs)[22], liquid-crystal side chain BCPs[23], and BCPs blended with liquid crystals[24]. The phenomenon that gives the block copolymers their structure is microphase separation and is brought about because of the repulsion of the respective polymer chains which are (usually) immiscible but are covalently linked forcing the

system to phase separate on a small length scale. This scale is determined by the length of the polymer chains and the extent of their immiscibility. The structural morphology of these block copolymers is controlled by the volume fraction of the constituent polymers with a symmetric 50-50 diblock forming a lamellar structure. The remainder of this chapter will explore the temperature-related photonic properties of a PS-P2VP copolymer swollen with highly selective solvents.

4.3 Thermochromic Behavior of a Photonic Gel BCP in Highly Selective Solvents

The specific system under investigation is a symmetric poly(styrene)-poly(2-vinylpyridine) (PS-P2VP) BCP with a molecular weight of 57kg/mol (PS) – 57kg/mol (P2VP) and a polydispersity of 1.08 purchased from Polymer Source (Duvall, Canada). Samples spun onto slide glass were immersed in several different liquids and cooled to a temperature just above their freezing points. In order for the PS-P2VP to reflect visible light, it is immersed in a solvent and one or both domains can swell depending on the affinity of the solvent to the polymers that constitute the block copolymer. In the present case, extremely preferential solvents for the P2VP block were used such as acetic acid and methanol. These solvents do not swell the PS block which remains rigid and glassy (see chapter three for more details). The temperature-related behavior in a selective solvent was probed from 1°C to 23°C for a quaternized PS-P2VP sample in de-ionized water and for PS-P2VP samples immersed in 1M, 0.1M, and 0.01M acetic acid. The temperature-dependence of the reflectivity peak was also explored from -17°C to 41°C in PS-P2VP samples immersed in methanol. Transmission spectra were collected on a CARY 6000i UV-vis spectrophotometer using a purpose-built liquid cell with a volume

of approximately $100cm^3$ (see figure 4.5). Three different sample sets were investigated to elucidate the thermochromic behavior in the PS-P2VP system: methanol swollen PS-P2VP, acetic acid-water swollen PS-P2VP, and de-ionized water swollen PS-quaternized P2VP.

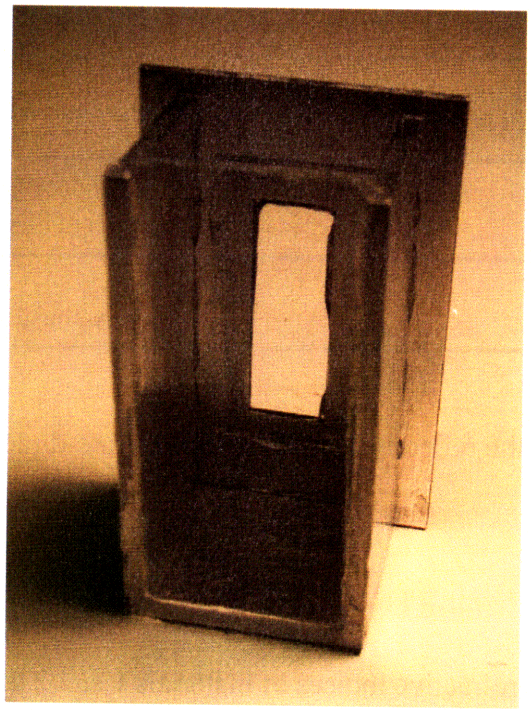

Figure 4.5: Spectrophotometric sample holder for temperature dependent reflectivity – Experiments were run by filling the chamber with the desired liquid and then quickly transferring the PS-P2VP sample (on a glass slide) into the holder. Samples were soaked in the measurement liquid for at least one hour prior to the experiments to allow the sample to equilibrate at room temperature. The front glass plate is 1.5" wide by 3" tall.

Although all samples were produced using the same block copolymer, choices in solvent and processing conditions (quaternization) have large effects on the thermochromic behavior of the photonic gel polymer. Possible factors affecting the reflectivity peak position and intensity are listed in table 4.2. The behavior of each sample set can be understood by knowing which mechanisms are operating with a given solvent or processing condition.

Table 4.2: Factors affecting the temperature related color change in a 1-D block copolymer gel photonic crystal

Index of Refraction	*Layer Spacing*
dn/dT (PS, MeOH, P2VP)	**α** (Thermal expansion of PS, MeOH, P2VP)
$\Phi_{solvent/P2VP}$ (Volume fraction of solvent in the P2VP layer)	**pKa** (chemical dissociation constant – acid and P2VP)
	Δδ (solubility)
	χ (Flory-Huggins interaction parameter)

The position of the reflectivity maximum for a one-dimensional photonic crystal is given by[25]:

$$\lambda_{max}(T)= 2[n_1(T)d_1(T) + n_2(T)d_2(T)] \quad (4.2)$$

where n_1 and n_2 are the refractive indices of materials 1 and 2 and d_1 and d_2 are the respective thicknesses of the layers. These four parameters will control the behavior of the reflector and it is the temperature dependence of these parameters that needs to be understood in order to understand the cause of any temperature-related peak shift. Table 4.2 shows the possible factors affecting the peak position in the lamellar BCP gel system with more emphasis placed on factors affecting the solvent-swollen P2VP domain since the glassy PS layers are essentially fixed except for thermal expansion and density changes (which change in index of refraction). Indeed, the optical path length (index multiplied by the layer thickness) of the P2VP layers (for the solvent concentrations of interest) is approximately ten times that of the PS layers and hence dominates the tuning

of the reflectivity peak. In other words, a 10% shift in the PS optical path length generates a change of ~1% in the total optical path length while a 10% change in the P2VP layer generates a ~9% change in the total optical path length. The change in index of refraction with temperature (dn/dT) is generally negative as most materials become less dense with increasing temperature while thermal expansion is generally positive (a notable exception is water near its freezing point), causing the material to expand. These two factors offset in the case of the PS layer leaving only the Flory-Huggins interaction parameter (χ) which is not a factor for optical path length changes because the PS chains are not mobile below their glass-transition temperature (~100°C). Since the PS layers do not contribute to the change in reflectivity with temperature, the contribution of the P2VP-solvent layers must be understood to explain the phenomena.

4.3.1 Thermochromic Behavior in Methanol

The 57k-57k PS-P2VP samples were immersed in a liquid cell filled with methanol (99.9+% from Alfa Aesar.) Upon immersion the P2VP domains absorb the methanol, swelling to approximately 87% by volume methanol while the PS domains remain unswollen. Figure 4.6 illustrates a typical dataset for a methanol-swollen sample. As the temperature is lowered, longer wavelengths are reflected and as figure 4.6 shows, the process gives a linear change in wavelength for a given change in temperature. Figure 4.7 also shows disparities between two samples (as discussed in Chapter 3) but while the peaks are shifted by 10 nm the slope of the temperature-peak wavelength curve is quite close (-0.69 nm/°C vs. -0.78 nm/°C.)

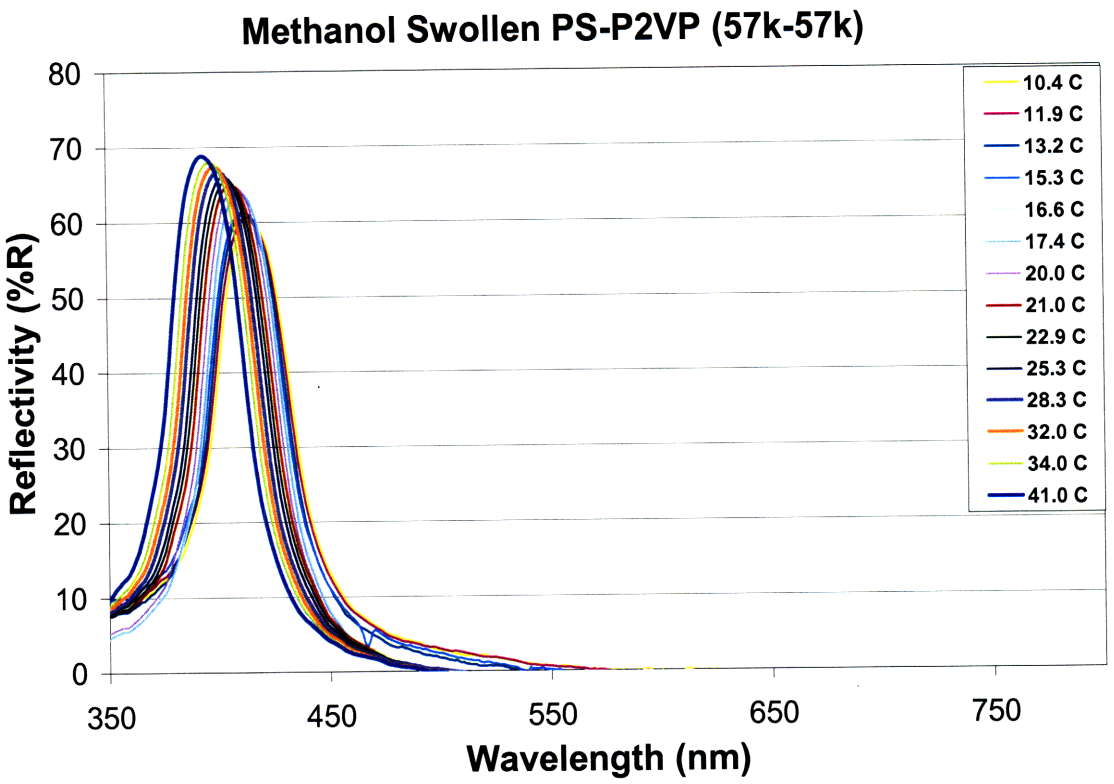

Figure 4.6: Methanol swollen PS-P2VP (57k-57k) – As the temperature of the system is decreased, the reflectivity shifts toward longer wavelengths (red-shift). The P2VP expands as the sample is cooled rather than contracting as one might expect from a thermal expansion driven change. Only peaks from 10-41°C are shown for graphical clarity. Although fogging of the cell window was a problem at lower temperatures (-17°C to ~5°C), peak positions were still clearly evident.

The change in reflected wavelength with temperature in methanol can be explained through the investigation of the parameters in table 4.2. As discussed in the proceeding section, only the change in the index of refraction and thickness (optical path length) of the P2VP/solvent domain needs to be investigated. Three factors influence the temperature-related refractive-index changes of the methanol/P2VP layers: the change in index with temperature of P2VP (dn_{P2VP}/dT) and methanol (dn_{MeOH}/dT) and the change in the effective index due to the gain/loss of methanol when the layers swell or shrink ($\Phi_{solvent/P2VP}$). This last parameter is found through modeling the 1D photonic crystal with a transfer matrix method calculation and (assuming a linear change in index with

concentration of methanol) is found to be quite small ($+1.15 \times 10^{-4}$/°C.) dn_{P2VP}/dT could not be found in the literature, but is assumed to be similar to dn_{PS}/dT which is -1.42×10^{-4}/°C.[26] dn_{MeOH}/dT was approximately three times as large (-4.7×10^{-4}/°C)[27] and since the P2VP/methanol layers are mostly methanol, it is the dominant effect. Combined, these three factors account for a reflectivity peak shift of -0.09nm/°C out of a total of -0.74 nm/°C, thus the majority of the temperature-related shift occurs through a change in spacing of the P2VP/methanol layers.

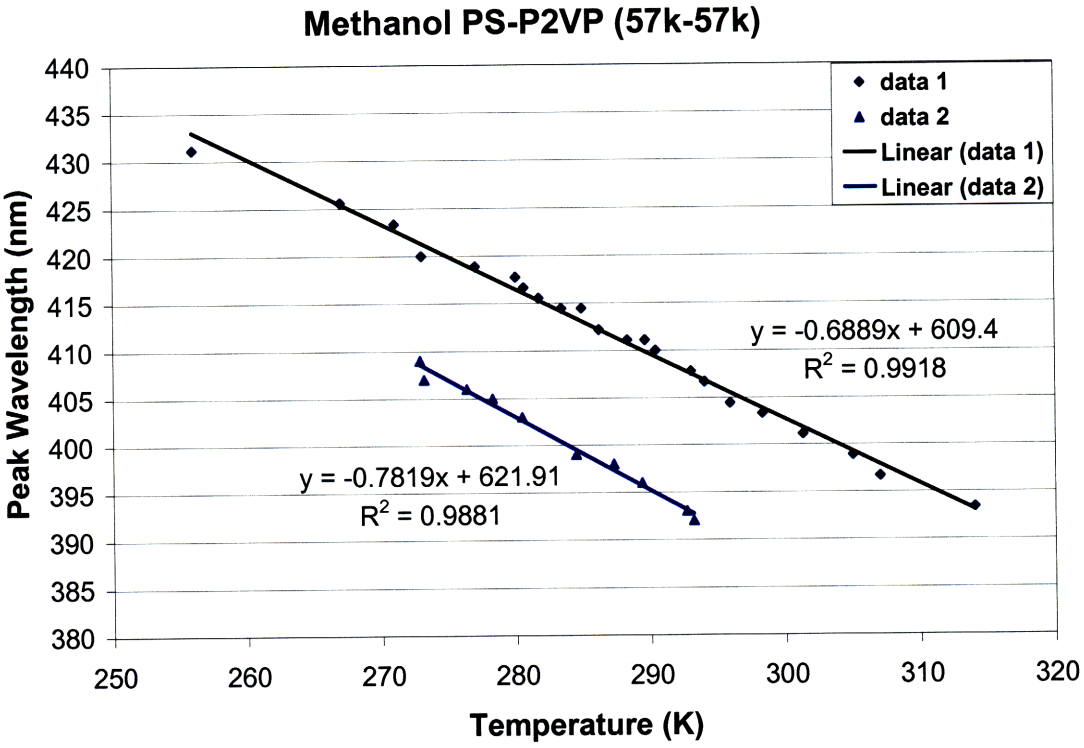

Figure 4.7: Shift in peak wavelength with temperature in methanol – Two representative samples displaying temperature-related color change in methanol. Over a range of approximately 60 degrees Celsius the samples displayed a linear change in reflected wavelength with temperature (~-0.7 nm/°C). Although the annealing process produces samples that do not reflect precisely the same wavelength at a given temperature, the rate of change with temperature is comparable.

The thickness of the P2VP/methanol domains is controlled by the affinity of the methanol for the P2VP. The solubility parameters of the polymer ($\delta_{polymer}$) and the

solvent ($\delta_{solvent}$) can give a measure of solvent quality. A loss of solvent affinity due to a change in temperature is usually indicated by an increasing difference between solubility parameters. Although all interactions contributing to the solubility parameter (dispersion, polar, and hydrogen bonding) are temperature sensitive, the hydrogen bonding component is the most sensitive[28] but has been tentatively ruled out as a contributing factor (see chapter 3.4). The reduction in solubility with increasing temperature has been suggested as a reason why other gel systems such as poly(n-isopropylacrylimide) display lower critical solution temperature (LCST) behavior.[29] In LCST systems, the polymer and solvent are miscible below the LCST and when the temperature is raised above the LCST, phase separation occurs. It has been shown experimentally that the solubility parameter of methanol changes with temperature at a rate of -0.0382 $MPa^{1/2}/^{o}C$ (from 0 to 60°C).[30] Assuming that the percent change in the thickness of the swollen layers is equivalent to the percent change in solubility with temperature, a -0.44nm/°C peak shift can be attributed to solvation effects.

Similarly, a change in affinity between a polymer and a solvent can be measured by the change in the Flory-Huggins χ parameter which is related to the difference in solubility parameters (see Background and Introduction section). Although no report of χ P2VP-MeOH could be found, a literature report for the similar P2VP-ethanol system found a slight increase in χ with increasing temperature (0.43 at 20°C to 0.44 at 40°C.)[31] This increase in χ with temperature suggests that at higher temperatures, the ethanol has a lower affinity towards the P2VP, thus corroborating the argument that solvation effect hypothesized above.

An alternative mechanism of solvent affinity change occurring in P2VP/methanol is the protonation of P2VP to P2VP+. There are a finite number of protonated P2VP monomers along the polymer backbone in a methanol solution due to the auto-dissociation of methanol (pKa 15.5)[32] into H+ and methoxide ions (P2VP pKa ~4.5 yielding [P2VP]/[P2VP+] ~ 1:200.) This change from P2VP to P2VP+ causes a large change in the solubility of P2VP chains in methanol as shown by the shift from blue to red when a PS-P2VP photonic crystal is immersed in methanol upon full protonation or quaternization of the P2VP. If the percentage of monomers that were protonated on the P2VP chains were to be affected by temperature, the amount of solvent in the gel would be affected and thus shift the reflectivity peak. This scenario is quite possible because of the temperature dependence of the pKa of P2VP. This link between solubility and pKa will be explored in depth in the next section.

4.3.2 Thermochromic Behavior in Acetic Acid – Water Solutions

Acetic acid - water solutions swell the PS-P2VP system to a differing degree depending on the pH of the solution (see Chapter 3). As the pH of the solution decreases, the vinylpyridine becomes more protonated causing an increase in solubility and thus an uptake of solvent, swelling the P2VP layers. Three different acetic acid concentrations (0.01M, 0.1M, and 1.0M) were selected to test the reflectivity response when the P2VP blocks were protonated to different degrees. As with the methanol case, differences between samples with the same degree of protonation showed a shifting of the temperature-peak wavelength data, but the slopes of the curves were almost identical for all the data sets (-1.45 nm/°C vs. -1.48 nm/°C for the two data sets shown). Samples

swollen with the 0.1M and 1M acetic acid solutions show little to no change in reflectivity respectively over the temperature range of 1 to 20°C.

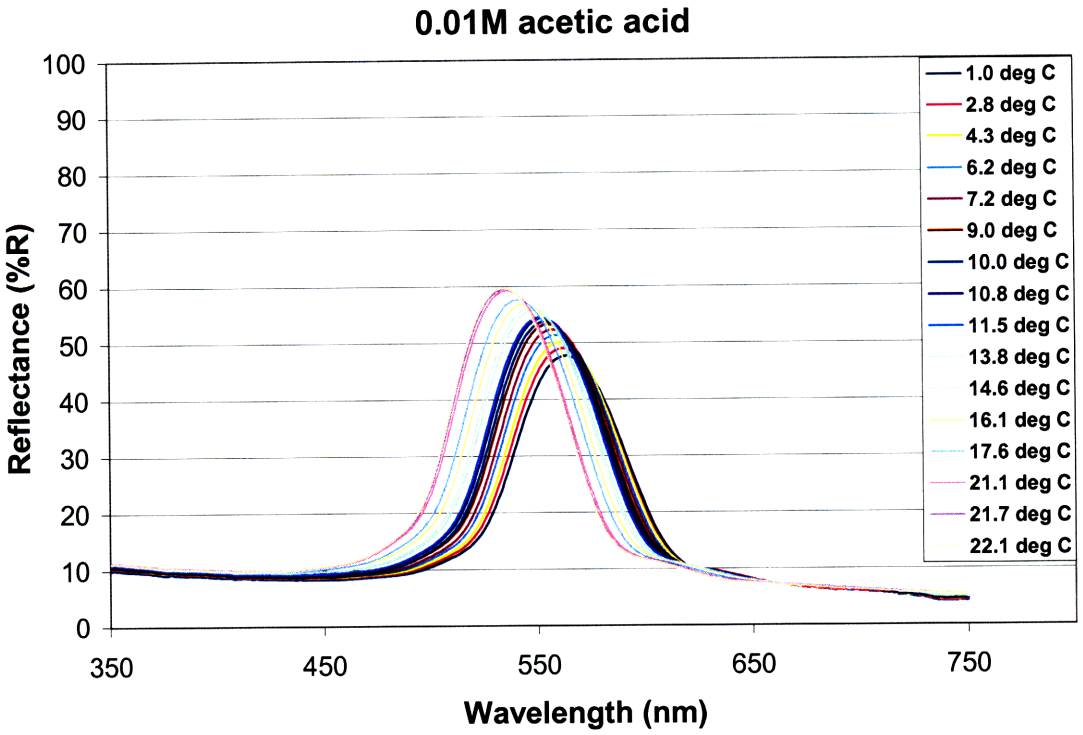

Figure 4.8: 0.01M acetic acid swollen PS-P2VP (57k-57k) - As the temperature of the 0.01M acetic acid-water solution is decreased, the reflectivity shifts toward longer wavelengths. All experimental data points (1 to 22.1°C) are shown. The increased intensity at shorter wavelengths is attributed to the change in index of refraction with wavelength leading to a greater difference in index between the two layers and thus higher reflectivity.

As discussed earlier in the chapter, χ is a measure of the relative interaction strength between the two types of polymer segments in the BCP and could possibly play a role in the thickness of the P2VP domains. As the temperature increases, the entropy of mixing term ($-T\Delta S_{mix}$, see background information section) in the free energy of mixing grows and as it is negative, repulsion between the two polymers is reduced, reducing the domain size (assuming the chains of both blocks are mobile). The effect of temperature on χ in the poly(styrene)-poly(vinylmethyl ether) system[33] and the poly(styrene)-

poly(methyl methacrylate) system[34] has been studied and found to vary in the form of $\chi \sim a + b/T$. Others have investigated the actual temperature dependence of the domain spacing resulting from a change in χ at a temperature greater than the glass-transition temperature for both blocks. A theoretical prediction for the domain spacing in block copolymer melts (in the strong segregation limit) was proposed by Semenov[35] to be $d \sim aN^{2/3}\chi^{1/6}$. Since $\chi \sim T^{-1}$, the change in domain spacing in a block copolymer melt would vary as $\sim T^{-1/6}$. Experimentally $d \sim T^{-1/3}$ behavior has been found in the poly(styrene)-poly(butadiene) (PS-PB) system[36], with PS spheres in a matrix of PB and a solvent that was selective for PB (n-tetradecane.) The temperature dependence of the domain size was also explored for a lamellar poly(styrene)-poly(isoprene) block copolymer in a neutral solvent[37] (a solvent that is equally good for either block) and was found to scale as $\sim N^{2/3}(\Phi_p/T)^{1/3}$ where N is the degree of polymerization, Φ_p is the polymer volume fraction, and T is temperature in Kelvin.

Certainly a change in the interaction parameter between two polymers can cause changes in the domain spacing, and has been suggested as the major cause of temperature dependence in a photonic block copolymer in a neutral solvent[22], it is not the controlling factor in the temperature-dependent reflectivity of the samples under study because in these PS-P2VP samples, swollen in extremely selective solvents, the polystyrene layers are 'frozen' because the temperature of the experiment is below its glass-transition point of the PS and the extremely selective solvent serves to screen the interactions of the P2VP with the PS segments. This coupled to the experimental observation that there are no systematic peak shifts in all samples: both the quaternized (figure 4.15) and highly protonated (figures 4.10 and 4.11) samples showed no peak shift while the methanol and

0.01M acetic acid samples showed different $d\lambda_{peak}/dT$ values. If domain spacing changes were driven by the temperature dependence of the χ parameter between the PS and P2VP, all samples should show a systematic peak shift with temperature.

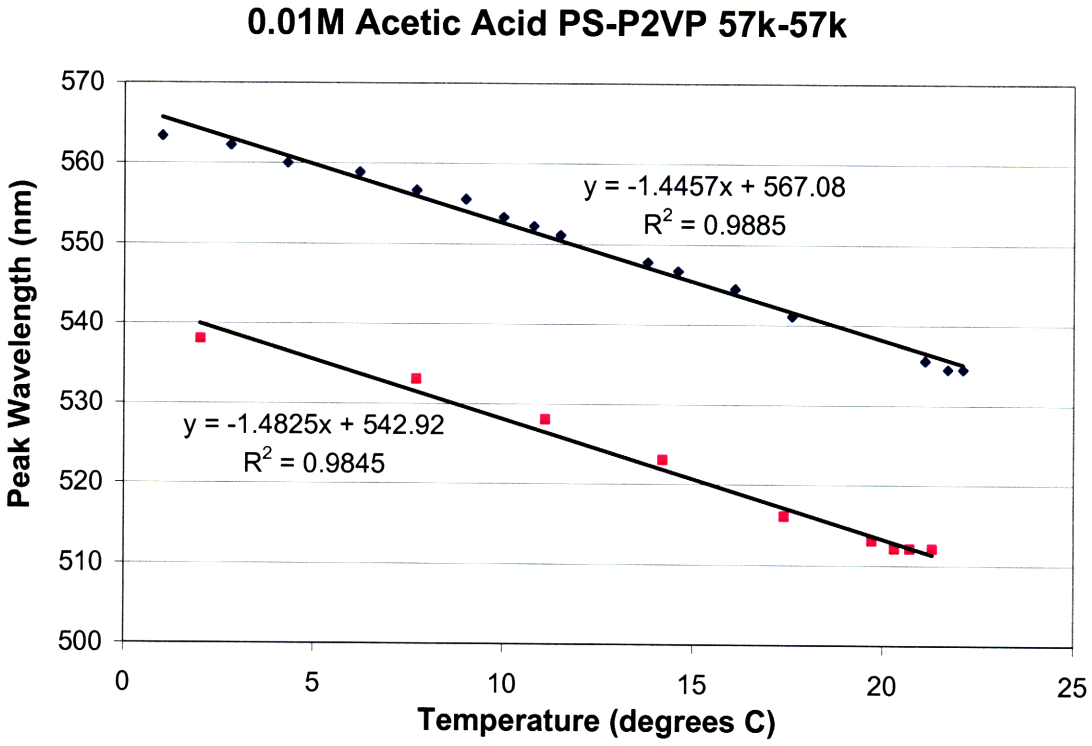

Figure 4.9: Shift in peak wavelength with temperature in 0.01M acetic acid - Two representative samples displaying temperature-related color change in 0.01M acetic acid. The linear change in peak wavelength with temperature of approximately 1.45nm/°C from 1 to 22 degrees Celsius is repeatable although the precise position of the reflectivity peak depends on sample preparation.

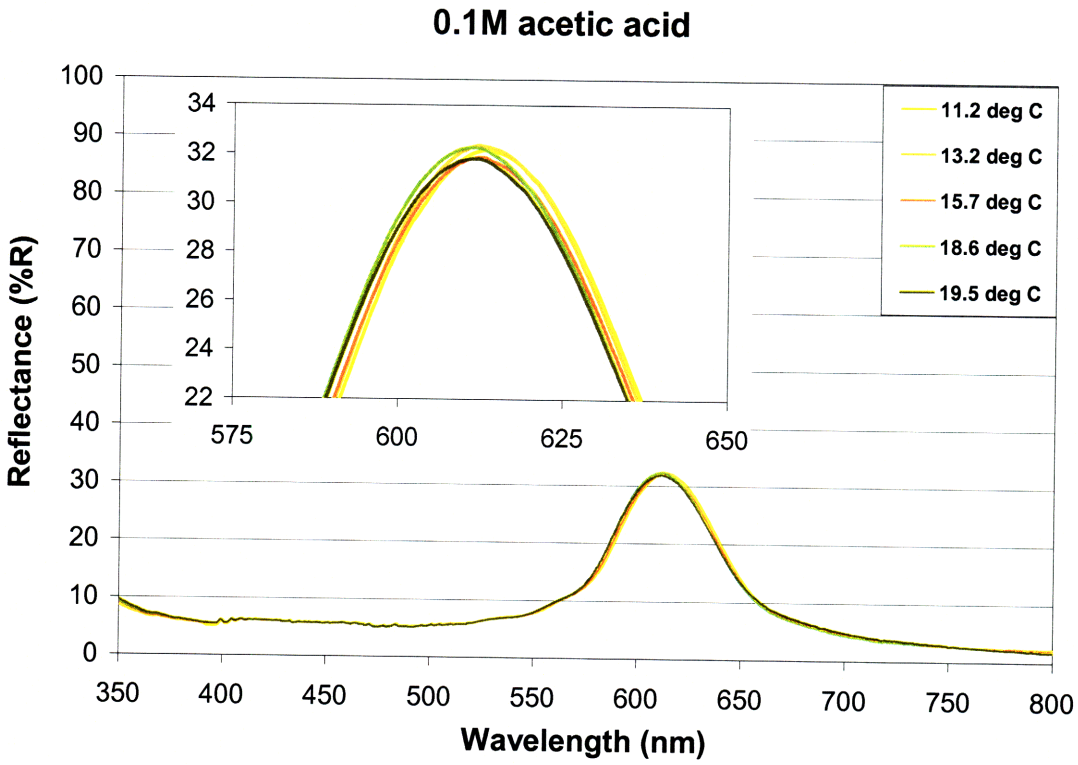

Figure 4.10: 0.1M acetic acid swollen PS-P2VP (57k-57k) - As the temperature of the 0.01M acetic acid-water solution is decreased, there is little change in the reflected wavelengths of light. The P2VP layers are almost fully protonated and thus do not change their spacing with a change in temperature.

Taking a closer look at the protonated samples it is apparent that the rate of color change ($d\lambda_{peak}/dT$) mimics that of the rate of change of color by changing the pH ($d\lambda_{peak}/d\text{-}\log[H^+]$). The 0.01M sample has a high degree of color tunability with temperature while the 1M sample does not change color at all. This correspondence suggests that the change in temperature is causing a change in protonation of the P2VP. There are two possible reasons for the change in protonation: a change in the pKa of the acid and a change in the pKa of the P2VP. A change in the pKa of the acid results in a change in pH while a change in the pKa of the P2VP results in a change in the number of protonated P2VP monomer units for a given pH level. The equilibrium constant of acetic

acid ($K_{eq}=10^{-pKa}$) is known to change with temperature as shown in figure 4.12[38]. Converting from the K_{eq} data in figure 4.12 to pKa, a shift from a pKa value of 4.75 at room temperature to 4.78 at 5°C is seen which indicates that the solution is less acidic when cooled down. This increase in pH when cooling the solution from 25°C to 5°C accounts for a theoretical +0.2 nm/°C shift in the reflectivity peak (calculated by using a quadratic fit to the acetic acid pH-reflectivity curve - see figure 4.13).

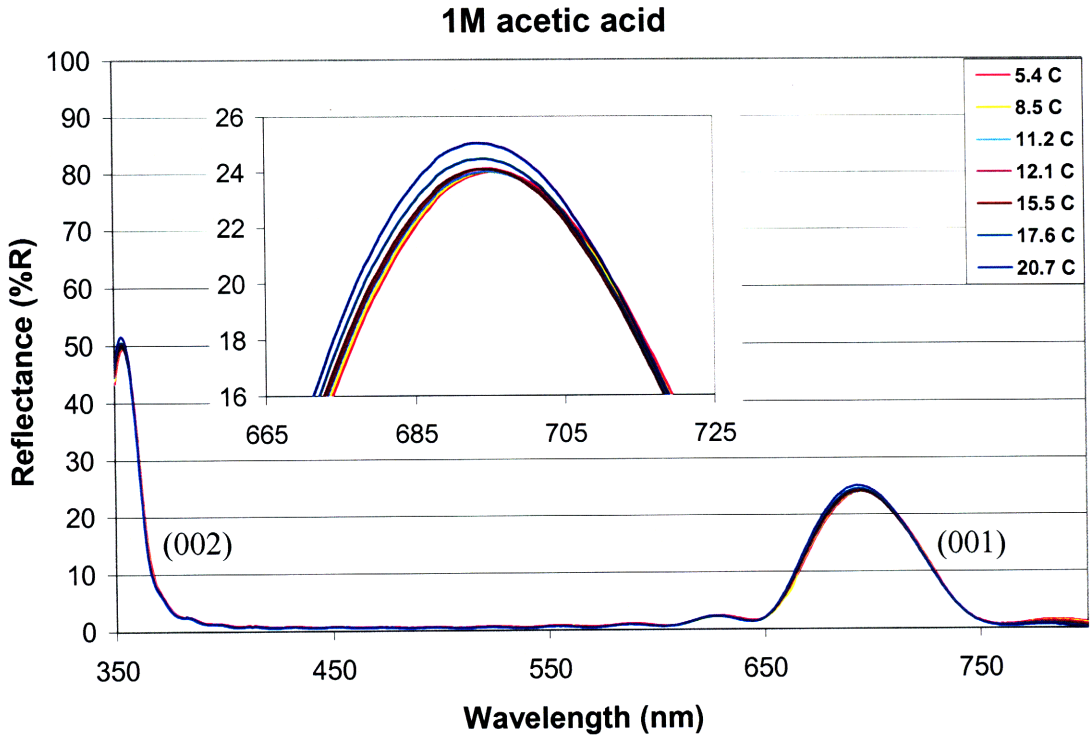

Figure 4.11: 1M acetic acid swollen PS-P2VP (57k-57k) - As with the 0.1M acetic acid solutions, as the temperature of the 1M acetic acid-water solution is decreased, there is little change in the reflected wavelengths of light. The sample is fully protonated thus the change in pKa of the P2VP does not influence the degree of protonation and thus the sample does not swell with a decrease in temperature. The secondary reflection peak can be seen just above 350nm. The (001) and (002) labels denote the first and second order reflectivity peaks respectively.

Data on a temperature-related shift in K_{eq} for the conversion of un-protonated to protonated P2VP could not be found in the literature but reports in the literature suggest

an increase in pKa as temperature decreases for organic bases[39,40,41]. Temperature-related shifts in the pKa of pyridine in a 50% methanol-water solution show an increase in pKa from 3.81 at 50°C to 4.14 at 20°C [40] and the change in pKa with temperature for pyridine in aqueous solutions is ~-0.011/°C.[41] The shift in the pKa of P2VP from 25°C to 5°C can be calculated using a relationship given in reference 40:

$$d(pKa)/dT = -(pKa-0.9)/T$$

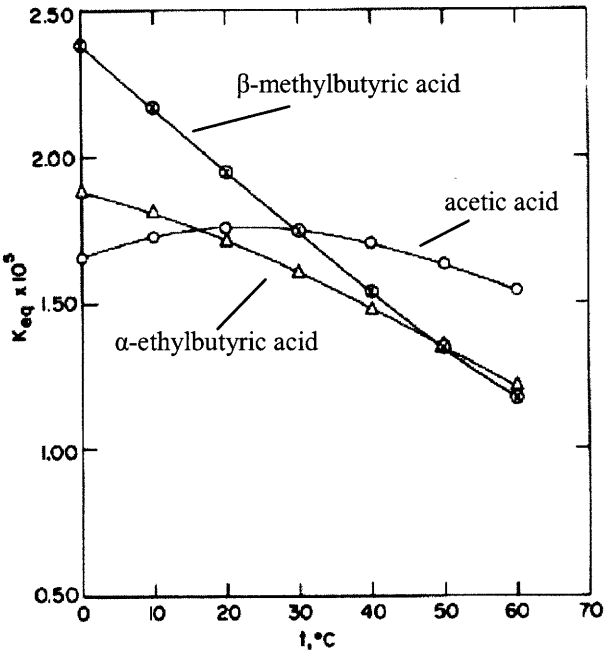

Figure 4.12: The dependence of Ka for alkyl acetic acids – A small temperature dependence on equilibrium constant is seen in acetic acid (open circles) leading to a small increase in pH as temperature is decreased. β-methylbutyric acid (closed circles) and α-ethylbutyric acid (triangles) are also shown. These acids are attractive candidates to increase the reflectivity peak shift with temperature because of their decreasing acidity with increasing temperature. (figure adapted from reference 38)

To find the change in pKa with temperature, the pKa value of P2VP must be known. The pKa of P2VP has been reported to be 4.5 in a 0.5M potassium chloride solution (in water) at room temperature (electro-polymerized P2VP)[42] and 3.45 in a 45% ethanol/55% water solution[43]. Although neither of these values was measured in the

same solution (or using the same polymerization technique) as those under consideration, an examination of the pH versus peak wavelength graph in figure 4.13 would indicate that the latter value of 3.45 is closer to the correct value which gives a d(pKa)/dT value of $-8.6 \times 10^{-3}/^{\circ}C$ and thus a theoretical pKa of 3.62 at 5°C (see table 4.3).

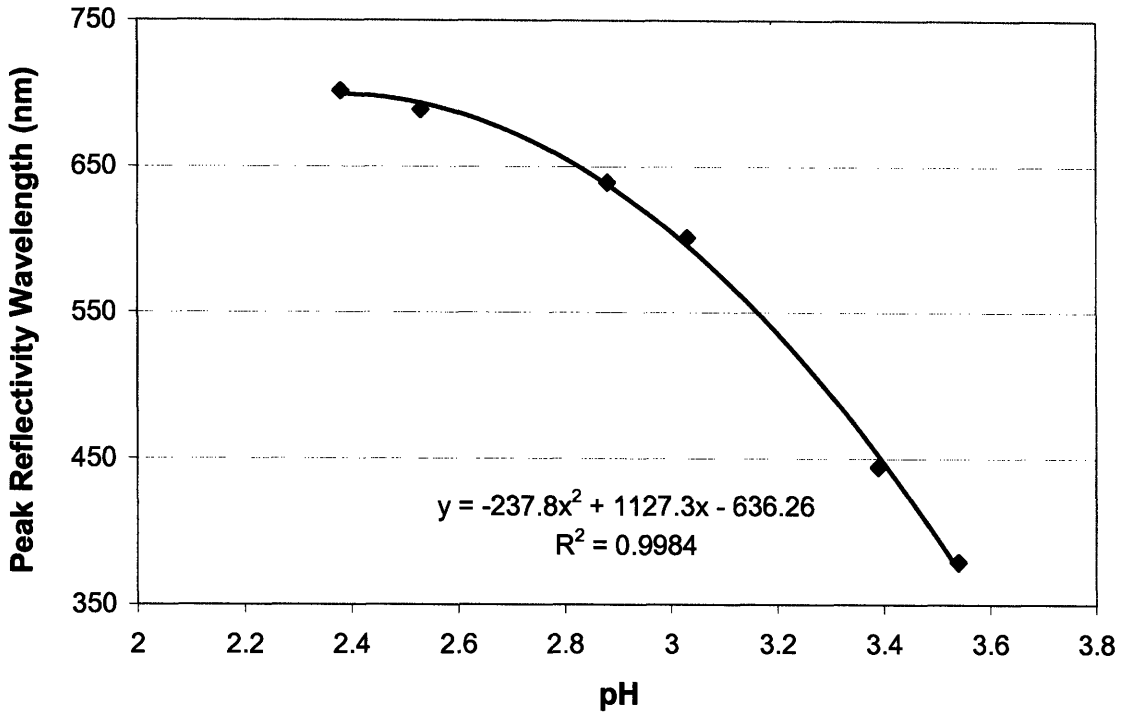

Figure 4.13: Reflectivity peak position in acetic acid for PS-P2VP (57k-57k) – As the solution becomes more acidic, more P2VP is protonated (P2VP+). Since P2VP+ has a higher solubility, the layers expand and reflect light of increasing wavelength. Maximum conversion occurs around pH 2.4 where no further P2VP can be converted to P2VP+. A quadratic fit to the data provides a correlation between pH level and reflectivity peak position.

By calculating the percent ionization of the P2VP at room temperature for different pH levels and plotting that against the peak wavelength values for those same pH values, a master curve (see figure 4.14) can be created that indicates the reflected wavelength for a given P2VP protonation percentage. This allows for the theoretical calculation of the reflected wavelength if the pKa and pH are known which permits percent ionization to be calculated through the relationship below (see chapter 3 as well).

$$\% \text{ Protonation} = 100/(1+ 10^{\text{pH-pKa}})$$

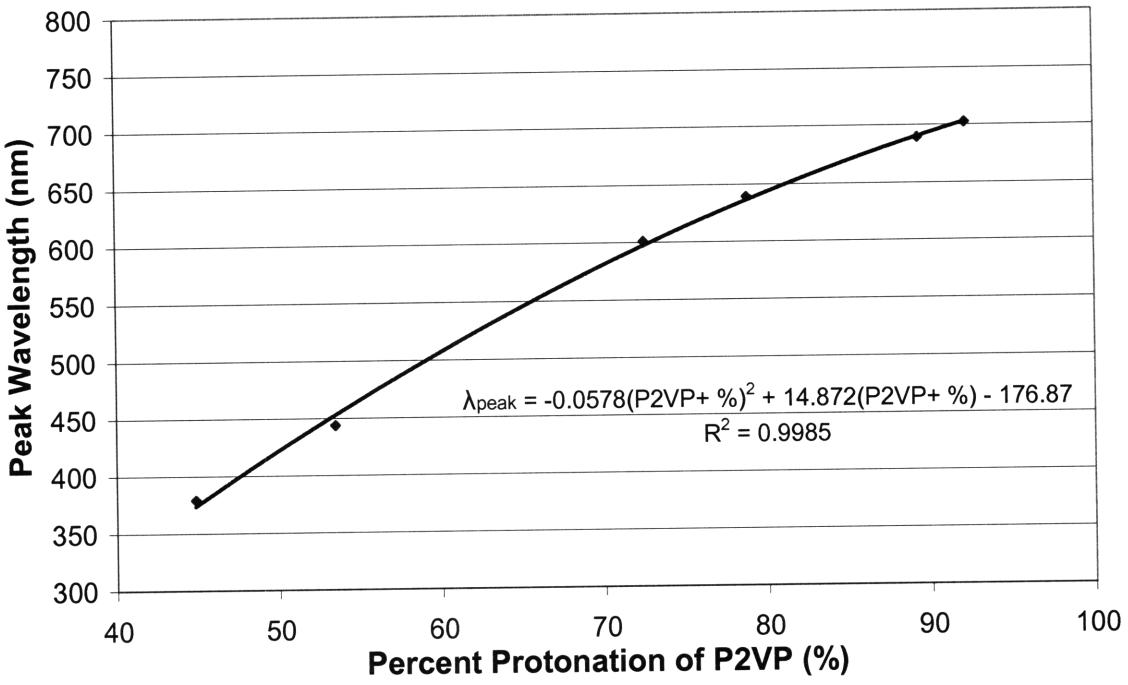

Figure 4.14: Reflectivity peak position dependence on percent protonation of P2VP – Using an estimation of the pKa value for P2VP at room temperature, the percent protonation of the P2VP can be calculated at a give pH level. The data points on the graph are calculated from data in figure 4.14. A quadratic fit to the data allows an estimation of the peak position for a given protonation. This equation can then be used to calculate theoretical peak shifts when solution pH and P2VP pKa values are calculated for other temperatures.

Table 4.3: Calculated and predicted values for the parameters affecting the thermal behavior of PS-P2VP

Temperature	pH (.01M acetic acid)	P2VP pKa
25°C	3.39	3.45
5°C	3.40	3.62

Using the equation in Figure 4.14 with the values for percent ionization at 25 and 5°C, a peak shift of -3.6 nm/°C is calculated. This is roughly a factor of two higher than the observed ~-1.45 nm/°C but can be attributed to errors in the prediction of the pKa of P2VP at 5°C which assumes the entropy of the solution (ΔS^{o}) is constant with temperature. This leads to errors the further from 25°C that the pKa is extrapolated.

Quaternized PS-P2VP has a negligible amount of color change with temperature in de-ionized water. This is because all available pyridine groups have been quaternized and thus the polymer cannot be further protonated by the addition of an acid.

4.3.3 Thermochromic behavior of a quaternized PS-P2VP BCP in de-ionized water

A third set of experiments was carried out on a quaternized PS-P2VP BCP to examine the temperature response when no acid was present but the P2VP was still charged (the quaternization procedure can be found in chapter two of this thesis). The percent quaternization was estimated to be approximately 75% by comparing the peak position with the curve in figure 4.14. Upon cooling the sample to 5.4°C, the peak position decreases by approximately four nanometers. When the sample is warmed, the reflectivity peak shifts to longer wavelengths and eventually surpasses the original position. The extremely small blue-shift is ascribed to the thermal expansion of the PS as well as the change in index of refraction of the constituent materials with temperature. The small but observable red shift is attributed to the replacement of the bromine counter ions (introduced during the quaternization procedure) with more hydrophilic hydroxide ions from the water. (This shift with a change in counter ion is irreversible unless the sample is immersed in a solution with excess bromide ions present allowing them to diffuse back into the film.) As with the 0.1M and 1M acetic acid, there was no substantial peak movement over the temperature range probed by the experiment.

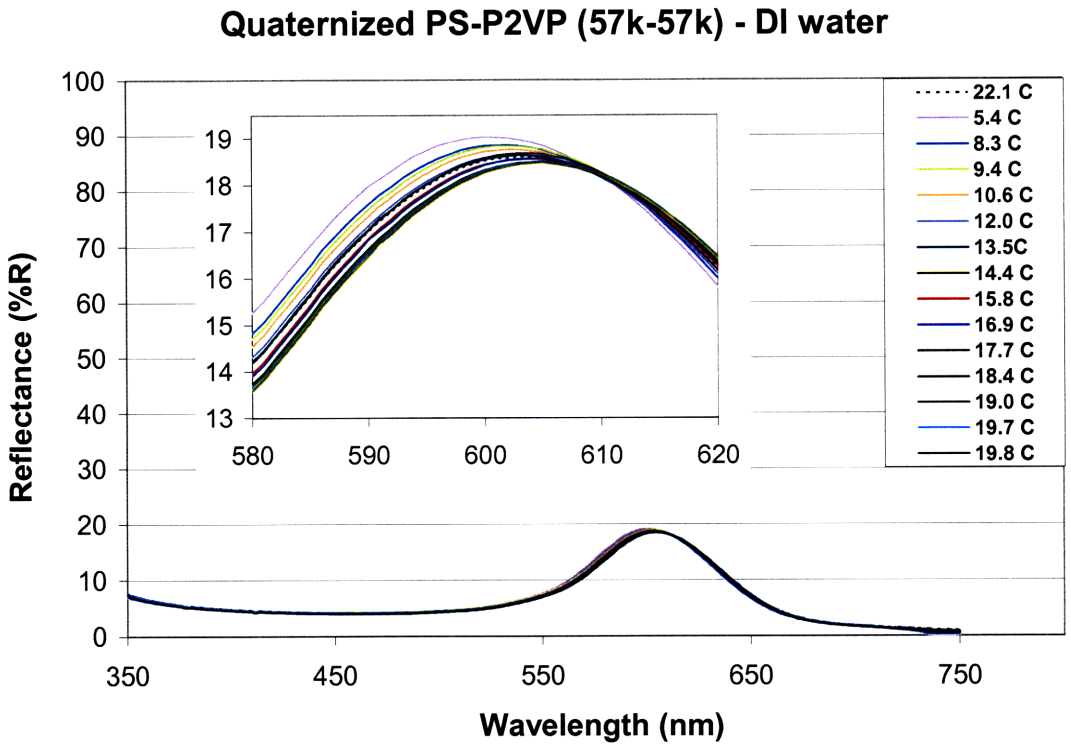

Figure 4.15: De-ionized water swollen PS-QP2VP (57k-57k) – Temperature effects on the quaternized PS-P2VP sample were minimal. There was a slight shift to shorter wavelengths upon cooling and then a progression towards longer wavelengths which is attributed to anion exchange between the bromine counter ions and hydroxyl ions in the de-ionized water.

4.4 Conclusions

The thermochromic behavior of P2VP in acetic acid solutions was found to be caused by a temperature-induced change in the pKa of P2VP. Temperature-dependent behavior in methanol was also investigated and found to be principally derived from a change in solubility due to hydrogen bonding although a change in solubility with temperature due to a change in protonation was also thought to be a second contributing mechanism. The reflectivity peak position of quaternized PS-P2VP and PS-P2VP in 0.1M and 1M acetic acid was not affected by a change in temperature which might be useful if a sensor with no temperature dependence is desired (e.g. measurement of ion

concentration over a range of temperatures.) If a high value of $d\lambda_{peak}/dT$ is desired, using an acid which decreases strength with increasing temperature would enhance the effect. Possible candidate acids can be seen in figure 4.12.

4.5 References

1 Walton, B.M., Bennett, A.F., Temperature-dependent color change in Kenyan Chameleons, Physiological Zoology, 66(2), 270-87 (1993)

2 Burrage, B.R., Comparative ecology and behaviour of Chamaeleo pumilus (Gmelin) and C. namaquensis A. Smith (Sauria: Chamaeleonidae). Ann. S. Afr. Museum, 61, 1-158 (1973)

3 Atsatt, S.R., Color changes as controlled by temperature and light in the lizards of the desert regions of southern California, Publications of the University of California at Los Angeles in biological sciences, 1(11), 237-276 (1939)

4 Sherbrooke, W.C. and Frost, S.K., Integumental chromatophores of a color-change, thermoregulating lizard Phrynosoma modestum (Iguanidae; Reptilia), American Museum Novitates, No. 2943, 1-14, (1989)

5 Bagnara, J.T., Kreutzfeld, K.L., Fernandez, P.J., and Cohen, A.C., Presence of pteridine pigments in isolated iridophores, Pigment Cell Research, 1, 361-5 (1988)

6 Rohrlich, S.T. and Porter, K.R., Fine structural observations relating to the production of color by the iridophores of a lizard, Anolis carolinensis, J. Cell Biol., 53, 38-52 (1972)

7 Morrison, R.L., Sherbrooke, W.C., and Frost-Mason, S.K., Temperature-sensitive, physiologically active iridophores in the lizard Urosaurus ornatus: an ultrastructural analysis of color change, Copeia, 4, 804-12 (1996)

8 Morrison, R.L., A transmission electron microscopic (TEM) method for determining structural colors reflected by lizard iridophores, Pigment Cell Research, 8, 28-36 (1995)

9 White, M.A. and LeBlanc, M., Thermochromism in commercial products, Journal of Chemical Education, 76(9), 1201-5 (1999)

10 Mitov, M. and Dessaud, N., Cholesteric liquid crystalline materials reflecting more than 50% of unpolarized incident light intensity,Liquid Crystals, 34(2), 183-193 (2007)

11 Mitov, M. and Dessaud, N., Going beyond the reflectance limit of cholesteric liquid crystals, Nature Materials 5, 361-364 (2006)

12 Hikmet, R.A.M. and Kemperman, H., Switchable mirrors of chiral liquid crystal gels, Liquid Crystals, 26(11), 1645-53 (1999)

13 Hikmet, R.A.M. and Polesso, R., Patterned multicolor switchable cholesteric liquid crystal gels, 14(7), 502-504 (2002)

14 Fergason, J., Goldberg, N., Nadalin, R., Cholesteric structure-II chemical significance, Mol. Cryst., 1(2), 309-323 (1966)

15 Zhou, J., Sun, C.Q., Pita, K., Lam, Y.L., Zou, Y., Ng, S.L., Kam, C.H., Li, L.T., and Gui, Z.L., Thermally tuning of the photonic band gap of SiO2 colloid-crystal infilled with ferroelectric $BaTiO_3$, Applied Physics Letters, 78(5), 661-663, (2001)

16 Weissman, J.M., Sunkara, H.B., Tse, A.S., and Asher, S.A., Thermally switchable periodicities and diffraction from mesoscopically ordered materials, Science, 274, 959-960 (1996)

17 Matsubara, K., Watanabe, M., and Takeoka, Y., A thermally adjustable multicolor photochromic hydrogel, Angew. Chem. Int. Ed., 46, 1688-92 (2007)

18 Ueno, K., Matsubara, K., Watanabe, M., and Takeoka, Y., An electro- and thermochromic hydrogel as a full color indicator, Advanced Materials, 19, 2807-12 (2007)

19 Debord, J.D. and Lyon, L.A., Thermoresponsive photonic crystals, J. Phys. Chem. B, 104(27), 6327 -6331 (2000)

20 Hu, Z., Lu, X., and Gao, J., Hydrogel Opals, Advanced Materials, 13(22), 1708-1712 (2001)

21 Kumoda, M., Watanabe, M., and Takeoka, Y., Preparations and optical properties of ordered arrays of submicron gel particles: interconnected state and trapped state, Langmuir, 22, 4403-7 (2006)

22 Yoon, J.S., Lee, W.M., and Thomas, E.L., Thermochromic block copolymer photonic gel, submitted to Angewandte Chemie, April (2008)

23 Osuji, C., Chao, C.Y., Bita, I., Ober, C.K., and Thomas, E.L., Temperature-dependent photonic bandgap in a self-assembled hydrogen-bonded liquid-crystalline diblock copolymer, Advenced Functional Materials, 12(11-12), 753-8, (2002)

24 Valkama, S., et. al., Self-assembled polymeric solid films with temperature-induced large and reversible photonic-bandgap switching, Nature Materials, 3, 872-6, (2004)

25 Land, M.F., The physics and biology of animal reflectors, Prof. Biophys. and Molec. Biol., 24, 75-106 (1972)

26 Brandrup, J.; Immergut, Edmund H.; Grulke, Eric A.; Abe, Akihiro; Bloch, Daniel R. Polymer Handbook (4th Edition). John Wiley & Sons.

27 El-Kashef, Hassan, The necessary requirements imposed on polar dielectric laser dye solvents, Physica B, 279, 295-301 (2000)

28 Hansen, C.M., Hansen Solubility Parameters: a user's handbook, CRC Press, Boca Raton, FL (1999)

29 Yan, L., Zhu, Q., and Kenkare, P.U., Lower critical solution temperature of linear PNIPA obtained from a Yukawa potential of polymer chains, J. App. Poly. Sci., 78, 1971-6 (2000)

30 Mizerovskii, LN and Vansyatskaya, LN, Temperature dependence of the solubility parameter of organic liquids, Izvestiia vysshikh uchebnykh zavedenii. Khimiia I khimicheskaia tekhnologiia, 31(4), 51-4 (1988)

31 Pouchly, J. and Zivny, A., Correlation of data on intrinsic viscosities in mixed solvents by means of the modified Flory-Huggins equation, Makromol. Chem., 184, 2081-96 1983

32 Dean, J.A. Lange's Handbook of Chemistry (15th Edition). McGraw-Hill. (1999)

33 Han, C.C., Bauer, B.J., Clark, J.C., Muroga, Y., Matsushita, Y., Okada, M., Tran-cong, Q., Chang, T., and Sanchez, I.C., Temperature, composition and molecular-weight dependence of the binary interaction parameter of polystyrene/poly(vinyl methyl ether) blends, Polymer, 29(11), 2002-2014 (1988)

34 Russell, T.P., Hjelm Jr., R.P., Seeger, P.A., Macromolecules, Temperature dependence of the interaction parameter of polystyrene and poly(methyl methacrylate), 23(3), 890-3 (1990)

35 Semenov, A.N., Contribution to the theory of microphase layering in block-copolymer melts, Soviet Physics JETP, 61(4), 733-42 (1985)

36 Sibayama, M., Hashimoto, T., and Kawai, H., Ordered structure in block polymer solutions. 1. selective solvents, Macromolecules, 16, 16-28 (1983)

37 Hashimoto, T., Shibayama, M., and Kawai, H., Ordered structure in block polymer solutions. 4. scaling rules on size of fluctuations with block molecular weight, concentration, and temperature in segregation and homogeneous regimes, Macromolecules, 16, 1093-1101 (1983)

38 Calder, G.V. and Barton, T.J., Actual Effects Controlling the Acidity of Carboxylic Acids, Journal of Chemical Education, 48(5), 338-40 (1971)

39 Hall, N.F. and Sprinkle, M.R., Relations between the structure and strength of certain organic bases in aqueous solution, J. Amer. Chem. Soc., 54(9), 3469-3485 (1932)

40 Castells, C.B., Rafols, C., Roses, M., and Bosch, E., Effect of temperature on pH measurements and acid-base equilibria in methanol-water mixtures, Journal of Chromatography A, 1002, 41-53 (2003)

41 Perrin, D.D., The effect of temperature on pK values of organic bases, Aust. J. Chem., 17, 484-8 (1964)

42 Tantavichet, N., Pritzker, M.D., and Burns, C.M., Proton uptake by poly(2-vinylpyridine) coatings, Journal of Applied Polymer Science, 81, 1493-7 (2001)

43 Ferruti, P. and Barbucci, R., Linear amino polymers: synthesis, protonation and complex formation, Advances in polymer science, 58, 55-92 (1984)

Chapter 5:
Cephalopod Inspired Electrochemical Color Tuning of a Photonic Gel

Whereas previous chapters have focused on the effects of global, homogeneous solution parameters (pH, solvent, and temperature) in producing color change in the PS-P2VP system, the focus of this chapter will be on using electrochemistry to produce local changes in solution properties to affect the swelling behavior of the gel. The use of electrochemistry to create display technology is powerful in two ways: there is enormous energy available to drive chemical reactions in the electrochemical cell at relatively small voltages compared to those in common experience (e.g. 120V household power) and the use of electrons to change color lends itself nicely to incorporation of a PS-P2VP pixel into a compact and easily tunable system because of modern advances in electronics.

5.1 Introduction to Electrochemistry

Before beginning the discussion of the electrochemical pixel, a brief introduction to electrochemistry is in order such that the intricacies of making a device can be understood. Electrochemistry is the study of the interconversion of electrical and chemical energy and deals with many different subjects including, but not limited to: batteries, corrosion, fuel cells, electroplating, and the production of industrial materials (e.g. aluminum). Although the field of electrochemistry is large, this chapter will focus on the oxidation or reduction of chemical species by an applied potential and thus the introduction will focus solely on those aspects. An electrochemical cell (see figure 5.1) is composed of at least two electrodes, an electrolyte and a power source to drive the electrochemical reaction. When an electric potential is applied to the circuit, the electrochemical reaction takes place at the ***interface*** between the electrodes (electronic conductors) and the electrolyte (ionic conductor) and nowhere else. The electrodes that carry electrons to and from the electrolyte are usually made of very chemically stable materials such as platinum, gold, and carbon, but in certain cases other materials are used such as indium-tin-oxide (ITO) when a transparent electronic conductor is needed.

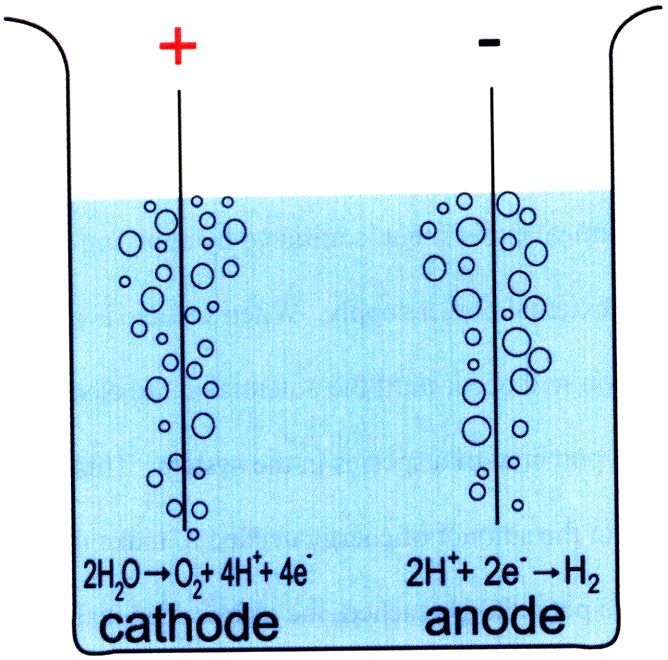

Figure 5.1: An electrochemical cell featuring the oxidation of zinc at the anode - Oxidation always happens at the anode and reduction always takes place at the cathode. In this example the electrolysis of water is occurring at two immersed electrodes producing hydrogen and oxygen gas. In reality, a salt is usually added to the water because of the poor conductivity of pure water.

Although under some circumstances the electrodes will participate in the electrochemical reaction (e.g. the conversion of lead (Pb) to Pb^{2+} in a car battery) other times it is not desired that the electrodes participate in the electrochemical reaction, such as with ITO electrodes where reduction of the coating (removal of oxygen from the ITO) reduces the optical transparency of the material. With the latter case, it is important to pick the electrolyte and the electro-active species such that neither electrode participates in the reaction. Also, the range of applied voltage (potential window) is an important parameter since an electrode will eventually participate in the reaction if a sufficiently high or low potential is applied. Thus, the electrolyte selected must be compatible with the electrodes and have a suitably high ionic conductivity. Salts that dissolve in the electrolyte and dissociate into their constituent ions are sometimes used to increase the

conductivity of the electrolyte. Frequently salts such as tetraethylammonium hexafluorophosphate (TEAP) are used because of their resistance to electrochemical breakdown.

The electrochemical experiment is initiated by applying a voltage across the two electrodes through an external power supply. When voltage is applied to the cell, no electrochemical reaction will occur until the potential at the electrode reaches the oxidation or reduction potential of a species in the system. This oxidation or reduction potential corresponds to the amount of energy needed to make the reaction energetically favorable and once this potential is reached, the electrochemical reaction proceeds at a rate determined by a number of factors including the ease of electron transfer across the electrode/electrolyte interface, the conductivity of the electrolyte, the surface area of the electrode, and the availability (concentration) of reactant at the electrode/electrolyte interface. In the present chapter this local production of chemical species is used to swell or de-swell a structured gel located on the electrode causing a change in color. This is actually quite similar to the way certain aquatic mammals control the color of their skin; by secreting chemicals that change the spacing between plates in multilayer reflectors[1].

By controlling absorption, reflection, and texture, cephalopods display an incredible ability to manage and manipulate light[2] – a goal of modern display technology. With these and several other aquatic species, *tunable* structural color plays a fundamental role in creating vivid and eye-catching color[3,4] which is produced in part by using and modulating one-dimensional reflectors known as iridophores. The change in reflectivity of these biological reflectors is accomplished by the local introduction of chemical species that either change the spacing between high refractive index platelets or change

the thickness of the platelets themselves. Efficient, refined mechanisms of visual communication –such as iridophores- are key to cephalopod survival. The next generation of display materials could benefit from the lessons learned over millions of years of evolution in order to produce inexpensive, robust, low-energy, high-contrast displays[5].

5.2 Electrical control of photonic crystals

The present chapter reports on a bio-inspired, electrochemically-tunable, full-color pixel based on a self-assembling block copolymer (BCP). Imitating cephalopod reflectin proteins that form layered, highly reflective structures,[6,7] the lamellar structure of these block copolymers has a periodic variation in its refractive index. Such structures are commonly known as 1D photonic crystals and yield photonic stop bands which reflect incident electromagnetic radiation of a wavelength range dependent on the angle of incidence of the light, the index of refraction of the respective layers, and their periodicity. Partial color tunability has been demonstrated in numerous photonic crystal systems[8,9,10,11] which have been intensely investigated due to their inherent structural color which negates the need for light-absorbing color filters common in other technologies. A growing number of photonic crystal devices have attained full color tunability using direct or indirect electrical control through various technologies such as cholesteric liquid crystals,[12] synthetic opals,[13,14,15] and diffraction gratings.[16] This electrical control is highly sought after for display applications because of the ease with which it can supply a local stimulus.

Although partial color tunability of photonic crystals was first reported in 1999,[17] full color tunability in a photonic crystal was first accomplished in 2002 in a cholesteric liquid crystal[12] through the direct application of voltage which caused a change in helical orientation and changed the reflected wavelength of light. Thirty volts was required to move the reflectivity peak from 600nm to 450nm and at 55 volts the device became colorless. Reflectivity peaks in the device at higher voltages were quite broad undoubtedly causing poor color saturation.

Another recent approach to full-color tunability is the electrostriction of elastomers under an electric field. Extremely high voltages are needed for electrostriction - a phenomenon in dielectric materials involving a contraction in response to an electric field. The first attempt at constructing an electrostriction based tunable photonic crystal was by the Foulger group at Clemson who used a colloidal crystal array filled with an acrylate elastomer. With voltages of under 0.5 to 3 kilovolts the reflectivity peak shifted from 580 to 600nm.[10] Aschwanden and Stemmer achieved full color tunability in electrostrictive elements using a tunable diffraction grating. A shift from 450 to 600nm was observed when 4.5 kilovolts was applied which caused an elongation of the period of the silicone diffraction grating.[16]

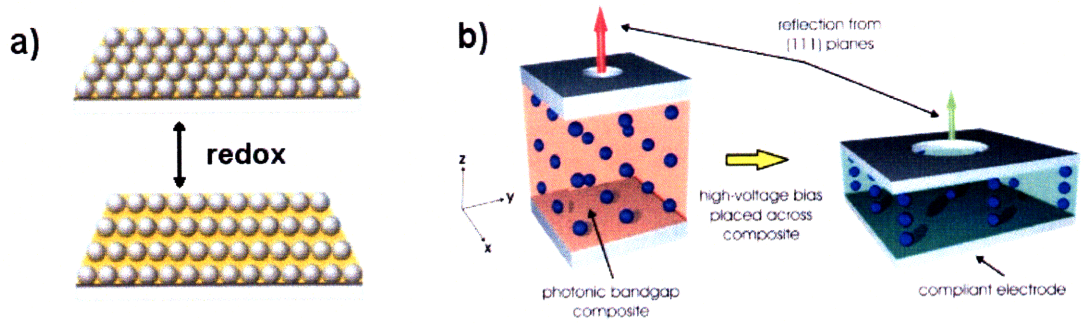

Figure 5.2: Common methods of producing an electroactive photonic crystal – a) A colloidal crystal infiltrated with an electroactive polymer which swells under an electrochemical stimulus. Polymeric fillers are chosen that undergo a collapse/swell transition due to a pH gradient produced by the hydrolysis of water or have electro-active groups which can be oxidized or reduced. (adapted from reference 14) b) Electrostriction involves a dielectric material sandwiched between two electrodes which is compressed by an applied voltage. Although very high voltages are required, there is little current passed through the device as it is essentially a capacitor (adapted from reference 10).

High-voltage piezoelectric drivers have also been used to mechanically deform a colloidal crystal array (±120V for a shift from 480 to 520nm)[15] but the most successful approach (lowest energy required with a large wavelength shift across the visible spectrum) thus far has been to use electrochemistry to drive changes in the index of refraction or spacing of colloidal crystalline arrays. Poly(3,4-ethylenedioxythiophene) (PEDOT) coated silica spheres in a hydrogel infiltrated colloidal crystal were oxidized (+1.2V) and reduced (-0.8V) to produced a shift from 575 to 585nm by changing the complex refractive index of the PEDOT.[11] Larger shifts have been produced in a polystyrene colloidal crystal infiltrated with poly(ferrocenylsilane) (PFS) which underwent a redox reaction upon the application of 2 volts producing a shift of between 150-200nm depending on the amount of crosslinking in the PFS.[14] Reproducible peak shifts (from 510nm to 610nm) for over 1000 switching cycles have been demonstrated in this system. An even greater wavelength range was demonstrated by infiltrating a copolymer of methacrylic acid and *N*-isopropylacrylamide into a colloidal crystal. After the application of 1.8 volts, the reflectivity peak shifted from 800 to 575nm. Further

tunability was accomplished by raising or lowering the temperature of operation (21°C: 800-625nm, 31°C: 800-350nm). [13]

Previously, BCPs have been used as photonic crystals but with limited tunability arising from changes in temperature[18], mechanical strain[19], and solvent concentration[20]. In chapter three, and a recently published paper, [21] a hydrophilic/hydrophobic block copolymer (polystyrene-b-poly 2-vinylpyridine) that showed a very substantial shifting (over 575%) of a stop band from the ultraviolet to near infrared wavelengths by simply changing the concentration of salt in the solvent was described. Here we employ the same block copolymer to create our bio-mimetic pixel. Certain cephalopod species have the ability to change the iridescent colors reflected from their skin in real time by the secretion of the neuromodulator acetylcholine which alters the periodic spacing of the lamellar structure of the iridophores.[22] The lamellar structure of this PS-P2VP block copolymer and the behavior of the stimulated hydrophilic P2VP gel block closely mimic the action of these reflectin proteins in cephalopods. In this chapter the challenge of active color variation has been met by electrically addressing and controlling a photonic crystal. This is achieved by coupling the structure forming ability of a block copolymer with the extensive tunability of a gel.

Polyelectrolyte polymer gels are well known for their stimuli responsiveness[23,24] and have been shown to react to electric fields[25] and changes in pH caused by electric fields[26]. By selecting a glassy domain (polystyrene) to limit the gel forming domain (poly 2-vinylpyridine) to expansion only in one dimension, we control the swelling behavior of the gel and magnify the response to external stimuli. Modest molecular-weight (100kg/mol – 100kg/mol and 57kg/mol – 57kg/mol), photonic-gel forming, polystyrene-

b-poly 2-vinylpyridine (PS-P2VP) block copolymers are used in combination with a simple electrochemical cell to produce red, green, and blue color through electrochemical stimulation.

This bio-mimetic color pixel is constructed by means of a simple electrochemical cell in which the local chemical environment at the electrode/electrolyte interface can be changed by applying sufficient voltage that will perform electrochemical oxidation or reduction. Because polymeric gels can undergo significant shape change in response to changes in their chemical environments, this chemical stimulus at the electrode can have major effects on the swelling behavior of the gel as is the case in color changing iridophores in nature. Fish such as the blue damselfish[27], neon tetra[28], and paradise whiptail[29] all employ one dimensional photonic crystals in which the lamellar spacing is controlled through chemical secretion by the sympathetic nervous system. Color change in the squid *Lolliguncula brevis* is also thought to be controlled by secretion of a chemical trigger causing changes in the thickness of the high refractive index protein platelets within the iridophore causing a change in reflected color[30]. In the present synthetic case, several conditions must be met for color change to occur: the electrolyte and electro-active species must be selected such that they swell the P2VP layers, the electrochemical reaction products must induce a change in the P2VP block polymer conformations, such that there is a corresponding variation in the P2VP layer thickness, and the electrolyte must possesses a large enough electrochemical window such that the electrodes do not participate in the electrochemical reaction. Because of this last point, non-aqueous electrolytes were utilized since the ITO coated glass electrodes have been

shown to react with the hydrolysis products of water reducing or eliminating the conductivity and transparency of the coating[31].

As seen in figure 5.3c, the electrochemical cell is composed of top and bottom electrodes (ITO coated glass) which contain an electrolytic fluid separated by an inert 200μm fluoropolymer spacer. To make the structured, responsive BCP gel layer, the PS-P2VP is first dissolved in a five percent by weight solution of propylene glycol monomethyletheracetate (PGMEA) and then spun onto the bottom ITO glass slide that had been previously coated with an adhesion promoter. By controlling the spin-coating speed or the initial concentration of the polymer in solution, a film of approximately 1 micron thick (approximately 15 periods) is deposited. The film is then annealed in chloroform vapor for at least 8 hours to achieve a well-aligned lamellar morphology as evidenced by inspection of a cross-section using transmission electron microscopy (see TEM image in figure 5.3d). Since the PS and P2VP polymers have almost identical refractive indices (n_{ps}=1.59, n_{pvp}=1.62), and the dry BCP layer period is quite small (48 nm), the annealed films are transparent to the eye. The uniformity of the alignment over the film surface (25mm x 50mm) can be checked by spraying methanol onto the film surface which causes the P2VP domains to swell and the film to uniformly reflect blue light.

Three different approaches were tried when experimenting with the electrochemically tunable color pixel. Broken down into broad categories, these approaches were: quaternized, protonated, and solvent based devices. The next three sections will describe each approach in detail.

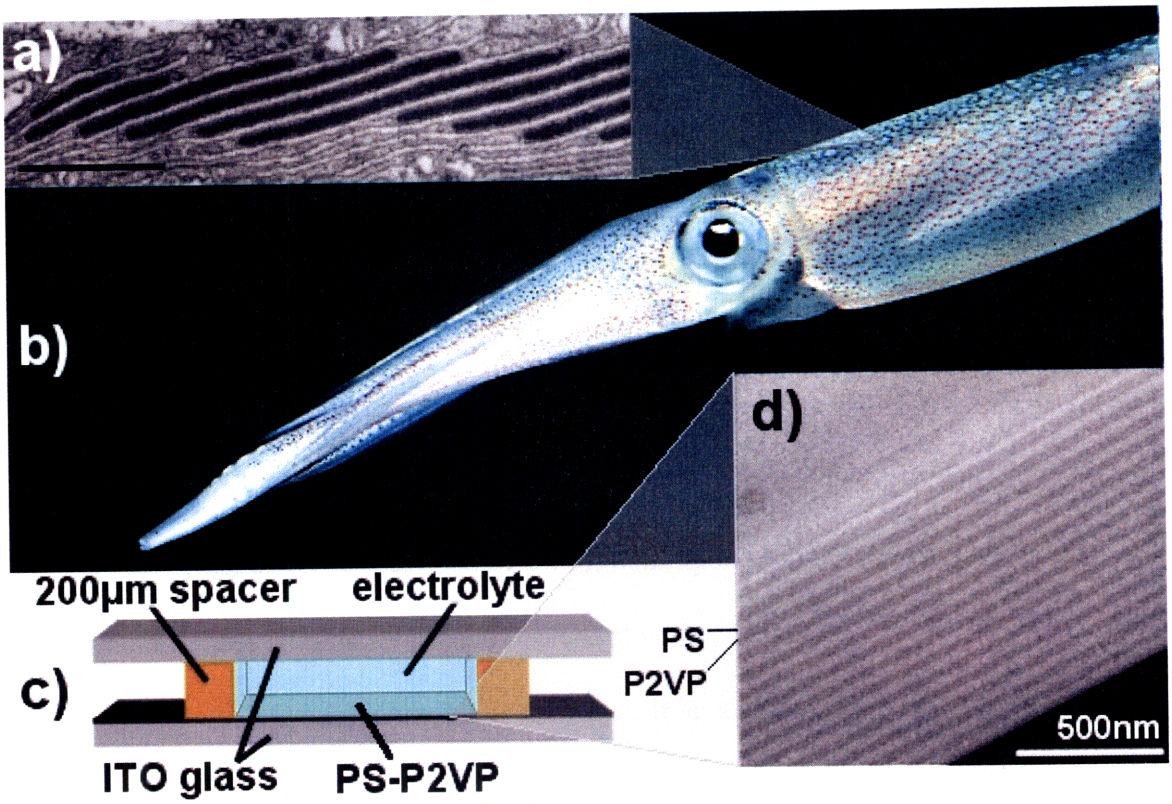

Figure 5.3: Bio-inspired color changing pixel. Squid such as *Loligo pealeii* (a) use protein based multilayer reflectors to manipulate light. Structural uniformity is also clearly evident in the cross-sectional TEM micrograph. The structural similarity between the squid's natural self-assembling protein (b – scale bar 1μm) and the lamellar block copolymer system (d – scale bar 500nm) are evident when TEM cross sections of the elements are compared. A simple electrochemical cell (c) is fabricated by introducing an electrolyte between two ITO coated glass slides, one of which has been previously covered with an approximately one micron thick layer of the gel forming photonic block copolymer. Credits: (a) adapted from reference 3, (b) Dr. R. Hanlon, Marine Biological Laboratory, Woods Hole, MA 02543, (d) R. Mickiewicz.

5.3 Electro-tuning case 1: The quaternized polymer device

One path of exploration, in conjunction with Dr. Youngjong Kang, lead to the modification of the P2VP polymer (57k-57k PS-P2VP), in essence, using chemistry to create a permanent polyelectrolyte out of the P2VP domains and thus alter their properties. This modification to convert the P2VP to a permanent polyelectrolyte was accomplished by way of a quaternization reaction – converting P2VP to poly(2-vinyl ethyl pyridinium bromide) (QP2VP). The amount of conversion from P2VP to QP2VP

depends on the amount of time the reaction is allowed to proceed. Maximum conversion takes place in approximately one day at 40°C[21] and will produce a film that reflects a dark red color (λ_{peak}~700nm) when immersed into water.

The electrochemical cell was constructed by placing a polymeric spacer (the orange frame in figure 5.3c) on top of the quaternized film (film electrode), filling the cavity with ethanol, and sealing the cell with another ITO covered slide on top (counter electrode). The positive lead from the power supply is connected to the substrate containing the PS-QP2VP and the ground lead is attached to the superstrate (defined as forward bias). When voltage is applied to the cell electrodes and the redox potential of ethanol is reached, H^+ is produced at the anode and ethoxide$^-$ (and OH^- due to the small amount of water in the system) is produced at the cathode. This localized change in chemistry induced large changes in the polyelectrolyte block conformation and thus changes in the QP2VP domain thickness, directly influencing the optical properties of the dielectric stack.

For a fully quaternized vinylpyridine block, when a positive voltage is applied to the film electrode (anode), H^+ ions are produced at the electrode but there is no color change since all available pyridine groups in the P2VP are already quaternized and no further protonation is possible (bottom right figure 5.4.) When the leads are reversed and a negative bias is applied to the film, it unexpectedly expands and turns red. This behavior (which is completely opposite from the protonated case described below) can be understood because of the difference in swelling caused by the replacement of the bromide counter ions normally associated with the pyridinium groups with hydroxide counter ions. The hydroxide counter ions, being more hydrophilic, cause the gel to swell

more (by increasing its solubility in water) and thus produce a red shift in the reflected spectra. However, once the hydroxide ions have displaced the bromide counter ions, the device is not responsive to the application of positive or negative voltage because of the superior stability of the OH^- counterion with the pyridinium group.

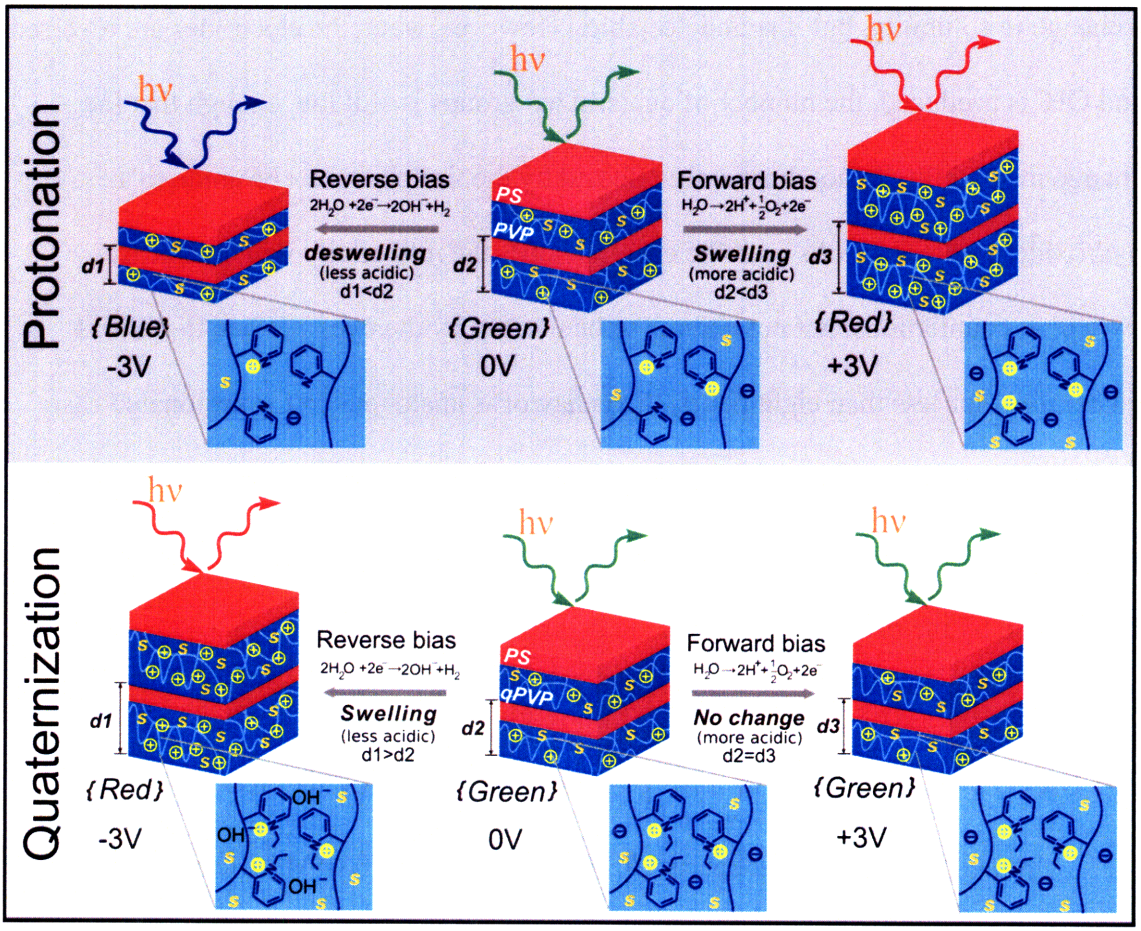

Figure 5.4: A schematic representation of the mechanism for electrochemical color change. Color change occurring under two different scenarios: The first, when the P2VP is protonated by an acidic electrolyte, and the second when the P2VP has been chemically modified via a quaternization reaction to become a permanent polyelectrolyte. In the protonated case, OH^- ions are produced when a negative voltage is applied to the cell (film electrode attached to ground.) This causes the film to shrink because of the decreased affinity for water in the P2VP layers and the color blue shifts. If the electrodes are reversed, H^+ ions are produced and the film swells causing a red shift. In the second case when the P2VP has been fully quaternized there are no pyridine groups available to protonate. When the film electrode is the anode and H^+ is produced no extra protonation can take place and the film maintains its thickness and color. Reversing the electrodes causes OH^- ions to be produced which replace the bromine counterions and the structure swells producing a red shift.

An interesting transition occurs when the P2VP blocks are *partially* quaternized. For example if we employ a sample that was quaternized for eight hours, there is no

change in color upon application of a voltage no matter the polarity or magnitude of the voltage. In this situation since a sufficient number of the P2VP repeat units were converted to QP2VP, no major changes in solubility can be brought about by changing the local pH through the production of H^+ by hydrolysis. (The change in pH may produce a change in solubility, but it is undetectable.) However, when the electrodes are reversed and OH^- is produced, the number of quaternized groups is still low enough that the change in solubility is not drastically effected by the switch from a bromide to a hydroxide counter ion. (As with the change in pH, the reflectivity will change by switching counter ions, but not enough to be noticed by the eye). When the film is quaternized for less than eight hours, the behavior is analogous to the protonated case described in the next section where an acid is used to protonate the P2VP producing a polyelectrolyte. In the protonated polymer, the extent of the polyelectrolyte character is determined by the pH of the solution.

5.4 Electro-tuning case 2: The protonated polymer device

Immersing the dry, transparent PS-P2VP film into a 0.05M trifluoroacetic acid (CF_3COOH) solution in ethanol causes the P2VP domains to swell and the film to reflect blue light. The electrochemical cell is constructed in the same manner as above by placing a polymeric spacer on top of the film and sealing in the trifluoroacetic acid solution with another ITO slide on top. The positive lead from the power supply is connected to the substrate containing the PS-P2VP and the ground lead is attached to the superstrate.

Upon application of five volts (DC), H^+ and trifluoroacetate ions are produced by the electrolysis of the trifluoroacetic acid and the film responds to the pH gradient that is set up in the cell and red-shifts from blue to green due to the increased protonation of the P2VP which brings in an increased amount of ethanol into the domain (top scheme in figure 5.4). If the electrochemical driving force (voltage) is further increased (~10V), more H^+ ions are produced and the P2VP layers expand further and reflect red light. This voltage level cannot be maintained for very long due to the electrochemical reduction of the ITO which is not stable at such high voltages in this particular solution.

By reversing the electrodes such that the negative lead from the power supply is connected to the polymer film side, the swelling behavior can be reversed. Applying five volts causes the gel to shrink and reflect in the ultraviolet. The greater the applied voltage, the more trifluoroacetate ions are produced at the cathode, and the more deprotonated the adjacent BCP film becomes. This is because the trifluoroacetate ions are basic (electron acceptors) and will deprotonate the P2VP which causes a decrease in solubility, collapsing the gel and blue-shifting the reflectivity peak.

5.5 Electro-tuning case 3: The solvent swollen device

In this case the electrochemical cell is filled with 2,2,2-trifluoroethanol (TFE). When liquid TFE (n_{TFE}=1.295) is initially applied to the film, the polymer (100k-100k PS-P2VP) swells immediately and reflects red light with a maximum reflectivity of 40% at 675nm (see figure 5.7). The negative lead from the power supply is then connected to the substrate containing the PS-P2VP and the positive lead is attached to the superstrate (counter electrode). When voltage is applied to the cell electrodes and the redox potential

of TFE is reached, the TFE undergoes an electrochemical reaction forming trifluoroethoxide ions (TFX) at the film electrode (cathode) interface and H^+ and trifluoroacetaldehyde 2,2,2-trifluoroethyl hemiacetal at the anode (see figure 5.5).[32] Because of the formation of the acidic H^+ and basic TFX species, a pH gradient is believed to be formed between the electrodes similar to that due to the hydrolysis of water in other systems[13,33,34]. This localized change in the chemical nature of the solvent induces a large change in the P2VP conformation and thus changes in domain thickness; directly influencing the optical properties of the dielectric stack by de-protonating the P2VP layer and thus reducing its thickness.

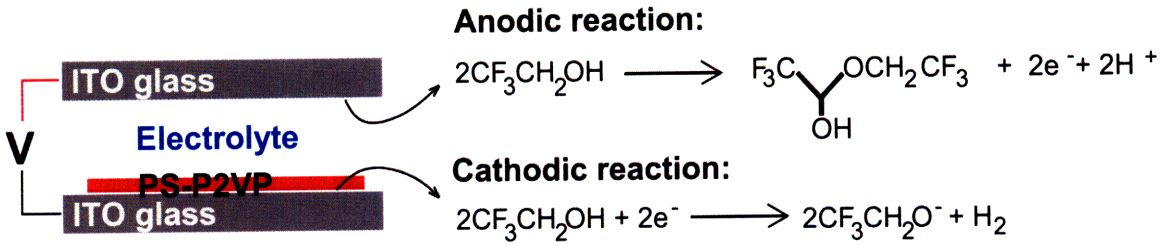

Figure 5.5: The electrochemical half-cell reactions for the decomposition of 2,2,2-trifluoroethanol – When the redox potential of the system is reached the anode produces trifluoroacetaldehyde 2,2,2-trifluoroethyl hemiacetal and H^+ ions whereas at the cathode, trifluoroethoxide ions and hydrogen gas are produced. The trifluoroethoxide ions are very basic in nature and will deprotonate the $P2VP^+$ which is formed by protonation of P2VP by hydrogen from the auto-dissociation of trifluoroethanol.

At 25°C, TFE has a pKa value of 12.5.[35] From this value, the equilibrium concentration of H^+ ions in found to be $2x10^{-6}$M which allows a pH value to be calculated (pH = 5.6). The pKa of the pyridinium ion has been experimentally found to be 4.5 (in an ethanol/water solution at 25°C)[36] and can be used to calculate the ratio of protonated to unprotonated P2VP (15.8:1). This means that at room temperature a little over 6% of the P2VP is protonated by dissociated hydrogen. The protonated P2VP has a higher solubility and thus swells more in the TFE. By de-protonating the P2VP through the

electrochemical production of TFX, P2VP domains will shrink and the reflected wavelengths will blue-shift (see figure 5.5).

By applying five volts to the film, the color changes from red to green over the course of a few seconds with a maximum reflectivity of 40% at 563nm because of the reduced solubility of the polymer chains in the TFX. The color of the film can be changed even further by increasing the applied voltage to 10 volts. The increase in voltage increases the driving force for the electrochemical reaction and more TFX is formed pushing the reflectivity to even lower wavelengths where the block copolymer has regions with different layer spacings as evidenced by the very broad blue reflectivity peak. The inhomogeneous color of the film is most likely due to local variations in the electrical resistance of the electrolyte which affects the rate of the electrochemical reaction.

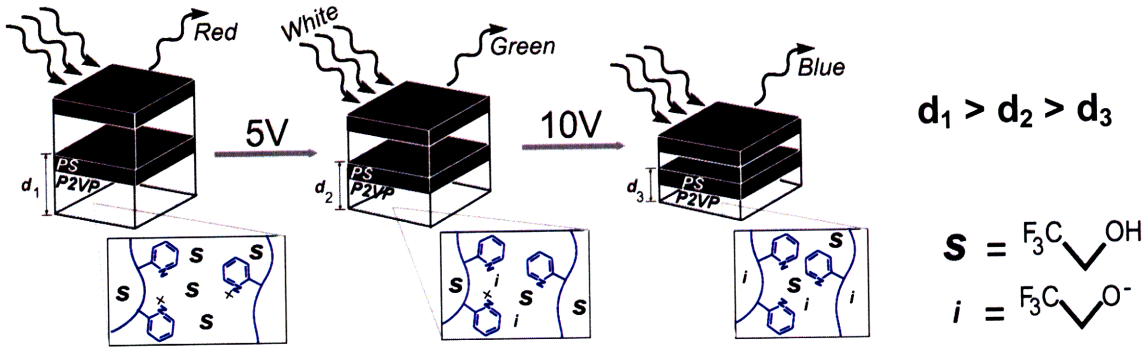

Figure 5.6: A schematic representation of the mechanism for electrochemical color change. When the P2VP is swollen by the trifluoroethanol (TFE – labeled s in the figure) the polymer reflects red light. By applying five volts to the substrate the polymer film turns from red to green because of an electrochemical reaction that is set up which produces trifluoroethoxide ions (TFX – labeled i in the figure). TFX does not swell the P2VP as well as TFE and thus the addition of TFX causes the P2VP domains to shrink, blue-shifting the reflected light. Increasing the voltage applied to the cell to 10 volts causes more TFX to be produced and the domains collapse even farther causing the polymer to reflect blue light.

In order verify that the color change was due to an electrochemical reaction and not capacitive ion movement, Maxwell stress induced dimensional changes, or other non-electrochemical mechanisms, PS-P2VP was spun onto ITO glass that had been passivated by the deposition of poly cyclohexyl methacrylate-co-ethylene glycol diacrylate, forming a barrier to electron movement. When voltage was applied to the lamellar BCP on top of this film there was no response until relatively high voltages (~25V) when the barrier layer broke down and pinholes were formed allowing an electrochemical reaction which locally changed the color of the adjacent surrounding BCP film.

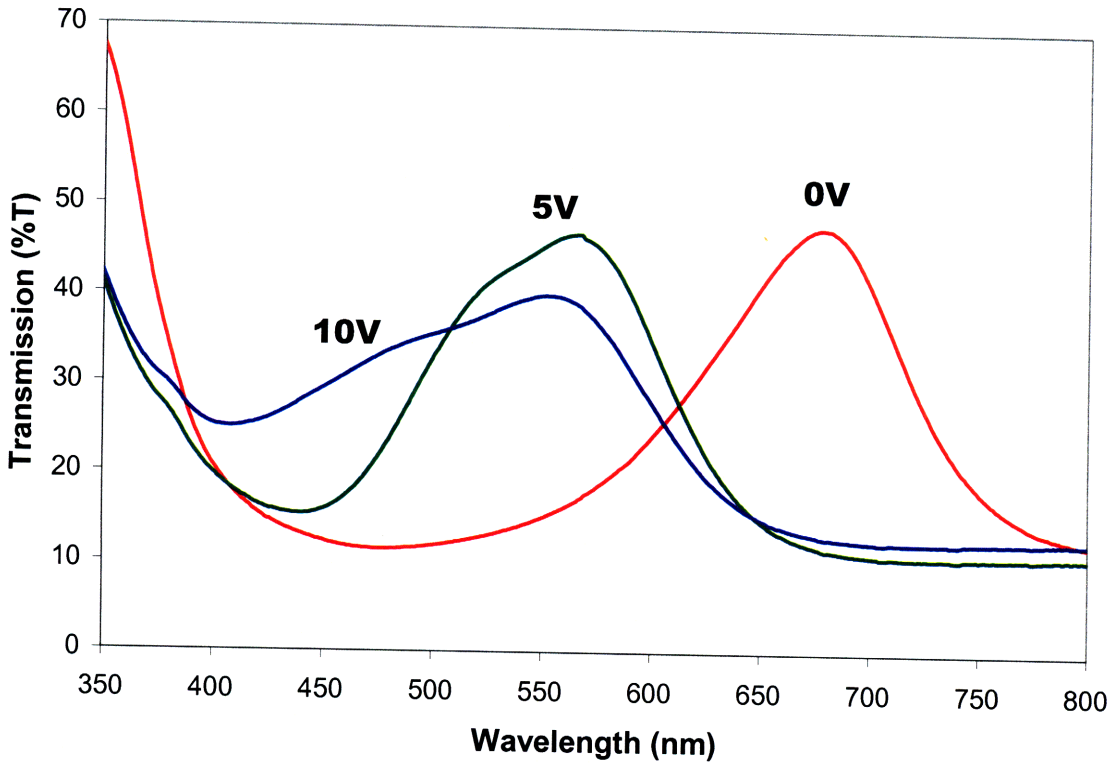

Figure 5.7: Electrochemically tuned reflectivity spectra. When using trifluoroethanol as the electrolyte the block copolymer produces a red reflection at normal incidence (no applied voltage). After applying five volts to the cell the color shifts from red to green in about five seconds. At ten volts the color of the PS-P2VP is blue with regions of green as shown by the wide reflectivity peak.

5.6 Conclusions

In summary, the full-color tunability of a bio-inspired photonic crystal pixel has been demonstrated in a simple lamellar forming block copolymer. As with numerous one-dimensional photonic crystals found in the animal kingdom, the PS-P2VP system can then be tuned by external chemical stimuli to produce rapid changes in reflected wavelengths. The thin form factor, low turn-on voltage, and high reflectivity lends itself nicely to static and dynamic displays and with suitable choice of molecular weight, signaling devices such as infrared or ultraviolet reflectors that would operate outside the range of human sight.

5.7 References

1 Land, M.F., The physics and biology of animal reflectors, Prog. Biophys. and Molec. Biol., 24, 75-106 (1972)

2 Hanlon, R.T., Cephalopod dynamic camouflage, Current Biology, 17(11), R400-R404 (2007)

3 Cooper, K.M., Hanlon, R.T., Budelmann, B.U., Physiological color change in squid iridophores, Cell and Tissue Research, 259, 15-24 (1990)

4 Mäthger, L.M. and Hanlon, R.T., Malleable skin coloration in cephalopods: selective reflectance, transmission and absorbance of light by chromatophores and iridophores Cell Tissue Research 329, 179–186 (2007)

5 Vaia, R. and Baur, J., Adaptive Composites, Science, 319, 420-421 (2008)

6 Kramer, R.M., Crookes-Goodson, W.J., Naik, R.R., The self-organizing properties of squid reflectin protein, Nature Materials, 6, 533-538 (2007)

7 Crookes, W., Ding, L.L., Huang, Q.H, Kimbell, J.R., Horwitz, J., McFall-Ngai, M.J., Reflectins: the unusual proteins of squid tissues, Science, 303, 235-238 (2004)

8 J. M. Weissman, H. B. Sunkara, A. S. Tse, S. A. Asher, Thermally switchable periodicities and diffraction from mesoscopically ordered materials, Science, 274, 959 (1996)

9 Schrenk, W.J., Shrum, W.E., Wheatley, J.A., Elastomeric optical interference films, US Patent 4937134 (1990)

10 Xia, J., Ying, Y., and Foulger, S., Electric-Field-Induced Rejection-Wavelength Tuning of Photonic-Bandgap Composites, Advanced Materials, 17, 2463-7 (2005)

11 Norton, J., Han M.G., Jiang, P., Creager, S. and Foulger, S.H., Electrochemical tuning the optical properties of crystalline colloidal arrays composed of poly(3,4-ethylenedioxythiophene) coated silica particles, Journal of Materials Chemistry, 17, 1149-1153 (2007)

12 Hikmet, R.A.M. and Polesso, R., Patterned multicolor switchable cholesteric liquid crystal gels, Advanced Materials, 14(7), 502-4 (2002)

13 Ueno, K., Matsubara, K., Watanabe, M., and Takeoka, Y., An electro- and thermochromic hydrogel as a full-color indicator, Advanced Materials, 19, 2807-12 (2007)

14 Arsenault, A., Puzzo, D., Manners, I., and Ozin, G., Photonic-crystal full-colour displays, Nature Photonics, 1, 468-472 (2007)

15 Foulger, S., Jiang, P., Lattam, A., Smith, D., Ballato, J., Dausch, D., Grego, S., and Stoner, B., Photonic crystal composites with reversible high-frequency stop band shifts, Advanced Materials, 15(9), 685-9 (2003)

16 Aschwanden, M. and Stemmer, A. Polymeric, electrically tunable diffraction grating based on artificial muscles, Optics Letters, 31(17), 2610-2612 (2006)

17 Busch, K. and John, S. Liquid-crystal photonic band gap materials: the tunable electromagnetic vacuum, Phys. Rev. Lett. 83(5), 967-70 (1999)

18 Osuji, C; Chi-Yang Chao; Bita, I.; Ober, C.H.; and Thomas, E.L. Temperature-dependent photonic bandgap in a self-assembled hydrogen-bonded liquid-crystalline diblock copolymer, Advanced Functional Materials, 12(11-12), 753-8 (2002)

19 Yoon, J.S., Block copolymer photonic crystals: towards self-assembled active optical elements, Ph.D. Thesis, Massachusetts Institute of Technology, (2006)

20 Yoon, J.S., Lee, W., and Thomas, E.L., Thermochromic block copolymer photonic gel, submitted to Angewante Chemie, (Apr. 2008)

21 Kang, Y.J., Walish J., Thomas, E.L., Broad wavelength range chemically tunable block copolymer photonic gels, Nature Materials, 6, 957 - 960 (2007).

22 Hanlon, R.T., Cooper, K.M., Budelmann, B.U., Pappas, T.C., Physiological color change in squid iridophores, Cell and Tissue Research, 259, 3-14 (1990)

23 J. H. Holtz, S. A. Asher, Polymerized colloidal crystal hydrogel films as intelligent chemical sensing materials, Nature 389, 829 (1997)

24 Li, Y. & Tanaka, T., Phase transitions of gels, Annu. Rev. Mater. Sci., 22, 243-277 (1992)

25 Tanaka T., Nishio, I. Sun, S.T., and Ueno-Nishio S., Collapse of gels in an electric field, Science 218(4571) 467 – 469 (1982)

26 Veil, S. Action of electric field on gelatin: effect of indicators *Comptes Rendus Hebdomadaires des Seances de l'Academie des Sciences*, 194, 454-456 (1932)

27 Kasukawa, H., Oshima, N., and Fujii, R., Control of chromatophore movements in dermal chromatic units of blue damselfish – II. The motile iridophores, Comp. Biochem. Physiol. 83C(1), 1-7 (1986)

28 Nagaishi, H. and Oshima, N., Neural control of motile activity of light-sensitive iridophores in the neon tetra, Pigment Cell Research 2, 485-492 (1989)

29 Mathger, L.M., Land, M.F., Siebeck, U.E., and Marshall, N.J., Rapid colour changes in multilayer reflecting stripes in the paradise whiptail, Pentapodus paradiseus, J. Exp. Biol., 206, 3607-13 (2003)

30 Cooper, K.M. and Hanlon, R.T., correlation of iridescence with changes in iridophore platelet ultrastructure in the squid *lolliguncula brevis* , J. Exp. Biol. 121, 451-455 (1986)

31 Raes, M.H.W. and Smeets, M., A novel measuring method of testing ITO protective coatings for use in mobile phone LCD's, Proceedings. International Symposium on Advanced Packaging Materials: Processes, Properties and Interfaces, 144-48 (2005)

32 Shirai, K., Onomura, O., Maki, T., and Matsumura, Y., Electrochemical oxidation of 2,2,2-trifluoroethanol to trifluoroacetaldehyde 2,2,2-trifluoroethyl hemiacetal, Tetrahedron Letters, 41, 5873-76 (2000)

33 Cabrera, C.R., Finlayson, B., Yager, P., Formation of natural pH gradients in a microfluidic Device under flow conditions: model and experimental validation, Anal. Chem., 73, 658-666 (2001)

34 Bier, M., Palusinski, O.A., Mosher, R.A., Saville, D.A., Electrophoresis: mathematical modeling and computer simulation, Science, 219(4590), 1281-1287 (1983)

35 Dean, J.A., Lange's Handbook of Chemistry (15th Edition) McGraw-Hill (1999)

36 Ferruti, P. and Barbucci, R., Linear amino polymers: synthesis, protonation and complex formation, Advances in polymer science, 58, 55-92, (1984)

Chapter 6:
Design and Construction of a Linear Shear Rheometer for Measurement of the Mechanochromic Properties of High Molecular-Weight Block Copolymers

Previous chapters have concentrated on the behavior of a PS-P2VP gel-forming lamellar block copolymer which produced changes in color through stimulation by application of different solvents, changes in temperature, and change in the local solvent environment through electrochemistry. The present chapter will continue the theme of 'tuning' the color of a lamellar block copolymer but through the mechanical deformation of solvated block copolymers via the design and construction of a linear shear rheometer. The change in color by means of an applied deformation is dubbed "mechanochromism" and in particular the work in this chapter will focus on a specific type of mechanochromism due to the *shearing* of solvent swollen lamellar block copolymers.

Shear mechanochromism has not been reported as a deformation mechanism in the literature and is especially interesting due to the relatively small deformations found necessary to produce large color shifts. Details of the design parameters of the linear shear rheometer will be discussed and data from solvent swollen poly(styrene)-poly(isoprene) and poly(styrene)-poly(methyl methacrylate) will be presented.

6.1 Introduction

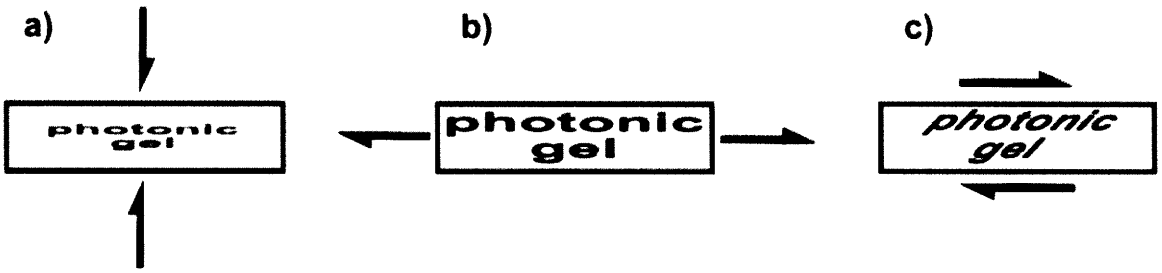

Figure 6.1: Possible modes of deformation for mechanochromic materials – a) Compressive (a) and tensile (b) stress are common modes of deformation used in mechanochromic liquid crystals and synthetic opals. Mechanochromism due to shear (c) has not yet been reported in the literature and is the focus of this chapter. The words "photonic gel" have been compressed, stretched, and sheared in each picture to match the type of deformation depicted in each illustration.

Photonic crystals derive their color through the interference caused by a periodic arrangement of high- and low-index materials. This array can be distorted or deformed through the application of a force or pressure. The three possible deformation modes are illustrated in figure 6.1. Both compressive and tensile forces are common stimuli and have been applied to cholesteric liquid crystals, synthetic opals, and one-dimensional multilayer homopolymer extrusions. A brief overview of mechanochromic photonic crystals is provided to familiarize the reader with developments in the field before discussion of linear shear deformation.

Twisted nematic liquid crystals (TNLC) have been used for decades in displays and work by selectively reflecting polarized light via changing the orientation of the

liquid crystal by an applied electric field. The orientation of the liquid crystalline mesogens in the device can also be changed by a stress field as is evident when touching a liquid crystal based flat panel monitor. Recent work has focused on making TNLC elastomers that change color in response to bi-axial tensile mechanical deformation, making these materials into ideal candidates for tunable filters or reflectors.[1,2,3,4,5] The reversible tunability of these TNLC elastomers comes about because of the change in the pitch with applied stress and the entropic elastic restoring force from the deformed crosslinked network. Temperature[6] and dopants[7] can also change the pitch of a TNLC making a wide parameter space available for changing the photonic properties of these materials. Liquid crystals have an added processing advantage via their ability to self assemble making large area applications possible.

Block copolymers (BCPs) can also self assemble into photonic structures active in the visible wavelengths if the molecular weights of the individual blocks are high enough and the block's indices of refraction are substantially different (as seen in previous chapters).[8,9] The lamellar BCP morphology corresponding to a simple layered structure that produces color via interference has been the most thoroughly studied although other morphologies such as the double gyroid and cylinders have also been utilized in forming photonic crystals.[10,11]

In general, interference filters created by layering materials of specific thicknesses on top of one another are known as Bragg stacks. Depending on the architecture of the stack and the materials chosen (specific dielectric tensors), these stacks will reflect light of specific wavelengths because the incident light interferes with itself. Usually these stacks are not 'dynamic' meaning the properties of the stack are essentially invariant to

various applied forces/fields. For example, sequentially evaporated semiconductors and/or oxides are frequently used to make extremely high-reflectivity mirrors (>98%) at specific wavelengths[12]. In the 1960s, Dow Chemical developed a co-extrusion process to make multilayer films of pairs of homopolymers that were used to create visible wavelength reflectors.[13] This technology has been licensed to 3M and is now commercially available. Wideband filters (mirrors) are also available from 3M and are stacks made from polymer layers with high birefringence.[14,15] The film co-extrusion method has also been applied to elastomers by Dow Chemical.[16] When stretched or compressed, these elastomeric materials are able to change color. The lamellar phase displayed by the aforementioned symmetric block copolymers is quite similar to these multilayer extrusions. High molecular weight styrene-isoprene block copolymers when plasticized with dioctyl phthalate (DOP) show mechanochromic behavior.[17] Preliminary experiments have shown that the reflectivity of equilibrated poly(styrene)-poly(isoprene)-dioctyl phthalate samples can be controlled by systematic compression.[25]

Self assembled structures have also been used as scaffolds or templates for producing mechanochromic materials; fcc sphere packs (synthetic opals) produced by self assembly of polystryrene or silica spheres, subsequently infiltrated with a poly(dimethyl siloxane)[18] or gel[19,20,21,22,23,27,28] precursor followed by crosslinking exhibit reversible mechanochromism.

Table 1.1 summarizes the tuning range for several different photonic mechanochromic technologies. Materials are compared by their change in wavelength with respect to the change in strain ($\Delta\lambda/\Delta\varepsilon$) because of the different thickness of all the various samples as well as the different modes of deformation. Note the difference in

performance between block copolymers and elastomer extrusion. Since these two technologies rely on the same phenomenon for coloration, block copolymer performance should be able to be improved with proper processing or copolymer selection, although it is possible that the different testing methods (compression vs. tension) could be a potential source of the disparity since the change in layer thickness depends in general on the full strain tensor..

Table 6.1: A comparison of several different mechanochromic materials by change in wavelength per change in strain

Material	$\Delta\lambda/\Delta\%\varepsilon$ (nm)	Reflectivity peak range (nm)	% strain (type of test)	Initial sample thickness (μm)
Block copolymer (PS/PI) (1D)[24,25]	1.48	562-642	50% (Compression)	100
Multilayer elastomer extrusion (1D)[16]	1.85	565-750	100% (Uniaxial tension)	61
Polymer dispersed liquid crystals (1D)[1]	2.86	590-713	43% (Compression)	120
Cholesteric liquid crystals (1D)[26]	1.41	544-630	61% (Equi-biaxial tension)	250
Synthetic elastomeric opals (PDMS backfilled) (3D)[18]	1.5	560-590	20% (Uniaxial tension)	20
Synthetic elastomeric opals (Acrylate backfilled) (3D)[27]	5.25	466-550	16% (Compression and tension)	313
Synthetic elastomeric opals (Hydrogel backfilled) (3D)[28]	3.67	525-580	15% (Compression)	250

All of these examples rely on compression (z-axis deformation), uniaxial tension (x or y axis deformation), or biaxial deformation (x and y axis deformation) to provide the stimulus for the mechanochromic color shift. The lack of a report on the shear deformation behavior in the aforementioned systems is most likely due to the disruption to the ordered structure of the synthetic opals and liquid crystals that large amounts of shear might cause. Also it is relatively difficult to apply a controlled amount of shear to a thin film. As the mechanochromic films in Table 1.1 range from 20 to 250 microns thick,

10 percent shear strain (linear distance that the top and bottom surfaces move relative one another divided by the film thickness) would mean the top surface displaces between 2 and 25 microns.

6.2 Linear shear rheometer design parameters

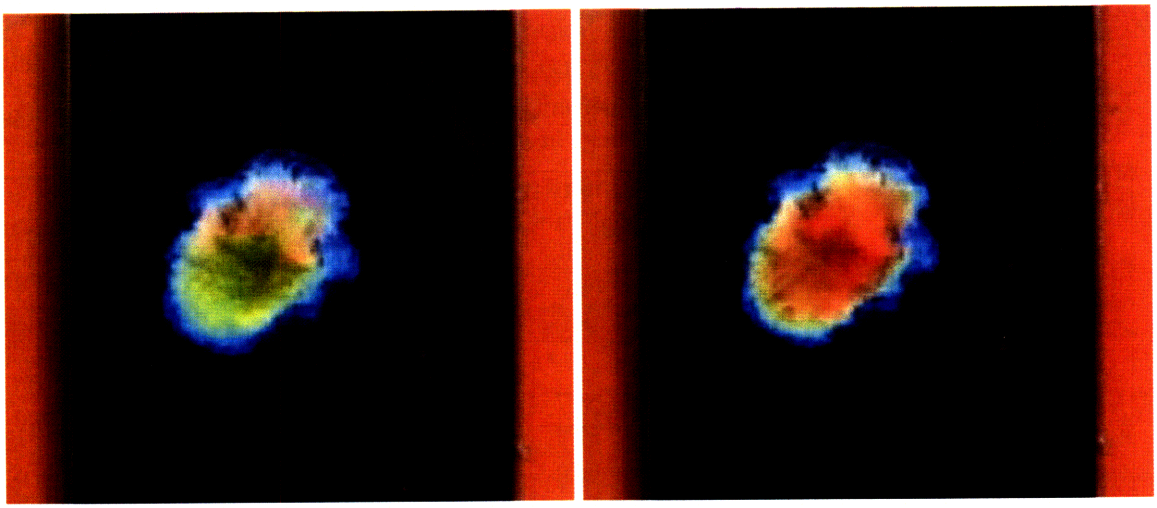

Figure 6.2: Shear induced mechanochromism in a 75% toluene/25% PS 290k-PMMA 360k photonic block copolymer – The sample is trapped between two glass slides (one inch wide). The un-deformed sample on the left displays green and yellow colors but when the top microscope slide is slightly displaced (~100 microns) to impart shear, the gel changes to a red-orange color. The back side of the bottom slide has been painted black for improved contrast.

The controlled measurement of the reflectivity of a photonic block copolymer under shear was the guiding principle in the design and construction of the BCP shear rheometer. Initial experiments, such as the one described in figure 6.2 showed a color change upon the application of a tiny displacement to the top glass slide. This small movement sheared the BCP gel and caused a color change. It was realized that a controlled study would have to be performed in order to rule out any inadvertent tensile or compressive forces that may have been applied to the sample.

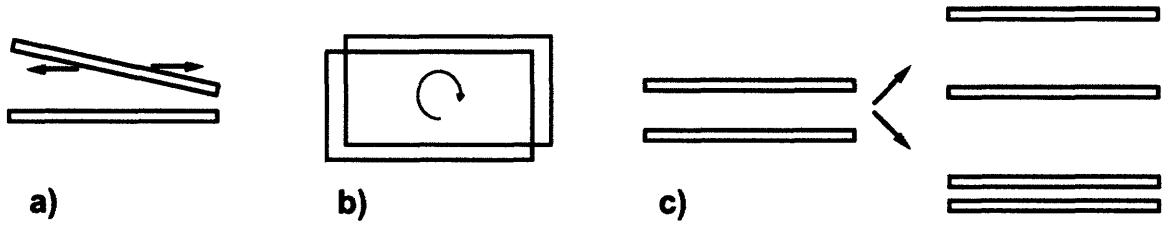

Figure 6.3: Conditions to be avoided in the shear rheometer – In order to make sure that the deformation of the sample occurs only through shear, the following conditions must be avoided. (a) (side view) If the top and bottom plate are not parallel the movement of the top plate relative to the bottom plate could cause some compressive or tensile deformation in addition to shear. (b) (top view) Rotational shear would impart multiple shear strains and shear rates and to simplify the analysis of the data, only linear shear is wanted. (c) (side view) The plates must be kept not only parallel but the same distance apart at all times lest vertical tensile or compressive forces come into play.

The proposed device features two parallel plates with a fixed bottom plate and a movable top plate. Figure 6.3 details some of the plate orientations that need to be minimized or eliminated in the device. The first and most important condition is that the plates must remain parallel. If one plate is inclined with respect to the other the BCP gel would be compressed or stretched depending on which way the top plate was moving creating stress states other than pure shear. If the plates are kept parallel, the top plate must only move in one direction. If the top plate is allowed to rotate with respect to the bottom plate resulting in rotational shear, multiple shear rates and shear strains would be present in the sample since the rotational shear strain would be zero at the center of rotation and increase radially. A third condition to avoid is the relative movement of the plates toward or away from one another. This will prevent the motor or motive force from compressing or stretching the sample although this last constraint may introduce complications depending on the Poisson ratio of the gel.

The distance between the plates was chosen to be approximately 100 microns. A thinner gap would lead to a smaller sample volume thus conserving the polymer but the smaller the gap becomes the smaller distance that the top plate has to move for a given shear strain. As an example, for a 100 micron gap, 10% shear strain would mean the top

plate would need to be moved 10 microns. For a 25 micron gap, 10% shear strain dictates a top plate movement of 2.5 microns and finding a motor or actuator that can precisely move those small distances becomes very expensive. Also, at smaller gap sizes other factors influencing the size of the gap play a bigger role (e.g. the roughness of the ball bearings.)

Because of its fast response time, a charge-coupled device (CCD) camera attached to an optical microscope was chosen to record the reflectivity spectra associated with the sheared block copolymer. To fit on the microscope stage, the device could be no wider than 120 mm and no taller than 35 mm. Measurement with the microscope/CCD placed no restrictions on the length of the device but the length of the device was chosen such that the option of mounting the device in a conventional spectrophotometer was left open as the need for more precise measurements than the microscope/CCD spectrometer could provide may be necessary in the future. The necessity of using a spectrophotometer dictates that at least one of the plates (superstrate or substrate) be transparent.

The device must also be able to measure the amount of shear strain applied to the sample as well as the strain rate in order for comparisons to compare the experimental results with other studies and to probe polymer gel viscoelastic behavior. Lastly, the device must be able to measure the force applied to the sample so that comparison between different types of mechanochromic materials can be made as well as comparisons between different BCP samples. The shear strain, shear rate, and load measurements must have sufficient resolution to capture the requisite phenomena. The shear strain imparted to the material may vary between 10 and 1000% with strain rates of

approximately 0.01 s^{-1} and loads between 0 and 2 Newtons were expected. In the future, adaptation for measuring the temperature dependent shear properties is desirable as well.

6.3 Linear shear rheometer design specifications

6.3.1 Materials

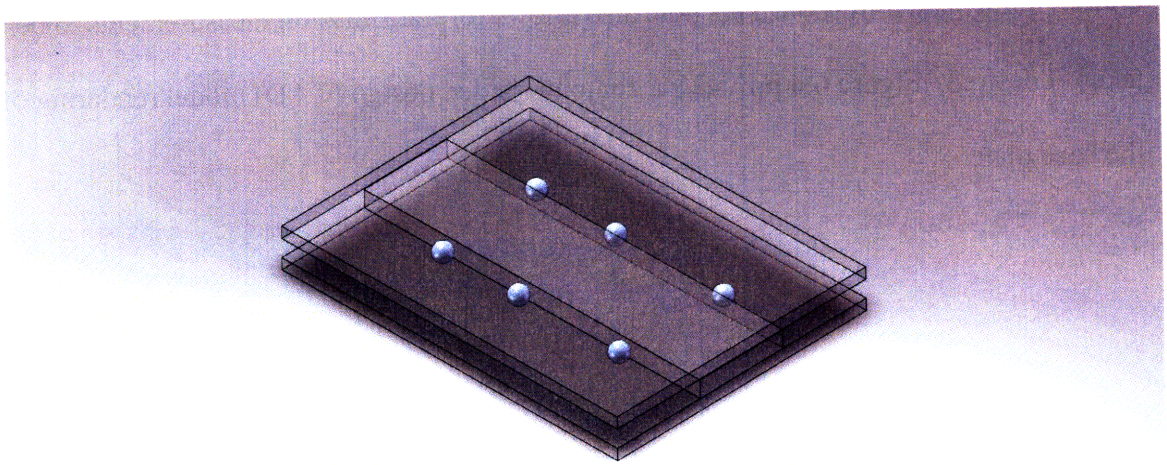

Figure 6.3: The glass-plate-on-ball-bearing design – Two plates are separated by ball bearings. The gap in which the sample is held is controlled by the insertion of a middle glass plate. The relative thickness of this glass plate and the diameter of the ball bearings determine the distance between the substrate and superstrate. The top plate can slide freely while the bottom is held fixed.

A glass-plate-on-ball-bearing design was chosen as the basis of the apparatus (see figure 6.4). The base structure of the apparatus in which the glass plates are held consists of a rectangular aluminum extrusion, with a length of 176mm and a width of 115mm, to which all subassemblies are fastened. In order to assure high stiffness, and thus discountable levels of deflection as well as a suitable thickness for fastening other components, a final thickness of 3/8" was chosen. Aside from various through and tapped holes for fastening subassemblies, the main feature of the base plate is a 0.125" relief step, machined into the top surface. This step allows the base plate to accept the lowermost piece of the sliding glass plate assembly and fully constrains it in the plane of

the base plate (the x and y directions), as well as assuring parallelism with the top surface of the base plate, which is critical when aligning the actuator/force measurement assembly.

The base plate also has a large hole machined in it, such that minimum amount of the bottom plate will be covered by the base plate. Only a ½" ledge was left for the bottom glass plate to rest on. This hole also allows for transmission measurements to be taken if desired. Figure 6.4 provides a computer aided design (CAD) model rendering of the base plate.

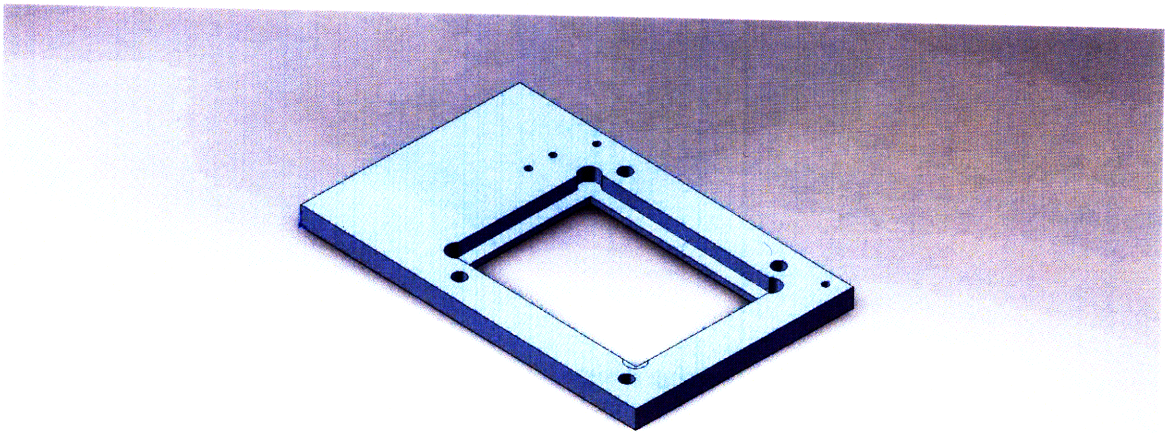

Figure 6.4: The base plate for the shear rheometer – The base plate provides the structure for the rest of the device. A four inch by three inch pocket is cut in the plate to house the bottom glass plate. A ½" step supports the glass plate and the remainder of the material below the bottom plate was removed to allow for transmission measurements.

6.3.2 Constraints

One of the objectives of this device is to maintain a ~100 micron gap between the substrate and superstrate, within which the sample is confined. In order to achieve this constraint with adequate precision, several designs were considered. The ideal method of accomplishing this task is to custom machine and grind upper and lower glass surfaces, with the proper features that accommodate restraints in all necessary directions. With this

in mind, a design that is relatively simple was considered employing the use of two parallel 'V' grooves machined into the mating surfaces of the plates (see figure 6.5). Riding within the grooves are high precision ball bearings. The desired gap between the plates is determined by the diameter of the bearing balls, as well as the depth and opening angle of the 'V' grooves.

The key feature of this design is that, with adequate machining precision, the 'V' grooves can constrain the motion to simply one degree of freedom, resulting in the shear cell having parallel top and bottom surfaces. Unfortunately, manufacturing this design was not cost effective due to quite high manufacturing costs associated with the high precision machining of glass (~$1400 for the two plates). Seeing as the design had not yet been tested the less expensive option shown in figure 6.3 was chosen. After extensive testing and refining the choice of plate design can be revisited as the base plate can accept both designs.

In lieu of the high cost precision of machined glass plates, a simpler, but less precise option was considered, in order to prove the concept. This design takes advantage of commercially available parts of relatively low cost. Two 3" x 4" x 1/8" pieces of glass were used as the upper and lower plates with a third piece of glass (1" x 4" x ~3/16") inserted between the two (see figure 6.3). The middle piece which serves as the lower surface for the sample was epoxied to the bottom glass plate which is held in the base plate. The top glass plate serves as the sample superstrate. The gap is produced because of the difference in the height of the middle glass spacer block and the diameter of the ball bearings. Two aluminum ball bearing retainers were made to keep the balls in line next to the middle glass plate. Unknown factors such as the durability of the glass plates

under the motion of the ball bearings and any other unforeseen design flaws could be tested on this less expensive version before investing in the precision machined glass plates.

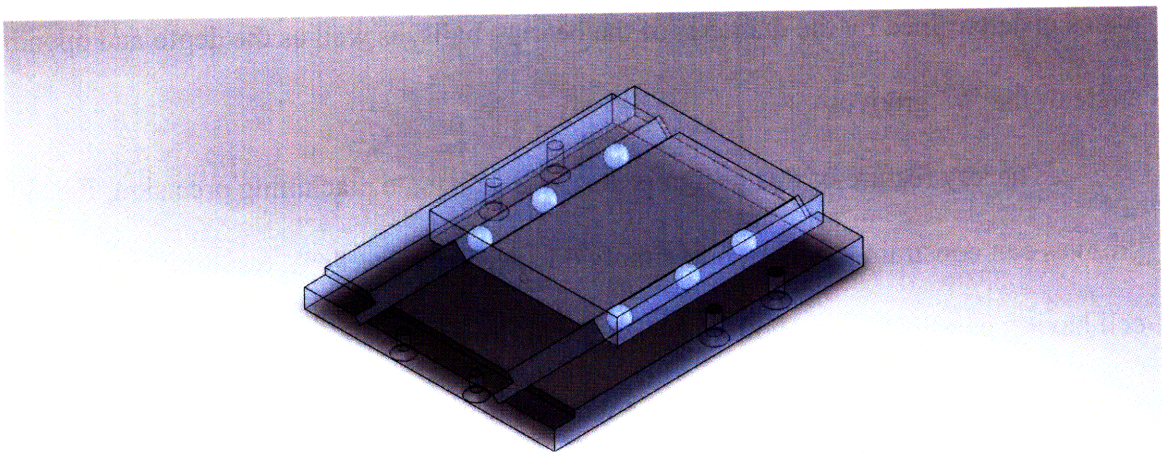

Figure 6.5: The precision machined glass plate concept – This higher precision device made from glass plates ground with two parallel 'V' channels was regarded as too expensive for the first version of the shear rheometer. A lower cost glass plate version was adopted for the final design.

It is necessary to apply a downward force upon the top slide, such that the top plate is always pressed against the ball bearings. This assures that the spacing between the superstrate and the substrate is always constant. This can be achieved in many ways, most simply by placing a large weight on top of the upper slide. However, the use of the optical microscope to observe the reflected light poses a problem as the weight may interfere with microscope objective lens or parts of the microscope. Because of this it was necessary to include features within the device that would apply the necessary downward force, while adding negligible drag to the system, such that force measurements would not be effected by the addition of this system, i.e. the system would not introduce drag into the mechanism. A roller-rocker arm system was manufactured which, with the assistance of torsion springs, applied a downward force to the upper glass

plate (see figure 6.6). The rocker arm is rigidly mounted to an addition to the base plate, and features a low friction roller bearing at the end which rests on the surface of the plate. 2.5 Newtons of downward force is applied at the end of the arm through the use of a torsion spring. One roller-rocker arm assembly is used per side for a total of 5N of downward force.

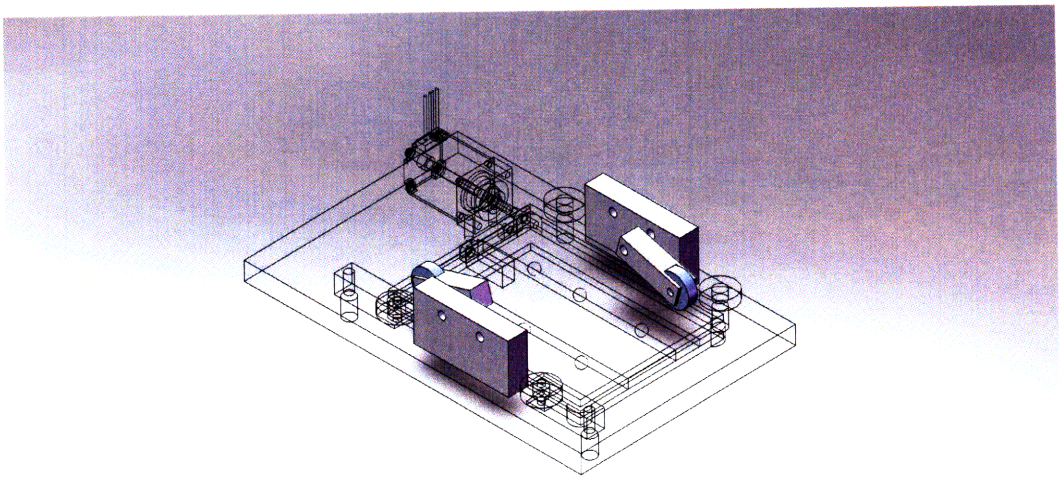

Figure 6.6: The roller-rocker arm assembly – In order to keep the top plate in contact with the ball bearings and assure a constant sample thickness, a roller-rocker assembly was implemented on the shear rheometer. Roller bearings at the end of the arms contact the glass plate and allow the glass plate to slide beneath them. Torsion springs (not shown) force the arms into constant contact with the top glass plate.

Since the 'V' groove design was not chosen initially due to high cost of manufacture, an additional restraint was necessary to limit the motion to the desired one degree of freedom (linear motion). The simplest way to address this problem was to use the spring loaded roller-rocker arm approach, very similar to that used for applying the normal force discussed earlier. One side of the device features two roller bearings, rigidly mounted to the base plate, acting as a limiting device. The other side hosts two torsion-spring mounted roller-rocker arms, exactly as in the vertical restraint system, but mounted directly to the base plate, and acting in the plane of the base plate/glass plates. The spring loaded roller-rocker arms were used instead of an additional rigidly mounted

ball bearing, in order to properly constrain the motion, and eliminate any possibility of binding of the system. The spring loaded arms also allow for easy displacement, in order for the user to easily install/remove the sample and glass slides, without any disassembly of the device.

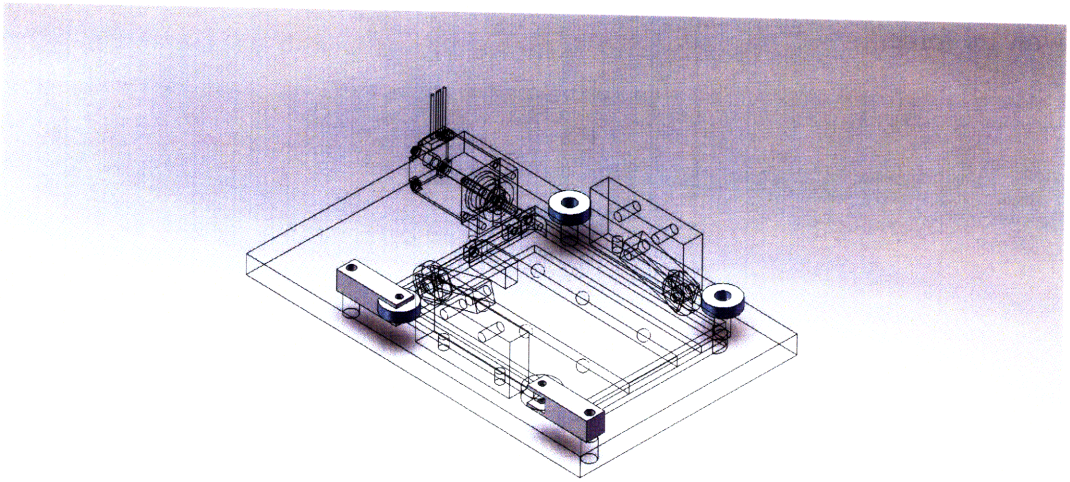

Figure 6.7: The horizontal constraint system – In order to limit the motion of the top plate to only one direction, a system of fixed roller bearings and torsion-spring roller-rocker arms were installed. The bearings in this system rested against the edge of the top glass plate.

6.3.3 Actuation

The desired increment of motion was quite small, preferably less than 10 microns. A suitable stepper motor driven linear actuator was sourced from Haydon Switch & Instrument (Waterbury, CT). Selecting the 21000 Series Size 'B' stepper motor (part number 21H4AB-5V-354), a step size of 5 microns was available for reasonable cost ($200). An electronic chopper drive control unit was also purchased for control of the linear actuator ($200).

Other actuation devices were considered, such as simple servo motors, but these did not provide the necessary amount of precision for this application. The selected linear actuator provides very precise motion, with the only degree of freedom being the

extension/retraction along the axis of the unit, and negligible deflection in any other direction. Most common servo motors available output simply rotational motion, resulting in an additional complex linkage to be designed into the device to produce the desired linear motion. The use of the thin-beam load cell would have also been complicated had an alternative actuation device been chosen, due to the fact that the relative motion of each side of the beam must be parallel to produce the desired bending effect.

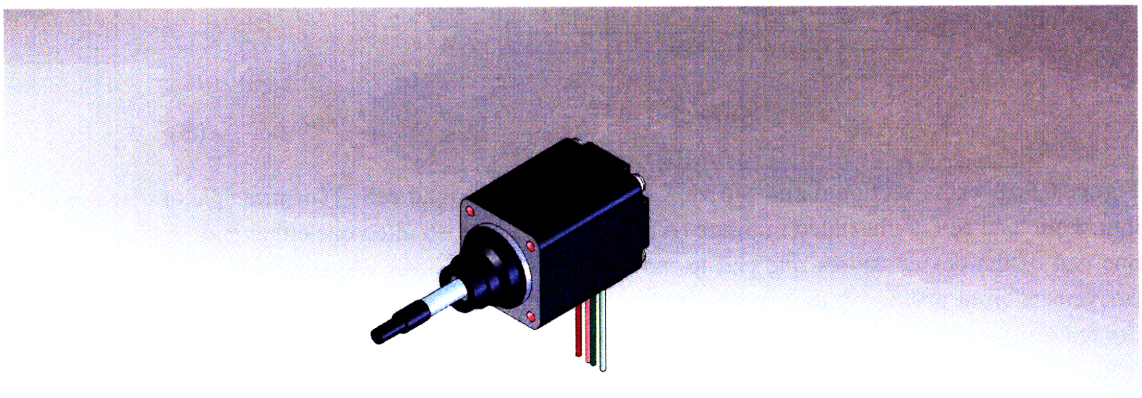

Figure 6.8: The linear actuator – A Haydon Switch and Instrument company linear stepper motor was chosen for the actuation due to its small step size and linear (rather than rotary) motion. The thin rod is extended and retracted from the motor when power is applied through the control circuitry. The stepper motor produces rotary motion but internal gearing translates this rotary motion into linear movement of the metal rod.

6.3.4 Instrumentation

Measuring and recording the force versus displacement of the apparatus is necessarily a high-precision task, as the estimated forces are on the order of 1 to 2 Newtons in magnitude. With this fact in mind, the available options for force measurement were somewhat limited. The most plausible options were to either

implement an inline tensile/compressive load cell or a thin-beam style load cell. The latter was chosen due to the reasonable price, comparative to the much more expensive inline load cell. The thin beam design is well suited for small force measurements, and was relatively easy to implement into the design of the device (see figure 6.10).

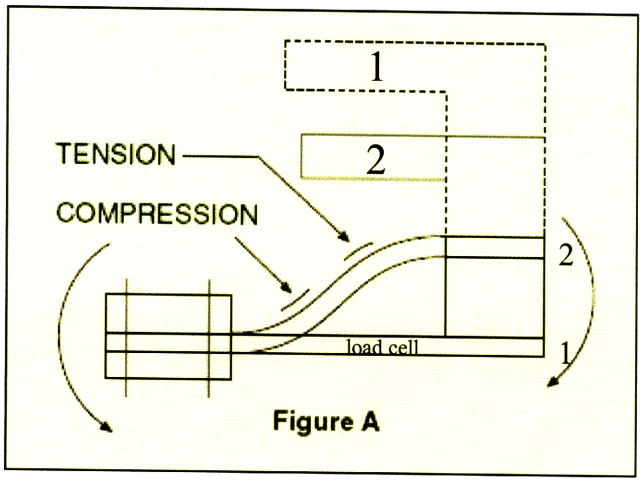

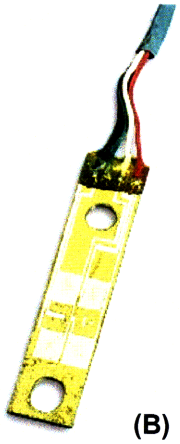

(B)

Figure 6.9: A cross-sectional and top view of the thin beam load cell – The principle of operation of the thin beam load cell is illustrated in figure (A) where the device is bolted one either end. A force applied to one end of the device causes one end to move relative to the other and produces bending in the gauge (movement from position 1 to position 2). This affects a change in the resistivity of the lithographically printed resistors on the top of the device (the patterning on top of the load cell in figure B). Two of the four leads connected to the device apply a voltage across the resistors arranged in a Wheatstone bridge. The remaining two wires are used to measure the output of the gauge. The voltage difference between these two leads is proportional to the force applied to the gauge.

The thin-beam load cell works on the principle of beam bending. The tensile and compressive strains associated with such deformations cause a change in resistance of one or more microfabricated thin-film resistors which are arranged in a Wheatstone bridge. The differential voltage between two parts of the bridge are measured which corresponds to the strain on the beam. Since the stiffness of the beam is known, the load can be measured (see figure 6.10).

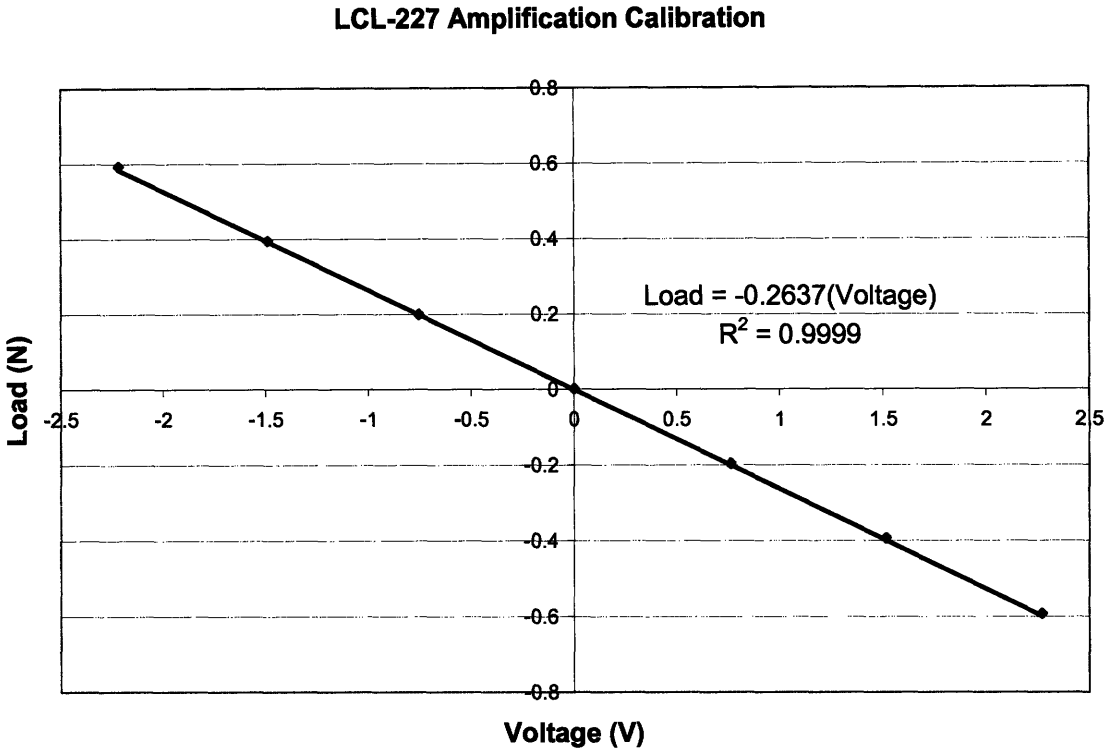

Figure 6.10: Calibration curve for the thin beam load cell – Weights of known mass were hung from the thin beam load cell such that force of gravity put the load cell into bending. The mass of the weight (and thus the force applied to the beam) was changed. A linear regression was performed on the data to obtain the calibration curve.

For proper operation, it was necessary to attach an aluminum block to the upper plate. This provided the necessary rigidity, as well as the sharp edge, to create the beam bending effect in the thin beam load cell. A thin beam load cell from Omega Engineering was purchased having a maximum load of 2.2 Newtons.

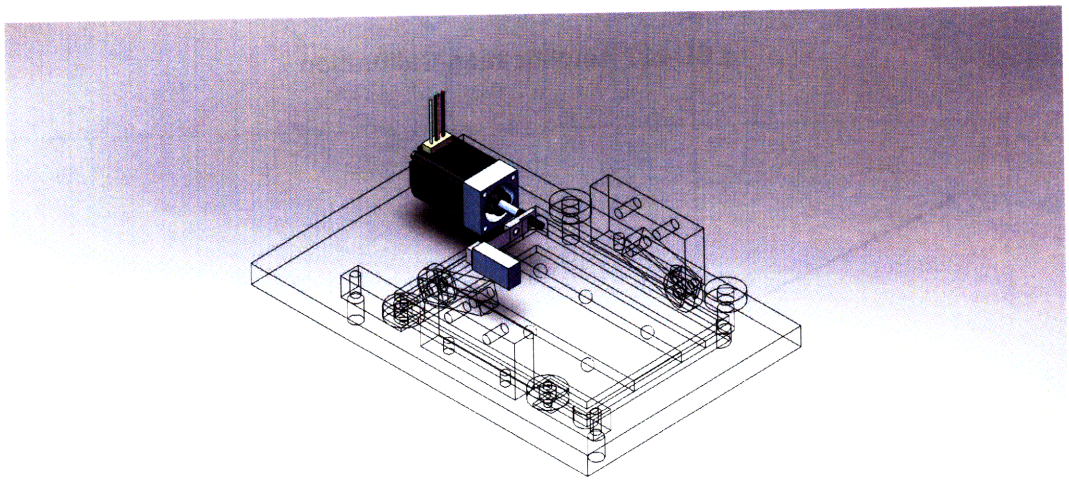

Figure 6.11: The linear actuator and thin beam load cell assembly – A stepper motor with a 5 micron step size was chosen for the actuation system because of its small step size and linear motion. The thin beam load cell was attached to the end of the linear actuator via a threaded adaptor. The load cell was then bolted to the adaptor on one end and to an aluminum block epoxied to the top glass plate on the other.

Operation of the strain gauge involves measuring the voltage output of the load cell after applying five volts to the device. The strain gauge produces approximately 1 millivolt of response per 0.24 Newtons of applied force. This small voltage must be amplified before recording with a data acquisition device since the signal-to-noise ratio when converting the analog signal to a digital equivalent for this small voltage is quite poor. Because of this, a Vishay Measurements Group 2120A strain gauge amplifier was used to amplify the signal 2000 times. An account of the operation of the strain gauge amplifier is provided in the experimental methods chapter (chapter 2).

The positional data are derived from an encoder on the end of the linear actuator. A US Digital (Vancouver, WA) E4P encoder with 200 counts per revolution (cpr) was chosen because of the ease of use with the linear actuator. The 200 cpr allowed 1:1 ratio between motor and encoder pulses. When power (5V) was applied to the encoder, every time the motor would incrementally move, a digital pulse would be sent from the encoder which was received by the data acquisition system (DAQ).

The National Instruments USB-6009 DAQ was used to monitor and record both the linear travel of the device as well as the load measured by the load cell. The data from both the load cell and encoder was continuously recorded through a National Instruments Labview control program running on a laptop. The amount of shear could be determined from the knowledge of distance traveled by the top plate and the thickness of the gap between the superstrate and substrate. The rate of shear was also calculated based on an internal timer in the program monitoring the rate at which the top plate was moving. The speed of the top plate could be set by adjusting a potentiometer in the electronic drive circuitry for the motor.

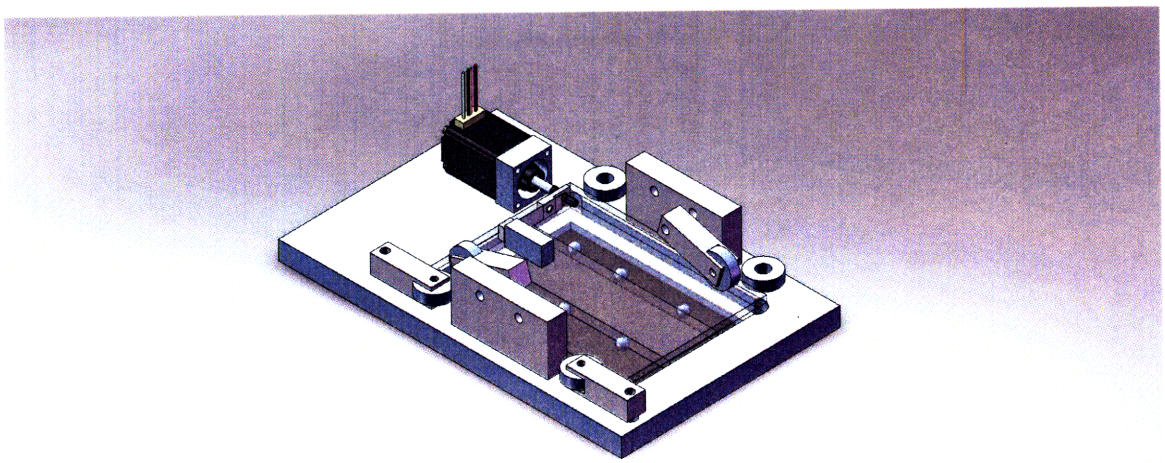

Figure 6.12: The full CAD model of the linear shear rheometer – The final CAD design is presented here complete with vertical and horizontal constraints. The motor in the upper left supplies the driving force which is channeled through the load cell and is used for moving the top glass plate relative to the fixed bottom glass assembly. Ball and roller bearings provide low friction movement.

6.4 The completed shear rheometer system

Figures 6.13 and 6.14 show the completed shear rheometer where motion is constrained to occur in only one direction and the color of the polymer film can be measured either in reflection or transmission. The distance between the top and bottom plates was measured to be 150 microns by changing the focal plane of an optical

microscope. A National Instruments data acquisition system installed on a laptop takes readings from the encoder on the motor and translates them into the linear distance that the upper plate has traveled as well as recording the amplified signal of the load cell.

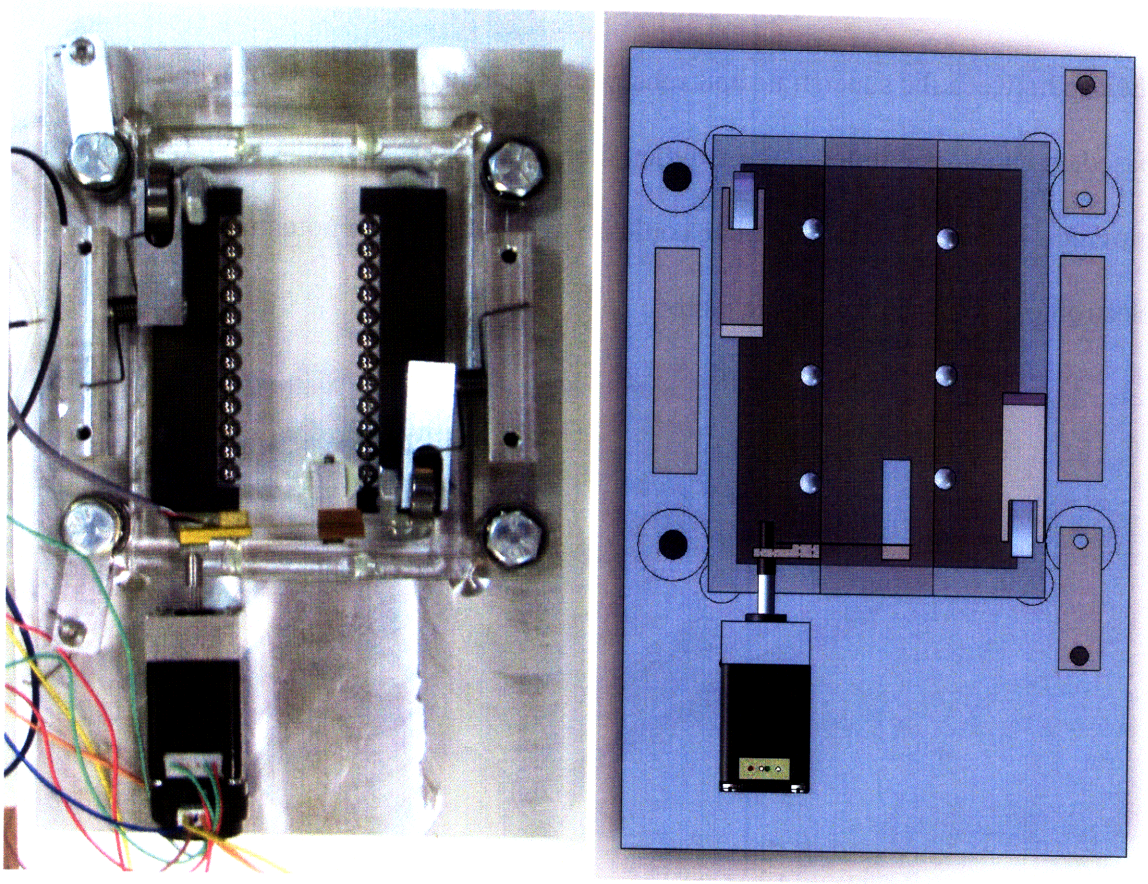

Figure 6.13: A top view comparison of the shear rheometer and the CAD model – The CAD model allowed the physical design of the device to be done on a computer where the packaging and layout of the device could be rapidly changed.

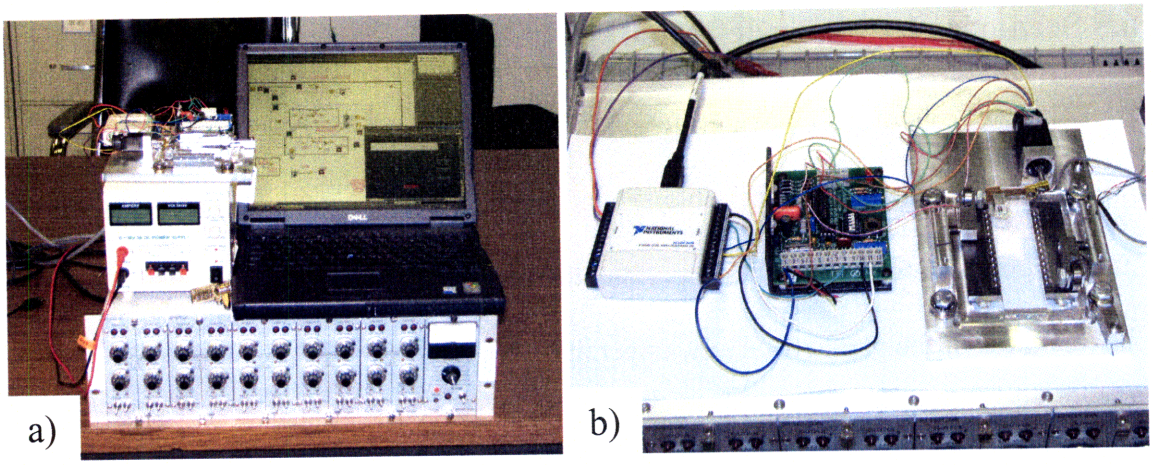

Figure 6.14: The linear shear rheometer with data acquisition system – (a) A laptop running National Instruments Labview software is connected to the data acquisition device (leftmost device in (b)) via a USB cable. A direct current power supply (left of laptop computer in (a)) powers the motor control electronics (middle device in (b)). A strain gauge amplifier (below laptop and power supply in (a)) conditions the output signal so that it can be accurately read by the DAQ. Only one of the ten strain gauge amplifier channels on this piece of equipment is used. The shear rheometer is pictured on the right in (b).

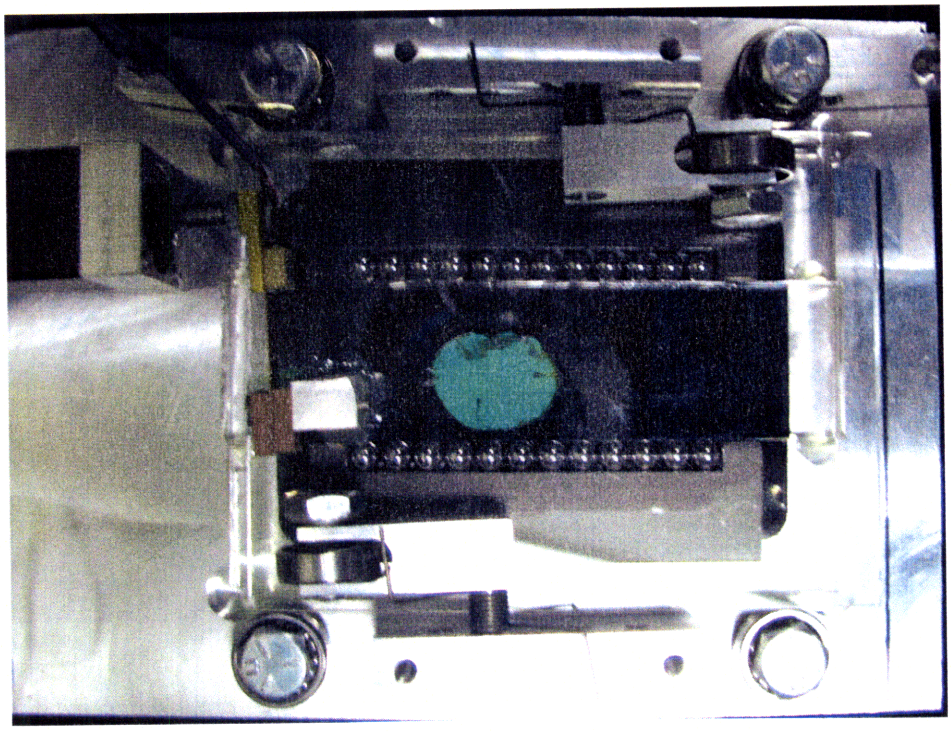

Figure 6.15: The linear shear rheometer with a photonic BCP sample – A 25% PS-PMMA (290k-360k) sample dissolved in toluene is sandwiched between the glass plates in the device. When the sample was deformed at a low strain rate the reflected color did not change. The sample did change color momentarily with high strain-rate, low-strain movements.

6.5 Scenarios for shear deformation

When studying the behavior of photonic block copolymers, a wide variety of experimental variables are accessible. Device-dependent parameters include the total strain applied to the sample, the strain rate, the type of strain (linear or cyclic linear), and the thickness of the gap between the upper and lower substrate. Tunable sample parameters include the types and molecular weights of the polymers used in the copolymer, the amount of crosslinking (if any), and the amount and selectivity of the solvent or plasticizer used to swell the copolymer. For simplicity, only the total strain and the strain rate were varied in the initial experiments.

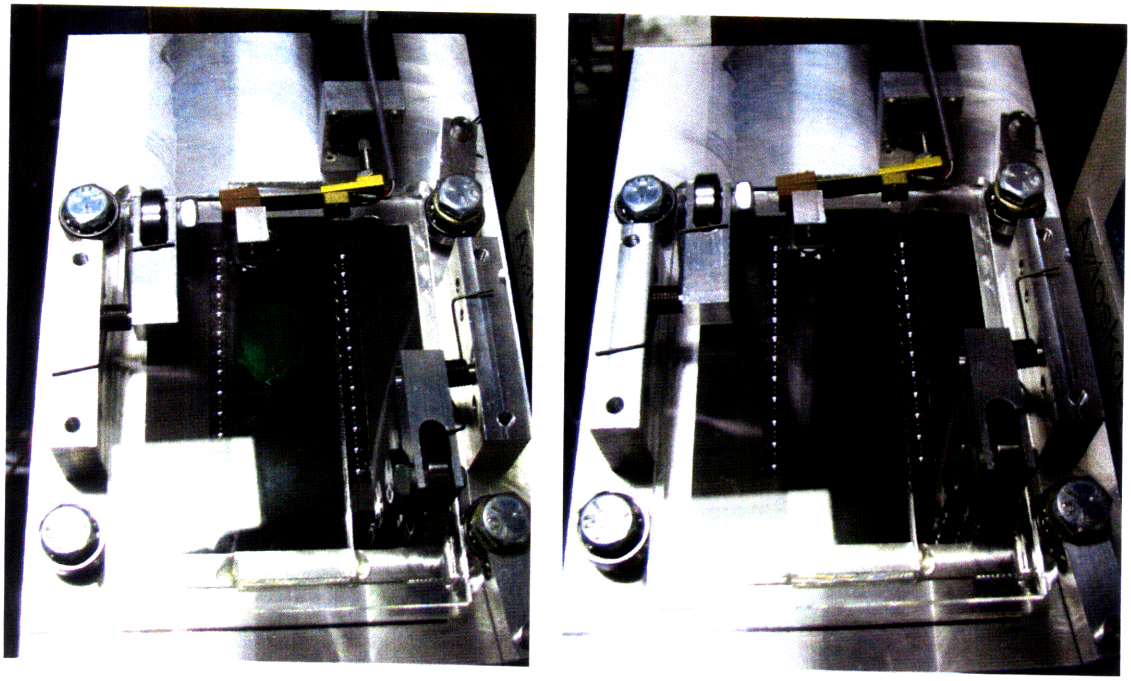

Figure 6.16: High strain-rate deformation of a photonic BCP gel – A 25% PS-PMMA (290k-360k) in toluene is sandwiched between the glass plates in the device. High strain and high strain-rate deformation caused the color to disappear from the sample. An alignment of the chains parallel to the direction of the shear is thought to be the cause of this color change.

A photonic block copolymer (25% PS-PMMA 290k-360k in toluene) was sandwiched between the two glass plates in the device which were separated by a 150

micron gap and strained at a rate of 0.1 s^{-1} producing no change in the green color of the sample (see figure 6.15). To check that shear induced color was present in the sample as had been seen with previous experiments, the top plate was slightly tapped by hand such that it moved towards the motor. This blue-shifted the reflected color turning the sample a green-blue color. When the top plate was tapped in the opposite direction the sample turned orange. When higher strain rates were applied (10 s^{-1}), the sample changed from reflecting to transparent. After several minutes the sample regained color.

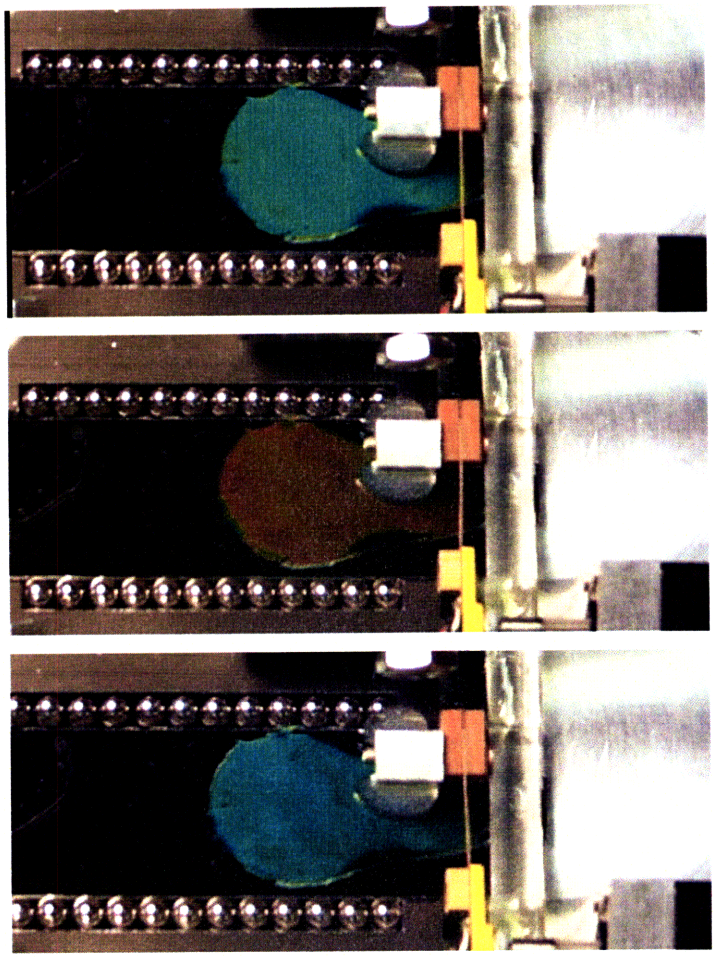

Figure 6.17: Cyclic shear of a block copolymer photonic gel – A 25% PS-PMMA (290k-360k) in toluene is sandwiched between the glass plates in the device. Cyclic shear (1 Hz) was used to observe transient color change in the photonic gel. A strain rate of 3.3 s^{-1} produced a change from green (a) to red (b) while reverse motion produced a slight blue-shift from the original sample color.

The transient color change observed by tapping the glass plates was investigated using cyclic, linear shear. Under these experimental conditions the top plate would be moved back and forth repeatedly at the same rate. The amount of shear was controlled through the Labview computer interface. As with the previous experiments, strain rates below ~0.1 s^{-1} produced no color change while extremely high shear rates (>10 s^{-1}) produced a change from reflecting to non-reflecting behavior. Intermediate strain rates, however, produced a change in color from green to red with forward motion (away from the motor) and a slight blue shift upon reversal (see figure 6.16).

While these preliminary observations are not completely understood, it is most likely that the red shift is caused by an increase in layer spacing in the lamellae. Changing the refractive index of one layer with respect to the other (e.g. by creation of nano-scopic voids through cavitation) would serve to broaden the reflectivity peak rather than shift it to longer wavelengths and tilting the lamellae will always blue-shift the reflected wavelengths of light (if the initial observervation angle is 90° from the layer normal). Since the position of the reflectivity peak in the sample before shearing is blue-shifted if observed from any angle off of normal incidence, a majority of the lamellae are assumed to be parallel to the glass plates. Although, this assumption is complicated by the relatively large space between the plates which could contain a number of lamellar grains not oriented parallel to the plates whose reflections are masked by the light reflected from the upper layers of the sample.

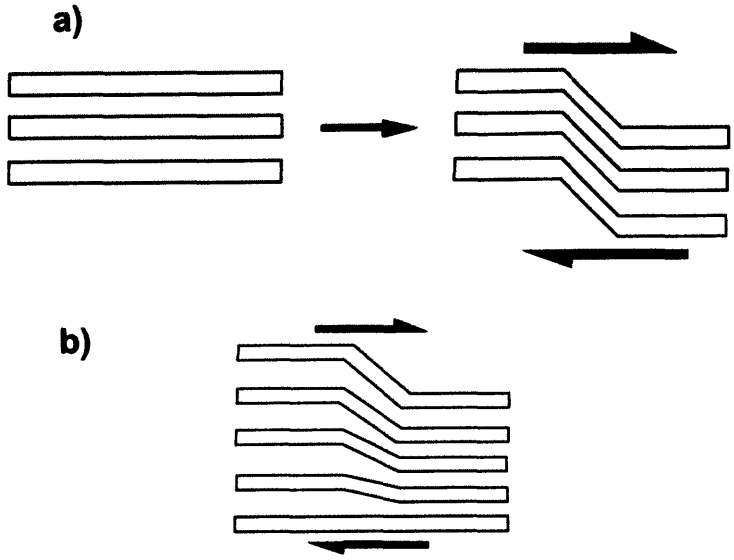

Figure 6.18: Kink band formation in a block copolymer – (a) When lamellar block polymers are sheared, kinking of the layered structure has been observed in lower molecular weight polymers under steady, rotational shear. (b) A possible explanation for the shift of the reflectivity peak to longer wavelengths could be the formation of kink bands in which the PS domains respond quickly to the applied shear while the PMMA domains, not plasticized as much by the solvent, take longer to respond. This might result in the extension of the PS domains while only bending occurs in the PMMA domains on the time scale of the experiment.

When sheared, previous experimental studies of lamellar block copolymers (largely using rotational shear) found the BCPs tend to form "kink" defects with lamellae which rotate due to applied shear.[29,30] In the sample under study, toluene is used to create the photonic gel which is slightly selective for the PS domains ($\chi_{PS\text{-}toluene}$=0.4, $\chi_{PMMA\text{-}toluene}$ =0.5).[31] A possible mechanism for this transitory color change is the stretching of the plasticized PS block when the domains try to rotate. The PMMA domains, which are not plasticized as much as the PS domains, respond slowly to the shear stress and remain initially fixed in position. For example, when the strain rate is slow, the color remains constant because the PMMA can respond to the deformation. However, at higher strain rates, the PS chains can immediately adapt while the PMMA chains are slow to respond which causes an extension of the PS domains while PMMA domains can only deform via bending (see figure 6.18b).

As discussed earlier, the use of extremely high shear rates is thought to cause an alignment of the chains parallel to the shear flow (lamellae rotate from parallel to the substrate to perpendicular). This rotation from an initially perpendicular to parallel chain orientation could explain the observed color change. The reflected wavelengths of light visible initially could be red-shifted through the sudden application of relatively high-stain shear if the chains closest to the top plate were to align parallel to the top plate (in the direction of the shear). This sudden alignment may cause a temporary expansion of underlying layers as they are pulled upwards by the rotating chains close to the top surface. This would cause a red shift in the rest of the structure while the top-most lamellae are either tilted or rotated such that they are no longer reflecting visible light. The intensity of the red reflection also seems to decrease with an increasing number of cycles suggesting that more and more chains could be aligning parallel to the shear direction with each successive cycle. Further experimentation utilizing the wide variety of variables available in the shear rheometer should be able to improve the understanding of the mechanisms of this color change.

6.6 Conclusions

A linear shear rheometer has been constructed with a fixed distance between the upper and lower plates for the application of linear shear strain. The device can be configured to apply cyclic, uni-axial shear (forward and backward motion) or continuous uni-axially shear (forward only or backward only). When high strain rates are used, it is difficult to observe a transitory change in reflected color before a large amount of shear has occurred so cyclic shear has been utilized. Fine measurements of the reflectivity are

unfortunately not possible using the microscope spectrometer because the microscope cannot focus on the sample through the thick upper glass plate of the instrument. Future improvements to the device might include a redesigned load cell. This is because the device measures load through a deflection and the distance that is measured from the encoder is not the true distance the top plate has traveled. This is compensated for by the software, but this deflection causes a phase lag when the direction of the plate is reversed in a cyclic shear test. It also dampens the response to the actuation since when a large force is applied by the motor, the beam bends and then the plate begins to move. Although preliminary color-change observations are not fully understood, the wide variety of tunable parameters available in this device should yield a more complete understanding of the behavior of high molecular-weight block polymers under shear in the future.

6.6 References

1 Holmstrom, et al., Mechanical tuning of holographic polymer-dispersed liquid crystal reflection gratings, Applied Physics Letters, 85(11), 1949-1951 (2004)

2 J.Y. Chen and L-W Chen, Photonic defect modes of cholesteric liquid crystal with spatially varying pitch, Physica B, 357, 282-289 (2005)

3 Warner, M., Terentjev, E.M., Meyer, R.B., and Mao, Y., Untwisting of a Cholesteric elastomer by a mechanical field, Pysical Review Letters, 85(11), 2320-2323 (2000)

4 Bermel, P.A., and Warner, M., Photonic band structure of highly deformable, self-assembling systems, Phys. Rev. E, 65, 10702-10706 (2002)

5 R. Zentel and G. Reckert, Liquid crystalline elastomers based on liquid crystalline side group, main chain and combined polymers, Makromol. Chem. 187, 1915-1926 (1986)

6 Masubuchi S, Akahane T, Nakao K, et al. Investigation Of Temperature-Dependence Of Pitch Of A Cholesteric Liquid-Crystal Molecular Crystals And Liquid Crystals 35 (1-2): 135-142 (1976)

7 Van de Witte P, Galan JC, Lub J Modification of the pitch of chiral nematic liquid crystals by means of photoisomerization of chiral dopants Liquid Crystals 24 (6): 819-827, (1998)

8 Edrington, A.C., Urbas, A.M., DeRege, P., Chen. C.X., Swager, T.M., Hadjichristidis, N., Xenidou, M., Fetters, L.J., Joannopoulos, J.D., Fink, Y., and Thomas, E.L., Polymer-based photonic crystals, Adv. Mat., (13)6, 421-425 (2001)

9 Fink, Y., Urbas, A.M., Bawendi, M.G. Joannopoulos, J.D. Thomas, E.L. Block copolymers as photonic bandgap materials Journal of Lightwave Technology, v 17 (11) 1963-9 (1999)

10 Urbas, A. M.; Maldovan, M.; DeRege, P.; Thomas, E. L. "Bicontinuous cubic block copolymer photonic crystals" Advanced Materials, 14, 1850-1853 (2002)

11 Deng, T., Chen, C., Honeker, C., and Thomas, E.L., Two-dimensional block copolymer photonic crystals, 44(21), 6549-6553 (2003)

12 Greenland, K.M. High-reflexion films Journal of Scientific Instruments, 23, 48-50 (1946)

13 Alfrey, T. Jr., Gurnee, E.F., and Schrenk, W.J., Physical Optics of Iridescent Multilayered Plastic Films, Polym. Eng. Sci., 9, 400-4 (1969)

14 Hebrink, T, et. al., Method for making coPEN/PMMA multilayer films, US Patent 6830713 (2004)

15 Weber, et al, Giant birefringent optics in multilayer polymer mirrors, Science, 287, 2451-2456 (2000)

16 Schrenk, W.J., Shrum, W.E., Wheatley, J.A., Elastomeric optical interference films, US Patent 4937134 (1990)

17 Urbas, A. M., Block copolymer photonic crystals, Ph.D. Thesis, Thomas group, (2003)

18 Fudouzi and Sawada, Photonic Rubber Sheets with Tunable Color by Elastic Deformation, Langmuir, 22, 1365-1368 (2006)

19 Ying, Y., Xia, J., And Foulger, S.H., Pressure tuning the optical transmission properties of photonic bandgap composites, Applied Physics Letters, 90, 071110, (2007)

20 Arsenault, A.C., Clark, T.J., Freymann, G.V., Cademartiri, L., Sapienza, R., Bertolotti, J., Vekris, E., Wong, S., Kitaev, V., Manners, I., Wang, R.Z., John, S., Wiersma, D., and Ozin, G.A., From colour fingerprinting to the control of photoluminescence in elastic photonic crystals, Nature materials, 5, 179-184, (2006)

21 Arsenault, A.C., Kitaev, V., Manners, I., Ozin, G.A., Mihi, A., and Miguez, H., Vapor swellable colloidal photonic crystals with pressure tunability, J. Mater. Chem., 15, 133-138 (2005)

22 Lawrence, J.R., Shim, G.H., Jiang, P., Han, M.G., Ying, Y., and Foulger, S.F., Dynamic tuning of photoluminescent dyes in crystalline colloidal arrays, Advanced Materials, 17, 2344-2349 (2005)

23 Lawrence, J.R., Ying, Y., Jiang, P., and Foulger, S.H., Dynamic tuning of organic lasers with colloidal crystals, Advanced Materials, 18, 300-303 (2006)

24 Cromie, MJ, Multifunctional Systems With Polymer Actuators: Mechanochromism And Peristaltic Pumping, Master's thesis, Thomas group, (2005)

25 Yoon, J.S., Block copolymer photonic crystals: towards self-assembled active optical elements, Ph.D. Thesis, Massachusetts Institute of Technology, (2006)

26 Heino Finkelmann, Sung Tae Kim, Antonio Munoz, Peter Palffy-Muhoray, and Bahman Taheri, Tunable Mirrorless Lasing in Cholesteric Liquid Crystalline Elastomers, Adv. Mater., 13(14), 1069-72 (2001)

27 Foulger, S., Jiang, P., Lattam, A., Smith, D., Ballato, J., Dausch, D., Grego, S., and Stoner, B., Photonic Crystal composites with reversible high-frequency stop band shifts, Adv. Mater., 15(9), 685-9 (2003)

28 Foulger, S., Jiang, P., Lattam, A., Smith, D., Ballatto, J., Mechanochromic response of poly(ethylene glycol) methacrylate hydrogel encapsulated crystalline colloidal arrays, Langmuir, 17, 6023-6026 (2001)

29 Polis, D.L., Smith, S.D., Terrill, N.J., Ryan, A.J., Morse, D.C., and Winey, K.I., Shear-induced lamellar rotation observed in a diblock copolymer by in situ small-angle x-ray scattering, Macromolecules, 32, 4668-4676 (1999)

30 Qiao, L. and Winey, K.I., Evolution of kink bands and tilt boundaries in block copolymers at large shear strains, Macromolecules, 33, 851-856 (2000)

31 Barton, A.F.M., CRC handbook of polymer-liquid interaction parameters and solubility parameters, CRC press, Boca Raton, FL (1990)

Chapter 7:

Design Optimization of a Liquid-Filled, Elastomeric Lens with the Finite-Element Method

While previous chapters have focused on the tunability of one-dimensional reflectors, the focus of the current chapter is on tuning the refractive components of optical elements, and is specifically aimed at improving the properties of the class of tunable lenses known as liquid-filled lenses. Man-made, fixed focal-length lenses have been around for many thousands of years. These fixed focal-length components have invariant properties because of their fixed indices of refraction and absorption coefficients and their static surface curvature and physical dimensions. In contrast to these traditional optical elements, *adaptive* elements are those that change their properties because of a stimulus that leads to a change in shape, thickness, and/or index of

refraction/absorption. These changes cause the elements to vary their optical properties (e.g. focal length, color, reflectance, etc.) The goal of this chapter is to model the behavior of an adaptive, liquid-filled lens to improve its performance by illustrating key parameters that control the shape of the lens (and thus its aberrations). Recent studies have pointed out the need for such work for the commercialization of this type of lens.[1,2]

7.1 Introduction

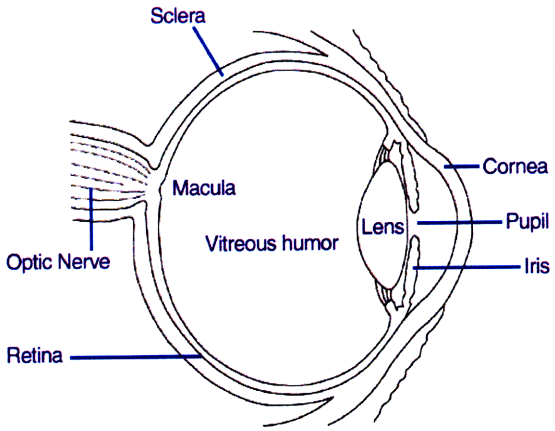

Figure 7.1: A diagram of the human eye – Light enters the eye and is refracted at the air/cornea interface. After passing through the pupil, the light is again refracted by the lens (which performs fine tuning of the focus by the modification of its shape), travels through the vitreous humor and forms an image on the retina where the information is collected and sent to the brain via the optic nerve. (Image from http://www.nei.nih.gov/health/eyediagram/eyeimages1.asp)

Humans have the ability to deform the lenses in our eyes which we use to focus on objects at different distances. The "crystalline lens," a small proteinaceous disk which resides behind the iris, fine tunes the focus of the eye when it is compressed or stretched (increasing or reducing its curvature) thus moving the focal plane closer or further away.[3] Optics of the human (Fig. 7.1 and 7.2a) and the bird (Fig. 7.2c) eye are quite similar and provide a model for a light-weight, tunable-focal-length, rapid imaging system. In the

human and bird eye, light passes through the cornea is refracted due to the change in index of refraction between air and the cornea and its surrounding fluids ($\Delta n \sim 0.33$). This light then passes through the pupil and is refracted again at the lens ($\Delta n \sim 0.05$ between the lens periphery and surrounding fluid), which has a static, spherical gradient index profile ($n_{center} - n_{periphery} \sim 0.02$), travels through the vitreous humor and finally is imaged on the retina.[3,4] The eye changes focal length (accommodates) by changing the shape of the lens which is deformed by the contraction of the ciliary muscles surrounding the lens. In humans, the refractive power of the cornea is about 2/3 of the total power provided by the cornea and lens together.

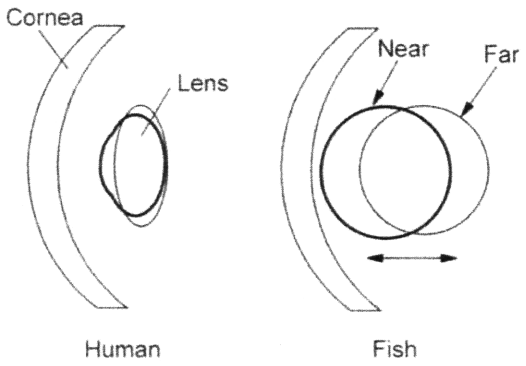

Figure 7.2: Accommodative imaging processes in humans and fish – Humans change the focal point of their eyes by squeezing an elastic lens to cause a change in curvature. Fish accommodate by moving their entire lens rather than using a mechanical deformation (adapted from reference 4).

7.2 Synthetic, tunable optics

The first tunable optical devices appeared in the late 19th century and are examples of liquid filled lenses and mirrors[5] (see figure 7.3). Later, devices produced for wavefront correction in astronomical telescopes and radar systems used sophisticated sensors and actuators to perfect an image that was distorted by atmospheric turbulence.[3] For example, reflecting telescopes use actuators that deform the mirror in different areas

to correct for the effect of atmospheric turbulence on the image.[6]

E. C. OHMART.
DEVICE FOR REFLECTING AND REFRACTING RADIANT ENERGY.
No. 504,890. Patented Sept. 12, 1893.

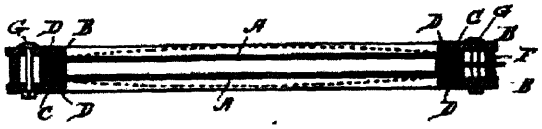

Figure 7.3: An early example of a dynamic lens/mirror from 1893 - A gas or fluid was pumped in or out of the cavity between the top and bottom surfaces to change their curvature and thus the focal length. The plates (labeled A in the figure) were either transparent giving a tunable lens or reflective giving a tunable mirror.

The interest in tunable optics was not limited to wavefront correction for mirrors as tunable lenses were first investigated around the same time. These lenses posses the unique ability to change their focal length by varying the curvature or index of refraction of the lens. The focal-length equation gives insight as to how each variable controls the focal length of the lens. The terms of the equation are: f, the focal length of the lens; n_{lens} and n_{air}, the indices of the lens and the air; and R_1 and R_2, the radii of curvature of the front and back lens surfaces.

$$1/f = (n_{lens} - n_{air})(1/R_1 - 1/R_2) \tag{7.1}$$

Technologies such as electrostriction[7], electrowetting[8,9,10,11,12,13], and the switching of liquid crystals[14,15,16,17,18,19,26] have been used to make tunable lenses and are attractive because the lens properties are under direct electronic control. Electrostriction-based lenses have been demonstrated, but very high electric fields (>1 kV/m) must be applied for them to be effective. Electrowetting lenses work by changing the shape of the meniscus between two immiscible liquids by applying a voltage between electrodes contained in the device (see figure 7.4). These devices have found commercial application in lenses for cell-phone cameras[20] and are the only commercially available

tunable lenses at this point in time. Liquid crystals have also been used to create dynamic focal length lenses but have not found widespread use or commercial applications. Tunable microlens arrays have also been demonstrated with electrooptical[21,22] or electrowetting[23,24,25] technologies. Although not directly electrically actuated, another category of tunable lenses, known as liquid-filled lenses, offer additional tunable parameters.

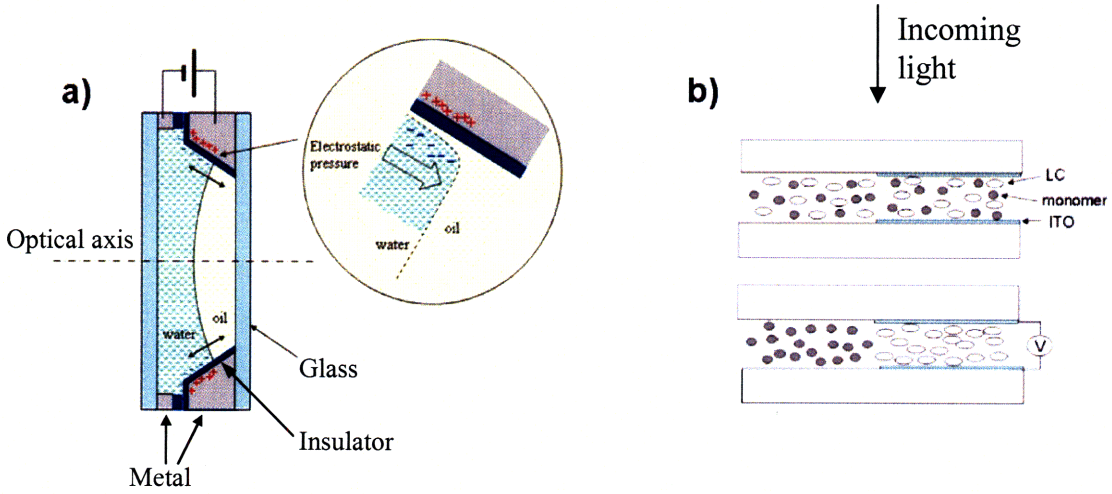

Figure 7.4: A tunable electrowetting lens design – a) When a voltage is applied to the electrodes, the contact angle of the water is changed. The other liquid is immiscible with water, but has the same density permitting the lens to be used in any orientation. b) A cross section of a liquid-crystal lens. The application of an electric field causes a redistribution of the liquid-crystal mesogens and monomer inside the cell. This creates a gradient-index lens. (Image a) adapted from Varioptic Corp., www.varioptic.com, image b) from reference 26.)

Electrostrictive, electrowetting, and liquid-crystal lenses all change only the index of refraction or the curvature of the lens to affect a change in focal length whereas liquid-filled lens designs have the ability to change both parameters giving greater tunability. The most common configuration for these liquid-filled lenses is a flexible membrane that is deformed by hydrostatic pressure to create the change in curvature[27,28,29,30] although an annular force on a membrane (much like the role of the ciliary muscles in the human eye) has also been used.[31] The work described in the rest of the chapter will be devoted to

improving the performance through creating a deformed lens shape to reduce spherical aberrations. This task will be undertaken by the modeling of the lens through the use of the finite-element method.

7.3 Modeling and optimization of a liquid filled lens

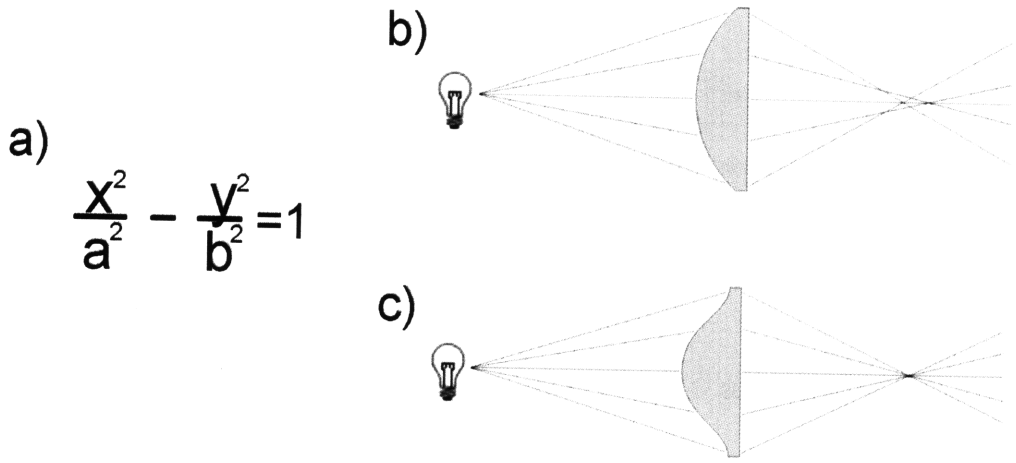

Figure 7.5: The equation for a hyperbola and a single lens with a hyperbolic surface profile in cross section - a) The equation is given physical relevance when a^2 is replaced by the index of refraction of the lens material and b^2 is the index of air. The higher the index of the lens, the flatter the lens should be in order to eliminate spherical aberration. (b) With a spherical surface, an inherent aberration causes light at the periphery to be refracted more than at the center of the lens. This leads to a reduction in resolution compared to the asphere. (c) With an aspheric lens, light originating from a point is focused back to a point. An asphere is a lens with a non-spherical refracting surface that eliminates spherical aberration.

Common optical lenses have spherical surfaces due to the nature of the production process (grinding). The spherical surface works well for focusing rays incident near the center of the lens (paraxial rays), but as the angle of the incident ray increases with respect to the local surface normal, aberration becomes more and more apparent (see figure 7.5c). This defect is known as spherical aberration and can be corrected by changing the shape of the refracting surface. The same is true of a liquid-filled lens which has one or more internal surfaces that can be distorted by changing the pressure of the liquid inside the lens.

In the present work, a transparent rubber (e.g. poly(dimethyl siloxane)) is used as the membrane material and when the liquid is pressurized, the rubber adopts a curved profile. This profile is very nearly spherical when measured more than twice the film thickness away from the edge of the lens[28] (approximately 100 – 200 μm). In order further reduce the spherical aberration, several methods are studied including changing the thickness, refractive index, or modulus profile of the lens material.

Spherical aberration can be eliminated from a single lens element by ensuring that all parts of a spherical wavefront originating from one point arrive at the same time when focused at another point (see figure 7.5b). Another way of saying this is that the optical path length (OPL) for all rays must be equivalent (the optical path length is the index of refraction multiplied by the distance traveled in that medium). For a single lens element, the equation of the cross section of the perfect aspheric surface is that of a hyperbola (figure 7.5a).[3]

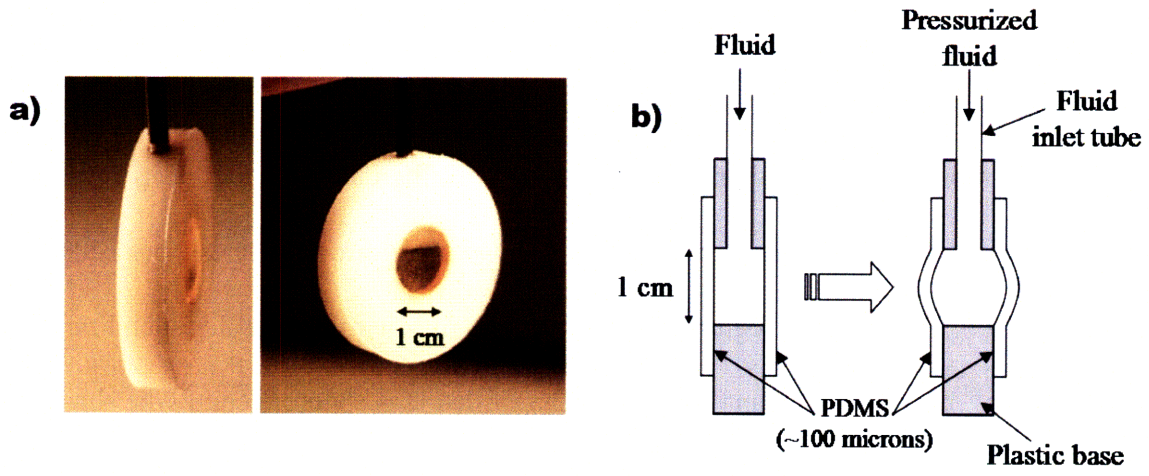

Figure 7.6: A prototype fluidic lens – a) The thin PDMS membranes are glued to the white plastic base. The metal tube provides the means for pressurizing or depressurizing the assembly. A high index liquid (Santolight SL-5267 n = 1.67) is shown filling the cavity. b) A cross-sectional schematic of the operation of a liquid filled lens. Increasing the pressure of the fluid increases the curvature of the membrane and reduces the focal length.

Because the elastomeric lens material is very thin in a liquid filled lens (~100 microns thick, where the lens is 1 cm in diameter - see figure 7.6), changing the refractive index profile to affect spherical aberration would be difficult due to the high values of the index of refraction needed. Controlling the shape of the liquid filled lens is a more readily achievable goal. In this study, the effect of changing the film modulus, the thickness, and the amount of pre-strain in the lens membrane, as well as looking at the effect of gradients in the elastic modulus will be investigated.

a)

$$z = \frac{w}{4T}(a^2 - r^2)$$

w = fluid pressure,
T = membrane tension,
a = radius of the lens,
r = radial variable

b)

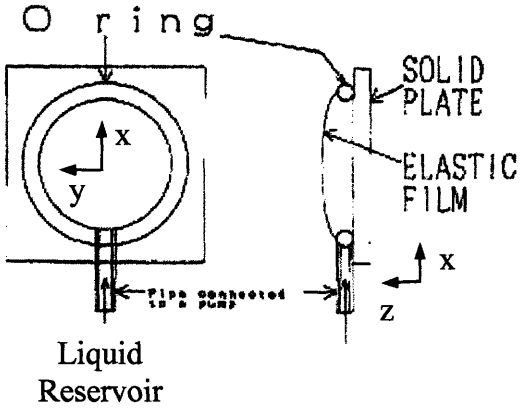

Figure 7.7: An analytical expression of the cross section of a liquid filled lens and a depiction of the apparatus - a) The analytical expression derived by Sugiura and Morita to describe the displacement of a liquid lens membrane with respect to the amount of tension and pressure applied to the membrane. b) The experimental setup used by the same authors. (adapted from reference 27)

To improve the optical properties of the liquid filled lens a model of its inflation behavior must first be constructed. The uniform loading of circular plates[32] has been studied for quite some time beginning with the work of scientific notables such Prantl[33] and Poisson[34] and is directly analogous to a fluid filled lens. More recently the shape taken by the flexible membrane of a liquid filled lens was calculated by Sugiura and Morita[27] and further elucidated by Rawicz and Mikhailenko[35] who have found the surface profile to be approximated by a parabaloid. However, this calculation assumes a simply supported boundary, rather than the fixed boundary conditions present in the liquid lens

system currently under study. Reichelt and Zappe devised a spherically corrected liquid filled lens by using several liquid filled membranes and two different liquids and assumed a spherical deformation shape for the membranes in their device. Although this produced a lens unit that was corrected for spherical aberration, multiple liquid-filled lenses had to be used. In the current study, a reduction of spherical aberration is sought through ensuring that the lens membrane deforms in a manner that eliminates spherical aberration through the production of desirable aspherical surfaces.

7.4 Finite-element analysis of a liquid filled lens

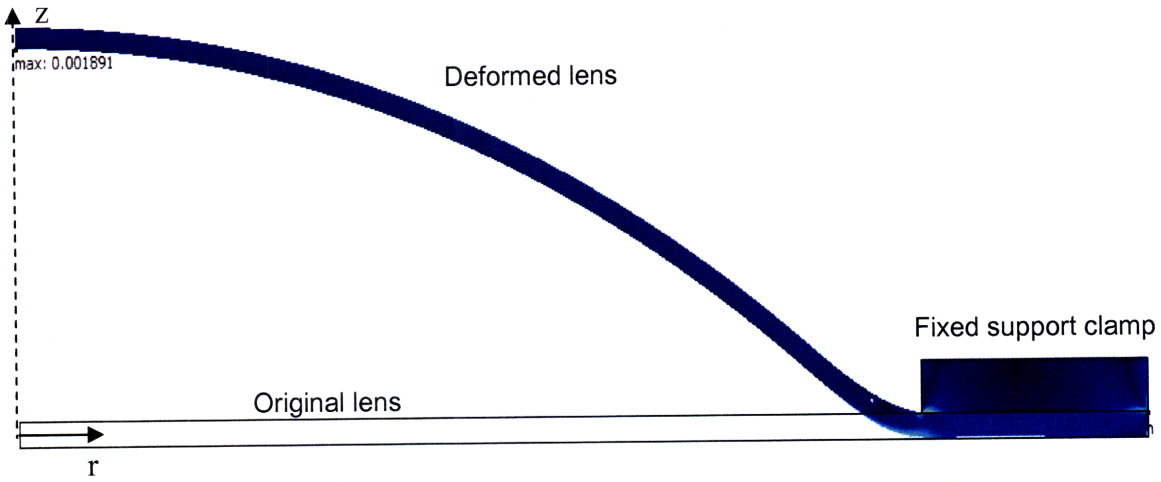

Figure 7.8: An axi-symmetric finite element model of a liquid filled lens - When properly configured, finite element modeling can predict what shape the lens membrane will take on under different conditions. The computation was simplified through the use of the axial symmetry (z-axis) of the lens through which only half the cross section needs to be modeled. A uniform pressure (1 psi) is applied to the bottom of this lens membrane and it deforms from its original shape (black outline). The rectangular shape on top of the lens membrane on the right is the cross section of the aluminum washer.

A finite-element model of a liquid filled-lens membrane was constructed using COMSOL Multiphysics with an axi-symmetric framework to minimize the computation time by taking advantage of the symmetries present in the lens (see figure 7.8). A hyperelastic material model was chosen and materials properties for PDMS and

aluminum were entered into the model. This model was then checked against experimental lens test data provided through collaboration with Rockwell Scientific (now Teledyne).

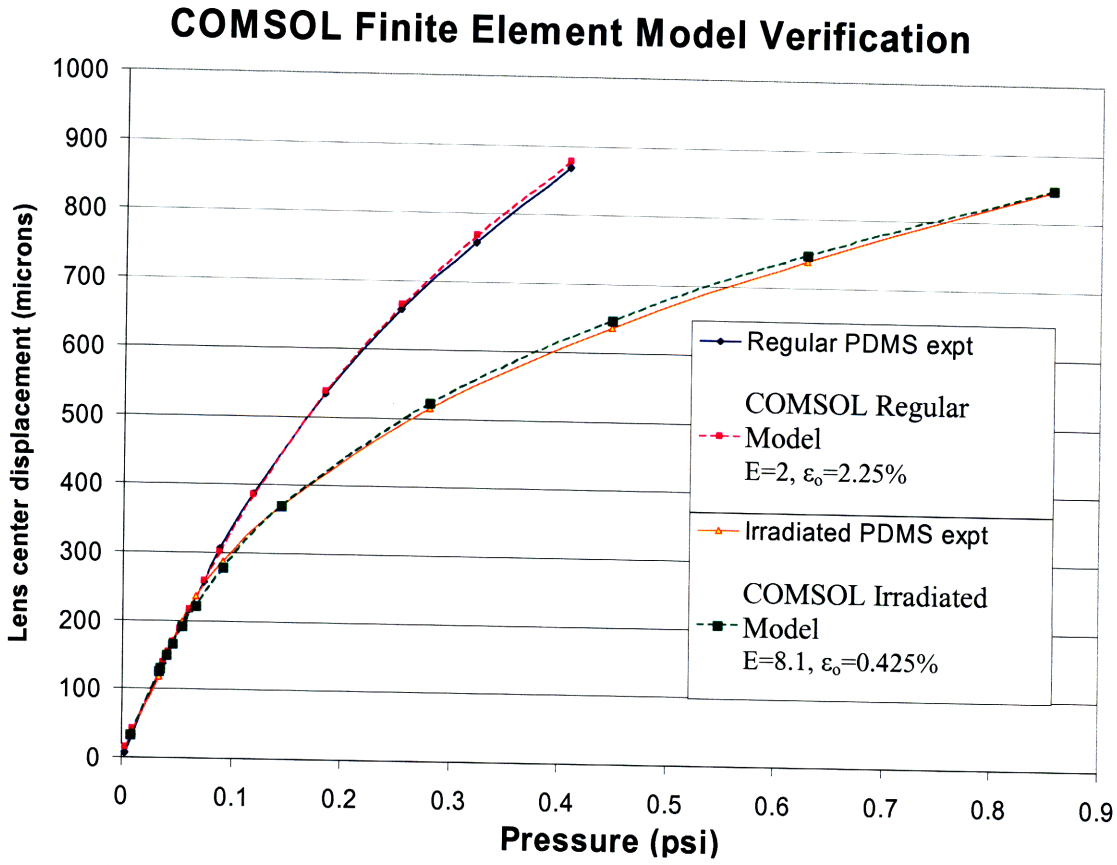

Figure 7.9: Verification of the finite element model – Displacement data for two different lenses was provided by the Rockwell Corporation which was used to check the accuracy of the finite element model. The model faithfully predicted the displacement of the center of the lenses under various inflation pressures. Rockwell produced two lenses, both where made from Sylgard 184 (PDMS) which had been cured at 40°C but one of the lenses had undergone a radiation crosslinking procedure which increased the modulus but decreased the residual tensile strain (ε_o) in the membrane.

After the model was validated, the various factors that might improve the imaging performance of the lens by reducing the amount of spherical aberration were studied. The surface curvature needed to eliminate spherical aberration is that of a hyperboloid (a conic section) whose exact profile is determined by the refractive indices of the media the ray traverses (e.g. air and glass)[3] (see figure 7.5.) For a lens inflated with a given pressure, a hyperbola was fit to the finite-element displacement data (see figure 7.10). In

this case, the hyperbolic form was expressed through the equation for a conic section in cylindrical coordinates found below where z(r) is the vertical displacement of the membrane for a given radial position, r is the radial position, R is the "initial" radius of the hyperbola, and K (kappa) is the negative square of the eccentricity of the hyperbola ($-\varepsilon^2$).

$$z(r) = \frac{r^2 / R}{1 + \sqrt{1 - (1+K)(r/R)^2}} \tag{7.2}$$

The optimum surface curvature is found by setting the eccentricity of the hyperbola equal to the index of refraction of the lens as dictated by geometric optics.[3] The variable R in the above equation is the only unknown and it is adjusted until the minimum error solution is found (see figure 7.10) for a given inflation pressure. The numerical value for the fitting error is retained as a measure of 'goodness of fit' between various computational trials.

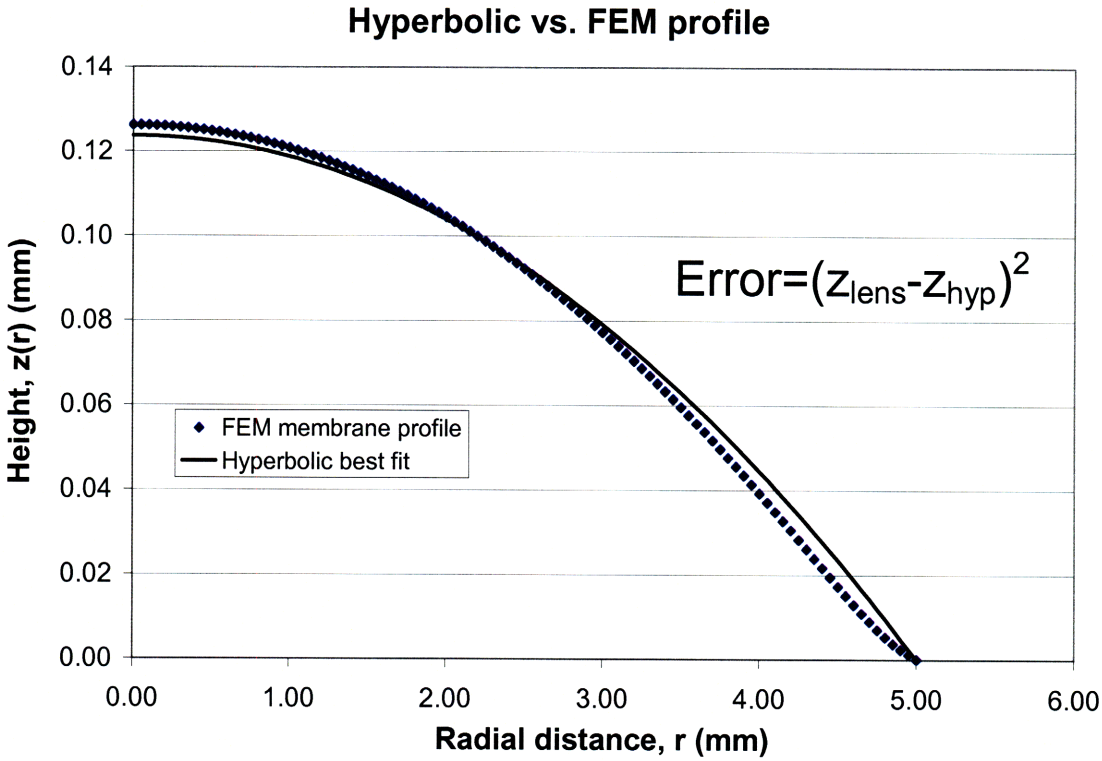

Figure 7.10: Finite element model prediction of the profile of a liquid filled lens and the best fit hyperbola – Here half of a cross section of the lens membrane (blue dots) and the best fit hyperbola (black line) are shown. Since the lens is symmetric about the center an only one half of the cross section is shown. The error at a singe radial position is defined as the square of the height difference between the hyperbola and the lens. The total error is then determined by summing the error at a pre-defined number of points along the radial direction. Points spaced 50 microns apart (100 points total) were used for all total error computations in this chapter.

7.4.1 Thickness effects

The effect of the membrane thickness was investigated using the finite-element model. The error between the best fit hyperbola and the inflated membrane shape were compared for each thickness. All membranes were modeled using 0.5 psi of pressure with modulus values of 3 MPa. The thinner the membranes were made, the better they performed, reducing the amount of error between the optimum hyperbolic curve and the inflated membrane shape. (While the term "error" is defined the sum of the square of the vertical distance between the between the two curves taken every 50 microns along the

radius in this study, a more objective function of lens quality such as the modulation transfer function may be more appropriate to use in the future.)

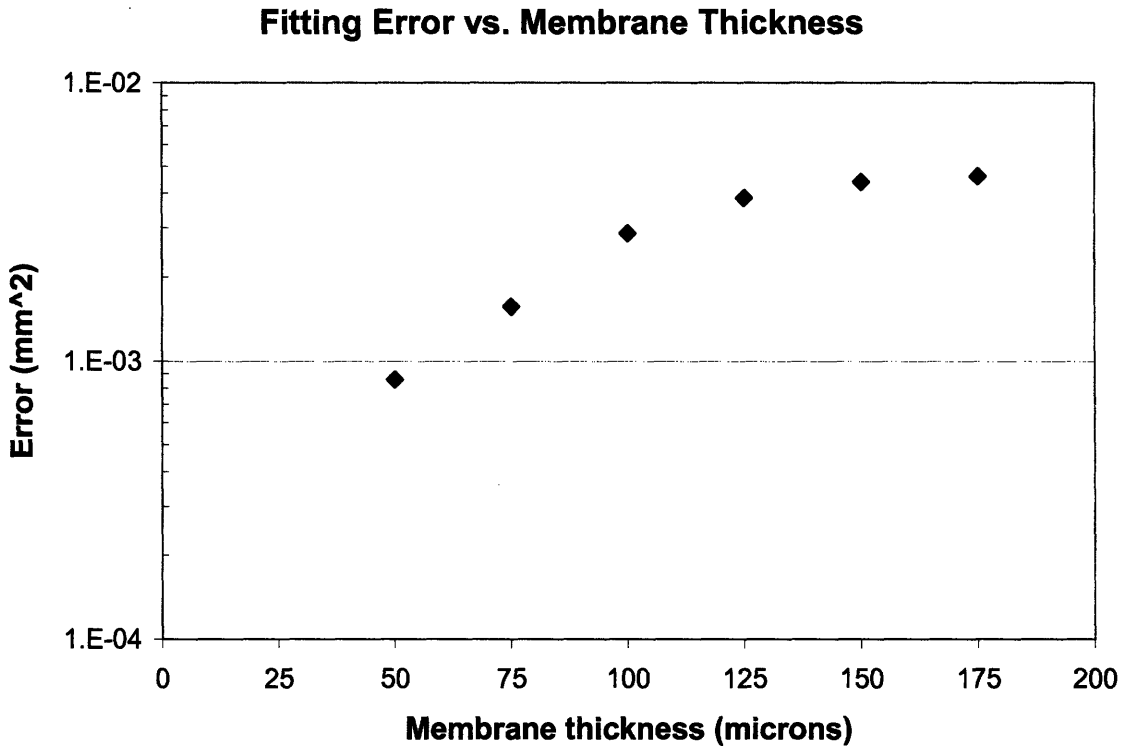

Figure 7.11: The change in fitting error with membrane thickness - The departure from the optimum shape is reduced by decreasing the membrane thickness. Membranes between 50 and 175 microns thick were chosen because of consideration with the ease of fabrication of the film and the strength of thin membranes to withstand the pressure of inflation. It is believed that while there may be additional benefits from making membranes thinner than 50 microns, there would be severe limits placed on the inflation pressures that the membranes could withstand.

7.4.2 Modulus and residual strain effects

The effect of modulus and pre-strain in the lens was also evaluated based on the same criteria as above. The modulus of the PDMS elastomer can be changed by increasing the crosslink density. This can be accomplished by increasing the cure temperature of the rubber or by crosslinking the already cured sample with radiation. For Sylgard 184 (PDMS), a room temperature cure (~25°C) produces a rubber with a modulus of ~2MPa. This can be increased to ~5MPa by increasing the temperature at

which the sample is cured (100°C). Crosslinking by irradiating the silicone can be accomplished by exposing the rubber to a flux of electron radiation such as that produced at the MIT High Voltage Research Laboratory by a high voltage van de Graff generator. Figure 7.12 details the radiation dose necessary for increasing the modulus of the silicone.

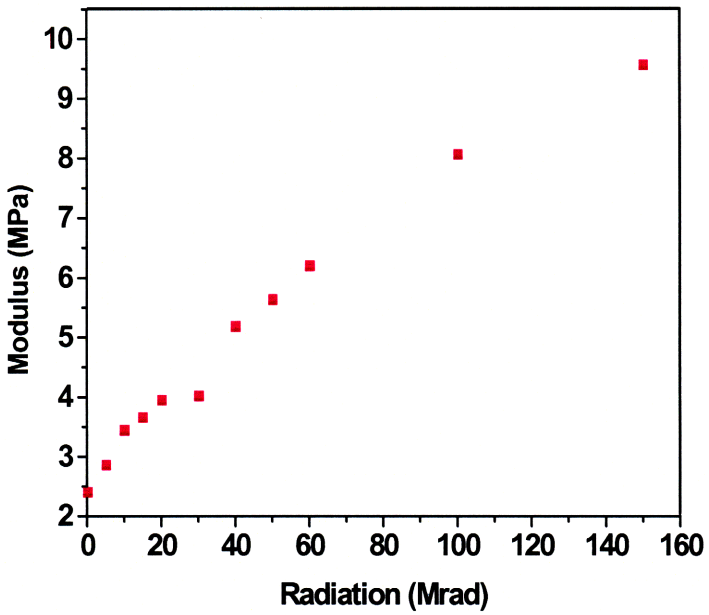

Figure 7.12: Modulus increase of cured PDMS samples upon exposure to electron radiation – As more radiation is supplied to the film, more crosslinks are created and the modulus of the silicone rises. The samples were cured at room temperature resulting in an initial modulus of 2MPa. The modulus can be increased by almost a factor of five through irradiation, although the samples were more brittle that experienced high levels of radiation lowering their strain to failure. (work done in combination with Dr. Z. Wu and Dr. A. Nolte.)

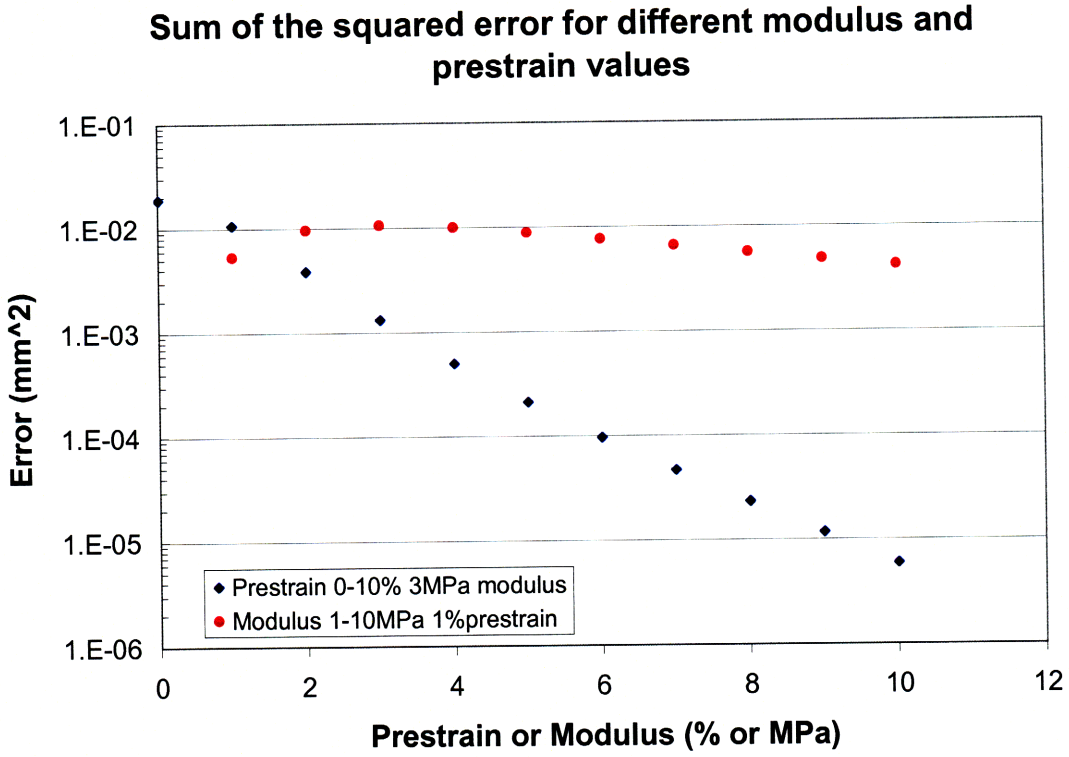

Figure 7.13: A comparison of the effect of changing the modulus and prestrain on the fitting error – By varying the amount of pre-strain in the membrane a much greater improvement is seen in the fit to the hyperbolic function. The red dots illustrate the response of the model to a sample with a fix amount of pre-strain (1%) whose modulus is varied from 1-10MPa. The blue dots show the response of the model with a constant modulus (3MPa) but with 0-10% pre-strain.

Pre-strain or residual strain is the other factor under consideration and can be purposefully introduced into the lens membranes through their fabrication process. To make the lenses, a two-part, addition-cure silicone (Sylgard 184) is prepared by mixing the crosslinker and polymer precursor together and spinning the viscous fluid onto a silicon wafer whose surface is treated with a flourosilane compound to promote wetting of the hydrophobic silicone (see chapter two for more details). The wafer with the PDMS film is then cured in an oven at elevated temperature (to speed the curing/crosslinking) process. The silicone and silicon have very different thermal expansion coefficients (~96 x 10^{-6}/C for silicone versus ~3 x 10^{-6}/C for silicon) and thus the film, crosslinked at

elevated temperature wants to shrink when cooled down to room temperature but it is constrained by the silicon wafer. The silicone film is then bonded to an aluminum washer using a plasma bonding process. This attaches the silicone film (membrane) to the aluminum washer but since it is bonded to the washer it still cannot relax. This residual stress from the curing process puts the film in tension and it is stretched across the aluminum washer. The higher the cure temperature, the more residual stress is introduced but practical limits are reached because the rate of curing increases as temperature increases so a film may be essentially fully crosslinked before reaching extremely elevated temperatures.

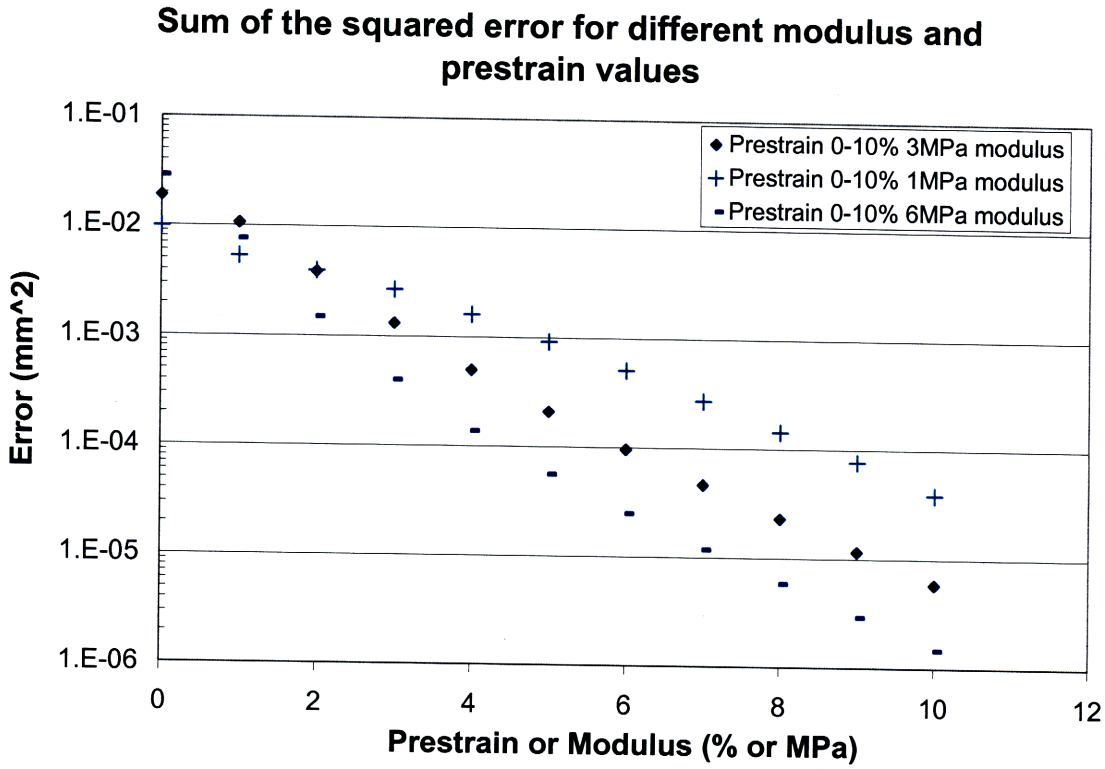

Figure 7.14: Slight improvement of error with the increase in modulus - The fit is improved by having a high pre-strain and a high modulus although as seen earlier, increasing the residual strain in the membrane leads to more substantial improvements in the reduction of lens error.

As can be seen in figures 7.13 and 7.14, the amount of error between the optimum

hyperbolic shape and the model-predicted membrane shape is reduced with increasing pre-strain and modulus although increasing the pre-strain has a much larger effect on the reduction in error than does the increase in modulus. If the lens is to have the least amount of error, both modulus and pre-strain should be maximized although increasing the modulus through irradiation might be avoided because of the decrease in residual stress that it produces.[36]

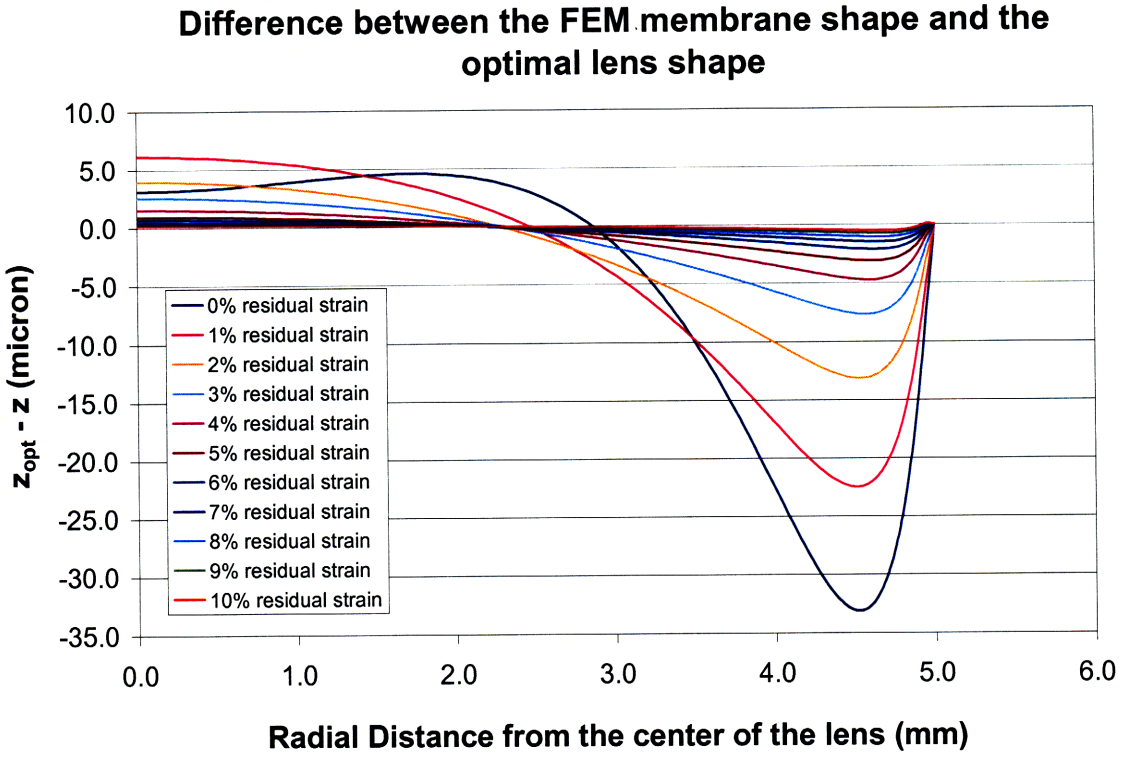

Figure 7.15: The difference between the FEM membrane shape and the optimal hyperbolic lens shape – Lenses with varying degrees of pre-strain are compared. For lenses with little or no residual strain, there is a large amount of error at the periphery and the center of the lens. This error decreases with increasing pre-strain but with diminishing returns.

In figure 7.15 the difference between the finite-element model and the best-fit hyperbolic function are plotted for lenses having several different pre-strains. It is interesting to note that a large amount of the total deviation from the hyperbolic form comes from the areas around the periphery of the lens and this large distortion from the optimal shape may not be that important since many lens designs only use the central

portion of the lens.

7.4.3 Gradient modulus effects

As seen in the previous section, increasing the modulus of the film reduced the error in the shape of the lens. Through irradiation induced crosslinking it is also possible to create *gradients* in the modulus of the film. Figure 7.16 shows the relation between the thickness of an aluminum mask and the modulus of the rubber underneath. The mask is placed over a slab of PDMS rubber serves to absorb the radiation and the thicker the mask is, the smaller the dose of radiation that gets to the rubber.

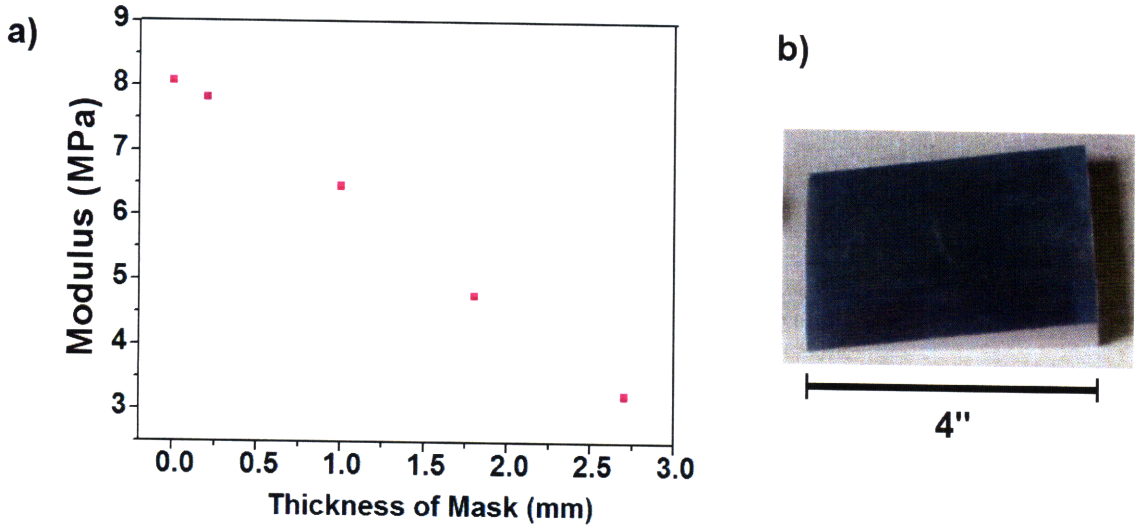

Figure 7.16: Modulus control of PDMS with an aluminum irradiation mask – (a) The modulus of Sylgard 184 can be controlled through electron irradiation. This work, done at the High Voltage Research Laboratory at MIT, allows for gradients in modulus to be made by placing a mask (b) with the appropriate geometry and thickness over the PDMS sheet and irradiating it. (Work done in conjunction with Dr. Z Wu, Rubner Group)

If the modulus of the film could be spatially controlled, the deformation behavior of the lens could be effected and provide another route to improving the performance of the lens. To produce lenses with gradient moduli, masks could be produced with cross-sectional thicknesses proportional to the modulus that was desired in certain areas (see figure 7.17).

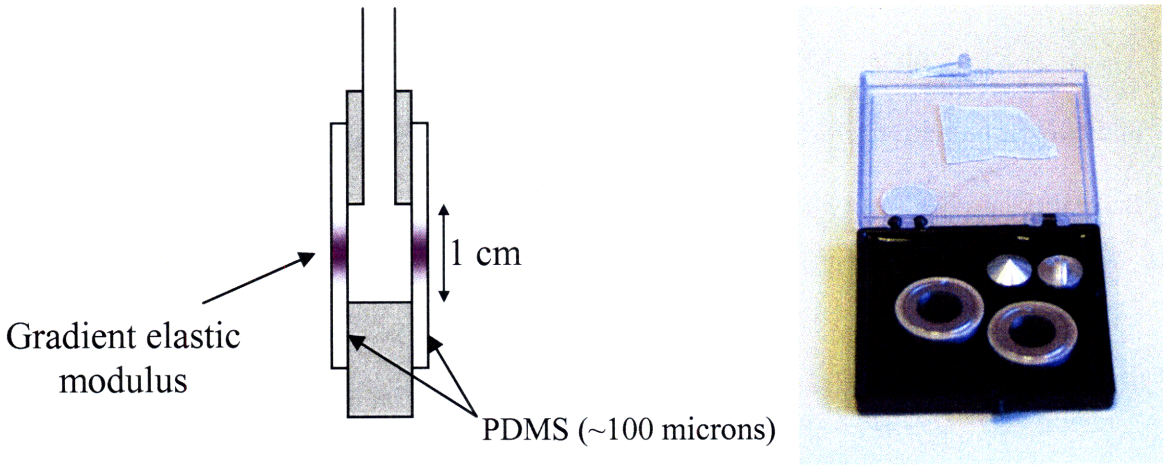

Figure 7.17: Schematic cross-section of a gradient-index, liquid lens and a set of aluminum masks and silicone lens membranes – The gradient in elastic modulus is used to change the deformation behavior of the lens. The masks cover the membranes during irradiation absorbing more radiation in areas with thicker cross-sections leading to a gradient in the elastic modulus in proportion to the geometry of the mask.

Three cases were simulated, a uniform modulus lens membrane, an increasing linear gradient, and a decreasing linear gradient in the elastic modulus. Figure 7.18 shows the comparative curvatures of these three cases illustrating that a change in shape of the membrane is possible with a gradient modulus.

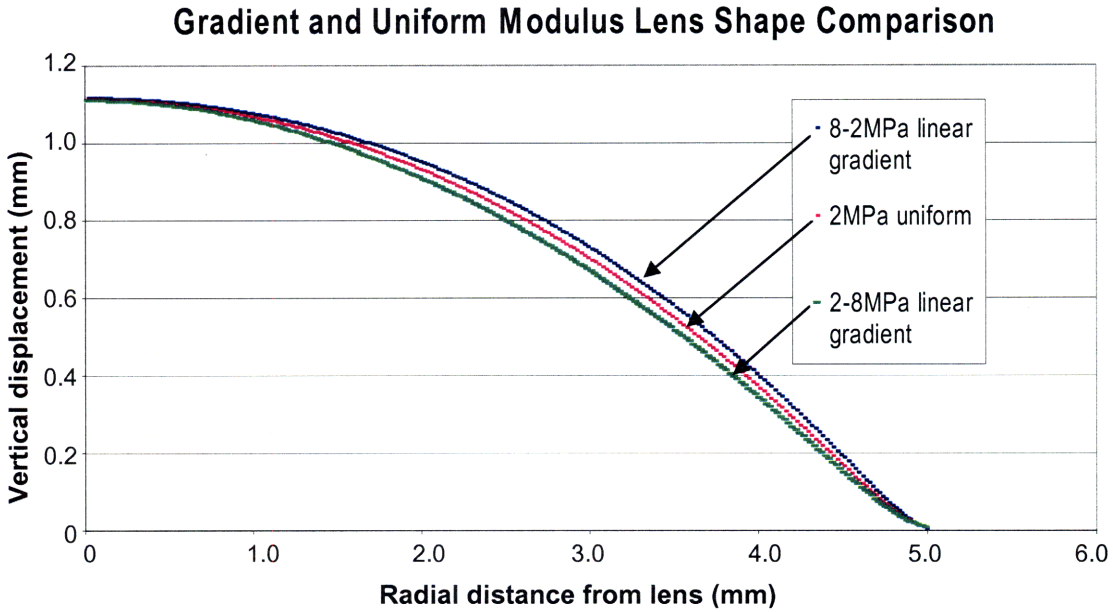

Table 7.18: A comparison of one uniform modulus and two linear gradient modulus membranes – A difference in inflation profile can be seen for all three cases pointing to the possibility of tailoring the modulus to achieve a certain inflation profile. The pressure applied to the films has been varied so as to achieve an identical center height.

A lens with an experimentally realistic gradient with no pre-strain was modeled and compared with uniform-modulus lenses. The gradient-modulus lens compared favorably and had an error lower than either of the two uniform-modulus lenses.

Table 7.1: A comparison of different elastic modulus compositions. The error for a gradient modulus lens is smaller than in either of the uniform modulus cases.

Modulus	Squared Error
Uniform 1MPa	9.83E-03 mm^2
Gradient 1-6MPa	7.74E-03 mm^2
Uniform 6MPa	28.4E-03 mm^2

7.5 Conclusion

Using the fitting errors as a comparative figure of merit, a study of the influence of various parameters on the performance of a liquid filled lens was conducted. This involved uniformly varying the modulus, pre-strain, and membrane thickness and analyzing their fit to the perfect hyperbolic form. The results show that the pre-strain has the most influence in terms of minimizing the fitting error. For every increase in pre-strain, there is a logarithmic improvement in the fitting error (the error decreases). Decreasing the membrane thickness did decrease the fitting error but the effect was not as pronounced as with the pre-strain. The relationship was more linear rather than logarithmic in nature and hence the effect was not as great until the thickness was reduced below 130 μm. Changing the modulus was found to be the least effective way of reducing the fitting error although for a given pre-strain, increasing the modulus did improve the fit. Lenses with a gradient in their elastic modulus were also modeled and

were found to have a more perfect refracting surface (because of the smaller deviation from the optimum profile) than their uniform modulus counterparts.

7.6 References

1 Reichelt, S., and Zappe, H., Design of spherically corrected, achromatic variable-focus liquid lenses, Optics Express, 15(21), 14146-14154 (2007)

2 Kuiper, S., Hendriks, B., Suijver, J., Deladi, S., Zoom camera based on liquid lenses, Proc. SPIE, 6466(64), 660F-1-64600F-7 (2007)

3 Hecht, Optics, 3rd edition, Addison-Wesley, Reading, Massachusetts (2001)

4 Walls, G.L. "The Vertebrate Eye and its Adaptive Radiation." Cranbrook Inst. Sci., Bloomfield Hills, Michigan (1942)

5 Ohmart US patent 504890 (1893)

6 Rigaut, F.; Cuby, J. G.; Caes, M.; Monin, J. L.; Vittot, M.; Richard, J. C.; Rousset, G.; and Lena, P., Visible and infrared wavefront sensing for astronomical adaptive optics, Astronomy and Astrophysics, 259(2), L57-L60 (1992)

7 Dow Corning BOSS project effort, unpublished.

8 Varioptic corporation, www.varioptic.com, accessed on 8/27/2005

9 Kuiper S, Hendriks BHW Variable-focus liquid lens for miniature cameras Applied Physics Letters, 85(7), 1128-1130 (2004)

10 Lopez CA, Lee CC, Hirsa AH Electrochemically activated adaptive liquid lens Applied Physics Letters, 87(13), 134102 (2005)

11 Zhang DY, Justis N, Lo YH Fluidic adaptive lens of transformable lens type Applied Physics Letters, 84(21), 4194-4196 (2004)

12 Zhang DY, Lien V, Berdichevsky Y, et al. Fluidic adaptive lens with high focal length tunability Applied Physics Letters, 82(19), 3171-3172 (2003)

13 Agarwall M, Gunasekaran RA, Coane P, et al.Polymer-based variable focal length microlens system Journal Of Micromechanics And Microengineering, 14(12), 1665-1673 (2004)

14 S. T. Kowel, D. S. Cleverly, and P. G. Kornreich, Adaptive Spherical Lens Appl. Opt., 23, 278 (1984)

15 Sato, S., Applications of liquid crystals to variable-focusing lenses Optical Review 6(6), 471-485 (1999)

16 Mao Y, Bin W, Sato S Liquid-crystal lens with a focal length that is variable in a wide range Applied Optics 43(35), 6407-6412 (2004)

17 Wang B, Ye M, Sato S Experimental and numerical studies on liquid crystal lens with spherical electrode Molecular Crystals And Liquid Crystals 433, 217-227 (2005)

18 Ye, M., Wang, B., and Sato, S., Realization of liquid crystal lens of large aperature and low driving voltages using thin layer of weakly conductive material, Optics Express, 16(6), 4302-8 (2008)

19 Li, G., Mathine, D.L., Valley, P., Ayras, P., Haddock, J.N., Giridhar, M.S., Williby, G., Schwiegerling, J., Meredith, G.R., Kippelen, B., Honkanen, S., and Peyghambarian, N., Switchable electro-optic diffractive lens with high efficiency for ophthalmic applications, Proceedings of the National Academy of Sciences, 103(16), 6100-4 (2006)

20 http://www.pcmag.com/article2/0,1759,1749481,00.asp Accessed on 1/17/2006

21 Kulishov, M., Tunable electro-optic microlens array. I. Planar geometry, Applied optics, 39(14), 2332-9 (2000)

22 Kulishov, M., Tunable electro-optic microlens array. II. Cylindrical geometry, Applied optics, 39(20), 3509-15 (2000)

23 Yang, S., Krupenkin, T.N., Mach, P., and Chandross, E.A., Tunable and latchable liquid microlens with photopolymerizable components, Advanced Materials, 15(11), 940-3 (2003)

24 Krupenkin, T., Yang, S., and Mach, P., Tunable liquid microlens, Applied Physics Letters, 82(3), 316-8 (2003)

25 Ren, H. and Wu, S.T., Tunable-focus liquid microlens array using dielectrophoretic effect, Optics Express, 16(4), 2646-52 (2008)

26 Ren, H., Lin, Y.-H., and Wu, S.T., Appl. Phys. Lett., 88, 191116 (2006)

27 N. Sugiura and S Morita, Variable-focus liquid-filled optical lens, Applied Optics, 32(22) 4181-9 (1993)

28 Zhang, D.Y., Justis, N., Lien, V., Berdichevsky, Y., Lo, Y.H., High performance fluidic adaptive lenses, Applied Optics, 43, 783 (2004)

29 Zhang, D.Y., Lien, V., Berdichevsky, Y., Choi, J., and Lo, Y.H., Fluidic adaptive

lens with high focal length tunability, Applied Physics letters, 82(19), 3171-2 (2003)

30 Zhang, D.Y., Justis, N., Lo, Y.H., Integrated fluidic lenses and optic system, IEEE journal of selected topics in quantum electronics, 11(1), 97-106 (2005)

31 Ren H, Wu ST Variable-focus liquid lens by changing aperture Applied Physics Letters, 86(21), 211107 (2005)

32 Way, S., Bending of Circular Plates with Large Deflection, Trans. ASME, 56(8), (1934)

33 L. Prandtl, Zur Torsion von prismatischen Stäben, Physikalische Zeitschrift, 4(26b), 758-9 (1903)

34 S.D. Poisson, Memoirs of the academy, Academy of Sciences, Paris (8) (1829)

35 Rawicz, A.H. and Mikhailenko, I., Modeling a variable-focus liquid-filled optical lens, Applied Optics, 35(10), 1587-9 (1996)

36 Personal communication with P. Kobrin of Rockwell Scientific (now Teledyne)

Chapter 8:
Summary and Future Work

In this thesis work, biologically-inspired, multilayer reflectors constructed from a self-assembling block copolymer were tuned through the application of numerous stimuli. Five different stimuli types were explored including a change in solvent environment, pH, salt concentration in solution, electrochemistry, and temperature. Chapters three through five illustrate the extensive tunability of hydrophobic/hydrophilic block polymers as stimulus responsive materials. The theme of block polymer photonics was also expanded upon in chapter six which details the design and construction of a shear rheometer for investigation of shear-induced mechanochromism of a photonic block copolymer. In the final research chapter of this thesis, the deformation behavior of a biologically-inspired tunable lens was modeled using the finite-element method. The deformation profile was

then compared to the optimal shape for a lens with no spherical aberration and several parameters were investigated for their ability to make the shape of the deformed lens match with the optimum shape. The following paragraphs will more closely examine the results of this thesis work on a chapter-by-chapter basis as well as giving suggestions for future research.

The self-assembled, multilayer structures studied in chapter three, comprised of a poly(styrene)-poly(2-vinyl pyridine) (PS-P2VP) block polymer, need to be swollen with a selective solvent in order to obtain the domain spacings and refractive index difference needed to strongly reflect ultraviolet to near-infrared light. Because of this, a study of their behavior in different solvent environments was undertaken. Building off of prior work on the effect of salt concentration on the reflectivity of a quaternized PS-P2VP, a study of the structural defects which contribute to the swift swelling of the structure was undertaken followed by the measurement of the reflectivity of different molecular weights of PS-P2VP in methanol. A single molecular weight (57k-57k) was then selected for further investigation and its reflectivity in different alcoholic solvents was measured as well as its response to a change in pH.

Further study of the temporal response of the system to the viscosity of the swelling solvent is needed as qualitative but not quantitative observations of a link between swelling time and viscosity have been made. The time that it takes for the polymer to swell in a given solvent is a function of not only the viscosity of the solvent but also the affinity of the solvent for the polymer, the number and size of the defects in the polymer film, and the number of layers. Another promising avenue of future work is the use of non-volatile solvents to swell the structure and further, getting rid of the liquid

all together and using a swelling agent that can be subsequently crosslinked or solidified giving the gel more robust mechanical properties.

Other polymers could also be incorporated into the hydrophilic/hydrophobic BCP architecture. The thoroughly studied poly(n-isopropyl acrylamide) is a candidate to replace the P2VP block. Multiple routes for creating hydrophobic/hydrophilic block copolymers should be investigated such as anionic synthesis and atom-transfer radical polymerization (ATRP). Changing the PS block in PS-P2VP to poly(isoprene) (PI) may yield insights as to how much of a role the rigid PS block plays in the swelling behavior of the film. The glass-transition temperature of PI is below room temperature so the chains are mobile inside the domain. This allows for the relaxation of stress in the PI layer which could lead to three-dimensional expansion of the whole structure rather than limiting it two a one-dimensional expansion with the glassy PS domains. PI can also be crosslinked and swollen with a solvent that is not compatible with the P2VP or the solvent swelling the P2VP. The use of two incompatible solvents to swell both domains could lead to reflectors in the mid IR.

In chapter four the thermochromic properties of these gels were investigated through the use of methanol, acetic acid, and a quaternized sample in water. The methanol swollen samples had a slightly negative change in reflectivity peak position with change in temperature (~-.7 nm/^{o}C) while the quaternized sample in de-ionized water displayed almost no change in reflectivity with temperature. The samples in acetic acid-water solutions displayed a range of behavior including a blue-shift in the reflectivity peak for lower acetic acid concentrations (0.01M) (~-1.45 nm/^{o}C) to almost no temperature related shift in the more acidic solutions (0.1M and 1M). The cause of

the variety of behavior in acidic solutions was shown to be the temperature dependence of the pKa of the P2VP. Future work in this area might include switching the acetic acid (which has relatively little variation in acidity with temperature) with an acid that shows a large variation in pKa (and thus acidity) with temperature such as β-methylbutyric acid (see figure 4.12).

Chapter five demonstrated a PS-P2VP reflector whose color could be changed by the application of an electrochemical stimulus. The behavior of the system was investigated and explained for several different electrolyte/BCP combinations including ethyl alcohol in quaternized P2VP, trifluoroacetic acid in P2VP, and 2,2,2-trifluoroethanol in P2VP. The quaternized polymer device was unresponsive (no color change) when the film electrode was the cathode (forward bias). When the leads were reversed (reverse bias), the reflected color red shifted due to a change in counterion species in the film which caused the qP2VP domains to expand. The reflectivity peak of the protonated polymer device could be red shifted by applying a forward bias to the film electrode. This caused production of acidic H^+ ions causing the film to swell because it was further protonated. By reversing the electrodes, the local electrochemical reaction creates a more basic environment, deprotonating the P2VP and deswelling the stack. PS-P2VP (102k-97k) swollen with 2,2,2-trifluoroethanol was also investigated and it was found that electrolysis under negative bias produced basic trifluoroethoxide ions which deprotonated the P2VP causing a blue shift. The original red color could be shifted to green by the application of five volts and further shifted to blue by the application of ten volts. Future work, in finding an optimal electrode/electrolyte system could lead to highly reflective displays based on the concepts laid out in the chapter. Any future

electrolyte under consideration must be able to swell at least one domain of the BCP while either being able to be reduced/oxidized itself or carrying a solvated electroactive species in which case it must be electrochemically stable in the range of potentials that are to be applied. Long term (high cycle) testing must also be completed to determine commercial viability.

Chapter six highlighted the design and construction of a shear rheometer for the controlled shear deformation of photonic block polymers. Both linear and cyclic linear shear were implemented and preliminary testing with a poly(styrene)-poly(methyl methacrylate) block copolymer was accomplished. Slow, linear shear produced no color change while extremely fast linear shear produced a transparent (non-reflective) sample. Fast, cyclic shear produced color change from green to red to green in a cycle. This was attributed to an alignment of the polymer chains in the direction of the shear flow (normal to their rest orientation) at the top plate which caused a stretching of the domains closer to the fixed glass substrate. Other measurement techniques should be employed in the future to definitively identify the mechanism such as ultra-fast freezing of the polymer to trap the microstructural details for observation with cryo-TEM. Other block copolymers could be investigated as well with various levels of selective and non-selective solvents to see what effect the level of plasticization has on the mechanochromism. One problem that should be addressed by future work is the re-design of the load measurement to use a stiffer link between the motor and top plate. Currently there is a phase-lag between the application of force by the motor and the movement of the top plate at high strain rates. Also, problems with the measurement of the reflectivity through the microscope spectrometer need to be addressed.

Finally, chapter seven details the finite element modeling of a liquid filled lens membrane. Several parameters including the thickness, modulus, and pre-strain in the lens were investigated for improvement of the spherical aberration in the lens. The use of a gradient in the elastic modulus of the lens was also preliminarily studied and future studies could be undertaken which optimized this gradient. Implementation of these suggested improvements in a real lens is also an avenue for future work.

Appendix A:

Spherical Gradient Index Lenses

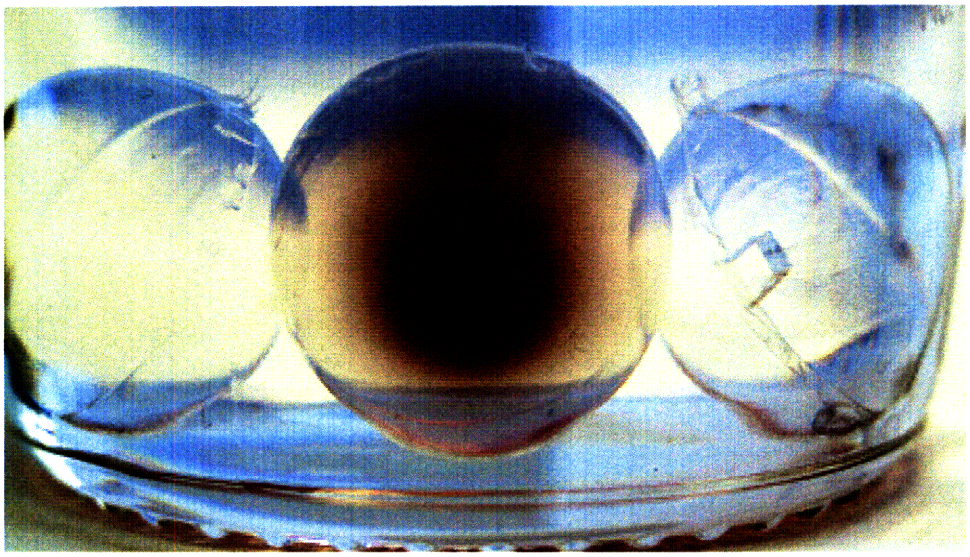

Figure A.1: A group of molded PDMS lenses in a solvent bath - The center lens originally contained a homogeneous dispersion of gold nanoparticles. After swelling in toluene, the nanoparticles close to the periphery diffused outwards leaving a higher concentration in the center of the lens. The two outer lenses are swollen, but do not contain any nanoparticles. These lenses are approximately 25mm in diameter.

The fish and mammalian eye are two interesting examples of nature's solution to the problem of directing light onto a detector while keeping the ability to focus on objects both near and far. Because fish live underwater, there is little or no refractive index difference between the water and the cornea, therefore refraction does not take place at the lens interface. To focus the available light, the lens of a fish eye has a gradient index of refraction[1]. The difference between the indices of refraction of the center and periphery of these lenses is approximately 0.2[2]. This can be mimicked with a polydimethyl siloxane (PDMS)/nanoparticle composite. PDMS is used because of its elastomeric properties and its high transmissivity in the visible regime. High dielectric constant nanoparticles with a diameter less than ~50nm are used because larger micron

sized particles would scatter light. Nano sized gold was used initially because of the ease with which it could be produced and functionalized with alkane and styrene pendant groups. The solubility of these nanoparticles in the PDMS was good enough to achieve mixing but more compatible functional groups may be necessary to achieve high loadings. The concentration of gold was 0.1 wt% for these initial studies.

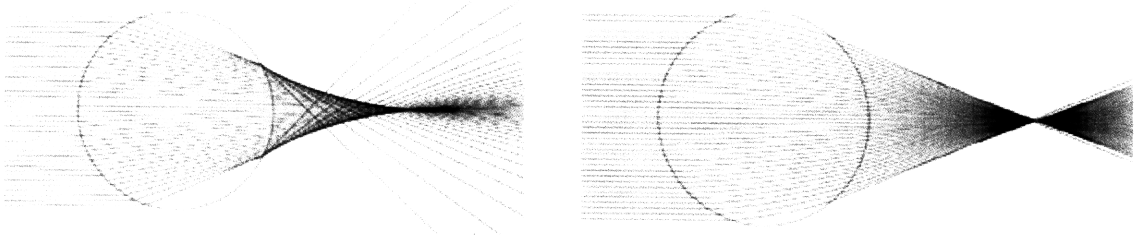

Figure A.2: a) Ray tracing for a sphere with uniform refractive index. The spherical aberration is evident by the distance over which the rays are focused (not at a single point. b) Ray tracing for a gradient index sphere. Note that the rays are now focused at a point rather than on a line, thus yielding higher resolution.

A gradient index (GRIN) lens was created by mixing the gold nanoparticles and PDMS. PDMS spheres (lenses) were produced by curing PDMS containing a uniform concentration of nanoparticles in a spherical mold cavity (see figure A.3 for the production methods and A.1 for the resulting lenses). Depending on the index of the nanoparticles used, concentrations will have to be much higher to get appreciable results. Gold nanoparticles have a very high plasmon absorption peak in the visible region therefore to make a usable lens, transparent, high-index particles must be used such as titanium dioxide (TiO_2).

The index of refraction change in a commercial gradient index lens is approximately (equal to or less than) 0.05. For example, for PDMS/TiO_2, around 10 – 20% by volume of the composite material (PDMS/nano TiO_2) would be TiO_2

nanoparticles. To get an index change of 0.05 from the center to the edge, titania nanoparticles (n=1.8) would make up 14% of the volume of the composite at the core (see table A.1). The spheres are uniformly loaded with nanoparticles before they are immersed in a solvent that will swell the PDMS. The solvent serves two purposes: to remove nanoparticles from the outer regions of the lens and to expand the lens itself so that diffusion is accomplished much more readily. Once sufficient time has elapsed for a gradient to form (~24 hours), the lens is de-swollen to its original shape. The gold nanoparticles absorb blue light so a visual color gradient can be readily seen in these lenses when there is a concentration gradient (see figure A.1).

Table A.1: A rule of mixtures calculation for determining the index of refraction of the nanocomposite material. The refractive index values of PDMS and the TiO_2 are measured values from real materials.

	PDMS	TiO_2		
Refractive Index	1.44	1.8		Rule of mixtures composite index of refraction
volume %	86	14		1.4904

Ideally these nanoparticles would be non-absorbing and have a high index of refraction while remaining compatible with the polymer matrix. Also, nanoparticles with refractive indices lower than PDMS could be dispersed in the solvent so that they would diffuse in as the higher index particles were diffusing out creating a steeper gradient.

The optimal shape of the spherical gradient (see table A.2) was first proposed by

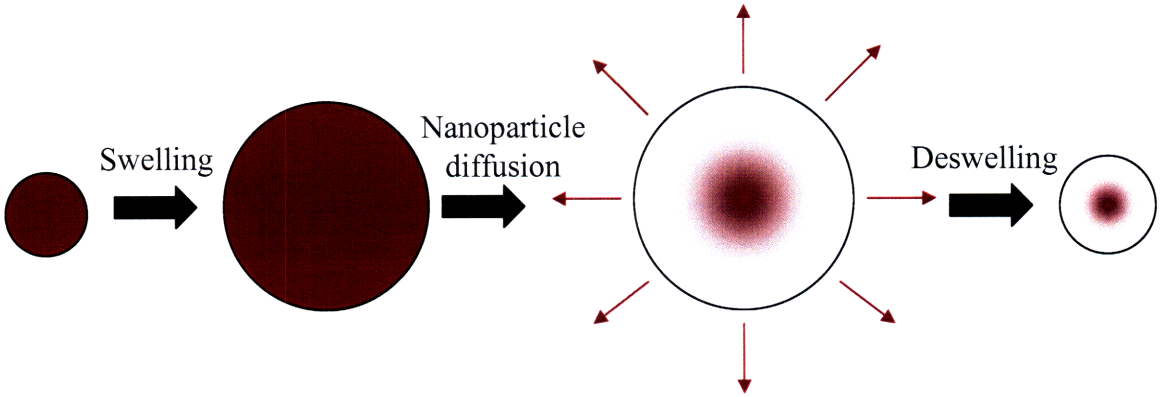

Figure A.3: Steps involved in making gradient-index silicone lenses - The steps are: 1 - molding a PDMS lens with a uniform distribution of nanoparticles, 2 – swelling in a solvent (toluene, THF, etc.), 3 - diffusion of the nanoparticles into the solvent, and 4 – deswellling which is sometimes done in steps (transferring the lens to a series of different co-solvents of different compostion) to avoid cracking/drying stresses.

Maxwell in 1854 after examining an eye from a fish he was eating for breakfast[3]. This simple gradient has spherical symmetry but can only form sharp images of points inside the lens. Luneburg proposed a slightly different gradient but requires a very large Δn of 1 ($n = 2$ at the center and 1 at the periphery)[4]. Others have suggested modified gradients with sophisticated profiles[5,6] (see table A.2).

Gradient name	Functional form
Maxwell fisheye (spherical)	$n(r) = n_0\left[1 + \left(\frac{r}{a}\right)^2\right]^{-1}$
Luneburg (spherical)	$n(r) = \sqrt{2 - \left(\frac{r}{r_p}\right)^2}$
Generalized Luneburg (spherical)	$n^2(r) = n^2(0)[1 + G_2(r/r_0)^2 + G_4(r/r_0)^4]$ for $r_0 \geqq r \geqq 0$, $n(r) = n_d$ for $r_0 + d \geqq r > r_0$,
Kikuchi (spherical)	$n^2(r) = n^2(0)[1 + G_2(r/r_0)^2 + G_4(r/r_0)^4]$ for $r_0 \geqq r \geqq 0$, $n(r) = n_d$ for $r_0 + d \geqq r > r_0$,
Ideal radial profile	$n^2(r) = n_0^2 \sec h^2(gr) = n_0^2\left[1 - (gr)^2 + h_4(gr)^4 - h_6(gr)^6 + ...\right]$
Simplified radial profile	$n^2(r) = n_0^2\left(1 - (gr)^2\right)$

Table A.2: Functional forms of common refractive index gradients - The Maxwell and Luneburg gradients are not used because of their optical performance (in the case of the Maxwell fisheye) and large Δn in the case of the Luneburg lens. The generalized Luneburg relation is generally accepted as being impossible to fabricate using traditional methods and therefore has not been adopted. In the modified Luneburg, G_2 and G_4 are constants that depend on the focal length and index of the ambient medium. The radial profiles are used for cylindrical lenses when light is traveling parallel to the cylindrical axis. The ideal radial profile is general and can be reduced to the parabolic simplified expression if there is a small index change and the paraxial approximation is satisfied.

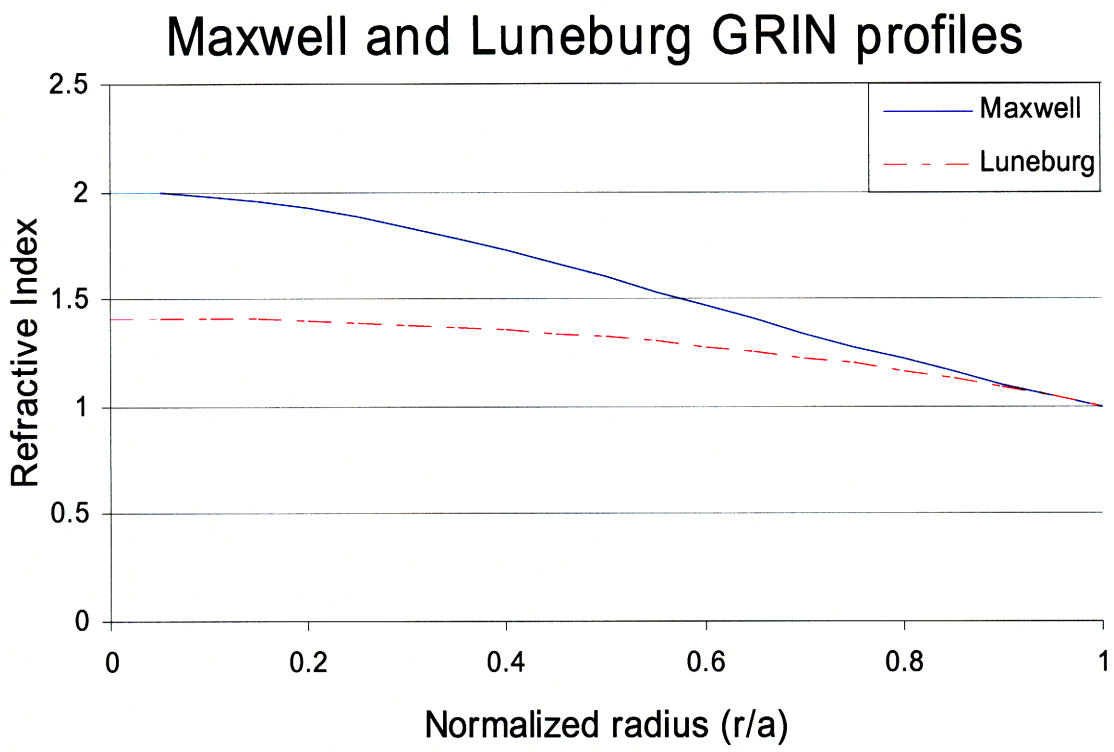

Figure A.4: The refractive index profiles of the Maxwell fisheye and Luneburg lenses - Both remain intellectual curiosities because of the difficulty in fabricating continuous gradients that vary continuously down to 1.

Cylindrical radial-gradient lenses

In addition to spherical radial gradients, cylindrically symmetric radial gradients (figure A.6) can also be made and are actually more technologically relevant. Cylindrical radial gradients were first explored by the physicist Robert Wood[7] and the gradient index cylindrical lenses with planar faces bear his name. The ideal and simplified gradient profiles can be seen in figure A.7. These cylindrical radial gradient index lenses have found applications in telecommunications and imaging, for example, copy machines, fiber couplers, surgical endoscopes, and compact disk lenses are commonly made out of radial GRIN lenses[8]. It is proposed that PDMS radial GRIN optics could be produced by

the aforementioned nanoparticles diffusion methods. The flexibility of PDMS can be an attractive property since this could give not only focusing behavior but also the capability

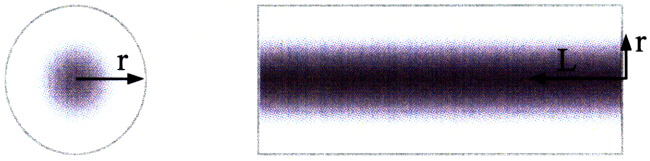

Figure A.5: Cylindrical radial gradient index lenses - The refractive index decreases as you move away from the center of the cylinder. Because of the gradient in the index of refraction, these cylinders are able to focus light even though both refracting surfaces are flat.

of 'steering' light as well similar to a gradient index optical fiber. The low density of PDMS combined with the compact designs allowed by radial GRIN optics would be of interest in portable devices such as binoculars where neither size nor weight are desirable.

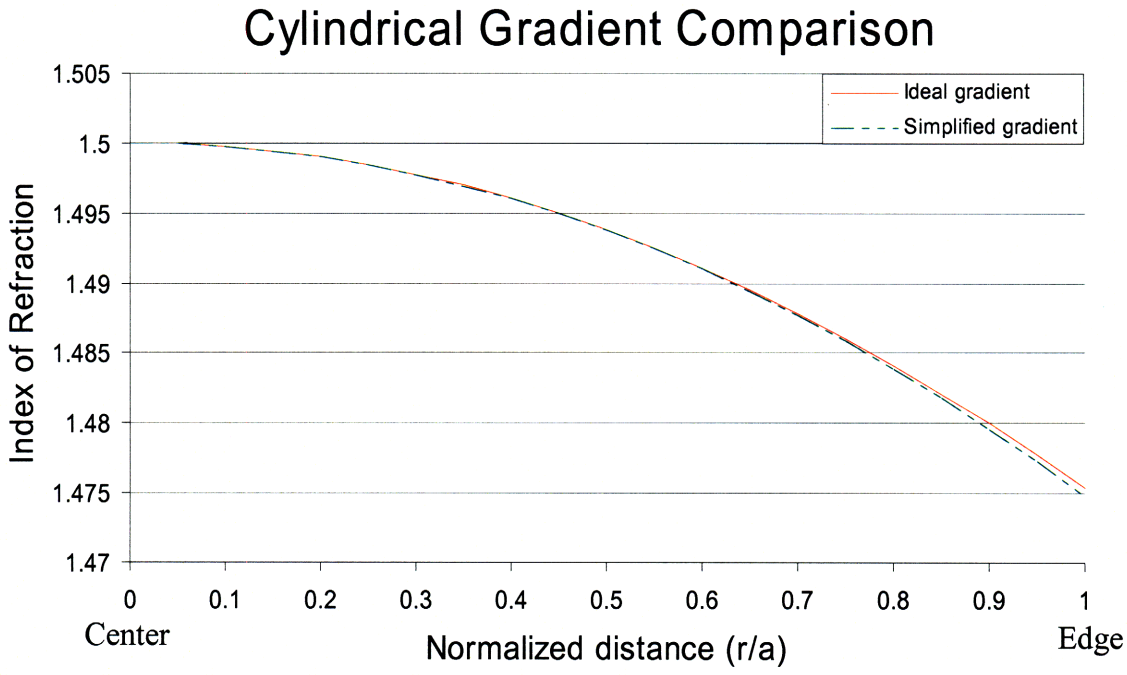

Figure A.6: **The ideal and simplified gradient profiles for a cylindrical gradient index lens** - The simplified equation (see table A.2) is that of a paraboloid and the index profile has traditionally been achieved by diffusion of ions into and out of preformed glass.

1 Pumphrey, R.J., "Concerning Vision," The Cell and the Organism, Cambridge University Press, 1961

2 McIlwain, J.T., An Introduction to the biology of Vision, Cambridge University Press, 1996

3 E. W. Marchand, Gradient Index Optics, Academic Press Inc., New York, 1978

4 R. K. Luneburg, Mathematical Theory of Optics, University of California Press, Berkeley, CA, 1964.

5 S. P. Morgan, "General Solution of the Luneberg Lens Problem," J. Appl. Phys. 29, 1358 (1958).

6 K. Kikuchi, T. Morikawa, J. Shimada, and K. Sakurai, "Cladded Radially Inhomogeneous Sphere Lenses," Appl. Opt. 20, 388 (1981).

7 R. W. Wood, Physical Optics, Macmillan, New York, NY, 1905.

8 D. Kindred, et. al., Axial and radial gradient-index titania flint glasses, Appl. Opt., Vol. 29, No. 28, p. 4036 – 4041, 1990

Appendix B:
Finite Element Modeling of the Phononic Behavior of a Polymer Multilayer

The following COMSOL Multiphysics code was used for modeling the behavior of a co-extruded polymer multilayer film. The results of the simulation, which can be seen in the following reference, was used for modeling the data presented in figures four and five:

W. Cheng, N. Gomopoulos, G. Fytas, T. Gorishnyy, J. Walish, E. L. Thomas, A. Hiltner, and E. Baer, Phonon Dispersion and Nanomechanical Properties of Periodic 1D Multilayer Polymer Films, Nano Lett. Vol. 8, **2008** Web Release Date: 26-Mar-2008

```
% COMSOL Multiphysics Model M-file
% Figure 5
% 1-16-07  Joe Walish
% Finding BLS peaks with q=0.0152nm^-1, symmetric layers, and different
% layer thicknesses (see the d vector for exact numbers)

clear

maxfreqs=15;                %determines the number of eigenfrequencies to find
maxkvals=200;               %the number of k values to find eigenfreqs for
l=50;                       %layer width
d=[12,24,49,98,195,391];    %layer height
maxsolutions=length(d);     %number of times the loop will run
kx_max=pi/l;                %maximum kx value
%ky_max=pi/(2*d);           %maximum ky value (not used in this simulation)
kxfract=.025/kx_max;        %the fraction of kspace in x direction that we are exploring
kyfract=0.3;                %the fraction of kspace in y direction that we are exploring

k_x=0.0152;                 %As specified in Figure 5
k_y=0;

dcnt=1;                     %counter for the changing the d spacing - corresponds to
                            column of the d vector

while dcnt<(maxsolutions+1)

dStr = num2str(d(1,dcnt));

    % Geometry (defining the shape of the unit cell)
    g1=rect2(l,d(1,dcnt),'base','corner','pos',{'0','0'},'rot','0');
    g2=rect2(l,d(1,dcnt),'base','corner','pos',{'0',dStr},'rot','0');
    g3=geomcomp({g1,g2},'ns',{'g1','g2'},'sf','g1+g2','edge','none');

    %k_xStr=num2str(0);

    k_xStr=num2str(k_x);

    % Constants
    fem.const = {'l','50', ...
      'd','391', ...
```

```
    'kx_max','pi/l', ...
    'ky_max','pi/d', ...
    'k_x',k_xStr, ...
    'k_y','ky_max*0'};

% Geometry
clear s
s.objs={g3};
s.name={'CO1'};
s.tags={'g3'};


fem.draw=struct('s',s);
fem.geom=geomcsg(fem);


% Initialize mesh
fem.mesh=meshinit(fem);


% Refine mesh
fem.mesh=meshrefine(fem, ...
                    'mcase',0, ...
                    'rmethod','regular');

% (Default values are not included)

% Application mode 1
clear appl
appl.mode.class = 'FlPlaneStrain';
appl.gporder = 4;
appl.cporder = 2;
appl.assignsuffix = '_pn';
clear prop
prop.analysis='eigen';
appl.prop = prop;
clear equ
equ.rho = {1300,1190};
equ.thickness = 10000;
equ.nu = {0.38,0.341};
equ.E = {4.11e9,6.26e9};
equ.ind = [1,2];
appl.equ = equ;
fem.appl{1} = appl;
fem.frame = {'ref'};
fem.border = 1;
fem.units = 'SI';


% Coupling variable elements
clear elemcpl
% Extrusion coupling variables
clear elem
elem.elem = 'elcplextr';
elem.g = {'1'};
src = cell(1,1);
clear bnd
bnd.expr = {{'u',{},{}},{'v',{},{}},{{},'u',{}},{{},'v',{}}};
bnd.map = {{'1','1','1'},{'1','1','1'},{'1','1','1'},{'1','1','1'}};
bnd.ind = {{'1','3'},{'2'},{'4','5','6','7'}};
src{1} = {{},bnd,{}};
elem.src = src;
geomdim = cell(1,1);
clear bnd
bnd.map = {{{},{},'2'},{{},{},'2'},{{},'3',{}},{{},'3',{}}};
bnd.ind = {{'1','2','3','4'},{'5'},{'6','7'}};
geomdim{1} = {{},bnd,{}};
elem.geomdim = geomdim;
elem.var = {'uconstr_x','vconstr_x','uconstr_y','vconstr_y'};
map = cell(1,3);
clear submap
submap.type = 'unit';
```

```
    map{1} = submap;
    clear submap
    submap.type = 'linear';
    submap.sg = '1';
    submap.sv = {'4','5','6'};
    submap.dg = '1';
    submap.dv = {'1','2','3'};
    map{2} = submap;
    clear submap
    submap.type = 'linear';
    submap.sg = '1';
    submap.sv = {'3','6'};
    submap.dg = '1';
    submap.dv = {'1','4'};
    map{3} = submap;
    elem.map = map;
    elemcpl{1} = elem;
    % Point constraint variables (used for periodic conditions)
    clear elem
    elem.elem = 'elpconstr';
    elem.g = {'1'};
    clear bnd
    bnd.constr = {{'0','0','uconstr_y-(u*exp(i*k_y*2*d))','vconstr_y(v*exp(i*k_y*2*d))'}, ...
      {'uconstr_x-(u*exp(i*k_x*1))','vconstr_x-(v*exp(i*k_x*1))','0','0'}};
    bnd.cpoints = {{'2','2','2','2'},{'2','2','2','2'}};
    bnd.ind = {{'5'},{'6','7'}};
    elem.geomdim = {{{},bnd,{}}};
    elemcpl{2} = elem;
    fem.elemcpl = elemcpl;

    % Multiphysics
    fem=multiphysics(fem);

    % Extend mesh
    fem.xmesh=meshextend(fem);

    % Solve problem
    fem.sol=femeig(fem, ...
                   'conjugate','on', ...
                   'solcomp',{'u','v'}, ...
                   'outcomp',{'u','v'}, ...
                   'neigs',maxfreqs);

    % Save current fem structure for restart purposes
    fem0=fem;

    %disp(sprintf('eigenvalue %E', fem.sol.lambda(1)*i/2/pi()))

    %obtaining a vector populated by all of the eigenfrequencies up to the
    %maximum number set by maxfreqs
    eigcnt=1;
    while eigcnt<(maxfreqs+1)
        Eigfreqs(1,eigcnt)=fem.sol.lambda(eigcnt)*i/2/pi;

        titleinfo=sprintf('k_x=%f Eigenfrequency = %f Surface: Total Disp [m] Arrow: Disp
[m]',k_x,Eigfreqs(1,eigcnt));

        % Plot solution
%         postplot(fem, ...
%                  'tridata',{'disp_pn','cont','internal'}, ...
%                  'trimap','jet(1024)', ...
%                  'arrowdata',{'u','v'}, ...
%                  'arrowxspacing',15, ...
%                  'arrowyspacing',15, ...
%                  'arrowtype','arrow', ...
%                  'arrowstyle','proportional', ...
%                  'arrowcolor',[1.0,0.0,0.0], ...
```

```
%                   'solnum',eigcnt, ...
%                   'title',titleinfo, ...
%                   'axis',[-25,1+25,-25,2*d+25,-1,1]);
%
%         imgname=sprintf('L128_50-50_k%iEig%i', kcnt, eigcnt);
          %saveimage(imgname)
          eigcnt=eigcnt+1;
      end

      Eigfreqs=real(Eigfreqs);

      DataMatrix(dcnt,:)=[k_x d(1,dcnt) Eigfreqs];

      dcnt=dcnt+1;

      %asdf1=sprintf('L128_50-50_k%fEig%f', k_x(1,kcnt), Eigfreqs(1,1))

end

%save L128_50-50.txt DataMatrix -ascii -double
%saving the data
            filename='Figure5Data_Thickness-EigFreq.txt';
            form = '%15.7e';
            fid = fopen(filename,'wt');
            fprintf(fid,'k   d   EigenFreq1 EigenFreq2 EigenFreq3 EigenFreq4 EigenFreq5
EigenFreq6 EigenFreq7 EigenFreq8 EigenFreq9 EigenFreq10 EigenFreq11 EigenFreq12
EigenFreq13 EigenFreq14 EigenFreq15\n');
            plp = 1;
            while plp <= size(DataMatrix,1)
                str = num2str(DataMatrix(plp,:),form);
                fprintf(fid,'%s ',str(:));
                fprintf(fid, '\n');
                plp=plp+1;
            end
            fclose(fid);



% Figure 4
% COMSOL Multiphysics Model M-file
% Loop over k_x values and store eigenfrequencies and plots at each k_x

clear

maxfreqs=15;     %determines the number of eigenfrequencies to find
maxkvals=200;      %the number of k values to find eigenfreqs for
l=50;            %layer width
d=391;           %layer height
kx_max=pi/l;     %maximum kx value
ky_max=pi/(2*d);     %maximum ky value
kxfract=.025/kx_max;     %the fraction of kspace in x direction that we are exploring
kyfract=0.3;     %the fraction of kspace in y direction that we are exploring

k_x=[0:(kx_max*kxfract)/(maxkvals-1):kx_max*kxfract];       %a vector with ten equally
spaced values from zero to kx_max
k_y=[0:(ky_max*kyfract)/(maxkvals-1):ky_max*kyfract];       %same as k_x but for ky

dStr = num2str(d);

kcnt=1;          %counter for the k loop
while kcnt<(maxkvals+1)

    % Geometry (defining the shape of the unit cell)
```

```
g1=rect2(l,d,'base','corner','pos',{'0','0'},'rot','0');
g2=rect2(l,d,'base','corner','pos',{'0',dStr},'rot','0');
g3=geomcomp({g1,g2},'ns',{'g1','g2'},'sf','g1+g2','edge','none');

%k_xStr=num2str(0);

k_xStr=num2str(k_x(1,kcnt));

% Constants
fem.const = {'l','50', ...
  'd','391', ...
  'kx_max','pi/l', ...
  'ky_max','pi/d', ...
  'k_x',k_xStr, ...
  'k_y','ky_max*0'};

% Geometry
clear s
s.objs={g3};
s.name={'CO1'};
s.tags={'g3'};

fem.draw=struct('s',s);
fem.geom=geomcsg(fem);

% Initialize mesh
fem.mesh=meshinit(fem);

% Refine mesh
fem.mesh=meshrefine(fem, ...
                    'mcase',0, ...
                    'rmethod','regular');

fem.mesh=meshrefine(fem, ...
                    'mcase',0, ...
                    'rmethod','regular');


% (Default values are not included)

% Application mode 1
clear appl
appl.mode.class = 'FlPlaneStrain';
appl.gporder = 4;
appl.cporder = 2;
appl.assignsuffix = '_pn';
clear prop
prop.analysis='eigen';
appl.prop = prop;
clear equ
equ.rho = {1300,1190};
equ.thickness = 10000;
equ.nu = {0.38,0.341};
equ.E = {4.11e9,6.26e9};
equ.ind = [1,2];
appl.equ = equ;
fem.appl{1} = appl;
fem.frame = {'ref'};
fem.border = 1;
fem.units = 'SI';

% Coupling variable elements
clear elemcpl
% Extrusion coupling variables
clear elem
```

```
elem.elem = 'elcplextr';
elem.g = {'1'};
src = cell(1,1);
clear bnd
bnd.expr = {{'u',{},{}},{'v',{},{}},{{},'u',{}},{{},'v',{}}};
bnd.map = {{'1','1','1'},{'1','1','1'},{'1','1','1'},{'1','1','1'}};
bnd.ind = {{'1','3'},{'2'},{'4','5','6','7'}};
src{1} = {{},bnd,{}};
elem.src = src;
geomdim = cell(1,1);
clear bnd
bnd.map = {{{},{},'2'},{{},{},'2'},{{},'3',{}},{{},'3',{}}};
bnd.ind = {{'1','2','3','4'},{'5'},{'6','7'}};
geomdim{1} = {{},bnd,{}};
elem.geomdim = geomdim;
elem.var = {'uconstr_x','vconstr_x','uconstr_y','vconstr_y'};
map = cell(1,3);
clear submap
submap.type = 'unit';
map{1} = submap;
clear submap
submap.type = 'linear';
submap.sg = '1';
submap.sv = {'4','5','6'};
submap.dg = '1';
submap.dv = {'1','2','3'};
map{2} = submap;
clear submap
submap.type = 'linear';
submap.sg = '1';
submap.sv = {'3','6'};
submap.dg = '1';
submap.dv = {'1','4'};
map{3} = submap;
elem.map = map;
elemcpl{1} = elem;
% Point constraint variables (used for periodic conditions)
clear elem
elem.elem = 'elpconstr';
elem.g = {'1'};
clear bnd
bnd.constr = {{'0','0','uconstr_y-(u*exp(i*k_y*2*d))','vconstr_y-(v*exp(i*k_y*2*d))'}, ...
  {'uconstr_x-(u*exp(i*k_x*l))','vconstr_x-(v*exp(i*k_x*l))','0','0'}};
bnd.cpoints = {{'2','2','2','2'},{'2','2','2','2'}};
bnd.ind = {{'5'},{'6','7'}};
elem.geomdim = {{{},bnd,{}}};
elemcpl{2} = elem;
fem.elemcpl = elemcpl;

% Multiphysics
fem=multiphysics(fem);

% Extend mesh
fem.xmesh=meshextend(fem);

% Solve problem
fem.sol=femeig(fem, ...
               'conjugate','on', ...
               'solcomp',{'u','v'}, ...
               'outcomp',{'u','v'}, ...
               'neigs',maxfreqs);

% Save current fem structure for restart purposes
fem0=fem;

%disp(sprintf('eigenvalue %E', fem.sol.lambda(1)*i/2/pi()))

%obtaining a vector populated by all of the eigenfrequencies up to the
```

```
    %maximum number set by maxfreqs
    eigcnt=1;
    while eigcnt<(maxfreqs+1)
        Eigfreqs(1,eigcnt)=fem.sol.lambda(eigcnt)*i; %Now omega since not divided by /2/pi

        titleinfo=sprintf('k_x=%f omega = %f Surface: Total Disp [m] Arrow: Disp
[m]',k_x(1,kcnt),Eigfreqs(1,eigcnt));

        % Plot solution
%         postplot(fem, ...
%                  'tridata',{'disp_pn','cont','internal'}, ...
%                  'trimap','jet(1024)', ...
%                  'arrowdata',{'u','v'}, ...
%                  'arrowxspacing',15, ...
%                  'arrowyspacing',15, ...
%                  'arrowtype','arrow', ...
%                  'arrowstyle','proportional', ...
%                  'arrowcolor',[1.0,0.0,0.0], ...
%                  'solnum',eigcnt, ...
%                  'title',titleinfo, ...
%                  'axis',[-25,1+25,-25,2*d+25,-1,1]);
%         imgname=sprintf('L128_50-50_k%iEig%i', kcnt, eigcnt);
        %saveimage(imgname)
        eigcnt=eigcnt+1;
    end

    Eigfreqs=real(Eigfreqs);
    DataMatrix(kcnt,:)=[k_x(1,kcnt) Eigfreqs];
    kcnt=kcnt+1;
    %asdf1=sprintf('L128_50-50_k%fEig%f', k_x(1,kcnt), Eigfreqs(1,1))

end

%save L128_50-50.txt DataMatrix -ascii -double
%saving the data
           filename='Figure4Data_FractPC-Omega.txt';
           form = '%15.7e';
           fid = fopen(filename,'wt');
           fprintf(fid,'k Omega1 Omega2 Omega3 Omega4 Omega5 Omega6 Omega7 Omega8 Omega9
Omega10 Omega11 Omega12 Omega13 Omega14 Omega15\n');
           plp = 1;
           while plp <= size(DataMatrix,1)
               str = num2str(DataMatrix(plp,:),form);
               fprintf(fid,'%s ',str(:));
               fprintf(fid, '\n');
               plp=plp+1;
           end
           fclose(fid);
```

Appendix C:

Research Related Artwork

The job of a researcher is not only to construct experiments and interpret results but also to communicate those results with others throughout the world. This often takes the form of written communications which are accentuated by the addition of pictures and figures which hopefully convey the results in a succinct but visually appealing manner. The figure below shows my attempt at creating cover art for the journal Nature Materials. The figure was adapted somewhat as my artistic sensabilities did not match those of the editors of Nature Materials.

Figure C.1: The initial submission for cover art – As our article on the color changing block polymers was set to be printed in the fall, I thought changing colors of leaves would make a nice cover. Here, the gel is patterned into the shape of a leaf and then exposed to solutions with differing pH causing a change in color. Pictures were taken of this leaf in the solutions and then digitally combined to form the picture above.

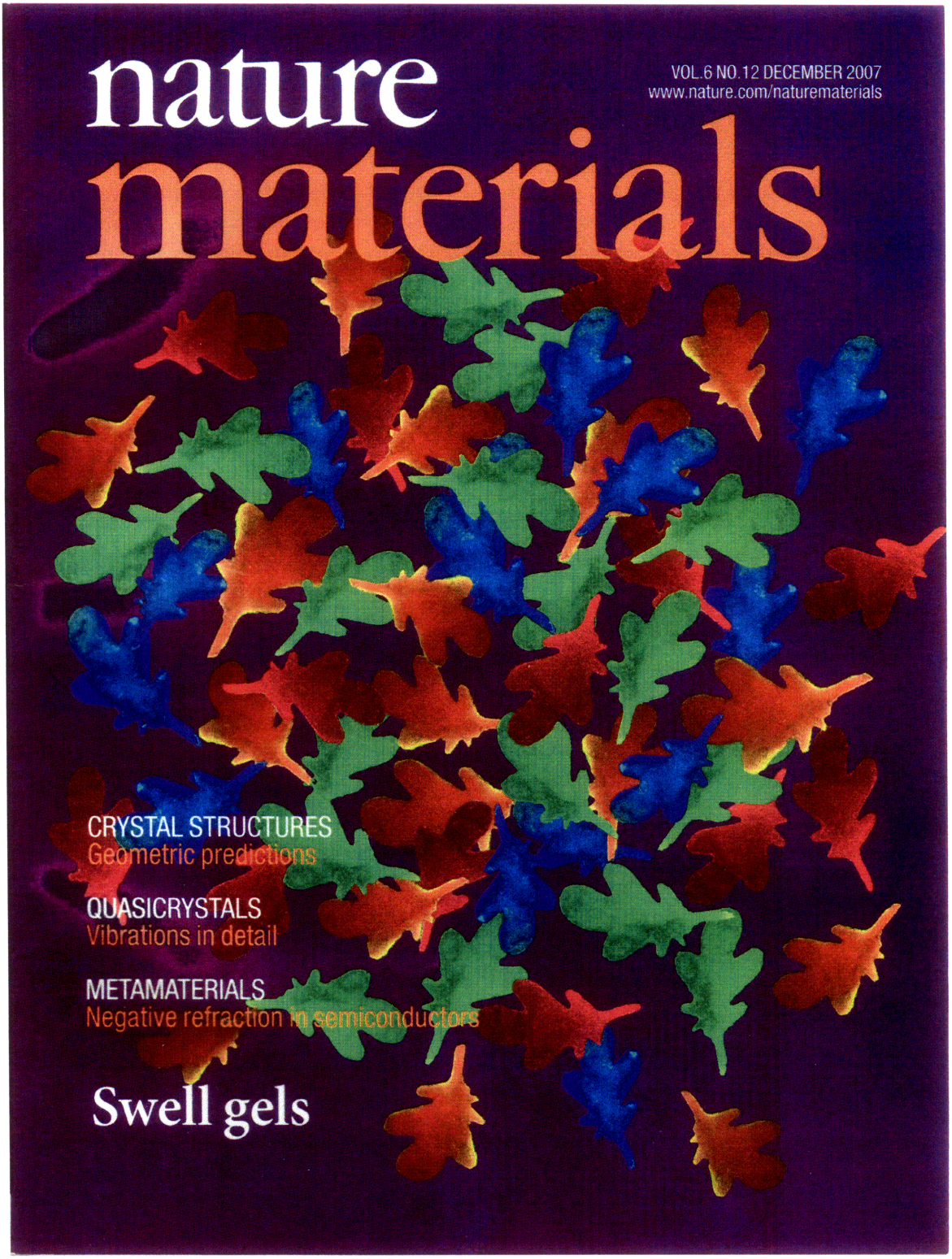

Figure C.2: The cover of the December edition of Nature Materials – My original artwork was modified to produce the cover seen above. Unfortunately the credit for the cover art went to the person who manipulated my image. Also, surprisingly, everyone who I have talked to likes the Nature Materials cover better than my original image suggesting my artistic tastes may not be aligned with general consensus.